Acoustic Emission Monitoring of Rolling Element Bearings Failures

Othman A Alshatti

Thesis submitted in candidature
of the degree of Doctor of Philosophy
at Cardiff University

Tribology & Performance Machines, Structures & Materials
Research Group
Cardiff School of Engineering
Cardiff University

2nd of January 2024

Abstract

Acoustic emission (AE) is a condition monitoring technique used for rotating machinery components that is gaining ground in the industrial field, due to its sensitivity to high frequency range, which makes it advantageous compared with traditional vibration techniques in the detection of incipient damage at the early stages of failure. This thesis presents an investigation using three types of similarly-sized cylindrical roller bearings, yet with different characteristics and qualities on a high speed test rig, with maximum rotational speed set at 5980rpm. The bearings under investigation are normal clearance SKF Types NU202ECP and NU202EM budget bearing, NU202ECP/C3 with higher radial clearance. This work aims to investigate the healthy bearings characterisation tests to deliver a well-defined foundation of the AE signal results, as well their operational lubrication regimes. Secondly, to investigate the underlying early stages and presence of naturally propagated damage within a rolling element bearing under heavily loaded operational conditions. Lastly, to compare the results from the 3 types of bearings. The healthy bearing characterisation tests identified that load and speed influenced the generated AE signal, with speed having a greater impact on the AE signal. It has also shown that the higher radial clearance bearing generated lower levels of energy excitation. The experiments principally operated within the hydrodynamic lubrication regime for both SKF bearings, while within the mixed lubrication regime for the budget bearing. The Run to Failure tests were then conducted to replicate natural failures in an accelerated yet controlled manner, by reducing the life expectancy of a roller bearing through exceeding the specified operational limits. It was shown that as the damage propagates, the AE signal levels increase. Based upon the 3 types of bearings adopted for the test, maximum AE activities indicating failure emerged into the life span of 66 hours for SKF NU202ECP, 88 hours for SKF NU202ECP/C3 and 22 hours for NU202EM. It is concluded that the data analysis process characteristically showed that the AE RMS signal is a robust technique and capable of perceiving present damage within the rolling element bearing.

Acknowledgments

Praise to God, The Almighty, who gave me the strength, patience and wisdom to fulfil this thesis in good health and peace of mind.

I would like to thank the Kuwaiti Ministry of Defence for giving me the opportunity and full support to pursue my doctoral degree. I would like to express my deepest gratitude towards my supervisor's Dr Alastair Clarke, Dr Davide Crivelli and Dr Rhys Pullin for their guidance, knowledge and support. As for Dr Alastair Clarke, it is an honour and a privilege to have worked with a man such as you.

I see myself fortunate to have been assigned in the Tribology office, where I have met great colleagues and friends, Dr Salem Almail who has pushed me to persue my PhD and recommended Cardiff University, Dr Simon Hutt, Dr Kostas Karras, Dr Aaron Cockeril, Dr Dewi Griffiths, Dr Ben Cahill, Dr Andrew Niland, Sujit, William Britton, George Hunt-Pain, Adrien Monteil and Paul Revill. Thank you all for everything especially Paul who I am highly indebted to for his support. Also, one must not forget to thank the technical workshops at the School of Engineering for their time, support and help.

Faisel Almudaihesh, Abdullah Alsabah and Ahmed Alghanim you have all made life in Cardiff an amazing and an unforgettable experience.

To my dear parents and siblings, thank you for everything. The continuous encouragement, the love and prayers during my life abroad in the past and the present, I love you all.

To my amazing in-laws thank you from all my heart for supporting me and my family throughout my PhD, you have definitely made life a lot easier while abroad.

To my beloved Moniah, whom I have been blessed with. No matter how much I write it will never stand up to what you have done for us. Thank you for standing by me and being there. Thank you for the patience, the will, the love and support to go through what we have been through. Thank you for our beloved sons Abdulmohsen and Ahmad.

Contents

1 Introduction 1

2 Literature Review 5

  2.1 Chapter Overview 5

  2.2 Unfolding Tribology 5

  2.3 Lubrication and its essence 7

  2.4 Rotating Machinery 8

    2.4.1 Rolling Element Bearings 9

    2.4.2 Gears 10

  2.5 Tribology of Rolling Elements Bearings 11

    2.5.1 Elastohydrodynamic Lubrication (EHL) 12

    2.5.2 Rolling Contact Fatigue Failure 15

    2.5.3 Other Failure Modes 17

  2.6 Condition Monitoring and its Necessity 20

    2.6.1 Condition Monitoring Techniques 25

    2.6.2 Vibration Monitoring 25

    2.6.3 Acoustic Emission Monitoring 26

  2.7 Rolling Element Bearing Monitoring from Vibrational to AE Methods 34

  2.8 Review on AE Monitoring of Rolling Element Bearings 39

  2.9 Conclusion 59

3 Equipment and Supporting Materials 61

3.1 Chapter Overview 61

3.2 Acoustic Emission Hardware 61

3.2.1 Acoustic Emission System 61

3.2.2 Sensors 62

3.2.3 Amplifiers 65

3.3 Software 66

3.3.1 Peak Value 66

3.3.2 Root Mean Square (RMS) 67

3.3.3 Fast Fourier Transforms (FFT) 67

3.3.4 Short Time Fourier Transform (STFT) 68

3.4 Tribological Numerical Analysis of Roller Element Bearings 70

3.4.1 Hertzian Contact 71

3.4.2 Load Distribution 74

4 High-Speed Rig Design and Experimental Set Up 80

4.1 Chapter Overview 80

4.2 High-Speed Test Rig 80

4.3 Design Modification on the High-Speed Test Rig 82

4.4 Data Acquisition 88

4.5 Bearing Operational Conditions: Load, Contact Dimension and Film Thickness 90

4.6 Experimental Procedure 93

4.6.1 Overview of Characterisation Experiment 93

4.6.2 Experiment Type 1: Bearing run in test 95

4.6.3 Experiment Type 2: Speed Increments under one load 95

4.6.4 Experiment Type 3: Load Increments under one speed 96

4.6.5 Experiment Type 4: Speed Increments, Load Held 96

4.6.6 Experiment Type 5: Load Increments, Speed Held 97

4.6.7 Locations of the Nano 30 AE Sensors 97

5 Healthy Bearing Characterisation Tests 99

5.1 Chapter Overview 99

5.2 Raw Signal Analysis 99

5.3 Acoustic Emission Statistical Parametrises 103

5.4 Acoustic Emission Sensitivity 110

5.5 Frequency Analysis 115

5.6 Conclusion of Healthy Bearing Characterisation Tests 121

6 Run to Failure Tests 122

6.1 Chapter Overview 122

6.2 Run to Failure Experimental Set-Up 123

6.2.1 Endured obstacles and setbacks to preliminary attempts and recertifications 124

6.3 Test Bearings Synopsis 134

6.3.1 First SKF NU202ECP Bearing 137

6.3.2 Second SKF NU202ECP Bearing 138

6.3.3 First SKF NU202ECP/C3 Bearing 140

6.3.4 Second SKF NU202ECP/C3 Bearing 141

6.3.5 First Budget Bearing NU202EM 142

6.3.6 Second Budget Bearing NU202EM 144

6.4 First SKF NU202ECP Bearing Run to Failure Test Results 145

6.4.1 AE RMS Analysis 145

6.4.2 Raw Signal Analysis 147

6.4.3 Short Time Fourier Transform (STFT) Analysis 148

6.5 Second SKF NU202ECP Bearing Run to Failure Test Results 150

6.5.1 AE RMS Analysis 150

6.5.2 Raw Signal Analysis 152

6.5.3 Short Time Fourier Transform (STFT) 154

6.6 First SKF NU202ECP/C3 Bearing Run to Failure Test Results 156

6.6.1 AE RMS Analysis 156

6.6.2 Raw Signal Analysis 158

6.6.3 Short Time Fourier Transform (STFT) 160

6.7 Second SKF NU202ECP/C3 Bearing Run to Failure Test Results 162

6.7.1 AE RMS Analysis 162

6.7.2 Raw Signal Analysis 164

6.7.3 Short Time Fourier Transform (STFT) 165

6.8 First Budget Bearing Run to Failure Test Results 167

6.8.1 AE RMS Analysis 167

6.8.2 Raw Signal Analysis 168

6.8.3 Short Time Fourier Transform (STFT) 170

6.9 Second Budget Bearing Run to Failure Test Results 172

6.9.1 AE RMS Analysis 172

6.9.2 Raw Signal Analysis 174

6.9.3 Short Time Fourier Transform (STFT) 176

6.10 Frequency Analysis of all tests 178

6.10.1 First SKF NU202ECP Bearing 178

6.10.2 Second SKF NU202ECP Bearing 180

6.10.3 First SKF NU202ECP/C3 Bearing 182

6.10.4 Second SKF NU202ECP/C3 Bearing 184

6.10.5 First Budget Bearing NU202EM 186

6.10.6 Second Budget Bearing NU202EM 188

6.11 Chapter summary 192

7 Conclusion 193

7.1 Critical Findings 193

7.2 Novelty 194

7.3 Further Work 195

References 197

List of Abbreviations

AE	Acoustic Emission
BPFI	Ball Pass Frequency of the Inner Race
BPFO	Ball Pass Frequency of the Outer Race
BSF	Ball Spin Frequency
CAE	Computer Aided Engineering
CBM	Condition-Based Maintenance
DLC	Diamond Like Carbon
EDM	Electric Discharge Machining
EHL	Elastohydrodynamic Lubrication
EI	Energy Index
FFT	Fast Fourier Transform
FTF	Fundamental Train Frequency
HCT	Hertzian Contact Theory
HDT	Hit Definition Time
HN	Hsu-Nielson
IE	Information Entropy
KS-test	Kolmogorov-Smirnov test
NDT	Non-Destructive Testing

PHM	Prognostics and Health Management
PLB	Pencil Lead Breaks
PVC	Pressure Viscosity Coefficient
RCF	Rolling Contact Fatigue
RMS	Root Mean Squared
RPM	Revolutions per Minute
RUL	Remaining Useful Life
SNR	Signal to Noise Ratio
SPM	Shock Pulse Meters
STRMS	Short Time RMS
VI	Virtual Instrument
WEA	White Etching Areas
WECs	White Etching Cracks
WSF	White Structure Flaking

Nomenclature

Symbol	**Description**	**SI Unit**
a	Acceleration	m/s^2
a_1	Life Modification factor for Reliabilty	-
askf	SKF Life Modification Factor	-
A_0	Asymmetric Mode	-
C	Basic Dynamic Load Rating	N
E'	Relative Modulus of Elasticity	N/m^2
F	Force	N
h_{min}	Minimum Fluid Film Thickness	m
L_{10}	L_{10} Life of a bearing	Million Revs
m	Mass	Kg
n	Life Equation Exponent	-
N	Number of Rollers	-
P	Equivalent Bearing Load	N
R	Relative Radius of Curvature	m
RPM	Revolutions per Minute	rpm
R_q	RMS Surface Roughness	m
S_0	Symmetric mode	
SF	Shaft Frequency	
μ	coefficient of friction	-
ū	Mean Speed	m/s
w'	Load Per Unit Length	N/m
α	pressure viscosity coefficient	
η	Oil viscosity under pressure	cSt
η_0	Oil viscosity at atmospheric pressure	cSt
λ	Lambda Ratio	-

1 Introduction

Condition monitoring has developed into a key tool within a range of industry sectors, where underproductivity due to unplanned maintenance or machinery breakdown would cause loss of revenue and in some cases worse, as human lives are endangered. Many dominant sectors in the industry have implemented online Condition-Based Maintenance (CBM) for critical components within a system as standardised practice. Rolling element bearings are a key component in the industrial machinery field, where it is imperative that they operate in an efficient and reliable manner. As a result, the manufacturing industries continue to adopt prognostics and health management (PHM) strategies to avoid undertaking costly unplanned maintenances (Jardine et al. 2006; Rastegari 2014; Cahill 2018).

Over the years, vibration monitoring techniques have been widely developed and form the backbone of monitoring the conditions of machinery. In recent years, acoustic emission has been introduced in the monitoring field and has gained significant attention from researchers (Elforjani and Mba 2010; Cockerill 2015; Naumman 2016; Alsadoon et al. 2019; Patil et al. 2020). Acoustic emissions are transient high frequency waves that are spontaneously released in solid materials instigated by rapid release of strain energy, ensuing irreversible changes as the deformation propagates through a surface. The early applications of the acoustic emission approach were primarily for non-destructive testing of materials. Subsequently, its application was expanded in the field of condition monitoring for a broad assortment of rotating machinery such as bearings, gearboxes, pumps, etc.

Researchers have established that acoustic emission is generated by contacting surfaces in relative motion, however the frequency and amplitude levels differ depending on the surfaces in contact. For rolling element bearings, where rotational speed and loads can be excessive, subject to the operational conditions proper lubrication is deemed crucial, as tragic damage threatens the bearing components. Elastohydrodynamic Lubrication is a particular regime of lubrication mechanism that appears in concentrated contacts that are heavily loaded. The crucial element of

Elastohydrodynamic regime is that the relative motion and geometry of the contacting bodies entrains a thin film of highly pressurised oil into the contact zone generated by means of elastic deformation of the surfaces. In normal operational conditions, this film thickness could significantly change as it hinges on several variable parameters, such as temperature, load and speed, but is typically of the order of a few microns at best. Whilst much research has been performed to corroborate the advantages of acoustic emission over vibration, substantial efforts were conducted with emphasis on artificially seeded defects.

1.1 Aims of the study

This work aims to perform healthy bearing signal characterisation tests under normal operational conditions and investigate the AE signals, as well as the consequential impact of lubrication regimes. As the majority of previous research focused on artificial defects as opposed to natural damage propagation, the second aim of this work was to investigate the underlying early stages and presence of naturally propagated damage within a rolling element bearing under heavily loaded operational conditions carrying out life tests. This thesis also aims to demonstrate the benefits of using AE as a condition monitoring technique on a variety of test bearings, each incorporating unique qualities. In addition, to determine if the support bearing AE signals would aid in the perceiving naturally failed bearings from the test bearing.

1.2 Objectives

This thesis aims to expand on the research topic of condition monitoring of roller bearings through:

- Investigating the generation and characteristics of AE by performing healthy bearing characterisation test on three different types of bearings on a modified high speed test rig, each bearing incorporating different qualities yet similar size.

- Demonstrate the AE sensitivity as a technique, determining the effect of operational condition such as speed, load, lubrication regimes, reliability and repeatability on the high speed test rig set up procedure, as well as the response of AE to a variety of natural defects.

- Create a meaningful data base from which further analysis work can be performed in future analysis.

1.3 Novelty Statement

This research presents novelty in the following areas:

- Contributes to the discussion of how speed, load and Lambda ratio contribute to the generation of AE, as well as increases the knowledge surrounding these variables through extensive tests on the characterisation of a healthy bearing.

- Draws comparisons between the AE signals between the test bearing and the support bearing, as the majority of previous investigations focused solely on the test bearing results.

- Demonstrates how the frequency analysis of AE can be used in the analysis of roller bearing in the detection of damage growth, as the majority of previous investigations focused on artificially seeded defects.

- Demonstrates the sensitivity off AE in detecting changes caused by natural and progressive damage in naturally failed bearings.

- Demonstrates that the increasing complexity of test rigs introduces a number of challenges and obstacles that may affect the application of AE to wider industries.

1.4 Thesis Structure

The thesis is structured as follows. Chapter 2 discusses the surrounding literature of the aforementioned topics in more detail. Chapter 3 focusses on the relevant experimental equipment used for the research, as well as the derivation of applied equations to define the tribological conditions of the mechanical components investigated. Chapter 4 describes the test rig set up and the experimental procedure for the healthy bearing characterisation experiments. Chapter 5 presents the healthy characterisation experiments, results and discussion distinct to each type of bearing. Chapter 6 presents the Run to Failure Tests, setbacks, further modifications to the test rig, further specific results for each bearing. Chapter 7 concludes with a summary of the critical findings, the novelty of the research as well as offering proposals for future work within the subject.

2 Literature Review

2.1 Chapter Overview

This Chapter reviews the literature surrounding this thesis. It begins with the history of tribology and how it evolved. Then, the reader will be introduced to the fundamental components of rolling element bearings, including a brief explanation of their development along with common applications where knowledge vis-à-vis their condition is considered as critical. Following this, discussion on the various methods of condition monitoring and how essential they are in modern industry are reviewed with the focus on AE. The chapter will carry on discussing the current progressive techniques of condition monitoring used to detect damage within such bearings and a brief history of AE techniques and applications.

2.2 Unfolding Tribology

The word ‘Tribology’ originated from a Greek word ‘Tribos’, which means rubbing (Bhushan 2013). Jost (1992) stated that tribology, as a term and concept, was initially enunciated in a British Government report as early as 1966 published in the journal of Industrial lubrication and tribology, where the department of education and science reported that tribology is well-defined as, “The science and technology of interfacing surfaces in relative motion and practices related thereto”. In other words, the simplified scientific interpretation would be the science of rubbing. In modern days, it is acknowledged as the study and science of friction, lubrication, and wear. Bhushan (2013) also described tribology as the art of employing operational analysis to matters related to economic consequences, maintenance, reliability, and principally wear of technical equipment; the scope of tribology is tremendously vast right from domestic equipment to the highest end of modern machineries. To comprehend tribology and its remarkably complex surface interaction entails knowledge of diverse disciplines including materials science, heat transfer, rheology, thermodynamics, solid and fluid mechanics, applied mathematics, physics, chemistry, machine design, lubrication, consistency and performance.

Dowson (1998) reported that the term tribology is quite novel, nevertheless the study or practices of tribology is of an earlier time than the records suggest. Throughout the Palaeolithic age which dates from over 2 million years ago, tools made for drilling holes were fixed with bearings, typically these bearings were made from either antlers or bones. Similarly the use of stones to grind cereals along with potters' wheels necessitated some type of bearing arrangement (Davidson 1957). In addition, a ball thrust bearing was discovered in Rome near Lake Nemi, which approximately dates to 40 AD. Apparently, our predecessors used wheels since 3500 BC and that the reduction of friction throughout translationary motion was a concern since then.

Ancient awareness of friction and lubrication was confirmed by devices such as sleds lubricated with water utilised to transport large blocks of stones intended for substantial structures. Figure 2-1 shows a sledge operated circa 1880 BC, to transport a massive statue by prehistoric Egyptians. In addition, Dowson (1998) made a remarkable calculation: the painting from El-Bersheh which illustrates 172 men who he assumed could exert the average force of 800 N, giving a total dragging force of 172 x 800 N, or 137.6 kN. Assuming the weight of the colossus is 600 kN, he calculated the coefficient of friction as $\mu = 137.6 / 600 = 0.23$ and compared it with that of wet wood-on-wood ($\mu = 0.2$), concluding that "the sledge was indeed sliding over lubricated planks of wood". A worker also standing in front on the sled is supporting or guiding the monument, who could have been one of the most primitive lubricant employers, as another seems to pour some kind of liquid lubricant in front of the sled. The confirmation of lubricant usage ages ago was found in an Egyptian Tomb, as animal fat substances were used as lubricant in a chariot's wheel bearing.

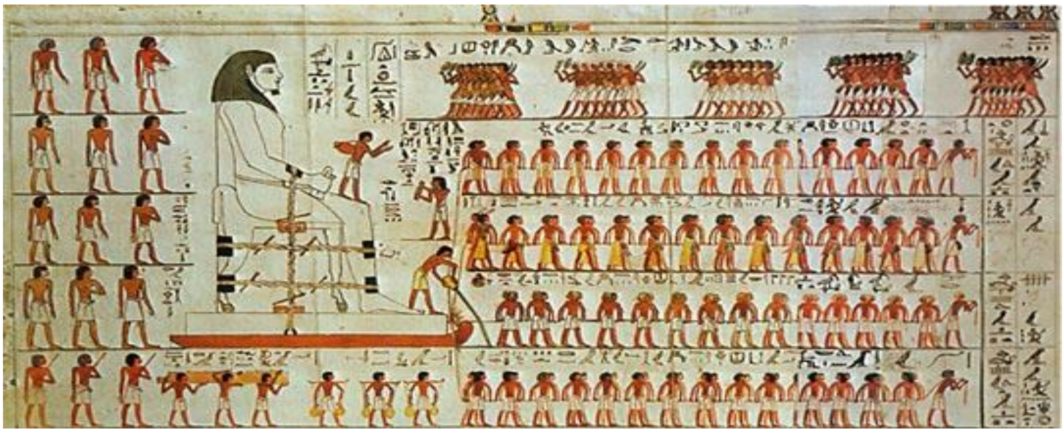

Figure 2-1: Egyptians moving colossus by using Lubrication, El- Bersheh, circa 1880 BC (Bhushan, 2013).

Tribological principles were also used by military engineers to design war machinery along with methods of reinforcements during and after The Roman Empire. A systematic approach towards friction was primarily proposed by Leonardo da Vinci (1452-1519). Leonardo da Vinci deduced the guidelines governing the motion of a rectangular block sliding over flat surface. He also introduced the ratio of friction force to normal load which is the core concept of the friction coefficient. Paradoxically, there is no existing significant indication of influence from his theory to tribologists until halfway through the twentieth century, the reason could be that the work of da Vinci was unpublished for many years (Hutchings 2016). In 1699, French physicist Guillaume Amontons revived the laws of friction through the analysis of sliding two flat dry surfaces (Amontons 1699). He inferred that frictional force is directly proportional to the normal load and displays resistance at a sliding interface. He correspondingly proposed that the summation of friction force does not rely on the apparent or visible contact area. Charles Augustine Coulomb, also a French physicist, likewise confirmed the observation noted by Guillaume Amontons. Coulomb also contributed to the third law of friction, which claims that when motion starts then the force of friction is independent of velocity. Coulomb henceforth differentiated between static and kinetic friction (Coulomb 1785).

2.3 Lubrication and its essence

According to Schey (1984), friction as well as wear concerning two or more moving contact surfaces that are relative to each other could be reduced by means of appropriate lubrication with the correct properties, otherwise resulting in defects or damage. There is a significant difference between friction and wear, as friction is an acting force opposite to the direction of relative motion. The friction force is the force required to break the adhesive bonds between surface micro-asperities and the deformation (or ploughing) force required to make possible grooves when solid bodies of different hardness move against each other. Frictional force is related to heat production and energy consumption. In contrast, the process of ongoing loss of surface material caused by motion of the two surfaces is well known as wear. This is due to numerous reasons, such as adhesion, abrasion, tearing of asperities, fatigue, poor lubrications, and corrosion etc. These may influence or cause the surface structure, dimensions, alignment and mass of the body to be reluctantly modified.

Friction and wear are not advised to be reduced in all conditions, occasionally reducing wear alone may be beneficial for instance in oil bath clutches or perhaps friction requires reduction and not wear in such circumstances like polishing and grinding operations. The desire to reduce both friction and wear in numerous applications can be realised by means of lubrication. Appropriate lubrication benefits equipment, machinery and mechanisms to function suitably with enhanced performances, optimized energy utilisation and decreased wear. On the other hand, consequences of poor lubrication will effectively lead to deterioration of the interacting surfaces and eventually components, leading to premature breakdown of parts, equipment or the entire system. These damages would reduce the running hours of factories, military machinery, railway systems, wind turbines and so on. Financial benefits can be grasped when the lubricants are correctly applied which results in preservation of materials, energy saving, lesser maintenance in addition to a positive effect on the environment (Wilson 1998).

Original practices of the lubrication process have been recognised since ancient times also found during archaeological studies. Modern lubrication arose since the second half of the 19th century due to rapid industrialisation, as the first governing equations of hydrodynamic lubrication were defined during this period. Since then, extensive investigative efforts and research have been carried out endlessly to comprehend and develop the knowledge on lubrication. During modern analysis it was found that different areas are yet to be studied with capable probable applications. It is obvious that the field of lubrication requests an ongoing research due to its vast scope (Reeves and Menezes 2016).

2.4 Rotating Machinery

Rotating machinery is an extensive phrase covering a wide range of mechanical systems utilised within numeral industrial sectors. Although machines differ individually in their overall design in this case bearings and gears, the common presence of fundamental components exists to facilitate transmission of power and energy during relative motion.

2.4.1 Rolling Element Bearings

Rolling element bearings are among the most frequently encountered and principal components in the vast majority of rotating machinery, their reliability and load capacity being important for the overall machine performance (Tandon and Choudhury 1999). Bearings are manufactured in a wide range of sizes and shapes, as their fundamental design is tailored to their specific applications. In general, bearings are categorised into two categories, plain bearings and rolling element bearings. The former, also known as sliding bearing, is the simplest type of bearing - as the name suggests plain. It is formed when two conformal contact areas are used to move relatively to one another, habitually with a liner or sacrificial bush between them. These bearings are often used in locations such as oscillating roles e.g. door hinges or more complex usage such as suspension rod ends, where it is difficult to provide lubrication. Either hydrostatically-generated or hydrodynamically-generated lubricant films are used for some forms of plain bearings to separate the two conformal bodies (Lin 1996). In addition, layers of dry lubricants such as PTFE are often applied to one of the contacting surfaces where liquid lubrication is difficult.

Rolling element bearings, on the other hand, are composed of an inner and outer raceway, separated by a number of rolling elements e.g. balls or rollers that are in most cases constrained within a cage Figure 2-2. In the absence of a cage, generally referred to as ‘full complement’ bearings, the additional space tolerates further balls or rollers to be added, hence the load capacity of the bearing increases. The rolling elements within the bearing are various in shape, such as balls or cylindrical, tapered, or spherical rollers. The arrangement of the rolling elements can be in a single or double row, whether they are caged or not to accommodate higher radial loads, as well as being angled or tapered to be able to sustain and adapt to axial force or displacement.

Typical SKF bearings are manufactured to the specification of ISO 683-17 (2014) from through-hardened carbon chromium steel (100Cr6), containing approximately 1%

carbon and 1,5% chromium. For some of the applications, the surface can be coated with Diamond Like Carbon (DLC) coatings that may improve the friction and wear properties of the bearing, or ceramic materials could be used where high temperatures or speeds are potentially encountered.

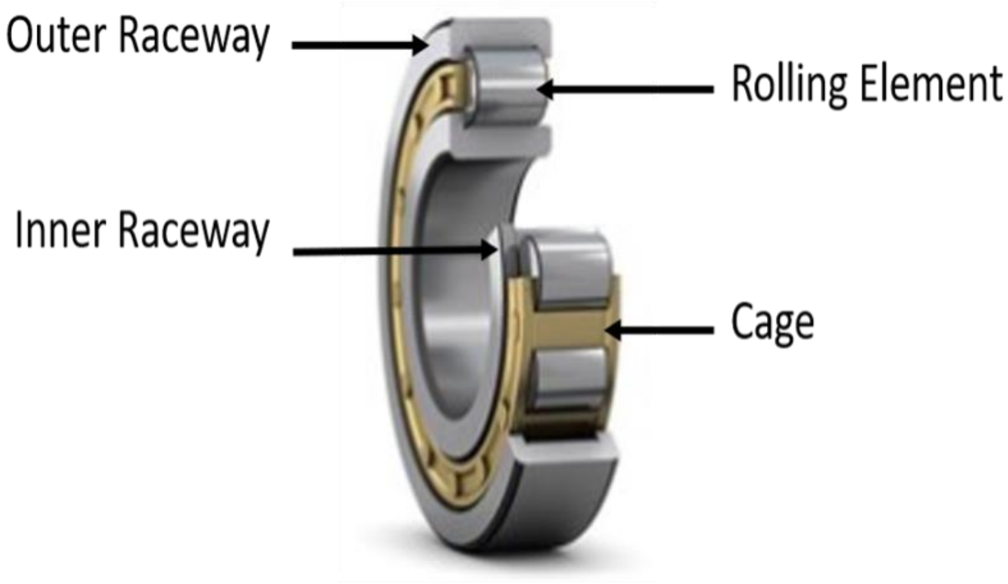

Figure 2-2: Single Row Cylindrical Bearing (SKF, 2018).

2.4.2 Gears

The Antikythera mechanism is an ancient mechanical Greek device which calculates the lunar and solar calendars, and is one of the oldest known uses of gears (Freeth et al. 2006). Despite the 2000 year old device, and the innovations made through all fields of modern engineering, gears are still a key mechanism used to control and transfer mechanical power in modern machinery. Over and over again gears are found within rotating machinery as well as roller bearings. The common use of gears is to enable the transmission of power and rotation between shafts, convert a form of energy or paired together in ratios to increase or decrease torque and speed governed by its application. Comparably to bearings, gears also come in a variety of designs and are capable to transmit power between both perpendicular and parallel shafts. Typical gear types, as shown in Figure 2-3, include spur gears, helical gears, bevel gears and worm gears.

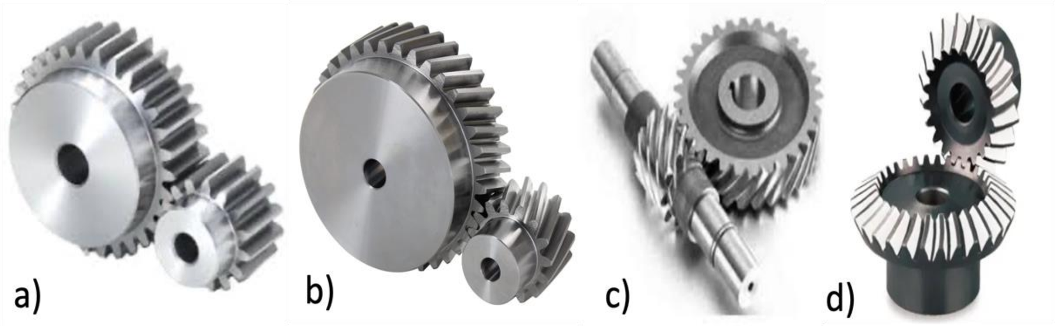

Figure 2-3: Types of gears a) Spur Gear, b) Helical Gear, c) Worm Gear and d) bevel gear.

2.5 Tribology of Rolling Elements Bearings

The study and science of friction, lubrication and wear known as tribology, reveals that metallic surfaces are certainly not perfectly smooth and that they possess numerous peaks (asperities) and valleys. Rolling element bearings depend on the relative sliding and or rolling of two interacting bodies and when these bodies sustain an applied force, consideration of the contact mechanics shows that asperities create the initial contact leading to plastic deformation due to the degree of stresses involved resulting in impending fractures or failures. The actual surfaces tend to have a varied topography across a wide range of scales. Therefore, the surface features are characterised in three lengths scales: form, waviness and roughness. The basic shape is expressed by the form, in some cases spherical or cylindrical, the waviness depicts the deviation within the form from its ideal shape in other terms ‘tolerance’ and the fine texture or surface finish is defined by the roughness. Figure 2-4 illustrates the form, waviness and roughness of a simulated surface. In terms of wavelengths, the form is the wavelengths which are of a similar scale to the dimensions of the component being measured. The roughness is usually separated from the measurement using a filter with a cut-off length chosen based on the likely surface finish. For the surfaces seen in these bearings, this would typically be 0.8 or 0.25 mm – meaning that the roughness is all wavelengths shorter than these lengths.

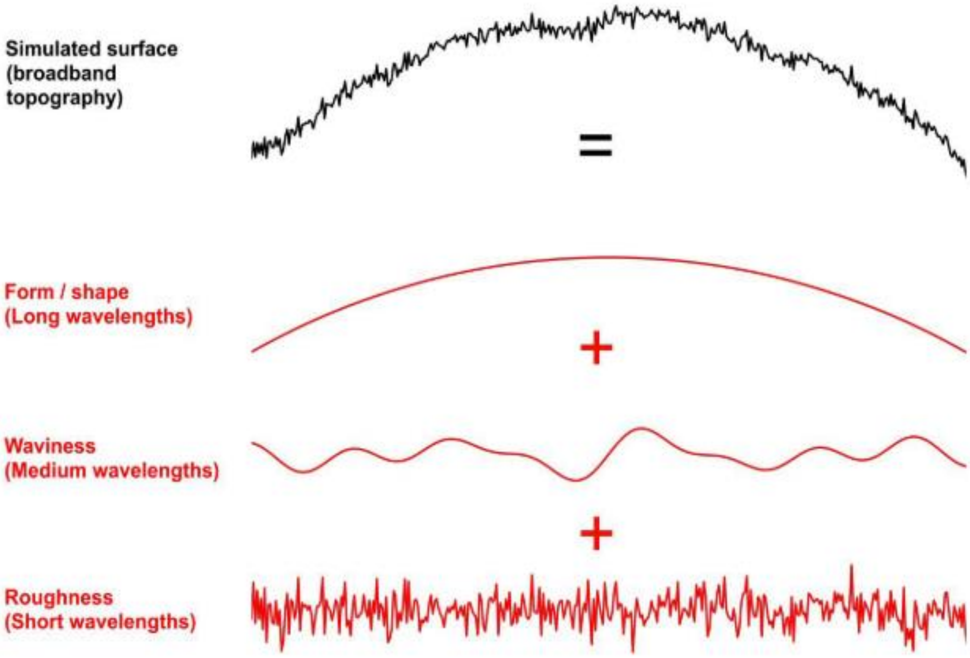

Figure 2-4: Simulated surface roughness sample representing form, waviness and roughness.

2.5.1 Elastohydrodynamic Lubrication (EHL)

To defy excessive wear, a form of oil lubricant is required, forming a thin film to aid the separation of the two bodies in contact with relative motion against one another. As the oil is driven into the converging gap amidst the bodies it comes to be pressurised, establishing a thin film (a few microns in thickness) to separate the two bodies. According to Zhu and Wang (2011) various lubricated machine parts, where the contacting surfaces do not conformally fit to one another have small but very highly-pressurised lubricated areas carrying the entire load through the formed oil film. Some settings of non-conformal surfaces are cam and followers, gear teeth transmitting load and rolling elements bearings. The concentrated loads lead to great contact pressures typically 1-2 GPa, resulting in an elastic deformation of the two surfaces which is noteworthy as it promotes the generation of a suitable oil film. This lubrication phenomena is known as elastohydrodynamic lubrication (EHL). Dowson and Higginson (1959) achieved the first numerical elastohydrodynamic solution for a line contact. They then fitted a regression equation to their numerical results to enable the rapid calculation of minimum film thickness without recourse to computers which were, at the time, of low power and scarce. Henceforth, the minimum thickness of this oil film between a smooth idealised raceway and a cylindrical roller is calculated by the Dowson and Higginson formula, Equation (2.1),

$$h_{min} = \frac{\alpha^{0.6}(\eta\bar{u})^{0.7}(E')^{0.03}R^{0.43}}{(w')^{0.13}} \tag{2.1}$$

where h_{min} is the minimum fluid film thickness, α is the lubricant's pressure viscosity coefficient (PVC), η_0 is the lubricant's viscosity at ambient pressure, $\bar{u}$ is the mean speed within the contact of the two bodies, E' is the relative modulus of elasticity, w' is the load per unit length and R is the relative radii of the contacting bodies. The formula includes the pressure-dependence of η, the oil viscosity, which escalates exponentially with pressure p, where α is the lubricant's PVC and η_0 is the viscosity at atmospheric pressure and is calculated by the Barus law as follows in Equation (2.2),

$$\eta = \eta_0 \, e^{\alpha p} \tag{2.2}$$

The Tallian parameter Lambda λ (Tallian 1967), is a commonly used to determine the lubrication regime, and represents the relationship between the minimum film thickness and the bodies' composite surface roughness where Rq_1 and Rq_2, are the root mean squared roughness of the two surfaces, is calculated in Equation (2.3),

$$\lambda = \frac{h_{min}}{\sqrt{R_{q1}^2 + R_{q2}^2}} \tag{2.3}$$

As the value of h_{min} escalates, the two surfaces are forced away from one other, resulting in reduced asperity contact. Figure 2-5 clarifies the different categories of lubrication regimes for contacting bodies along with the related change in friction, demonstrated by the Stribeck curve. Lambda is usually used to define the lubrication regimes present that describe the amount of friction and the capability of contacting bodies to be separated, which influences directly the wear behaviour of any specific lubricated system.

Characteristically, the lubrication regimes, by use of the λ parameter, are constructed as follows (Bowden and Tabor 1950; Lord and Larsson 2001; Spikes and Olver 2003;

Hamrock et al. 2004; Stachowiak and Batchelor 2006; Halme and Andersson 2010 and Balan et al. 2016): for boundary regime λ < 1, where λ ratio is very low and there is a large amount of asperities in contact and very high friction rate, as there is not enough lubricant film to effectively separate the two surfaces. The load is entirely carried by direct asperity contact. The second regime is known as the mixed lubrication regime, where the enlargement of fluid film thickness develops to be between 1 < λ < 3, where the number of asperities in contact and therefore friction are reduced significantly. The load in the mixed regime is carried by both a partial lubricant film and direct asperity contact. The third regime is known as EHL regime and occurs when 3 < λ < 5, it is then considered within this regime that the fluid film thickness is sufficient to force and separate the two surfaces apart ensuring no asperity contact. However, the friction level rises due to the shearing of the fluid within the contact area. Finally, during the hydrodynamic lubrication regime the surfaces are separated completely by the full fluid film, as the film is thick in contrast to the surface roughness and is thicker than the EHL conditions. It occurs when λ > 5 during rolling bearings contact within the caged rolling elements and between roller ends. The oil film thickness in hydrodynamically lubricated regime provides tribosystems with a significant amount of damping for dynamically loaded machinery.

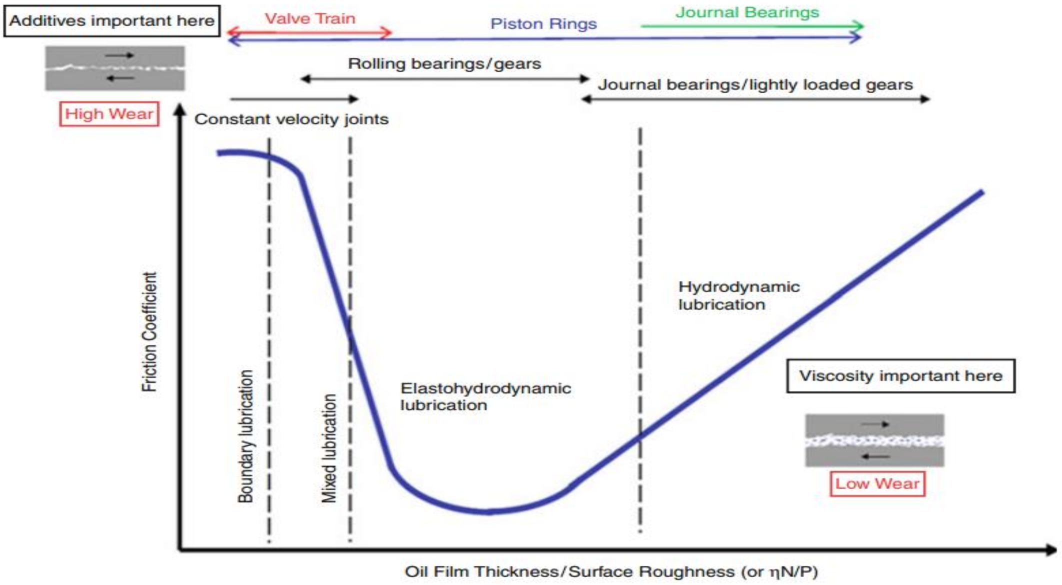

Figure 2-5: Stribeck Curve illustrating the lubrication regimes present within lubricated contacts (Jane Wang and Chung 2013).

2.5.2 Rolling Contact Fatigue Failure

"Failures other than that caused by classical rolling-element fatigue are considered avoidable if the component is properly designed, handled, installed, and not overloaded"

- (*Zaretsky et al. 1996)*

Principal aspects that determine a bearing's fatigue life (Liu et al. 1975): spalling is the result of subsurface or surface fatigue, where the material is physically detached following crack initiation below the contact area. Spalling is caused by surface irregularities and due to distress produced by inadequate lubrication or surface roughness. Spalling is predominantly a plastic deformation process. When these fractures are formed in the running surfaces, the rolling elements travel over these cracks, and pieces, or flakes, of material break away. Spalling is also known as "peeling" , "flaking", or "pitting". This type of failure can occur on the rollers, outer, inner raceways and is progressive and once initiated, it will spread as an outcome of further operational conditions (Ding 1997).

Rolling contact fatigue (RCF) is responsible for the failure of rolling element bearings, camshafts, gears and identified as cracking or pitting limited to the near-surface layer of bodies in rolling/sliding contact. There is an increased demand for improved life, reliability and load bearing capacity of bearing materials and future applications call for their use in more hostile environments (Stewart 2002). RCF may also be defined as damage process of contact surface or subsurface of rotating components, bearing long term alternating stress (Li 2013). RCF is a classical failure mode in rolling element bearings, set off by the cyclic loading and plastic deformation beneath the material surface as the rollers roll over a raceway within the loaded area (Neale 1995). The plastic deformation materialises at a typical depth equal to the position of the maximum shear stress in a Hertzian contact, which is roughly 0.7 times the contact dimension below the surface. RCF is regarded as a balanced diffusion of flaking across the loaded area of the race with a ripple or conchoidal pattern as can be seen in Figure 2-6. Throughout repeated loads and boundary dislocations, subsurface cracks start to form and as the cracks stretch to the surface, material comes to be dislodged.

The dislodged material may well over-roll, growing the stress concentrations on the raceway and hence producing an accelerated wear process, if not swiftly flushed out by lubrication.

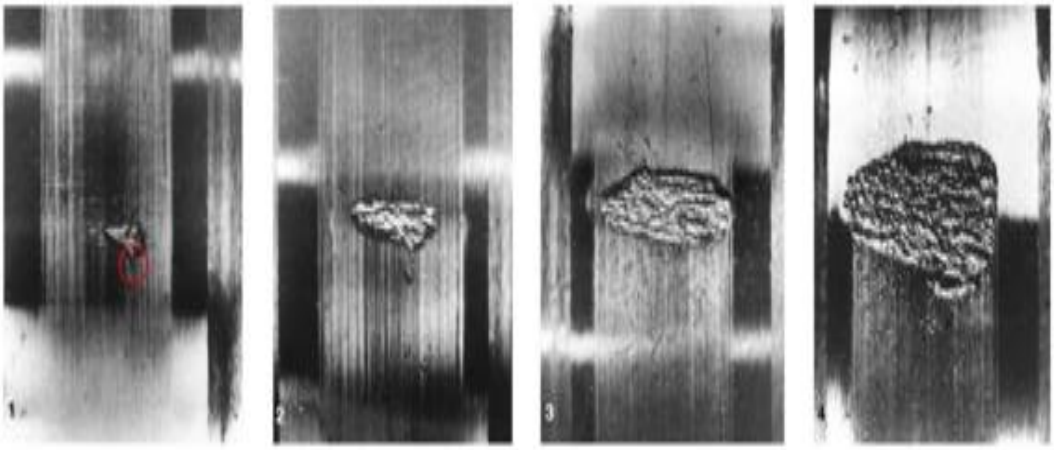

Figure 2-6 Progression of Fatigue Flake Damage of Rolling Bearings (MORALES-ESPEJEL and GABELLI 2015).

Lundberg & Palmgren (1947) had completed an abundant amount of statistical analysis on large data sets of natural failures of rolling element bearings, and these studies were used to produce ISO 281 (1990), a recognised standard to calculate the dynamic load ratings and rating life of a roller bearing. The most direct method to calculate bearing life is the L_{10} life, which solely depends on load and speed, where the L_{10} is the number of cycles of bearing rotation in millions of revolutions and assuming 90% reliability, and also where 10% of the roller bearings would theoretically fail. Of note, the L_{10} Life calculation does not consider lubrication, temperature and other key factors which can substantially affect bearing life. Proper handling, maintenance, treatment and installation are all simply assumed. That is why it is exceptionally difficult to foresee bearing fatigue and why less than 10% of roller bearings ever meet or surpass their calculated fatigue life (Rynearson 2022). Yet, both practical experience and laboratory tests demonstrate considerable variations in the fatigue life of identical bearings operating under similar conditions (SKF 2012), in some cases even when having identical roller bearings operating in the same operational conditions i.e., temperature, speed and load. It is possible to get different results of failures. The L_{10} Life Calculation is essentially obtained through an extensive and repetitive tests on a large number of bearings to reach such assumption. The L_{10} basic rating life is assessed through Equation (2.4),

$$L_{10} = \left(\frac{C}{P}\right)^{n} \tag{2.4}$$

where the basic dynamic load rating is *C*, the equivalent bearing load is *P* i.e. the load applied to the bearing during the investigation and n is an exponent of the life equation with two different values, for roller bearings n = 10/3 and for ball bearings n = 3, which was determined when the original rule was fitted and introduced (SKF 2012; Cockerill 2017). The basic dynamic load rating, C, is determined through extensive bearing testing and can be found in manufacturer's product data sheets. Ever since 1947, continuous research and investigation into the effects of material properties, lubrication purity and stresses have established better bases for the now improved life modification factor a_1 and is implemented in ISO 281 (2007). SKF, a leader in bearing manufacturing and is the world's largest bearing manufacturer (SKF 2017). As well as being the largest industrial distributor network in the industry with various locations encompassing 130 countries (SKF 2022). In addition, SKF is one of the top 5 vendors in the Wind Turbine Bearing Market from 2016 to 2020 (Technavio Research 2016). Respectively, SKF has the certainty in their bearing products to likewise provide their own modification factor known as a_{skf}, which similarly to ISO 281 (2007) takes account of the lubrication conditions but applies a superior safety factor founded on their manufactured bearing properties (SKF 2012). Accordingly, the latest life calculation for an SKF bearing is Equation (2.5),

$$L_{10} = a_1 \times a_{skf} \times \left(\frac{C}{P}\right)^{n} \tag{2.5}$$

2.5.3 Other Failure Modes

According to Fitch (2003) in Silent Assumptions of Bearing Reliability, there is an old saying that "bearings don't just die, they're murdered". This is essentially due to the bearing's operational conditions and includes the following, as well as their failure conditions illustrated in Figure 2-7:

- Excessive vibration, mechanical overloads on the bearing due to the misalignment.
- Exceeding the bearings dynamic load rating, known as overload.
- Overheating, oil starvation, moisture, incompatible lubricants, contamination due to debris – essentially changes in fluid properties.
- Inappropriate interferences, loose or tight fits regarding raceways, shaft and housing tolerances.

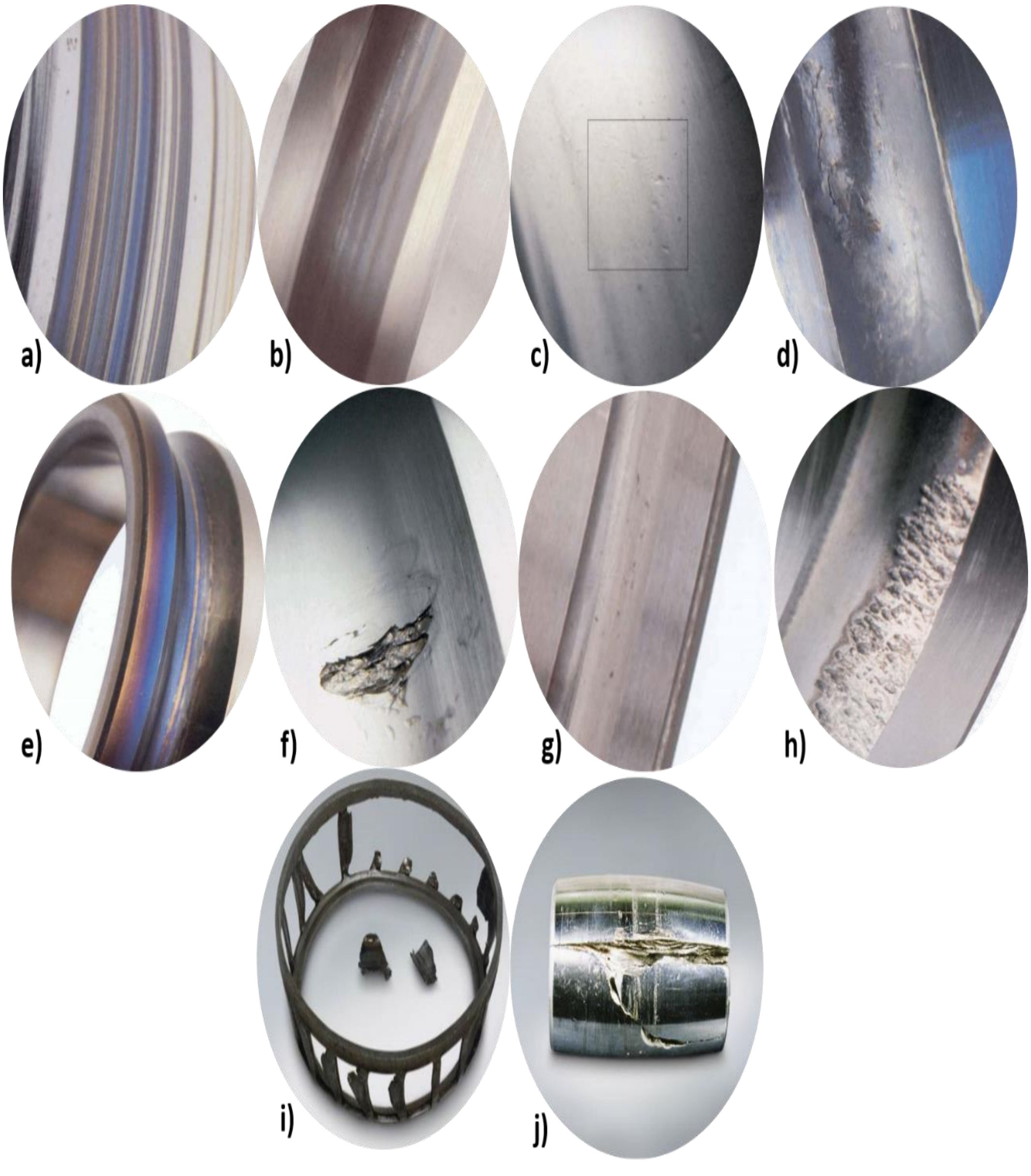

Figure 2-7: Bearing Failure Modes a) Tight Fit b) Loose Fit c) Contamination d) Lubricant Failure e) Overheating f) Normal Fatigue g) Misalignment h) Excessive Load i) Cage Failure and j) axial crack of roller - (Wysoclci and Feest 1997; NSK 2009).

Figure 2-7 demonstrates a range of bearing failures that are frequently found in the industry such as spalling or flaking of metal from surface, indentation or discoloration of raceway, roller cracking, cage failure and smearing of the raceway. Inadequate lubrication results in severe spalling on the raceway, in addition to an axial cracking of the roller which might be a result of overloading the bearing or inclusions within the steel itself. Some bearings, such as spherical roller bearings, are capable of operating effectively with misalignment due to the conformity between the raceway and its rollers. On the other hand, if the bearing is a cylindrical roller bearing and it is exposed to unnecessary misalignment, the radial load capacity is acutely reduced as the load becomes further concentrated near the end of the cylindrical roller. As this lessens the area of contact, the pressure (and therefore subsurface stresses) at the contact intensifies significantly.

One of the widespread failures in bearing raceways is white structure flaking (WSF) due to the formation of white etching cracks (WECs), typically ~ 1 mm below the contact surface. WECs are networks of microcracks associated with microstructural transformations or alteration called white etching areas (WEA) (Evans 2012). WECs are simply found recurrently in slow operating, heavily loaded bearings corresponding to those in wind turbine roller bearings (SKF 2018). Previous research proposed that the initiation and propagation mechanisms for WSF and WECs are due to: Surface instigation through two opposing mechanisms, subsurface initiation by non-metallic inclusions, adiabatic shear banding independent or including defects through impact events, cracks forming after microstructural changes occur, a multistage initiation of WECs as an effect of movement of carbon under shear stress and high localised energy (Gegner 2011; Evans 2013; Luyckx 2012; Bruce 2015; Gould 2016). This occurs typically at 1–20% of the bearing's L_{10} life, where the wind turbine lifetime is reduced from the anticipated 20 years to < 2 years (Richardson 2018). Figure 2-8 demonstrates 5 sections and how WEA spreads across the component, where the middle section is the origin of the WEA failure.

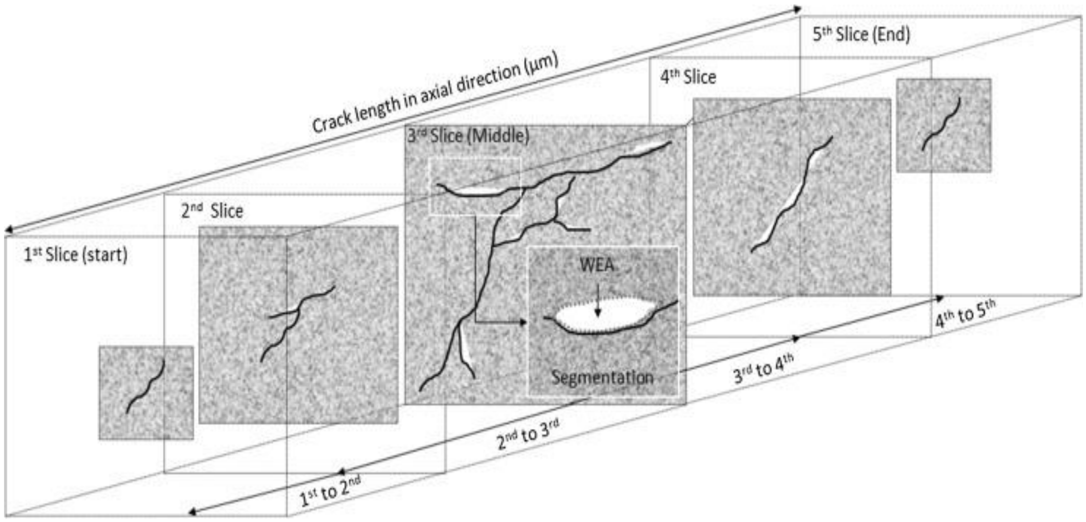

Figure 2-8: Illustration demonstrating the methodology of WEA volume measurements (Richardson 2018).

WECs has been exposed as one of the core cause of failure in numerous wind turbines roller bearings, and can be considered to be one of the most expensive technical failure modes for a wind turbine (Keller 2021). WECs is also a common cause of bearing failure in the gearboxes of wind turbines: around 60% of the industry's high speed bearing premature failures are caused by the phenomenon (Mobil 2020). Nevertheless, WECs have proven challenging to recreate at a benchtop scale; to date, no benchtop test has stated to recreate WECs using commercially available field lubricants (Gould 2019). This phenomenon has been investigated for years without yet reaching a justified cause of its occurrence (López-Uruñuela 2021).

Owing to tribological knowledge of friction and wear the following section will emphasise the motivation for undertaking condition monitoring and the essence of it.

2.6 Condition Monitoring and its Necessity

All products or systems are subject to failure or deterioration throughout their life cycle. A scheduled maintenance objective is to replace or overhaul components after their failure and keep a system or equipment in a condition in which it can accomplish its necessary functions by carrying out routine actions. For that reason, implementing a proficient maintenance strategy could allow industries to achieve their requirements such as maximum availability, enhance safety, high reliability and minimise the asset's life cycle costs as maintenance is a key factor of a systems lifetime. In order to achieve this, an adaptive strategy for these requirements in the form of CBM can be implemented. In fact, CBM is a maintenance platform based on the use of real time primary data collected to prioritise and optimise the upkeep of resources, in which tasks are arranged apropos to the asset's health status (Jardine et al. 2006).

With the dawn of the Digital Revolution, the world has reached unprecedented advanced leaps in terms of both existing technology and enhanced understanding of the sciences surrounding it. As further research and development is conducted, the present mechanical machinery continues to increase in complexity. Inevitably with advanced complexity pushing towards component longevity leads to greater costs, in both the required starting capital as well as operational and maintenance costs. In light of ever increasing requirements for system performance, condition monitoring emerged into a subject of extreme importance in recent decades, as industries attempt to improve reliability and reduce maintenance and downtime. Nowadays, engineers are able to hand-pick and tailor precisely what is needed in terms of a material's properties and characteristics, in ways such as exploiting surface coatings and toughness treatments and thus leading to sturdier and advanced capabilities of the surfaces and materials. With the aim of further improving the components design, use is made of Computer Aided Engineering (CAE) to simulate how a component could react to variable operating conditions. As well as empowering engineers to optimise the component's design to boost their resistance failure, CAE simplifies the process of calculating a component's theoretical lifespan, reducing the prospect of premature failure to the component. Nonetheless, as it is only a simulation through the use of CAE, the results are only accurate if the modelled parameters correspond to real life, even then a failure during the process is still possible from inherent randomness, mostly due to manufacturing variability and human error.

Condition monitoring as a whole is fundamental to energy generation industries, where not only is the demand growing but extraordinary pressure for the move to renewable and sustainable energy sources with the attempt to curb climate change with respect to global regulatory issues. The Compound Annual Growth Rate for onshore wind turbines in the next five years is 12%. Expected average annual installations are 110 GW, with a total of 550 GW likely to be built in 2023–2027. Growth in China, Europe and the US will be the backbone of global onshore wind development in the next five years (GWEC 2023). As the amount and size of the wind turbines escalates, the significance of reducing inspection and maintenance expenses has become extremely critical (García Márquez et al. 2012) and because of the access challenges and tough operating environments present for offshore wind turbines, greater reliability is a must when comparing them to their onshore counterparts (Yang et al. 2011).

A mechanical component’s failure in a wind turbine is never small nor inexpensive to restore. Not only would it influence the overall kilowatt-hour expenses but it calls for transporting engineers and technicians to the offshore site and dealing with repairs while offshore or, in worst cases, requiring to take out several tons from the massive wind turbine from the highly elevated stanchion (Hau and von Renouard 2006). To diminish the likelihood of unexpected failures, many high-value assets utilise a maintenance strategy set out with focus on maximising the assets life (Wiggelinkhuizen et al. 2008). Advanced methods of CBM gradually led to the emergence of PHM, with a broader framework and the use of new techniques, to extend remaining useful life (RUL) of a system, increase safety and maximise operations.

Principally, with compliance to (ISO/TR 13881:2000 2000), prognostics in the field of industry refers to “the time estimate for risk and failure of one or any existing and future failure events”. As for Health Management, it discusses the decision making competency to intelligently carry out logistics activities and maintenance based on diagnostics and prognostics records (Javed et al. 2015). Furthermore, it can be looked upon as an engineering discipline encompassing methods and technologies to evaluate the reliability of a component’s real life cycle conditions to determine the materialisation of a failure and alleviate system risk (Mathew et al. 2012). Concerning these definitions, PHM can be deemed as an empowering discipline for the CBM and it is commonly described with (OSA-CBM) architecture, the Open System Architecture for Condition-Based Maintenance (Lebold et al. 2002), which is set up of seven stages, as illustrated in the Figure 2-9:

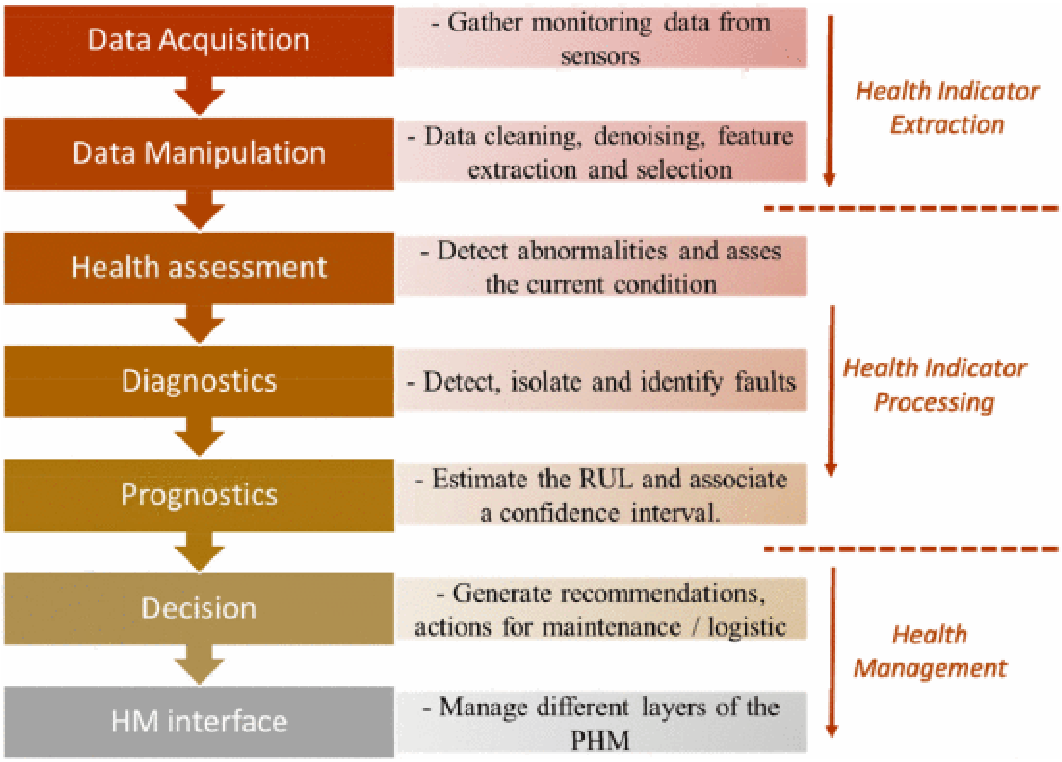

Figure 2-9: PHM architecture adapted from the ISO 13374 - Extracted from (Brahimi and Leouatni 2016).

Implementation of PHM has been made in a many industrial cases targeting a maintenance revolution. In the Military and Aerospace systems, for instance, PHM has been practiced for over 20 years with systems applications. During this past decade, the railway industry concentrated on maintenance matters and expressed a distinct interest in PHM systems. Similarly to wind turbines, railway maintenance, aerospace and military systems requires a large budget and extensive resources (Brahimi and Leouatni 2016).

Using the measures of RUL of a system or component acquired by the PHM, it is promising to change the maintenance plan away from corrective and towards a preventative plan. Originally the majority of industries utilised a corrective strategy, if unplanned then this strategy unfortunately is identified as run-to-break or failure-based maintenance. The details of different strategies can be found in Table 2-1.

Table 2-1 Distinct types of maintenance strategies adopted from (Cockerill 2017; Cahill 2018).

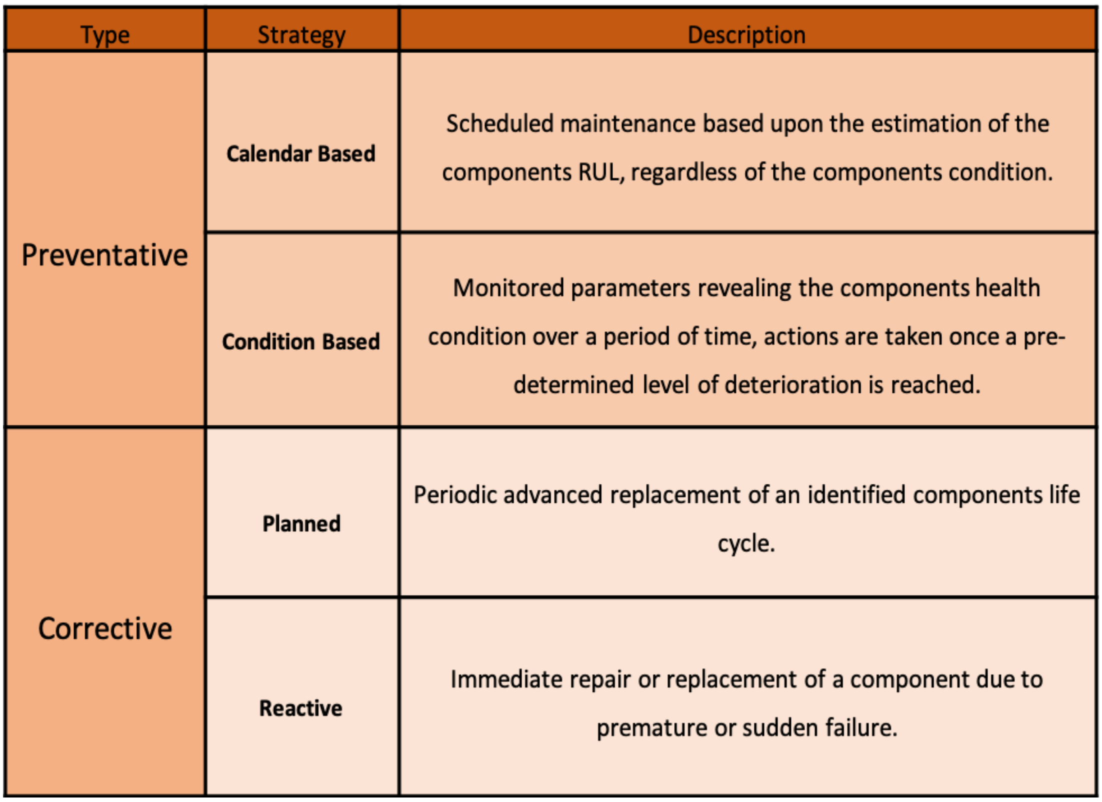

Type	Strategy	Description
Preventative	**Calendar Based**	Scheduled maintenance based upon the estimation of the components RUL, regardless of the components condition.
	Condition Based	Monitored parameters revealing the components health condition over a period of time, actions are taken once a pre-determined level of deterioration is reached.
Corrective	**Planned**	Periodic advanced replacement of an identified components life cycle.
	Reactive	Immediate repair or replacement of a component due to premature or sudden failure.

Inaccessible assets such as offshore wind turbines are one of the gravest, also other forms of critical conditions during a failure in helicopter would potentially endanger human life (Bashir et al. 1999). As a result, a vast majority of industrial sectors implement a planned maintenance routine consisting of two preventative maintenance strategies, condition and calendar based. Executing these inspections on a routine basis allows the inspector to capture any damage or irregularities in advance, permitting planned maintenance to be taken care of in due course (García Márquez et al. 2012). Nearly all sectors, where planned maintenance is an indispensable process to reduce unforeseen potential expenses, are keen on the progression of condition monitoring techniques as their capability to determine the component’s conditions accurately, the odds of sudden or catastrophic failure jeopardising the industry or worse human lives occurring before awareness is doubtful and seriously reduced. Moreover, accumulative information of the component or machinery conditions can be analysed and used to inform the precise timings on the calendar-based maintenances, further decreasing overheads.

2.6.1 *Condition Monitoring Techniques*

Present-day machinery is often equipped with an important number of gauges and sensors, to constantly monitor and measure their conditions against their predetermined thresholds. Using wind turbines as an example, the environmental data and operating systems acquired data often contains, and is by no means limited to, oil temperature, ambient air, individual components' rotational speed, torque, wind speed, power consumption and generation and so on. These gathered statistics are usually represented as Supervisory Control and Data Acquisition (SCADA) data, as it is logged in periodically for analysts to inspect the operating system's history if a fault occurs.

As an exceptional holistic procedure of monitoring a system, alarms triggered by surpassing a parameter's threshold which simplifies the indication of an estimated source of damage, however, fails to distinguish which component is at fault for the alarm besides indicating the fault severity. In order to rectify and adjust this issue, further condition monitoring techniques are available, such as: vibration and AE as these renowned techniques record waveforms over an arranged time period, where the acquired data are subjected to further analysis and processing to provide the identification and the potential source of a defect.

2.6.2 *Vibration Monitoring*

Vibration exists in all machinery due to the moving elements, which will inherently produce an undesired motion caused by insignificant faults or inadequate balancing. Despite the fact that the extent of vibration can be offset through dynamic counterbalancing and accurate designs, engineers need to anticipate that vibrations will persist within any machinery. As variations of vibration are potentially heard or noticed by experienced machine operators through either sound or touch, the next reasonable step is using sensors to imitate this ability. These sensors are generally known as accelerometers, which measure the acceleration of a surface or body. Acceleration is generally measured in *dv*/*dt* (delta velocity over delta time) or by

Newton's 2nd law of motion. Most accelerometers use quartz or ceramic crystals to generate a piezoelectric effect that is converted into an electrical output.

In order to convert mechanical motion into an electrical energy the majority of present accelerometer sensors enclose a small mass, m, positioned on top of a piezoelectric microscopic crystal structure which, when stressed by inertial forces, F, generates a small electrical charge. This electrical charge is generated as the location of both negative and positive ions are altered, building a spike in charge, illustrated further in Figure 2-10. A signal conditioner converts the high impedance charge output into a usable voltage signal (Jeevagan et al. 2014). If excited within a sensor's operational frequency range, the outputs comply with Newton's 2nd law of motion in Equation (2.6), where the applied force F is proportional to the acceleration a and a constant mass m.

$$F = ma \tag{2.6}$$

Their application is broad and varied, stretching from monitoring seismic activity to imbalance detection in motors and fans.

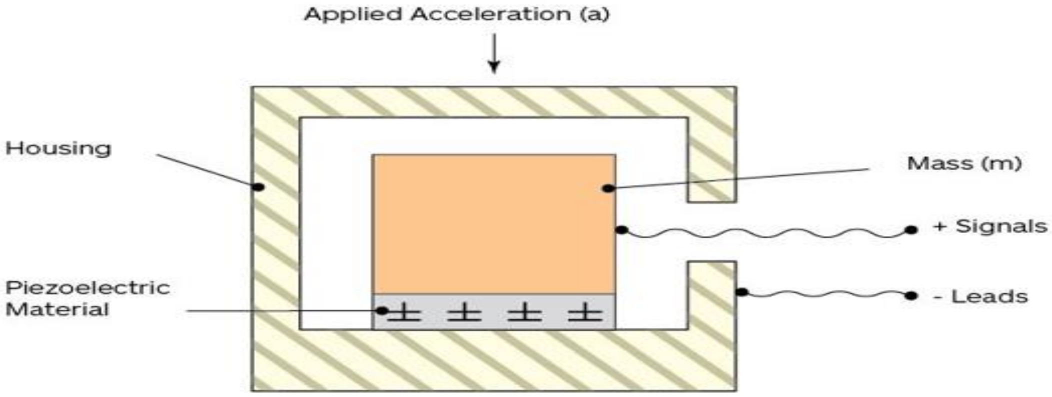

Figure 2-10: Basic accelerometer construction, enhanced from (Jeevagan et al. 2014).

2.6.3 Acoustic Emission Monitoring

AE's phenomena have been grasped since the 1960s, where it was first developed for detecting cracks in pressure vessels. AE is a transient elastic waves generated by a rapid release of strain energy prompted by damage or deformation from localised sources on or within the material's surface (Mathews 1983; Scruby 1987; Pollock

1989; ASTM E1316-13a 2004; Miller et al. 2005). The generation of AE can be related to numerous sources, including impacts, crack growth, turbulence, the movement of dislocations, cyclic fatigue, leakage and cavitation (Heiple, C. R and Carpenter 1987; Mba and Rao 2006).

These elastic waves propagate across the material's surface causing generated displacement which is then measured by the AE sensor, not dissimilar in functionality to the vibration sensors. AE sensors also employ the properties of a piezoelectric crystal to transfer mechanical motion into electrical energy. Yet, unlike an accelerometer, AE sensors do not enclose a sprung mass, thus their sensitivity is able to reach higher frequency ranges, ranging between 20kHz and 1MHz. A classic AE arrangement illustrated in Figure 2-11, where an AE sensor is mounted on the investigated structure to detect any displacement of the surface, thus converting any tiny movement to an electric signal by the piezoelectric crystal. The measured signal is pre-amplified and then transmitted to the main instrument, where it is filtered, amplified and digitised.

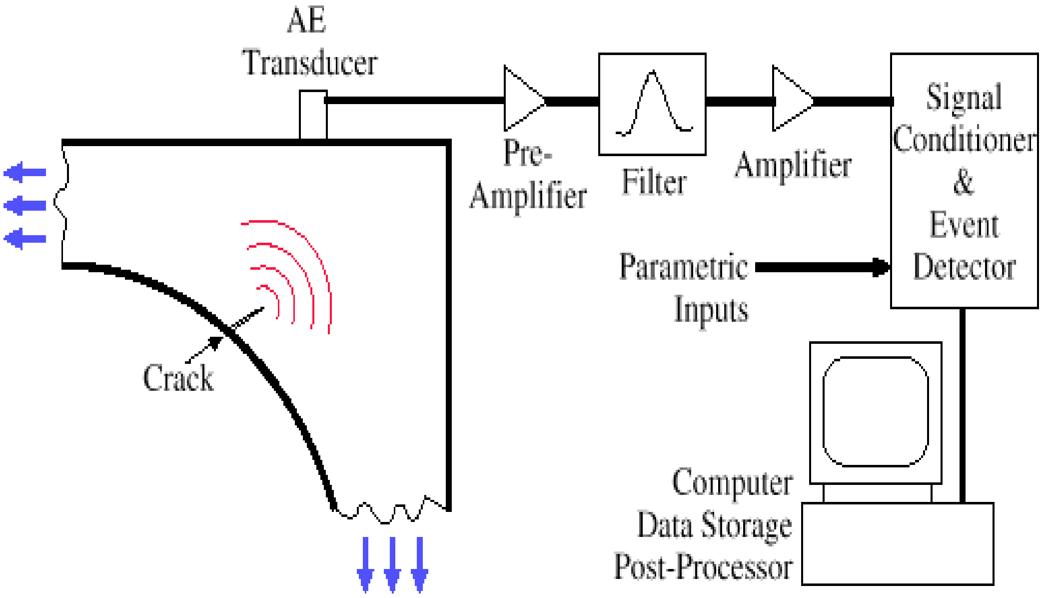

Figure 2-11: Typical AE setup (Huang et al. 1998).

For many years AE has been considered to be a primary candidate for non-destructive testing (NDT), examination or monitoring of structural failure or material faults and has established extensive applications in these fields, as AE has the potential to become a “global” monitoring instrument (Dornfeld 1992; Holford and Carter 1999; Qi 2000; Nair and Cai 2010). Advanced AE applications in modern days include monitoring the structural health of bridges, vessels, aircrafts, microseismic activity and other static structures where an intensification of AE activity is attributed to the plastic deformation of materials, crack initiation and propagation along with other possible sources determined by their application (Hase et al. 2012; Crivelli and Bland 2016).

A typical technique to simulate an AE source in a research facility or a laboratory environment is by pencil lead break, which emits a transient wave from the source usually referred to as the Hsu-Nielson Source. When the lead is broken on an infinitely large elastic body, propagation of elastic waves are formed in one of two components that travel along either as a longitudinal “compression” wave or a transverse “shear” wave Figure 2-12, as compression waves reaches the surface of a solid media, a further wave form may occur and is referred to as a surface wave or Rayleigh wave as shown in Figure 2-13. In some defect cases such as scratches and cracks attenuate the Rayleigh waves, besides the materials’ surface finish will affect the attenuation speed (Viktorov 1967).

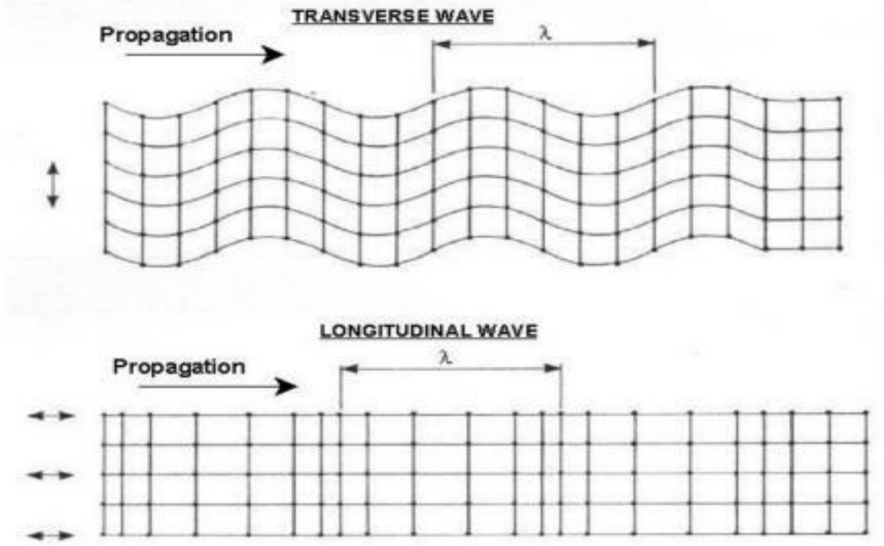

Figure 2-12: Forms of wave propagation in solid bodies (Rindorf 1981).

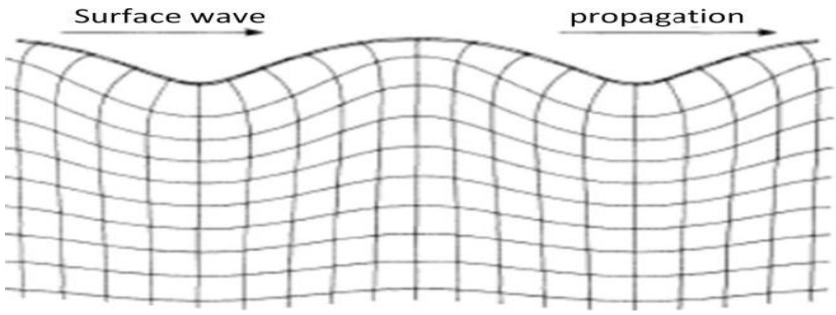

Figure 2-13: Passage of Rayleigh wave (Rindorf 1981).

For AE sources investigated on a thin plate test specimen (Holland and Sachse 2006; Aggelis et al. 2011), the propagated waves in this form of structure are called Plate or Lamb waves and they exist in two different modes, symmetric S_0 and asymmetric A_0 mode also referred to extensional and flexural modes respectively, displayed in Figure 2-14.

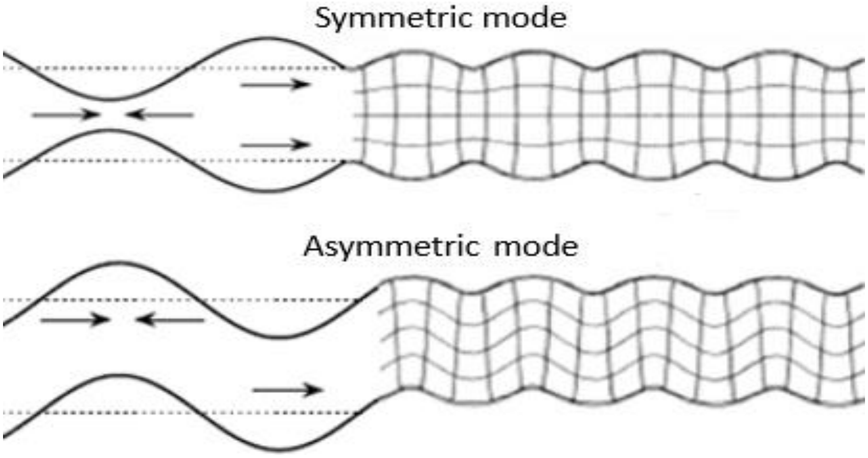

Figure 2-14: Lamb wave mode propagation in plates - adapted from (Rindorf 1981; Naumann 2016).

Travelling with different velocities, this is down to the fact that velocity of Lamb waves, are dependent on plate thickness and wave frequency, this is typically found in plate structures such as aircraft structures. This phenomenon is defined as wave dispersion (Torkamani et al. 2014).

The waves emitted at the source location are bulk waves. Bulk acoustic waves can be characterized in terms of three modal types of mechanical excitation. One of these is a compressional wave, termed the longitudinal bulk wave, that is polarized in the direction of the acoustic wave propagation vector. The other two wave components, terms *transverse* or shear waves, have their vibrational modes (i.e., their polarizations) perpendicular to the acoustic propagation axis (Campbell 1989).

Bulk waves are nondispersive, i.e., all waves have a constant velocity. Bulk waves attenuate quickly and can only be useful in very small specimens (Hellier 2020). As the investigation for the intended research is on a test bearing rig and the acquired AE data is from bearing housings, which is the main difference as the structure in use is a 3 dimensional piece of metal. Thus consideration of only bulk waves are to be produced for the research as bulk waves are predominant in gears and bearings. Demonstration of the two types of bulk waves are seen in Figure 2-15.

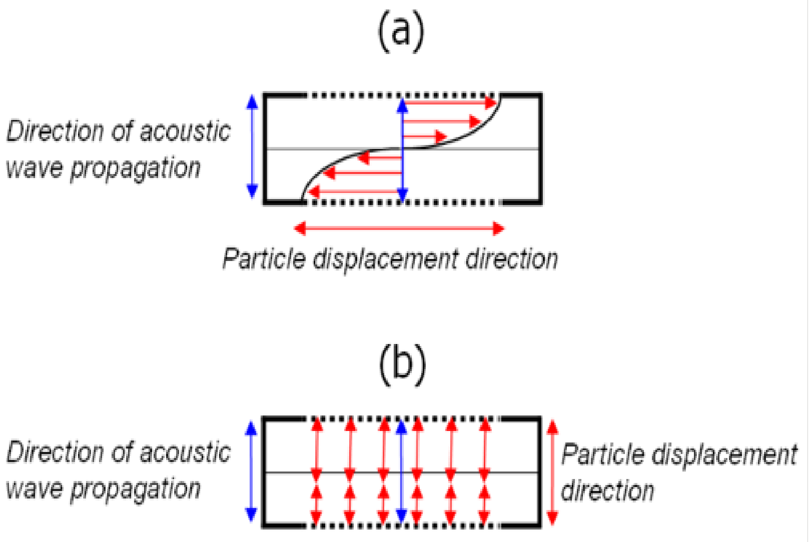

Figure 2-15: The two main types of bulk acoustic waves. a) The thickness shear mode illustrating particle displacement normal to the direction of wave propagation through the thickness of the crystal and b) the longitudinal bulk mode illustrating particle displacement parallel to wave propagation (Corso 2008).

Therefore, differences in velocity, causing different arrival times at the sensor, can be realised in the raw waveform of a pencil lead break. Figure 2-16 illustrates a recorded example of an AE wavestream as a pencil lead is broken near an AE sensor. Observations just after the initial peak, a following transient wave with a much higher amplitude is recorded by the AE sensor. The arrival time variance amongst the two peaks is very short, and it is possible to detect reflections of the S_0 mode within a waveform as it reflects from the boundaries of the material.

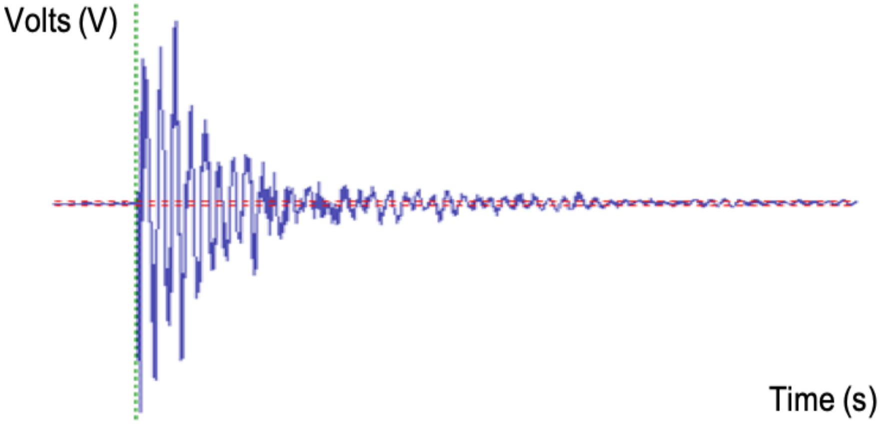

Figure 2-16: Example of an AE wavestream generated by a pencil lead break.

A defect's severity is translated from an AE 'Hit' generated within the features of a recorded raw signal by the user, correlating any increase in the signal features directly with an increase in signal length and amplitude. To prevent unwatned hits that may not have any relation to the damage, a predetermined level threshold or a Hit Definition Time (HDT) is set, which enables the system's user to determine the closure of an event or hit, then store the signal's measured attributes (Unnþórsson 2013). Within an AE raw signal, the most widely used parameters for signal features analysis are Amplitude, Rise time, Counts, Duration, and the measured area under the rectified signal envelope (MARSE) also known as energy counts described in Figure 2-17.

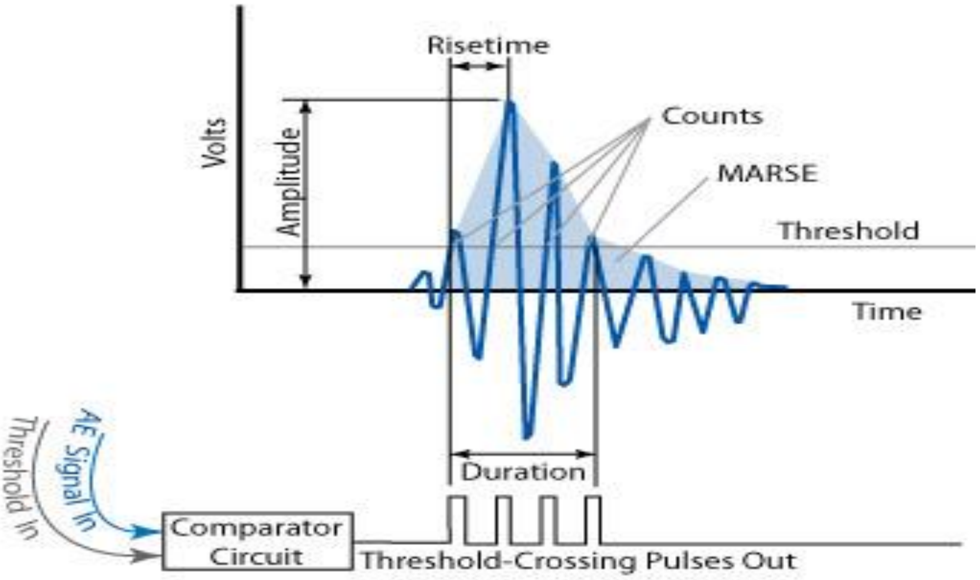

Figure 2-17: Description of a recorded AE signal features- extracted from (NDT Resource Center 2018).

Amplitude, **A:** This is the maximum measured voltage captured in an AE waveform and is expressed in decibels (dB), in scales of 1 µV at the transducer referrs to 0 dB, 10 µV as 20dB, 100 µV as 40dB etc. Amplitude is a crucial parameter as it determines the detectability of the event. Signals with amplitudes below the predetermined threshold are not recorded. Some of the factors affecting the amplitudes of an AE event are listed in Table 2-2.

Table 2-2: Factors influencing AE response (Miller et al. 2005)

Factors increasing AE amplitude	Factors decreasing AE amplitude
High strength	Low strength
High strain rate	Low strain rate
Low temperature	High temperature
Crack propagation	Plastic deformation
Large grain size	Small grain size
Materials containing discontinuities	Materials without discontinuities
Brittle failure (cleavage)	Ductile fracture (shear)

***Rise time*, R:** The time interval from the first threshold crossing and the signal peak, R is utilised for qualification of signals and as a measure for noise filter.

***Counts,* N:** Refers to the amount of emitted pulses by the measurement circuitry once the amplitude crosses over the threshold.

***Duration,* D:** The elapsed time between initial and final threshold crossings, measured in microseconds.

***MARSE Energy*, E**: Also known as energy counts, which represents the energy content of a signal. Energy is preferred over counts as it is more sensitive to duration and amplitude, and is less dependent on the operating system’s threshold settings and operating frequency.

Once a component is stressed, a release of elastic energy is emitted from the source. This emission from such source can be characterised as a continuous wave or a transient wave. The former type of waves are due to the effect of rapid recurring processes caused by continuous friction inbetween surfaces, machine vibrations, phase transformation and fluid flow. As shown in Figure 2-18 the amplitude and frequency keep fluctuating continuously.

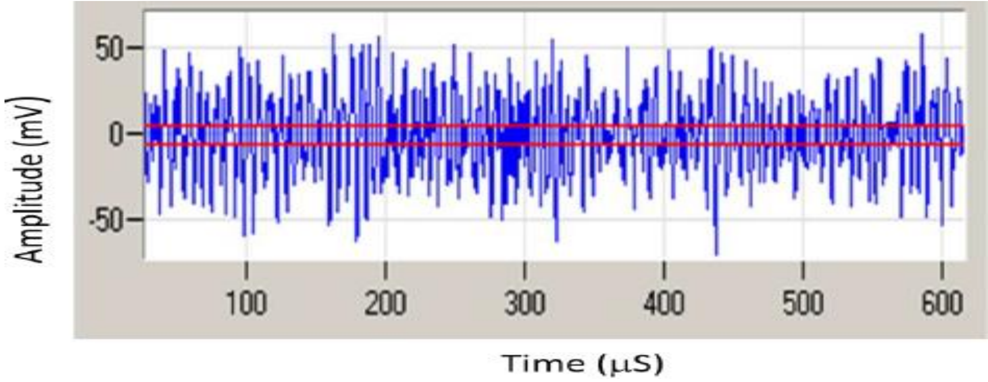

Figure 2-18: Example of amplitude and frequency of the continuous wave fluctuates but the signal does not end.

The latter waves are regarded as burst type signals emitted from an individual event in the form of abrupt or permanent change in the materials surface due to debris, brittle fracture, corrosion, impact and damage associated with the deformation process. They are identified by a clear start and end of a signal and it is evidently distinct from noise signal Figure 2-19.

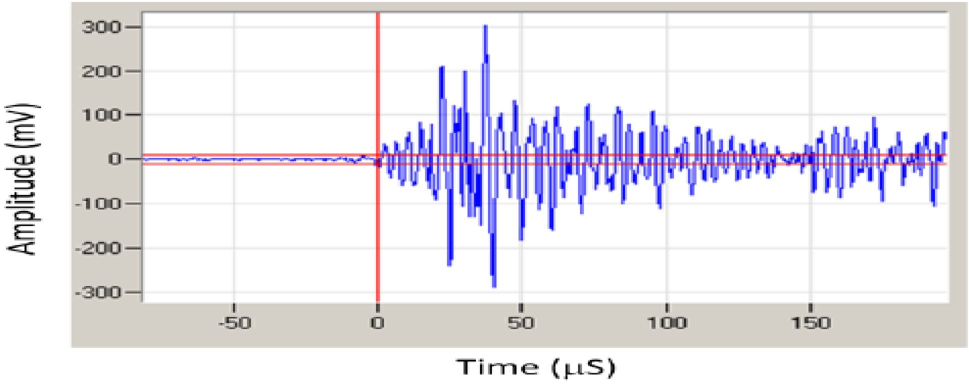

Figure 2-19: Example of a typical AE Burst.

The beforementioned signal features are the current standard parameters in use to observe the condition of solid structures in industries. Users can directly understand the output values and it is uncomplicated to spot any variance in the parameter alterations over time, which identifies damage within a component. However, such techniques applied to rotating machinery, where diverse signals from multiple sources may interfere by overlaping, presents many difficulties and complications, and is further discussed in following sections.

2.7 Rolling Element Bearing Monitoring from Vibrational to AE Methods

> *"If the forces, stresses and acceleration of bearing components could be measured directly, the task of monitoring the health of the bearing would be quite simple."*
>
> (*Howard 1994*)

Rolling element bearings are one of the most commonly used components in rotating machinery. Current condition monitoring techniques for detection and diagnosis of a bearing fault have become well developed as they are critical to avoid productivity decline and unexpected failure. Even though conventional vibration analysis techniques are the most common method to diagnose a bearing's condition, numerous other techniques could also be employed. These techniques include temperature monitoring, oil analysis and AE analysis. Various parameters and signal processing techniques have been explored, most of which are directly applicable to use for AE data or initially involve a degree of pre-processing adaptation. AE technology senses crack growth in fatigued material and is able to observe a bearings condition before visual defects are formed within the contacting surfaces. This advantageous AE method may be able to identify the fault propagation before the conventional method of vibration actually does (Yoshioka and Fujiwara 1987; Elforjani and Mba 2010; Liu et al. 2011). Both vibration and AE methods rely on detecting periodic features related to damage source localisation. For a roller bearing, both methods rely on the bearing's fundamental frequencies. These frequencies are generated once rollers pass over a surface inconsistency on either the raceways or a roller and are identified as fundamental fault frequencies.

These generated frequencies are a function of a roller bearing's geometry consisting of the roller diameter and pitch diameter, and the relative speed between both raceways. When the roller bearing's geometry is known, as defined in Figure 2-20, where SF is the rotational shaft frequency or the motor driving frequency, N is the number of rolling elements, P is the pitch diameter in mm, B is the roller or ball diameter in mm and θ is the contact angle in degrees°.

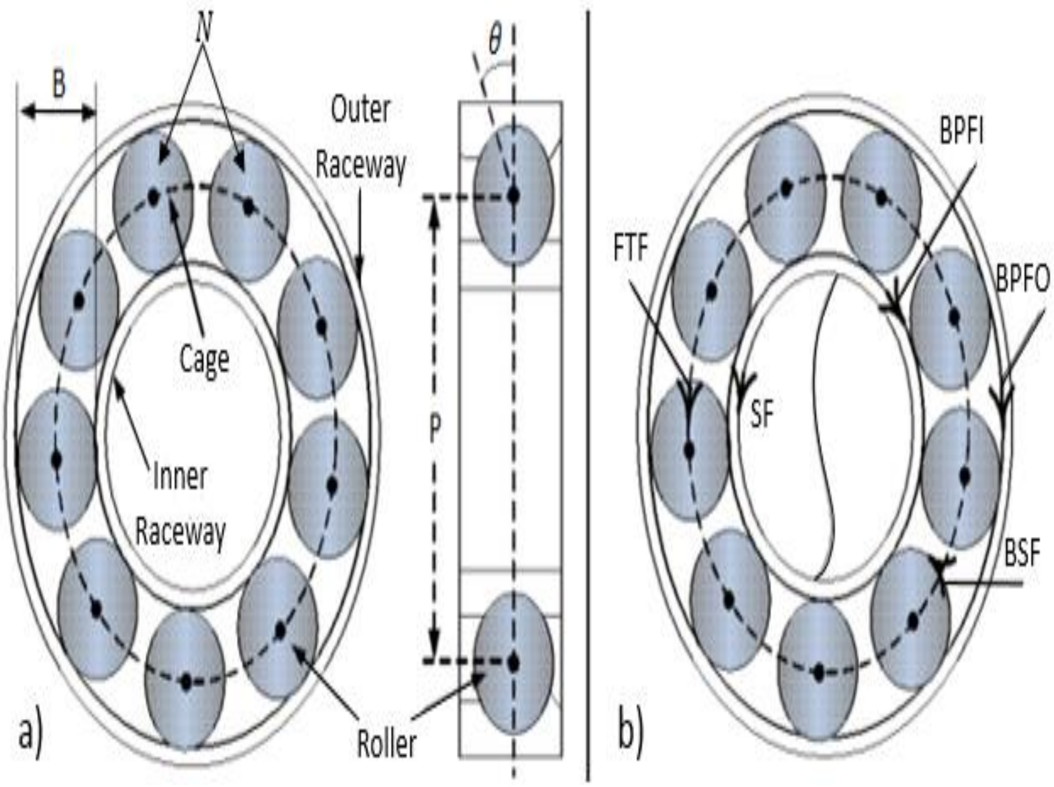

Figure 2-20: a) Roller Bearing Geometry and the Angle of Rolling Element relative to raceway b) Roller Bearings Basic Frequencies- adapted from (Tahir et al. 2017).

The fault frequency values are influenced by rotational speed, damage location and fault size. The key fault frequencies of a bearing can produce the ball pass frequency of the inner race (BPFI), the ball pass frequency of the outer race (BPFO), the fundamental train frequency (FTF) and the ball spin frequency (BSF). These aforementioned frequencies in Hz are mathematically calculated with the following Equations (2.7-2.10) (Graney and Starry 2011; Tahir et al. 2017).

$$BPFI = \frac{N}{2} \times F \left(1 + \frac{B}{P} \times \cos\theta\right) \quad (2.7)$$

$$BPFO = \frac{N}{2} \times F \left(1 - \frac{B}{P} \times \cos\theta\right) \quad (2.8)$$

$$FTF = \frac{F}{2} \times \left(1 - \frac{B}{P} \times \cos\theta\right) \quad (2.9)$$

$$BSF = \frac{P}{2B} \times F \left[1 - \left(\frac{B}{P} \times \cos\theta\right)^2\right] \quad (2.10)$$

Replicated from Halme and Andersson (2010), Figure 2-21 offers a visual illustration of cyclically recurrent defect signals, that are theoretically generated from a roller bearing where the rotational speed of the inner race is constant, static for the outer race and under a fixed radial load. For failures on the inner race, the BPFI signifies the passing of a roller over a defect situated on the inner raceway. The amplitude intensifies while the located defect on the inner raceway passes under the loaded area, then decreases as it rotates out. A defect on a static outer raceway, where the area of maximum load rests constant, emits an identical amplitude pulse for each individual roller passing over the defect, assuming that the size of defect remains the same. Finally, for a localised defect within a rolling element, which results in two pulses for each roller revolution, one occurs during contact with the outer raceway and the other while in contact with the inner raceway. Having said that, there is a significant difference between the two amplitude pulses, while the damaged roller passes beneath the loaded area there is a greater variance at the FTF, along with a smaller variance during the roller’s contact with the inner or outer raceway. This is due to the outer raceway typically being mounted closer to the sensor and for that reason the signal would not attenuate as fast as in the inner raceway. (Ehrich 1992; Tondon and Choudhury 1999; Orhan et al. 2006)

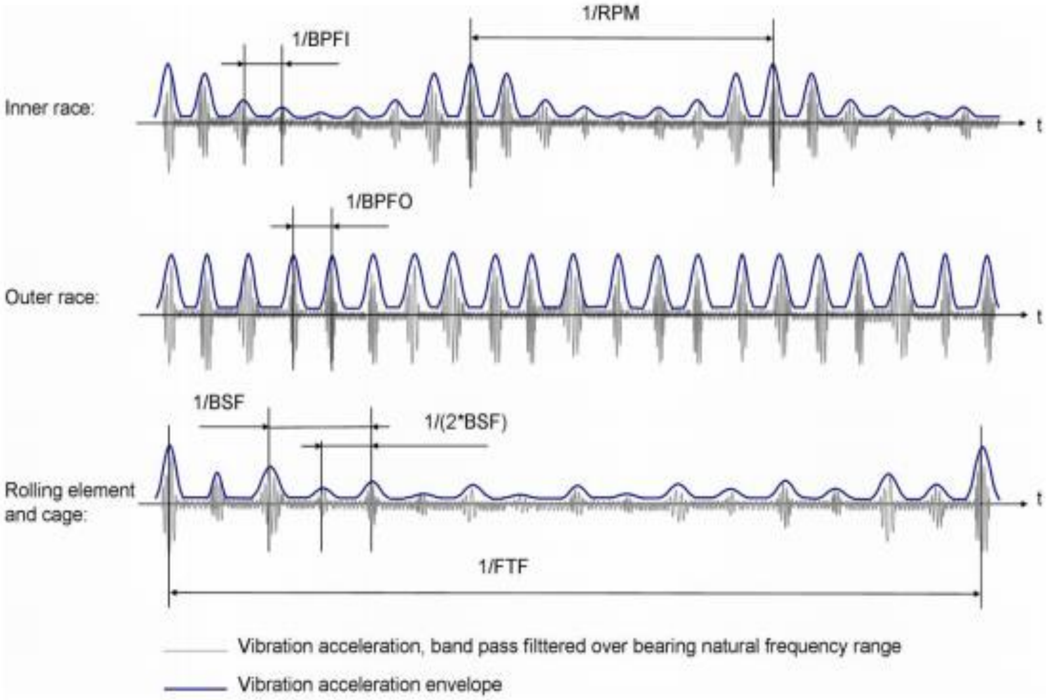

Figure 2-21: Visualisation of roller bearing defect responses for different frequency sources (Halme and Andersson 2010).

Extensive work into bearing damage detection through vibration analysis has been evolving and well developed over the years, and there is a substantial amount of work published in the academic literature. Unfortunately, monitoring and diagnosing the early stages of onset damage by the use of vibration analysis heavily depends on the nature and complexity of its application. Discussed by Howard (1994) the complications while using vibration sensors in an industrial environment, has different levels of difficulty depending on their wide applications. While this theory was intentionally defined for vibration analysis for bearing fault detection, it can also be said that AE analysis could be broken down by similar scales of complexity, as shown in Table 2-3. The scale of difficulties arises as a function of sensor mounting and the expected levels of noise from the surrounding environment in addition to the machine’s other components.

Table 2-3: Degree of Difficulty of Bearing Fault Detection as a Function of Machine Class – reproduced from (Howard 1994).

Class of Machine	Degree of Difficulty for Bearing Fault Detection	Machine Type
Easiest	1	Fans, Electric Motors, Generators
Slightly Complicated	2	Compressors, Pumps
Complicated	4	Industrial Gearboxes
Difficult	5	Turbines including Gas Turbine Engines
More Difficult	7	Helicopter Transmissions
Most Difficult	10	Specialised Rotating Machinery with Extreme Noise Environments

Accordingly, monitoring and detection methods with the use of AE analysis have been established with it being applied to numerous areas of rotating machinery from the determined work currently published investigating and expanding the condition monitoring field. The desire for an enhanced monitoring process with higher sensitivity to incipient failures influenced the consideration of AE techniques. However, the nature of AE generated from a tribological system is exceedingly difficult and has been the matter of considerable research. For analysis on static structures, it is viable to associate burst type emission with microscopic subsurface plastic deformation as well as the intensification of crack propagation right through the static structure. Although the emission type generated from rotating machinery depends fundamentally on the type of contact under inspection, namely rolling and sliding contact (Toutountzakis et al. 2005; Pullin et al. 2012; Cockerill 2017). Of note, vibration is the response of a structural component to something that is exciting it. Hence, in order to get such response, the defect has to reach a certain level of severity before it sets up measurable vibrations within the bearing. While with the use of AE the signal detection occur as the defect is initiated or grows. Therefore, the key factor of using AE in this research is essential to be able to detect abnormalities much earlier than vibration methods. Especially in a run to failure test in search of naturally failed roller bearings, to detect the initial phase of damage and acquire data for analyses. Where in the case of vibration, there has to be a wait for the system to respond to a presence of damage, and for that to happen it would be detection of energy that's released where the actual damage has grown already.

2.8 Review on AE Monitoring of Rolling Element Bearings

Rather than providing a widespread review of the contemporary AE techniques, this section introduces chronological methods investigated by AE researchers for rotating machinery monitoring with the focus on rolling elements, some of which are unique to AE technology.

Modern research on AE commenced in the 1950s though, the first documented assessment on the application of AE technology to identify artificially seeded defects in roller bearings was published by Balderston (1969). Simulated defects included ball defects, inner and outer raceways defects and lack of lubrication. Balderston went on to compare vibrations in the resonant range, audible range and AE, mentioning the advantages the resonant frequency range had offered over the audible vibration range. Balderston cited that the resonant technique was efficacious, as it presented a direct correlation between the rise in amplitude level of the resonant frequencies and defect severity, however suggestions to improve AE results necessitated sensor development. The author also noted from the experiment the types of AE signatures obtained. Burst type emissions were observed related to the seeded defects on the ball element, inner and outer raceways; and during the dry run experiment, continuous type emissions were observed due to lubricant starvation.

Rogers (1979) performed one of the earliest known AE studies on rolling element bearings following anxiety regarding the safety of personnel, performance and gross pollution in the case of component failure in slewing cranes on offshore gas production platforms. Instrumentation using AE was initially proposed as an alternative, as the produced vibration signals frequency ranged from 1 to 20kHz and strain gauges and accelerometers were not considered sensitive enough to detect incipient damage and sub-critical fatigue cracks in slow speed bearings. Two transducers were bonded diametrically opposite one another on the slew ring, where discrete AE events were logged whilst the crane was operational. As a result, high amplitude emission was witnessed during crane motion and rotation to 180° and back, yet little difference in amplitude distribution while the crane was off load or carrying high loads. As the investigation was on an undamaged slew ring, these observed emissions were considered to be due to friction amid the inner ring and the rolling elements or gear meshing noise. Moreover, Rogers stated had the investigated slew ring contained fatigue cracks, they would have produced a higher density of emission at particular points in the amplitude distribution plot with higher amplitudes.

Smith (1982) carried out a comparative experiment on AE monitoring besides vibration analysis, shock pulse transducers and jerk measurements. The stationary outer raceway had an arrangement of a high frequency accelerometer, an AE transducer and a shock pulse transducer while the inner raceway had a seeded scratch of 20µm. Additionally a back-to-back gear test rig was seated on the same base to simulate typical background noise. The bearing test rig was initially run solely, and the findings were similar between methods with regards to the signal to noise ratio. However, once the gear test rig started to run and its noise was present, no visual detection was possible of the seeded defect from the accelerometer or AE data at speeds below 1000rpm, whilst the shock pulse metering and jerk measurements were capable of defect detection at speeds beyond 500rpm. Further experiments were carried out at lower speeds and, even without the background noise, the majority of the defect signals were undetectable in the electrical noise of the measuring system, excluding the AE transducer as it responded each time a ball passes over the defected area. It was suggested that this was a consequence of the AE transducers’ sensitivity to base bending. Though no limit to low speeds was established, the defect was detected in the speed range of 10rpm up to roughly 300rpm. The experiment concluded that the use of AE ought to be considered in slow operating bearings. Of note, with regards to considerations of low speeds, the dynamic conditions dictating the bearing design are indicated by the linear speed at the bearing pitch line, or the pitch line speed. Pitch line speeds of less than 2.54 meters per second are generally considered low speed, and 2.54 m/s to 15.24 m/s are mid-range. Anything higher than 15.24 m/s is considered high-speed. Therefore, it could be stated that a very large bearing rotating at a 100 RPM might be considered high speed because of the linear speed at the bearing pitch line (Kaydon Bearings 2014).

Building on that, Mcfadden and Smith (1984) explored the monitoring of angular contact rolling element bearings with the use of AE at speeds ranging from 10rpm up to 1850rpm. A simulated fault was produced on the inner raceway by a fine scratch, which formed the foundation of the experiment. At very low speeds of 10rpm the AE sensor responded to minute strains caused by local distortions of the bearing housing due to the concentrated loading from each ball within the bearing. These minute strains acted as spurious spikes overlaid on the bearing’s ball pass frequency. Vibrational measurements failed to sense the strain on the bearing housing. Mcfadden and Smith (1984) concluded that, with steady loads at low rotational speeds, base bending of the bearing housing may well enable the AE sensor to detect signatures from exceptionally small defects in bearings.

Yoshioka and Fujiwara (1982; 1984) have also demonstrated that measurements from the conventional vibration method failed to match the performance of the AE method, as AE parameters have identified bearing defects earlier. Additionally, generated AE sources on a thrust-loaded ball bearing were distinguished during fatigue life tests.

A more direct comparison between vibration and AE analysis was undertaken by Hawman and Galinaitis (1988) to determine the least possible detectable defect size for each method. Defects on the outer raceway of a common ball bearing were initially scratched size of 0.006 in. (0.15 mm) wide and 0.002 in. (0.05 mm) deep. With a held constant load of 2400 lbf approximately (10.675 kN) and rotational shaft speed fixed at 5700rpm, considerably faster than prior investigations. The digitised signal of an AE transducer mounted directly on top of the outer raceway was analysed in both the time and frequency domains. Both domains were successful, where the AE time signal was able to distinguish defect pulse indications as soon as the defect width reached 0.01in (0.254mm) and bursts of AE energy from the demodulated AE signal indicated that the precise spectral peak occurred at a similar 443Hz rate of the outer raceway defect frequency. Reciprocally, vibration data did not yield any clear indication of a defect until the width had stretched to 0.065in (1.65mm). At this point, a 38% increase was observed in the overall Root Mean Square (RMS) from a hypothetical defect-free measurement, signifying that AE analysis is not just superior in the detection of incipient damage in high noise environments, but in fact has the ability to outline the damaged component. Furthermore, observation on the modulation of AE signatures at bearing fault frequencies were also proceeded by other researchers (Holroyd and Randall 1993). Similar results were noted, strengthening Yoshioka's statements that AE provided earlier fault detection in bearings than vibration analysis.

Tandon and Nakra (1990) showed the usefulness of some AE parameters such as counts and peak amplitude for defect detection in radially loaded ball bearings by introducing intentional defects of specific sizes in different elements of the bearing for various loads and low to normal speeds, with and without defects. The investigation demonstrated the AE counts parameters was able detect defects of 0.15mm on the inner race and greater than 0.2mm for the outer race of the ball bearings, also AE peak amplitude parameter produced indications of defects regardless of the defect size. AE events distribution by peak amplitude and counts was also investigated for bearing quality inspection (Bansal et al. 1990). Bansal noted that there was slight increase in the peak to peak amplitude level as load was increased for new and reconditioned bearings, however the reconditioned bearings peak values were 5 times the new bearing.

Tan (1990) measured the AE pulses caused by the rollers striking a defect, which were investigated through accumulated area count below the amplitude-time curve for a specific time interval. The analysis was based on time and frequency domain techniques. The results revealed that AE activity intensifies exponentially with rotational speed and defect size. Furthermore, the pulse duration and rise-time also increased with defect severity. The author cited several difficulties and drawbacks from the conventional AE count performance, primarily choosing the correct threshold level, secondly the count value’s dependency on the signal frequency and lastly indirect dependency of the count rate upon the amplitude of the AE pulses.

Investigations on early detection of defects was performed by Li & Li (1995) via advanced signal processing and pattern recognition techniques. The monitoring of undamaged and damaged bearing components was conducted using AE sensors with bandwidths of 20-90kHz, lower than the commonly used bandwidth in AE monitoring, appropriately reducing the data amount after sampling. The ‘peaks and valleys’ features acquired from the auto-correlation of the zero crossing rate and the short-time energy function were utilised as inputs to a pattern classifier which plotted both features in an attempt to realise a boundary segregating the undamaged from damaged roller bearings. The classifier training established a gradient descent algorithm procedure to label the data as defected or not. An extraordinary obtained success rate indicated a noteworthy enhancement in comparison to vibration monitoring. Furthermore, the investigation demonstrated the monitoring success of AE for seeded defects on rolling elements which introduced further challenges due to its transmission path and position variance in time, and also established that signal to noise ratios (SNR) were stronger in AE sensors than accelerometers when placed remotely from the bearing. The transmission path is what causes attenuation of the AE signal i.e., the difficulty of the transmission path is that the AE sensor is mounted on the bearing housing and the damage occurs at the roller element, with potentially a lubricant film that the AE signal has to passover. Then the AE signal has to go through the outer race as well as go across the interface between the outer race and the housing and transmit through the housing. Eventually the AE signal crosses the coupling material used to hold the sensor to the housing to reach the AE sensor. At every step through those interfaces the signal loses energy, so in these types of complex designs the attenuation of the signal can be quite heavy, when compared to monitoring a bridge as the AE sensors are attached to the same piece of concrete or metal that might fail and where the transmission path is not overly complex.

Shiroishi et al. (1997) conducted a collective experiment on vibration and AE for a tapered roller bearing, artificially defected via a scribe, operating at 1200rpm. Vibrational analysis offered better detection in contrast to AE, with the strongest indicator observed from peak amplitude, kurtosis, RMS with the least reliable being the crest factor. The authors also cited that defects on the inner race were undetectable by AE, it is believed that this was due to the lack of energy generated from the defects. In addition, the paper highlights the difficulty of an emitted source from an inner raceway needing to travel further than those from the outer raceway, crossing more interfaces hence being susceptible to higher attenuation. The arrangement of AE sensors in any investigation regrettably could potentially jeopardise prospective results, as this may have been one of the main reasons why AE results from this experiment differ from most previous ones. Moreover, a plausible explanation to this problem was the way the signal was demodulated and filtered. Even though the demodulation’s actual effects were not discussed, it was detailed that the data acquired was low pass filtered at 1kHz. Due to that, actual removal of the high frequency components of each individual energy burst, causing difficulties to properly analyse the defect’s high frequency components. This was a major issue faced in many of the early investigations using AE, as the signal was treated similarly to the vibrational signal instead of taking full advantage of the AE to analyse the full frequency spectrum generated.

A further challenging approach was to monitor contamination or starved lubrication as induced vibrations are not periodic hence incapable of monitoring through customary methods, in particular measurements of the enveloped signal and tracking the characteristic fault frequencies. Miettinen and Andersson (1998) used and compared AE with a number of methods based on vibration to monitor lubricated bearings with contaminated grease. In laboratory settings bearings with and without contaminated grease were investigated. The pulse count and RMS methods were employed as AE measures. A distinct intensification in AE activity was revealed with the inclusion of contaminants and besides the investigated methods, AE had the highest sensitivity. Further investigations (Miettinen and Andersson, 2000) established that contaminant weight concentrations as low as 0.02% could produce a clear rise in AE activity.

The usage of ring down counts also known as the “threshold crossing counts” is the number of AE transients or burst signals crossing the detection threshold, for defect detection was evaluated by Choudhury and Tandon (2000). The purpose was to quantify the effect on AE sensitivity of several operational conditions. They carried out experiments using cylindrical roller bearings with different bore diameters, with and without defects, which were tested under a series of speeds and loads. An automated threshold was employed to accordingly eliminate the variance in background noise. The investigated bearings were SKF type, NJ series cylindrical roller bearings having inner race bore diameters of 15, 20, 25, 30 and 35mm. The focus of the initial investigation was on ring down counts to quantify the influence of defect size on the AE signal together from the inner race and the bearing’s rollers. The amount of counts exhibited a sharp increase over the series of smallest investigated defects, however exhibited no additional increases once the defect size had progressed to 0.5-1mm, where a plateau was witnessed as the defect size increased, possibly due to the whole signal components crossing the threshold level. These results are illustrated in Figure 2-22. The authors concluded that the counts parameter would be suitable for defect detection yet not for size estimation. The volume of ring down counts has also been shown to be insensitive to applied load and bearing size, but did increase with rotational speed as demonstrated in Figure 2-23. The authors concluded that during a rolling element bearing test, the increase in AE amplitude with elevated rotational speeds was a consequence of dynamic stress growth. However, it has been revealed that for pure sliding contacts, surface roughness interactions in the form of asperities is the core cause of continuous emission (Boness et al. 1990; Boness and McBride 1991).

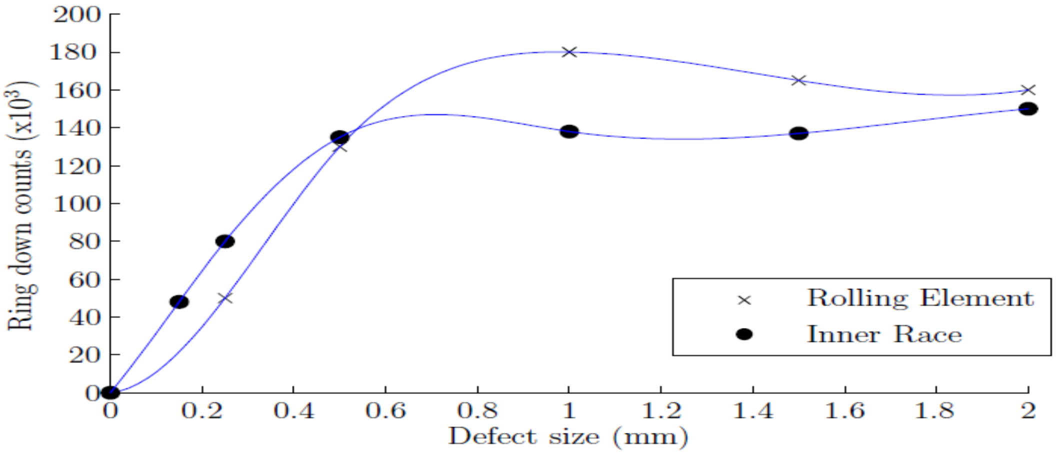

Figure 2-22: AE ring down counts at 75Kg and 1500rpm - extracted from (Naumann 2016).

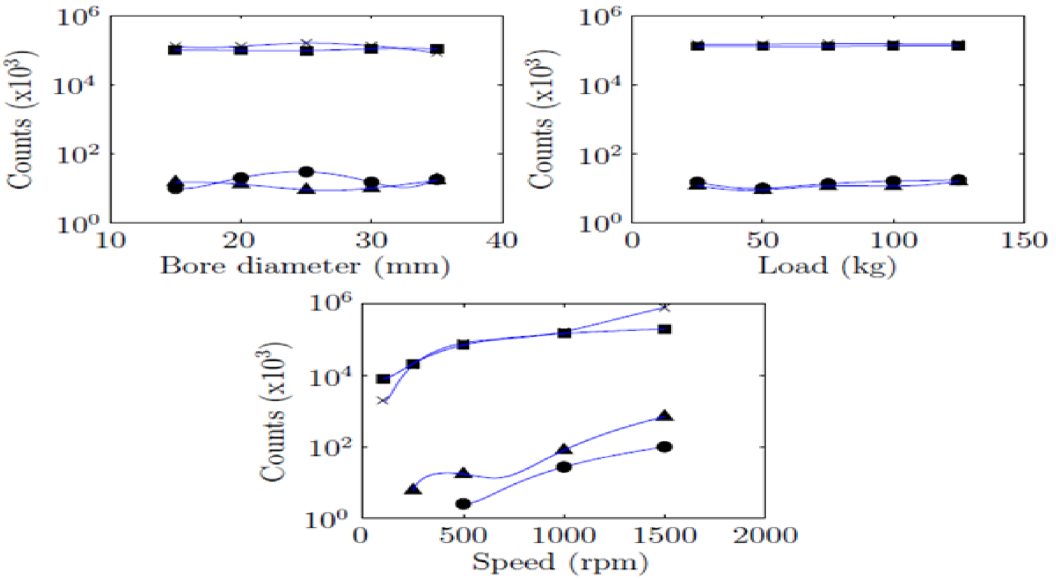

Figure 2-23: Ring down counts under varying conditions ● Rolling element (no defect), ▲ Inner race (no defect), ✕ Rolling element and ■ Inner race with defect reproduced from (Naumann 2016).

Kakishima et al. (2000) assessed monitoring and detection of artificially seeded defects created using an Electric Discharge Machine (EDM) in the inner raceway of two types of bearings, roller and ball bearing. The experiment compared both techniques vibration and AE, where analyses from AE were established from the spectrum of the enveloped AE signals. Kakishima concluded both techniques were able to detect the inner race surface defect similarly. In addition, it was noted that the growth in defect size caused an increase in both vibration and AE levels on the envelope spectrum.

Williams et al. (2001) performed a different kind of experiment from those with artificially seeded defects, in essence fatigue tests. Several accelerated life tests were conducted on two types of bearings, ball and roller at different operational conditions. The fatigue test on both bearings was operated at 6000rpm and at 60% and 67% of their dynamic rated load respectively. Implementation and comparison of vibration and AE techniques, with a noteworthy emphasis placed on the use of vibration. The AE results from the experiment might have been hindered as both techniques were sampled at 30kHz. As the authors used a general-purpose AE transducer from Physical Acoustics R15 with resonant frequency of 150kHz, thus with reference to Nyquist’s theory, 15kHz was the max detectable frequency. In spite of that, it was revealed that naturally propagated defects on the inner raceway were detectable through vibration and AE, although a delayed increase in RMS amplitude of approximately 10 minutes from the AE transducers in contrast to the accelerometer. Although outer race failures were detected via vibration, AE transducers failed to do so. This was likely to be due to the low sampling frequency employed.

Mba (2003) went on to certify the usage of RMS parameters for diagnosis and extended the efforts of (Choudhury and Tandon 2000) by establishing a suitable threshold for AE counts for monitoring roller bearings, through investigations on appropriate selections of threshold levels. Seeded defects were engraved on the inner and outer race. The bearing test rig operated under rotational speeds of 600rpm, 1500rpm and 3000rpm and loads of 0kN, 2.4kN and 4.8kN. Results demonstrated that for bearing diagnosis, RMS was validated as a powerful technique, typically indicating an increase with increasing speed, load and defect size. These findings are in agreement with published results from previous researchers (Yoshioka and Fujiwara 1982; & 1984; Tan 1990; Tandon and Nakra 1990; Choudhury and Tandon 2000) thus forming the basis from which to examine the influence of predetermined threshold levels for AE counts. The author concluded that the relationship between AE counts and the roller bearing’s mechanical integrity was shown to be independent of the threshold level which was calculated for each loading case as a percentage of the peak amplitude. A related approach was carried out by

Morhain and Mba (2003) however the use of maximum event amplitude and energy was also investigated. In addition to RMS and counts, the energy of AE events was found to correlate with load, speeds and defect size however for AE maximum amplitude only correlated with increasing speed. The investigation went on to observe and determine the most suitable threshold level for diagnosis via AE counts. Advice was given to set a threshold level of at least 30 per cent of the maximum background amplitude for the lowest operating speed and load conditions. In addition, the author proposed to consider background noise for all operational speeds, particularly on machinery operating over a series of speed conditions.

The majority of previous published research with regards to detection of failure within rotating machinery relied on the generated data from artificially seeded defects onto the running surface of roller bearings or a gear. Common devices to produce these superficial defects are engraving and EDM, unfortunately they do not offer a true representation of a natural defect yet the approach is able to rapidly generate data sets to investigate damage detection techniques. Engraving does not remove material but forces the material up and out of the artificial created hole thus instigating higher peaks of material in relation to the original surface around the circumference of the created crater. EDM on the other hand, removes excess material forming a crater with a smooth like circumference with no peaks. Realistically, neither of the methods accurately represent a naturally occurring defect as the AE generated is related to the bearing elements' interaction with an embedded defect. Tan and Mba (2005) argued that by material removal away from the contact area, the amount of asperities will be reduced, thus the potential source of AE may slightly diminish. The authors also went on to state that the peaks surrounding an engraved crater will yield higher emission due to increased stress concentrations from the protruded area, with emissions likely to decrease back to normal levels once the protrusions are flattened out. Orhan et al. (2006) in a different study on vibration, revealed that higher vibrational frequencies were phased out as the bearing is momentarily healed during the running process, in other terms 'self-peened'.

Although previously undertaken research gained ground and reinforced the use of AE parameters for bearing diagnosis, more detailed findings with regards to the fundamental AE sources from bearings with seeded defects and a first known attempt to signify a connection between AE burst duration and defect size was carried out by Al-Ghamd and Mba (2006). Two defect conditions were simulated for the experiments with a surface discontinuity, engraved by a carbide tipped machine firstly with material protrusions above the mean surface roughness of the bearing's outer raceway and the other without material protrusions. The presence of the smooth surface discontinuity could not be distinguished from the bearings, as the occurrence of random AE bursts were at a rate unrelated to any machinery phenomenon, which was presumed as a result of direct asperity contact. Furthermore, during the presence of the defect, such transient bursts related with vibration waveforms were not observed. A more direct assessment between burst duration and defect length was established through an analogy concerning AE and vibration analysis as a method of defining defect size. Observations were made of a linear correlated relationship between AE burst duration and the length of the seeded defect, a significant outcome for further research on bearing prognostics. In further experiments, maximum amplitude, RMS and kurtosis were measured with protruded material above the surface roughness. Kurtosis is a measurement of the tailedness of probability distribution. It clarifies whether the data is heavily-tailed or lightly-tailed. Data sets with high kurtosis have heavy-tails and more outliers, while data sets with low kurtosis tend to have light-tails and fewer outliers. Ruiz-Cárcel and Mba (2014) stated that kurtosis is also mathematically defined as the fourth moment of a probability density function, and it gives a measurement of the degree of impulsiveness in the signal, which is normally related with bearing faults. It was found that with increased defect size, AE max amplitude, RMS and kurtosis values increased correspondingly, whilst observations of the aforementioned parameters were disappointing from vibration measurements. The percentage rate of variations from the AE technique underlined the greater sensitivity to detect early defects.

According to Motor Reliability Working Group (MRWG) although the reliability of induction motors is great, they are still subject to specific modes of failures including considerable failure rates experienced by ball bearings. Tandon et al. (2007) undertook an experiment on a deep groove ball bearings SKF type 6205 with and without defects at 1440rpm. Comparisons were made between the following condition monitoring techniques; vibration, shock pulse meters (SPM), stator current and AE measurements. The comparative experiment concluded that AE peak amplitude was the most effective technique followed by SPM for both tested defect sizes.

Advanced investigations by Couturier and Mba (2008) aimed to address the significance of a specific film thickness λ in relation to AE energy RMS under isothermal conditions. The RMS of a split Cooper grease-lubricated bearing operating under varying sets of temperatures, rotational speeds and loads was recorded. As anticipated, the RMS levels demonstrated a reverse relation with λ, a decrease in λ was noted as a result of increased load. Correspondent increase in load would result in higher levels of asperity contact producing more friction. Conversely, a mirrored end result was presented whilst the speed was increased illustrated in Figure 2-24. Even though higher speeds resulted in greater film thicknesses, it was hypothesized that the consequential increase in strain rates experienced by contacting asperities was the source of increase in AE RMS suggesting similarly to Boness et al. (1990), although theoretically in further advanced speeds and λ shifting towards hydrodynamic lubrication, a decrease in AE levels will ensue as a result of no asperity contact within the bearing.

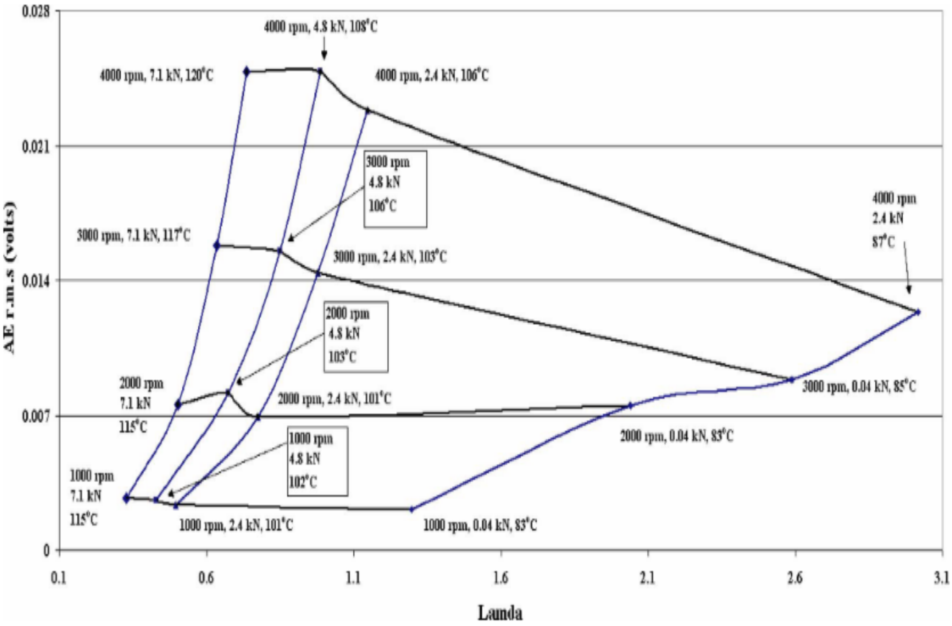

Figure 2-24: AE RMS levels for varying speed and load conditions – reproduced from (Couturier and Mba 2008).

The use of AE to detect subsurface cracking or naturally propagated defects in the rotating element bearings field has not been resourcefully exploited to date by many researchers. It seems to be chiefly due to the conventional method of seeded defects, concentration on signal processing, enhancement of weak signals in an attempt to indicate early damage detection, besides the difficulties presented by the usual background noise.

The previous studies, mostly focused on applications of AE technology for bearing condition monitoring, were conducted by correlating the artificial defect size with the defect signal characteristic parameters. Evidently a new approach needed to be considered, and an experimental accelerated life test on thrust bearings was performed by Elforjani and Mba (2008) to monitor natural degradation. They replaced one of the grooved races from the SKF 51210 thrust ball bearing with a flat race from SKF 81210 TN of the same dimension, as this arrangement led to higher contact stresses on the flat track thus inducing fatigue. Observations from traditional parameters suggested high levels of AE activity, which underlined the fact that traditional AE events are definitely as sensitive as the continuous measurement of AE parameters namely RMS and energy to changes in bearing mechanical conditions, reinforcing the findings of (Morhain and Mba 2003). To enhance the outcomes of the investigation, the concept of Kolmogorov–Smirnov test (KS-test) and the energy index (EI) were employed. Both techniques revealed higher sensitivity to the onset of fatigue, as EI showed the highest sensitivity associated with the transient type activity from naturally degrading bearings.

Al-Dossary et al. (2009) aimed to further build on the work of (Al-Ghamd and Mba 2006) by investigating the correlation between defect sizes and several AE waveform parameters. A strong correlation between defect sizes and AE burst duration were established for the outer race defects, although such a correlation could not be witnessed for the inner race defects, particularly as the latter has been reported to be fraught with difficulty (Shiroishi et al. 1997). It is believed this is due to the variation in the poor transmission path as the bearing rotates from the inner race AE source to the AE sensor. The differences between the two races is illustrated in Figure 2-25. The theoretical values do differ from the experimental values, which were based on the defect size and the relative speed of the passing elements. This is assumed to be an attribute of the signal decay which was not taken into consideration during the theoretical values calculations, as it would require the use of a considerably higher sampling rates to support discrimination. In addition, Figure 2-25 demonstrates no relative influence with regards to loads on the AE burst duration related with the defect.

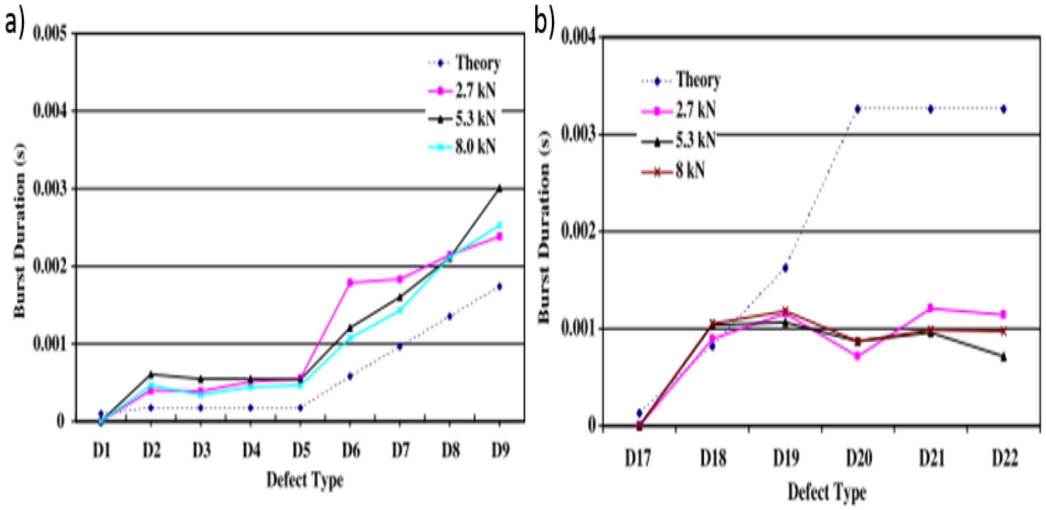

Figure 2-25: Burst duration for various defect sizes: a) outer race at 3000rpm b) inner race at 3000rpm– extracted from (Al-Dossary et al. 2009).

Raja Hamzah and Mba (2009) went on to determine that, for an operational rolling-sliding contact in a low λ regime, similar to the lubrication regime commonly observed in gear tooth interactions, generated AE is affected by the deformed plastic asperities since the surfaces are persistently in contact. Furthermore, the authors revealed that rolling contact, usually witnessed in rolling element bearings and pitch points of a gear teeth pairing contact, is responsible for initiating burst type emission. For gear teeth contacts, the AE source mechanism formed by the rolling-sliding is likewise believed to be a similar source of AE within rolling element bearings (Couturier and Mba 2008). Yet again, it was demonstrated for $\lambda < 3$ that the AE increases with respect to the increase of speed and load. Yet, for operational bearings with a higher λ ratio the AE response was not discussed. Speculation within the investigation stated that existence of asperity contact would be considerably lower, ensuing once the full film conditions are achieved hence a reduction in AE RMS.

One of the first known attempts to correlate AE activity and the initiation of natural defects in slow speed rotating shafts, as well as monitoring the mechanical integrity of the shaft was performed by Elforjani and Mba (2009a). In an effort to accelerate fatigue failure, a V-Notched shaft was designed. The rotational speed was held constant at 72rpm for two loads cases of 4kN and 8kN. Under 4kN and 95 minutes into testing, relatively high amplitude transients started to arise in the raw wavestreams and this was believed to be the primary detection of crack initiation at the V-Notch edges of the shaft. Eventually, a rapid surge in AE activity was detected around 456-570 minutes into the test till shaft failure. Inspections of the shafts were made, which revealed fatigue did occur at the V-Notched edges and the consequent high levels of transient AE events were due to the rapid propagation, rubbing and shearing of the observed cracked face. In the second case however, no clearly defined region of crack initiation could be identified or related to AE activity. The authors concluded that this attribute was the effect of higher loads as the time of the microscopic initiation phase till the accelerated crack propagation is significantly less than in lower loads, thus unobservable.

An experimental study carried out by He et al. (2009) to extract the defect frequencies by Short-Time RMS (STRMS) and autocorrelation functions, as well as employing the AE parameters such as amplitude, AE counts, energy and kurtosis to derive the characteristic defect frequencies, on a ball bearing with a corrosive pitting defect of 3mm and 5mm diameter created via electrical spark erosion. Observations of a close match between the actual measured frequencies and the anticipated frequency measurements, as the formers characteristic frequency is at 16.7Hz and the later at 17Hz, indicated that the utilised methods were ideal to determine damaged components. He et al. (2009) also related to the discussed assumptions of (Shiroishi et al. 1997; Al-Dossary et al. 2009) that AE is extremely sensitive to the bearings interface transmission resulting in attenuation. The aforementioned AE parameters sensitivities were investigated under several operating conditions. Constant radial load presented no obvious influence, whereas the rotational speed had a strong impact on all of the AE parameters further reinforcing the findings of (Choudhury and Tandon 2000).

Hao et al. (2009) inspected the frequency spectrum of a deep groove ball bearing with a 3mm circular defect on the outer race with a PAC R15a sensor at a sampling frequency of 500kHz. Results witnessed from the frequency spectrum presented dominant peaks at approximately 100kHz, 150kHz and 180kHz. It is understood that the detection of such frequencies corresponds to the sensor's excitation with its resonant frequency, thus generating a strong signal. Data analysis with a scalogram presented more information on the bearing defect than the frequency spectrum, which revealed that the continuous emission at 100kHz frequency had no relation with signal impulses and was treated as noise, whereas the impulse signals at 160kHz and 175kHz frequencies were burst type emission from passage of the ball over the circular defect. The core difference between these results and earlier published researches is mainly due to the use of a more suitable sampling frequency.

Al-Balushi et al. (2010) went on to further develop the EI technique in greater detail, which was initially investigated by (Elforjani and Mba 2008). The EI technique was proposed to detect masked AE signatures linked to the roller bearing's mechanical deterioration. Simulated and realistic defects signals were investigated. It was found that, by varying the AE bursts' amplitude, the EI could capture transients when the SNR was at 25%. In addition, EI technique was successfully applied to experimental signals contaminated with noise. The paper suggests that by choosing a suitable window size, the electrical noise signal effect can be minimised, as it tends to be of smaller duration than the defect signals. The authors cited an advantage of EI as it indicates where the impulsive sections are in a signal, in contrast to kurtosis which just gives a single value for the whole of the recorded section processed. Lastly, expectations from larger defects would produce a series of closely spaced short AE bursts, which could result in the signals appearance as if the AE burst has a lengthy duration. The occurrence of a new AE burst could initiate and overlap the previous one before it completely decays, forming a chain of AE bursts; falsely presenting a form of continuous AE signal.

Further development to the studies undertaken by Elforjani and Mba (2008; 2009b) built on the foundational work of (Yoshioka 1993) which could be regarded as the first direct investigation which attempted to identify the onset of natural degradation in rolling element bearings via AE. As Yoshioka successfully monitored the initiation of cracks, Elforjani and Mba advanced it further by monitoring its propagation to spalls or surface defects on bearings. The following investigation of Elforjani and Mba (2010) employed further parameters to improve sensitivity of AE to detect degradation. The wavestreams were recorded every two hours from a total of 20 operational hours at a low speed of 72rpm. Both kurtosis and crest factor were established as reliable indicators, but only in the existence of incipient defects as their responses were not significant enough to the bearing's increasing damage. Information Entropy (IE) proved to outperform them, as observations from IE were more sensitive and representative of natural degrading bearings due to periods of high transient AE activity. Supplemental investigations on the limitations of FFT in the form of leakage or resolution, hence applications of three non-linear power spectral approximation methods such as Prony's Energy, Eigen-Analysis and Auto-regressive spectra. Results revealed that FFT spectrum analysis was relatively noisier and was last to detect of the defect frequency, while the Prony's Energy method presented superior performance on the basis of producing larger frequency components.

Both studies by Choudhury and Tandon (2000) and He et al. (2009) exhibited that even though the volume of AE induced by a rolling element bearing is exceedingly reliant on the shafts speed, the peak amplitude shows inconsequential results during greater loads. Raharjo et al. (2011) revealed different results, based on a self-aligning spherical journal bearing, a plain bearing, and found that the statistical parameters such as peak amplitude, kurtosis, RMS and crest factor increased in amplitude with higher loads. This was believed to be caused by the increase of accumulated asperity contact, as a consequence of an increase in friction within the sliding contact.

In an attempt to determine whether AE has higher sensitivity to damage than the conventional vibration method and to develop an enriched understanding of the emitted signals, numerous studies were undertaken (Yoshioka and Fujiwara 1982 & 1984; Smith 1982 & 1984; Hawman and Galinaitis 1988; Li and Li 1995; Shiroishi et al. 1997; Kakishima et al. 2000; Al-Ghamd and Mba 2006; Tandon et al. 2007; Couturier and Mba 2008; Raja Hamzah and Mba 2009; Halme and Andersson 2010). Considerably similar to vibration, it has been revealed through previous studies, that

AE is able to detect increases in the characteristic fault frequencies caused by an existent damage on a component, whether on a bearing or a gear. A comparative study by Liu et al. (2011) concluded that AE performance, when employed for a roller bearing operating under high rotational speed, is a superior tool for the detection of gross surface defects with regards to the vibrational analysis on the same investigated defect.

Cockerill et al. (2015) carried out an investigation to detect AE signals arising from an SKF cylindrical roller bearing, type N204ECP with artificially seeded defects on the outer raceway. The rotational speed was held constant at 5780rpm and load ranged from 0.29kN to 1.79kN for 6 defect sizes. Figure 2-26 illustrates the results for RMS parameter against load for each defect size, bearing in mind the first two defects were point defects and the rest expanded to multiple points across the width of the outer race. It is shown that for the first two defects, RMS rises significantly, followed by a reduction for defect 3, although the RMS is still higher than the healthy bearing. The authors noted for the reduction in RMS values between defect 2 and 3, is considered to be a result of a larger contact area as the defect is spread across the outer raceway, also that the amplitude of RMS indicates that the generated AE from each defect depends on the defect size. This finding agreed with previous researchers results who have successfully measured a correlation between the statistical parameters and various defect sizes (Rao et al. 2013; Sandoval et al. 2013; Badgujar and Patil 2014).

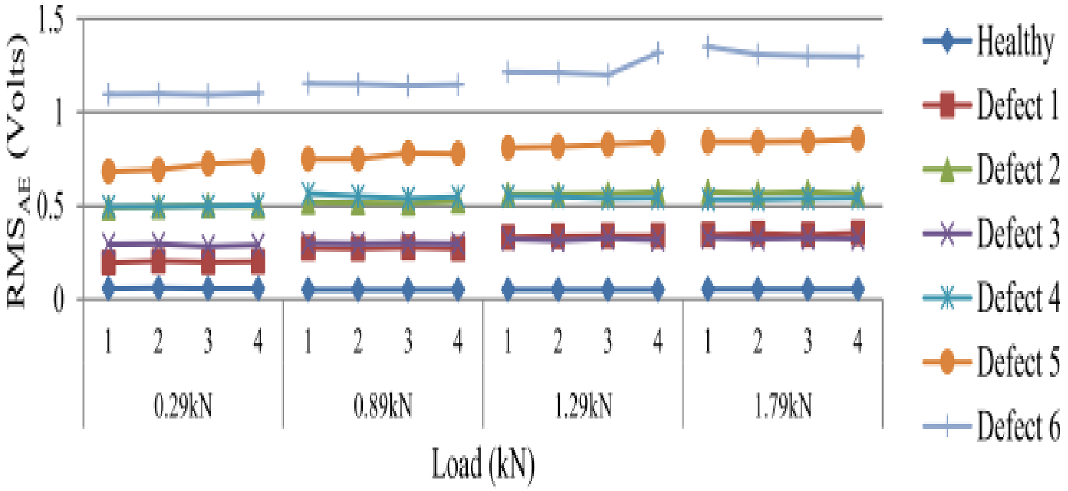

Figure 2-26: Comparative RMS values of healthy and different damaged size bearings- extracted from (Cockerill et al. 2015).

Further investigations on the collected waveform through stacked FFT were calculated in separate frequency bands of 0-75kHz and 75-150kHz. Unlike the low stacked FFT's, a clear increase in amplitude presented with higher loads for the 75-150kHz band. A noteworthy observation was presented as evidence of pre and post-test measurement of defect 2 revealed the absence of sharp peaks as they are flattened out during the test. Similar correspondence to previous findings, where the increase in energy amplitude of the frequencies around 100kHz could be due to the extent of plastic deformation taking place, as perceived by Ramadan et al. (2008), besides the accumulation of debris particles due to over rolling levelling the peaks, as expressed by Chang et al. (2009) in their study of particle interaction in the sliding contacts within a hard disk drive. Furthermore, as the sum of debris grows, the bearing friction likewise will increase, reinforcing the work of Ferrer et al. (2010).

Cockerill et al. (2016) went further, using the same bearings to investigate the outcomes of increased load and speed on an accelerated life test operational under the EHL regime. The results demonstrated that during the continuous wear period, an amplitude increase occurred in the bearing's resonant frequencies even during constant operational loads and speeds. However, higher frequency components at 115, 125 and 330 kHz all keep a constant amplitude yet out of the constant wear period. As the test progressed towards failure, the previous dominant frequencies become less so, as a series of broader frequencies were excited. The author concluded that this is attributed to the over rolling of accumulated debris bits, creating merged signals at higher frequency.

Schnabel et al. (2017) inspected plastic deformation instigated by particle contamination in roller bearings via AE. Two tests were performed in fully lubricated regimes, one with clean grease and the other with contaminated grease lubrication. The results revealed that one obvious difference in AE signals concerning clean and contaminated roller bearings is the amplitude parameter, which relates to the use of such methods as RMS value, counts as well as amplitude in previous research involving particle contamination and AE by (Miettinen and Andersson 2000; Tandon et al. 2007). The author established that the AE signals of roller bearings are dominated at high rotational speeds by transient force signals, thus masking the particle contamination detection. However, at lower speeds (in this case 100 rpm) there was a clear difference in the RMS value as the transient force signals made less of an impact and were sufficiently weak to detect plastic deformation.

In an attempt to extract AE statistical parameters from rolling elements bearing defects, (Alsadoon et al. 2019) carried out an investigation on a fault free single row deep grove ball bearing. The authors determined that the AE RMS value is a positive indicator for condition monitoring in addition to the responsiveness to the speed increments during the investigation. Similar resemblance was underlined for the Peak Amplitude signal analysis results.

Remarkable efforts were performed by (Patil et al. 2020) in deployment of a developed model to analyse the effect of speed, load and radial clearance at various values of 5 µm, 25 µm, 50 µm and 75 µm on the rolling element bearing’s AE signals. Moreover, evaluating the lubrication regime, the nature of arising asperities, form of contact and load distribution which warranted significant factors in AE generation. Statistical parametric analysis results Figure 2-27, determined that as the speed is increased the AE RMS increases up to a certain level with regards to the speed and then decreases at a later stage even if the speed is still increased, these results fall in line with previous research by (Tan and Mba 2005). As for load, AE RMS in the rolling element bearings increases as the load is increased, yet with superior AE RMS generation at lower speeds. The results fall in line with previous researches by (Raja Hamzah and Mba 2009; Fan et al. 2010; Sharma and Parey 2019) for the load effect on the bearing, as the AE RMS shows a linear trend. Finally, it was concluded that with higher radial clearances a noticeable decrease in AE RMS signal except the initial transient phase due to running in of the bearing, as this is in agreement with (Liu et al. 2017).

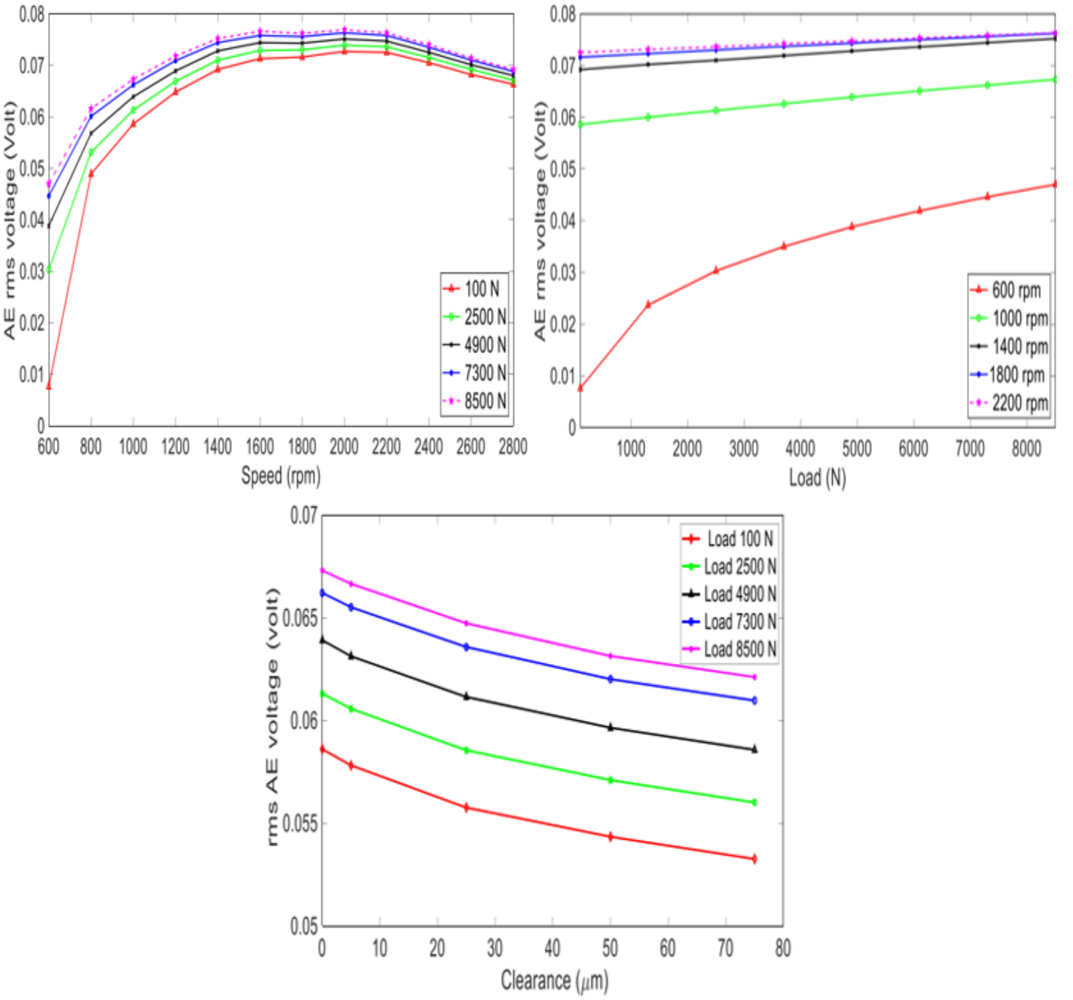

Figure 2-27: Effect of AE RMS from various speed, load and radial clearance - extracted from (Patil et al. 2020).

2.9 Conclusion

Since the official introduction of “tribology” in the 1960s, tribologists have focused on resolving the significant industrial issues of friction and wear by thoroughly understanding the surface phenomena, improved lubrication regimes and the use of improved materials. A series of material encircling tribology and the changes in the physical properties of the surfaces due to the effects of friction, wear and lubrication have been reviewed. In view of this, the integrity of any mechanical system hinges on the appropriate wear conditions. Hence, appraisal to whether it is possible to monitor and manage friction carefully by comprehending particular values and limitations of the mechanical components as well as complying with lubrication boundaries is in place.

A considerable amount of literature encompasses the implementation of AE and vibration methods to detect damage within mechanical systems as a condition monitoring technique. Numerous authors have endeavoured to establish whether AE has higher sensitivity to damage than the conventional vibration analysis (Smith 1982; Hawman and Galinaitis 1988; Li and Li 1995; Shiroishi et al. 1997; Al-Ghamd and Mba 2006; Tandon et al. 2007), while no clear indication of which method is more efficient has been established, a broad consensus that AE is superior at lower rotational speeds as reported by (Smith 1982; Jamaludin et al. 2001).

Furthermore, a common thread exists amongst various investigations with relation to AE parameters variations while under particular operational conditions with regards to speed, load, bearing dimensions and defect size. As the fluid film thickness plays a major role in the before mentioned conditions, only one notable study took the matter into account by (Couturier and Mba 2008). The focus on lubrication regimes proved worthy and effective as the authors reported an increase in rotational speed increases the AE activity when the fluid film thickness is exceptionally low as it fails to separate the contacting bodies, on the other hand as the fluid film thickness improves and separates the two bodies the emission is reduced as no asperity contact takes place.

The classification of frequency characteristics within a measured signal has facilitated the detection and localisation of certain defects within a roller bearing, however these defect signals occurred by means of artificially seeded or engraved defects onto the one of the bearing surfaces. Obtaining the knowledge of the damage location prior to analysis permits the researcher to concentrate their pursuit on them, but far less research has been performed to determine the detection and localisation of natural failures and propagation of defect within a bearing, and it is this problem on which this thesis is focussed.

3 Equipment and Supporting Materials

3.1 Chapter Overview

The previous chapter introduces the rudiments of AE in broad-spectrum, whilst this chapter explores particular hardware and software used to record and process the signals generated by the transient waves demonstrated in the research. Chapter 3 is split into three main sections, firstly describing the equipment, secondly the software used, and thirdly specifying numerical derivations for upcoming calculations in the thesis. Section 3.2 presents a brief overview of the AE hardware utilised during the research including the computers and sensors in use for the test rig, as well as a brief description of how to use the equipment. Subsequently, the architecture of the software used to acquire the data is presented along with providing a brief clarification of the analysis codes developed by the researcher to be used to implement the various analysis techniques in the section 3.3. The preceding section presents a thorough derivation of the methods applied to determine the dimensions of the Hertzian contact area in addition to the distributed load and the lubricant film thickness within the rolling element bearing contact between rollers and the raceways.

3.2 Acoustic Emission Hardware

3.2.1 Acoustic Emission System

The research is carried out using a PCI-2 AE system, which is an eight channel AE system, manufactured by Physical Acoustics, and has the potential of collecting data at up to 40 MSPS while gathering waveforms but is restricted to 10 MSPS at the most when wave streaming simultaneously over four channels and also features an 18-bit A/D converter. The PCI-2 AE system is engineered for research purposes and applications, due to its multipurpose key software, AEWin. The AEWin software conveys all the acquisition, graphing and analysis competencies that a researcher requires in an AE system to facilitate the visualization tasks and data analysis (Physical Acoustics 2017a).

3.2.2 Sensors

AE sensors are manufactured with a range of different characteristics such as bandwidth and direction of sensitivity, resonant frequency, tailored for various specific applications. However, regardless of the particular characteristics of each AE sensor, a piezoelectric crystal exists at the core of each AE sensor as shown in Figure 3-1, that outputs a charge or generates voltage as strain, force, pressure or acceleration is applied due to the electric potential created as electrons within the crystal move relative to each other. The crystalline structure, geometry and dimensions of the crystal element regulates the sensors' sensitivity and characteristics. Piezoelectric crystals are commercially presented as separate components however some companies secure and shelter the crystals within metallic housings to guard the crystal element against external forces in addition to the surrounding environment.

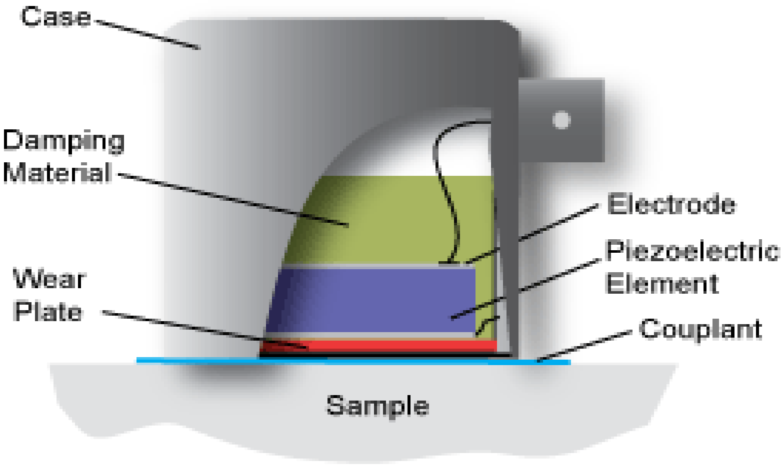

Figure 3-1: Typical structure of an AE sensor.

It is vital that the AE sensors' face is finely mounted and acoustically coupled to the surface, as AE waves travel and pass through the material surfaces. Accordingly, improper coupling will result in air gaps between the sensor face and the material, where substantial energy is absorbed by the air pocket leading to undesirable and imprecise sets of data. Coupling media exist in a varied range of products and it is habitually the users' preference and the test setting which governs the coupling medium required. Coupling mediums such as grease, silicone or ultrasound gel are commonly used to prevent damage to a ceramic faced AE sensor. On the other hand, superglue is often used on a sensor with a metallic face. It is vital to point out that when coupling using ultrasound gel or grease, the sensor is required to be in position, held by a tape, clamps, magnet or other means of supports during the test period. Although, silicone and super glue alike can secure the sensor onto the material. Operating conditions and environmental factors can also affect the choice of coupling media i.e., high temperature operational conditions, the presence of lubricants or fuels could deteriorate the adhesive bond, where the use of tape would be fine in a static structure without these harsh operational conditions, where the tape would fall off in a matter of minutes. With regards to environmental factors, these coupling methods are not always used in a lab or enclosed facility and their use in the industry depending on which field it is used in, could be effective due to change of heat waves, storms, rain and other weather changes that must be considered before the selection of the coupling bond.

The quality and validation of the bond between the sensor and material is ensured by standardised techniques, making pencil lead breaks close to the sensor to determine the accuracy of the source and location setup, generally known as a Hsu-Nielson source (Hsu and Breckenridge 1981; ASTM 2015). In addition, the operator would physically touch the sensor to check it's bond, if the bond is still strong and holding the sensor in its place or the need of removal then cleansing the area of any bonding material and recoupling it again. Lastly, a pencil lead break technique would take place again to ensure the reading of the signal is efficient. The pencil lead break generates an intense AE signal, relatively reminiscent of a natural AE source that the sensors detect as a strong burst, which aids the user to simulate an AE event using the breakage of a brittle graphite lead. The test instrument consists of a mechanical pencil, fitted with 0.5mm or 0.3mm diameter 2H lead and equipped with a 'Nielson Shoe'. The Nielson Shoe is a plastic component attached to the mechanical pencil; the dimensions of which are illustrated in Figure 3-2. The shoe is designed and intended to produce and replicate a repeatable source by preserving the angle where the pencil lead is broken. This technique has been performed during the investigation prior to every test, as well as following every test to ensure the sensors are reading in a correct form.

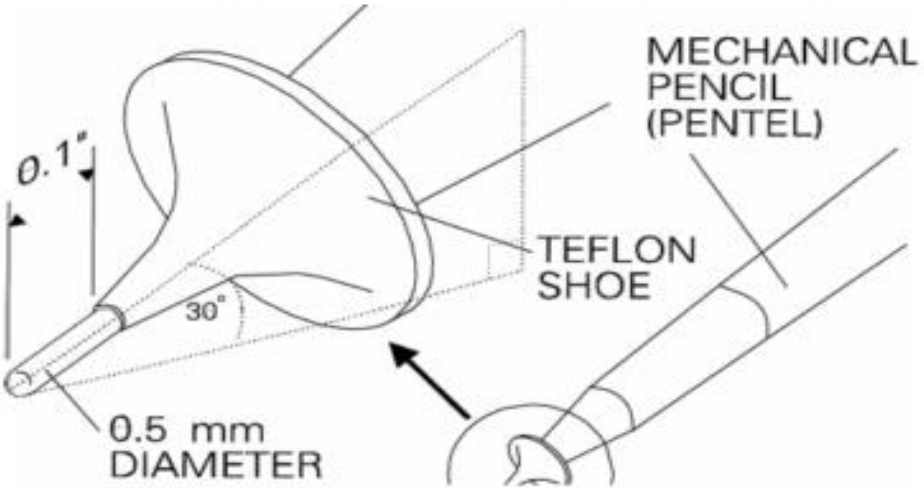

Figure 3-2: Dimensions of the Hsu-Nielson shoe (Extracted from (Hellier, 2012)).

The AE sensors used within the investigation are a PAC Nano30 AE sensors (Figure 3-3) and they are favoured due to their wide operational bandwidth, size and availability. PAC Nano30 sensors have a resonant frequency near 300kHz. Nano30 sensors are manufactured with ceramic faces, hence the use of super glue to secure them to surfaces under investigation is not possible.

As the bearing test rig used in this research is generally oily and operates at elevated temperatures for long periods of time it was believed that brown lithium grease, a generally used coupling medium, would melt and run out of the contact reducing the effectiveness of the couplant, also the problem with having a magnet to fix and hold the sensor in place for a long period of time during the research is not straightforward with grease melting. Therefore, Loctite 5910, a silicon-based engine gasket sealant, was preferred to secure the sensors on the bearing test rig. Silicon-based sealants are regularly used to bond sensors to surfaces, but the advantage of engine gasket sealant that it is designed not to deteriorate once exposed to elevated temperatures and oils for long periods of time and has proven to be successful in the work of (Cockerill 2017; Hutt et al. 2019) under similar operational conditions.

Before applying Loctite 5910 on the surface to bond the sensors, both surfaces need to be cleaned and degreased. A fair amount of silicone would be applied to the face of the sensor before placing it on the surface. To hold the sensor in place a magnet or a toolmakers clamp would be used, as the silicone requires about 24 hours to cure fully.

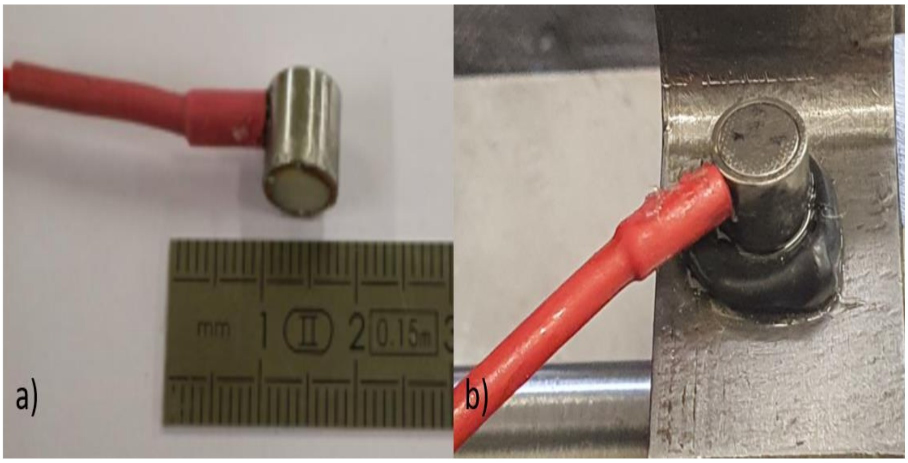

Figure 3-3: a) Nano30 AE sensor b) Nano30 AE sensor coupled to the one of the support bearing housings.

3.2.3 Amplifiers

The amplifiers used within this research are able to apply a selectable gain range of 20/40/60 dB through a switch, as well filtering incoming signals. Outputs of the AE sensors are initially connected to the amplifier then the signal is passed onto the AE hardware. Figure 3-4 represents a PAC 20/40/60 dB amplifier with a built-in bandpass filter of 20-1200kHz that is used throughout the investigational works herein. These amplifiers were chosen for consistency with previous work on the same test rig by (Cockerill 2017).

Figure 3-4: 2/4/6 Pre-Amplifier with built in bandpass s filter of 20-1200kHz by MISTRAS.

3.3 Software

For the experimental research performed in Chapter 5, a LabView Virtual Instrument (VI) was developed to enable the acquisition of parametric data, including bearing temperature and shaft speed. The front panel of the VI allows the researcher to specify a location for the text file to be saved, the rate and length of data acquisition, including granting the researcher the ability to start and stop the acquisition system whenever deemed necessary. The bearing test rig was not associated with a load cell to measure the applied load, which is applied by loading with weights, so for that reason the researcher has to physically add or remove the applied mass also manually enter the applied mass into the system in kilograms. The data acquisition VI outputs include total number of revolutions, applied load, shaft speed, number of data samples recorded, the temperature at each of the three bearings and the oil bath. The VI was modified by the author as required for the new test rig, based on the original code developed from previous research by Cockerill (2017).

To boost the post-processing efficiency of the data, several Matlab scripts were developed. The developed scripts allow the user to assign the analysis to a specific wavestream, or permit the data to be batch processed, writing image files automatically and saving data sets. The analysis techniques considered include Raw Wavestream Signal plotting, Peak Value, RMS, Fast Fourier Transforms (FFTs), Spectrogram: Short Time Fourier Transform (STFT), some of which are briefly clarified as follows:

3.3.1 Peak Value

The peak value of a signal (Volts) can be described as the mean of the absolute maximum and minimum of the signal as shown in Equation (3.1). Although, due to the theory behind large defects generating higher amplitude events, and that the peak value does not take into account all data points measured, it is not perceived as a reliable indicator of bearing health since noise and spurious data may possibly distort results (Naumann 2016).

$$Peak = \frac{1}{2}\left(\max\big(x(t)\big) - \min(x(t))\right) \qquad (3.1)$$

3.3.2 Root Mean Square (RMS)

The RMS value (Volts) provides an overall energy measurement of a signal and is largely applied in industry due to its ability and simplicity to be operated online. Equation (3.2) is given for RMS, where $x(t)$ is a discrete time series signal composed of N data points.

$$RMS = \sqrt{\frac{1}{N}\sum_{t=1}^{N} x(t)^2} \tag{3.2}$$

RMS is a robust method for bearing health monitoring when operational conditions are constant and is able indicate the occurrence of significant defects (Mba 2003; Mba 2004). Nevertheless, while RMS is determined across a pre-defined time constant it fails to contemplate the transient nature of a defect signal. The interval amid impulses occurring due to a roller impinging on a raceway is typically large in contrast to the duration of the impulses themselves, this is particularly true for slow rotating bearings with small defects. Transient bursts with an amplitude significantly weaker than the noise, for instance those occurring from incipient damage will consequently form a minimal contribution to the overall energy. Unfortunately, damage will have often advanced considerably prior to it being detected by RMS (Naumann 2016).

3.3.3 Fast Fourier Transforms (FFT)

Equation (3.3) for FFT is used to define the amplitude and phase of a frequency, k, within a signal noted as a complex number, X_k, where t is the current time sample, T is the overall number of samples and x_t is the value of the signal at current time t.

$$X_k = \sum_{t=0}^{T-1} x_t \cdot e^{-i2\pi kt/T} \tag{3.3}$$

Every recorded signal could be decomposed into numerous sinusoidal waves each with different amplitudes and frequencies by executing a Fourier Transform. The FFT fundamentally breaks down the signal to reveal the amount of energy (or amplitude) of the overall signal occurring at each of the frequencies contained. Figure 3-5 illustrates an example of how the FFT is determined where the signal is determined by Equation (3.4), showing that the FFT correctly demonstrates that the energy in this particular signal is contributed by equal amounts of energy at 5, 10, 20 and 50 Hz, as per Equation (3.4)

$$y = \sin(5x) + \sin(10x) + \sin(20x) + \sin\,(50x) \qquad (3.4)$$

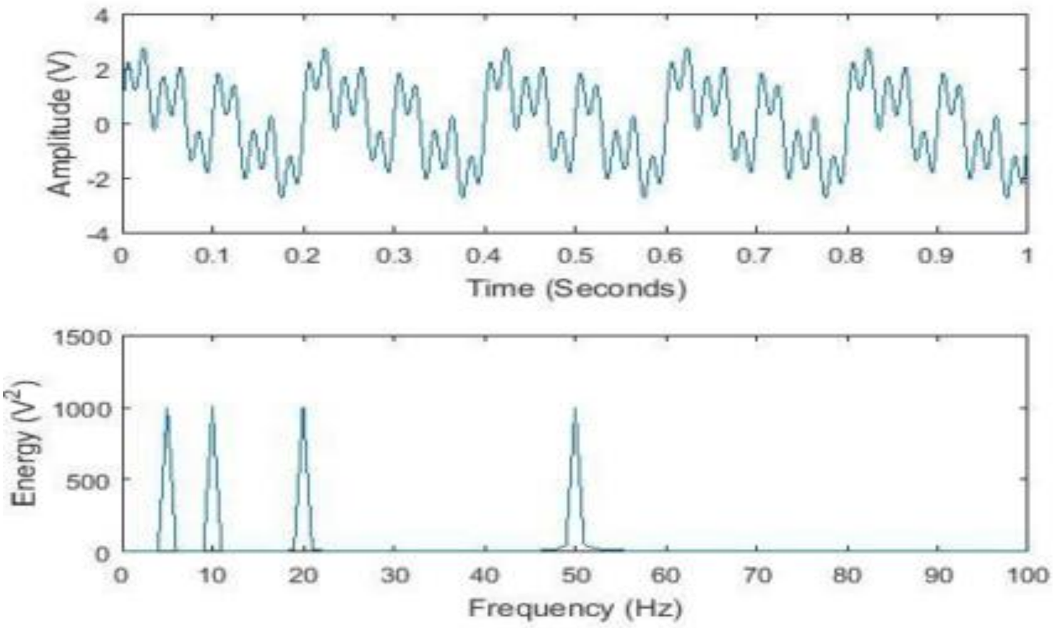

Figure 3-5: An example of FFT.

3.3.4 Short Time Fourier Transform (STFT)

As frequency content of a signal is computed, errors may actually arise when a limited-duration snapshot is taken of a signal that essentially lasts for a longer time. Windowing is a method to reduce such errors, although it is not able eliminate them completely. The STFT is one of many methods of analysing the frequency content of non-stationary signals. This method is based on time-frequency analysis of the signal, which is achieved gradually in shorter sections. A fixed window is used to select the individual sections and a Fourier transform is applied to them. The choice of window size or function has a major influence on the STFT result (Jaros 2022). A window function, usually a Hamming, Kaiser or Gaussian window, is multiplied by the signal and the Fourier transform is calculated (Khodja 2019;

Carvalho 2019 and Ayon-Sicaeros 2019). The window is shifted in time to create a 2D time-frequency illustration of the signal which can be graphically viewed as a spectogram (Naumann 2016). Spectrograms add time to the analysis of FFT allowing the localization of both time and frequency. Jaros (2022) stated that there are three configurable parameters, (1) a spectral window, which is used to limit the distortion in the frequency domain. (2) window length which determines the size of the window that moves along the length of the input signal. (3) number of overlapped samples for a window that moves along the signal, which must not be larger than the window. The key drawback of an STFT is resolution. A compromise between frequency resolution and time must be met by way of selecting a suitable window width for the application in hand. The wider the window the clearer the frequency resolution where similar frequencies may well be separated in the spectrum. If a shorter window is chosen, adjacent harmonics could be smeared one to another, but with an enhanced temporal resolution (Rother 2015 and Naumann 2016). Hence, the window size is a critical parameter. If the window size is wide, a high resolution in the frequency domain and a low resolution in the time domain are acquired. In contrast, in the case of a narrow window, a low resolution in the frequency domain and a high resolution in the time domain are obtained (Hubner 2020), this property is shown in Figure 3-6.Figure 3-6: Diagrams (a) STFT with narrow window, (b) STFT with wide window-extracted from Hubner (2020)

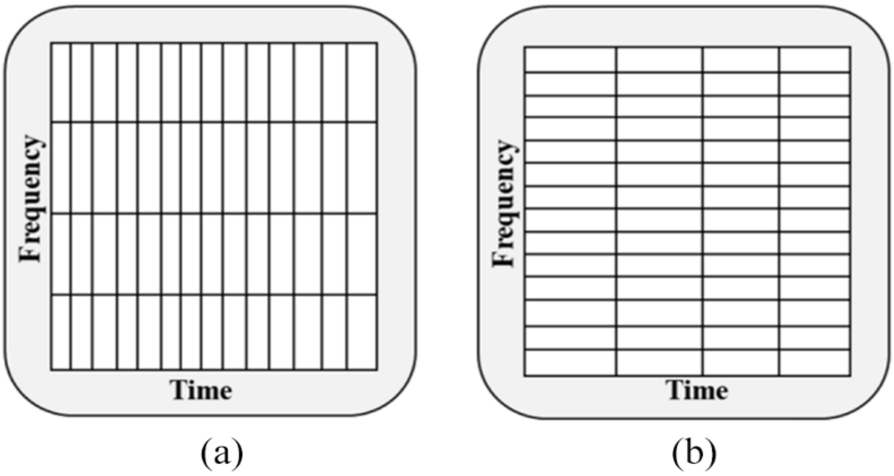

Figure 3-6: Diagrams (a) STFT with narrow window, (b) STFT with wide window-extracted from Hubner (2020)

Essentially, it depends on the application as the wider the window, the better the frequency resolution but the time resolution gets worse, works also vice versa (Jaros 2022). Figure 3-7 illustrates an example, where spikes due to defect signals are observed in the frequency content at around 0.045 and 0.11 seconds as a result of a roller passing through a defected area on the raceway.

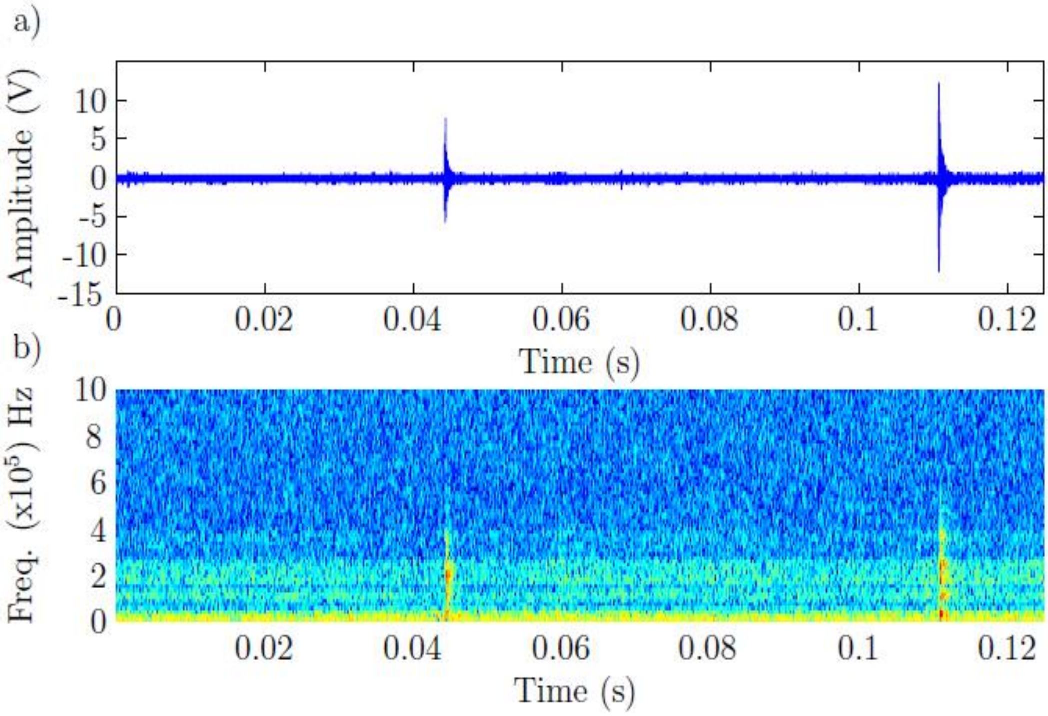

Figure 3-7: Example of STFT a) Damaged Bearing and b) Resultant Spectrogram.

3.4 Tribological Numerical Analysis of Roller Element Bearings

Prior to an experimental design, it is essential to realise how individual variables such as load, speed and temperature could influence the tribology of rotating machinery under investigation so that precise assumptions can be drawn. Moreover, the magnitude of stress experienced is mutually critical for the life of raceways and rollers and must be assessed to understand the operating restrictions of the roller element bearing while undertaking healthy bearing characterisation tests and to confirm that bearings will not be overloaded. On the other hand, calculating the contact stresses for higher loads will allow the preparation of an accelerated bearing failure test. In addition to the contact stress, the λ indicates the level of surface separation by lubrication within bearings, and if some asperity contact might be in effect, the process of which is documented in the following section in Equations (3.5-3.37).

3.4.1 Hertzian Contact

Vereins and Gewerbejeisses (1982) stated that Heinrich Rudolf Hertz was a physicist who became captivated by the question of how much distortion glass lenses experience when they were loaded against each other in an optical device. Therefore, Hertz (1882) initially inspected elastic deformation through optical lenses that were pressed together, to reveal the presently renowned contact theory which takes his name. Hertz's work proved to be revolutionary in the contact mechanic disciplines. Up to the present time, the investigation of elastic deformation along with contact stresses of loaded contacts remains almost totally based on the Hertzian contact theory (Johnson 1985).

Hertzian contact theory (HCT) is used to analyse and calculate confined contact stiffness in rolling bearings. An analytical explanation of Hertzian contact problems is beneficial to identify the influence each parameter has on the contact stress or stiffness, which allows materials and geometry to be optimized to improve rolling bearing performance. Adopting the mathematical Hertzian approach allows accurate calculation of the contact stress, displacement and dimensions.

Hence, R_x and R_y are the Principal Radii of Relative Curvature. When combined the radii of two bodies in contact is identified as the relative radius of curvature R. There are two types of contacts, non-conformal and conformal contact. Where the former also known as concentrated contact assembled by surfaces of unalike shapes, with smaller areas of contact and higher contact stresses. The latter consist of surfaces with similar shaped contacting bodies, with larger areas of contact and lower contact stresses.

Equation (3.5) is used for non-conformal contact,

$$\frac{1}{R}=\frac{1}{R_1}+\frac{1}{R_2} \tag{3.5}$$

and for a conformal contact Equation (3.6)

$$\frac{1}{R} = \frac{1}{R_1} - \frac{1}{R_2} \tag{3.6}$$

where R_1 and R_2 are the relative radii of curvature in a single axis of the bodies as illustrated in Figure 3-8. In view of that, the relative radius of curvature is then considered for the *x* and *y* axis in turn, fundamentally defining the form of contact. During applied load, initial contact occurs in the form of line or point contact, where if one of R_x or R_y are infinite, the contact is a line which spreads to a rectangular area under load. For point contacts, the loaded contact area is circular if $R_x = R_y$ and elliptical if $R_x \neq R_y$.

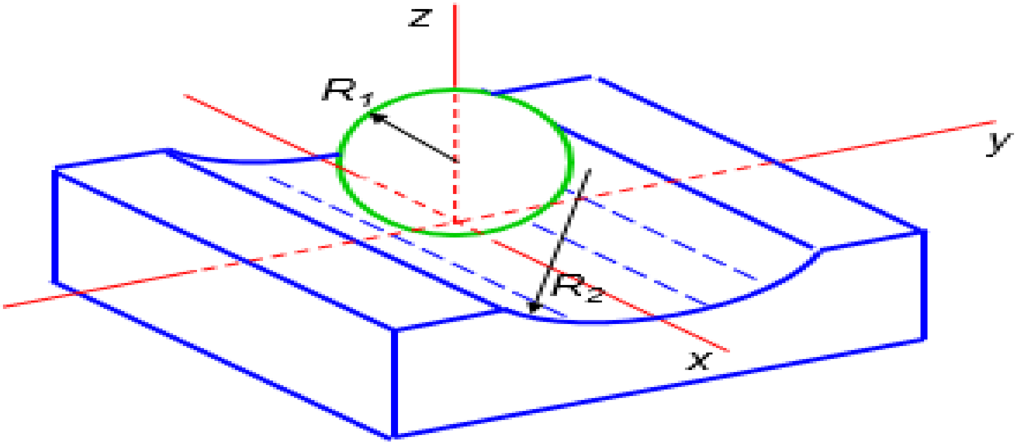

Figure 3-8: An illustration the Relative Radius of Contact Curvature– Extracted from Evans (2018).

Hertz established that, for a line contact, the mean contact pressure, p_m, over the contact area between two bodies, is a function of the Youngs' Modulus of Elasticity, E, Poissons ratio, v, semi-contact width, a and the deflection, δ, in such a way that

$$p_m \propto \frac{E_n}{1 - v_n^2} \frac{\delta_n}{a} \tag{3.7}$$

And accordingly,

$$\delta_n \propto \frac{1 - v_n^2}{E_n} a.p_m \tag{3.8}$$

While the pressure acts amid two surfaces, it is viable to state that

$$\delta_1 + \delta_2 \propto \left\{\frac{1 - v_1^2}{E_1}\right\} a.p_m + \left\{\frac{1 - v_2^2}{E_2}\right\} a.p_m \tag{3.9}$$

Correspondingly,

$$\delta_1 + \delta_2 = \frac{a^2}{2R_1} + \frac{a^2}{2R_2} \tag{3.10}$$

Therefore,

$$\left\{\frac{1 - v_1^2}{E_1} + \frac{1 - v_2^2}{E_2}\right\} p_m \propto \left\{\frac{1}{R_1} + \frac{1}{R_2}\right\} a \tag{3.11}$$

Furthermore, the replacement of the radius of curvature from Equation (3.5 and 3.6) and Young's modulus of each contacting body by their reduced values given by:

$$\frac{2}{E'} = \frac{1 - v_1^2}{E_1} + \frac{1 - v_2^2}{E_2} \tag{3.12}$$

and, using the equations for substitution to represent,

$$\frac{p_m}{E'} \propto \frac{a}{R} \tag{3.13}$$

allows us to determine that the contact dimension, a, is given by Equation (3.14)

$$a = \sqrt{\frac{8Rw\prime}{\pi E\prime}} = 1.569\sqrt{\frac{Rw\prime}{E\prime}} \tag{3.14}$$

and the mean pressure, $p_{m,}$ is given by Equation (3.15)

$$p_m = \frac{\pi}{4} p_0 = \sqrt{\frac{\pi E' w'}{32R}} \tag{3.15}$$

Figure 3-9 illustrates the semi-elliptically varied pressure over the contact-width, $2a$, for a line contact, and the maximum pressure, p_0, is determined as

$$p_0 = \frac{2w'}{\pi a} = \sqrt{\frac{E' w'}{2\pi R}} \tag{3.16}$$

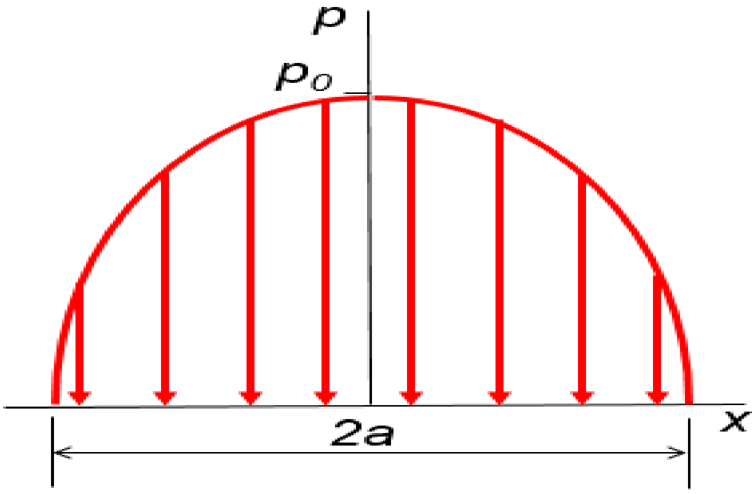

Figure 3-9: Pressure varies over the contact area as a semi-elliptical distribution Extracted from Evans (2018).

3.4.2 *Load Distribution*

Equation (3.16) established by Hertz defines the maximum Hertzian contact pressure, p_0, of a single roller contact. However, as the load is distributed among a number of rollers within the bearing, the accurate number of rollers in contact is determined by the bearing’s radial clearance as shown in Figure 3-10. To deduce specific roller loads occurring to each rolling element within the roller bearing collectively and as a result the maximum roller load, Harris and Kotzalas' (2006) method is used. This technique is intricate but yields detailed information on the load distribution within the roller bearing.

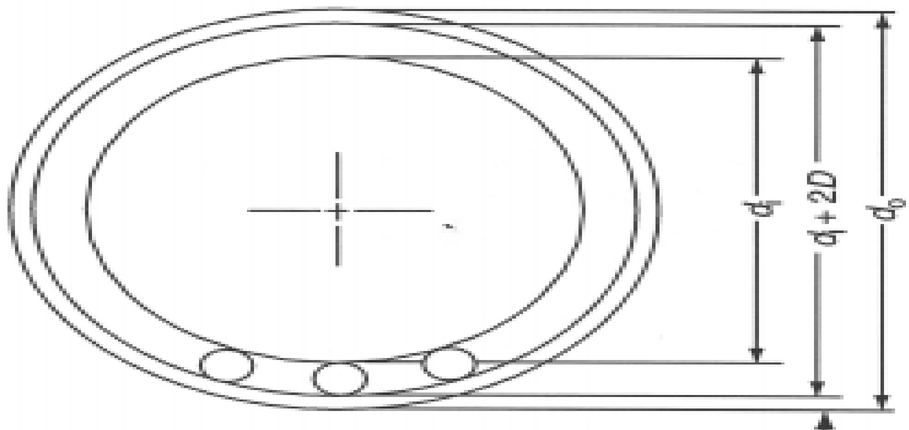

(a) Before displacement

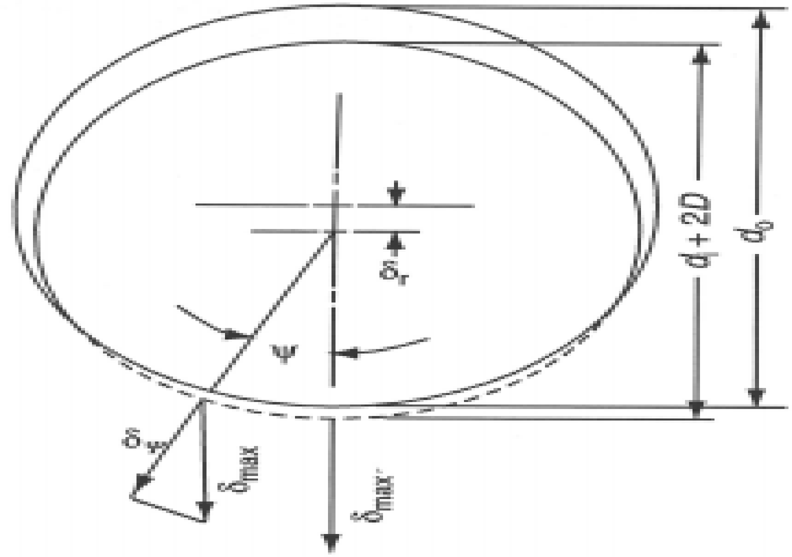

(b) After radial displacement

Figure 3-10: Load distribution calculation due to bearing ring displacement. Extracted from (Harris & Kotzalas 2006).

For a particular cylindrical rolling element under a pure radial load, Q, the experienced load on the inner and outer raceways Q_i and Q_o respectively are equivalent.

$$Q = Q_i = Q_o \tag{3.17}$$

For a line contact amongst two surfaces, the magnitude of deflection at the contact, δ, on any random cylindrical rolling element is proportional to the load, Q, to the n power, n=3/2 or 1.5 for ball bearings (point contact) and n=10/9 or 1.11 for roller bearings (line contact).

$$\delta \sim Q^n \tag{3.18}$$

Therefore, it can be said that, while K_n is the load deflection factor.

$$Q = K\delta^n \tag{3.19}$$

The total deflection, δ_n , of both raceways of the bearing loaded and separated by a rolling element can be expressed as in Equation (3.20), where the deflections between the roller and the inner and outer raceways respectively are δ_i and δ_o.

$$\delta_n = \delta_i + \delta_o \tag{3.20}$$

Therefore,

$$K_n = \left[\frac{1}{(1/K_i)^{1/n} + (1/K_o)^{1/n}}\right]^n \tag{3.21}$$

and,

$$Q = K_n\delta^n \tag{3.22}$$

For a steel ball-steel raceway contact Equation (3.23) and as the parameter relating to the contact geometry is Σ_ρ and δ^* is a non-dimensional deflection

$$K_p = 2.15 \times 10^5 \Sigma\rho^{-1/2}(\delta^*)^{-3/2} \tag{3.23}$$

Thus similarly, for a line contact of a steel roller-steel raceway,

$$K = 8.06 \times 10^4\ l^{8/9} \tag{3.24}$$

For a cylindrical roller bearing subjected to radial load, the load is distributed over a number of rollers and the radial deflection at any of the roller element angular location, δ_φ, can be calculated by,

$$\delta_\varphi = \delta_r cos\varphi - \frac{1}{2}\ P_d \tag{3.25}$$

where the radial ring shift at $\psi = 0$ is δ_r and the diametrical clearance is P_d. Thus, the rearrangement of Equation (3.25) in terms of maximum deflection results in

$$\delta_\varphi = \delta_{max}\left[1 - \frac{1}{2\varepsilon}(1 - \cos\varphi)\right] \tag{3.26}$$

Where,

$$\varepsilon = \frac{1}{2}\left(1 - \frac{P_d}{2\delta_r}\right) \tag{3.27}$$

The rearrangement of Equation (3.27) and P_d determines the load distribution's overall angle,

$$\varphi_l = cos^{-1}\left(\frac{P_d}{2\delta_r}\right) \tag{3.28}$$

The ratio between the angular load, Q_{φ}, and maximum load, Q_{max}, in Equation (3.22) is related to the ratio between angular deflection, δ_{φ} , and maximum deflection, δ_{max} as shown in Equation (3.29).

$$\frac{Q_{\varphi}}{Q_{max}} = \left(\frac{\delta_{\varphi}}{\delta_{max}}\right)^{n} \tag{3.29}$$

And henceforth, the exchange of Equation (3.26) from Equation (3.29)

$$Q_{\varphi} = Q_{max}\left[1 - \frac{1}{2\varepsilon}(1 - \cos\varphi)\right]^{n} \tag{3.30}$$

In the case of static equilibrium, the sum of the vertical loads at each of the rollers must be equal to the total applied load,

$$F_r = \sum_{\varphi=0}^{\varphi=\pm\varphi_l} Q_{\varphi}\, cos\,\varphi \tag{3.31}$$

or

$$F_r = Q_{max}\sum_{\varphi=0}^{\varphi=\pm\varphi_l}\left[1 - \frac{1}{2\varepsilon}(1 - cos\,\varphi)\right]^{n} cos\,\varphi \tag{3.32}$$

Equation (3.32) could be expressed as an integral in a manner that

$$F_r = NQ_{max} \times \frac{1}{2\pi}\int_{-\varphi_l}^{+\varphi_l}\left[1 - \frac{1}{2\varepsilon}(1 - \cos\varphi)\right]^{n} \cos\varphi\, d\varphi \tag{3.33}$$

or

$$F_r = NQ_{max}J_r(\varepsilon) \tag{3.34}$$

as N is the number of rolling elements and where

$$J_r(\varepsilon) = \frac{1}{2\pi}\int_{-\varphi_l}^{+\varphi_l}\left[1 - \frac{1}{2\varepsilon}(1 - \cos\varphi)\right]^n \cos\varphi \, d\varphi \tag{3.35}$$

In addition, from Equation (3.22) it is established that,

$$Q_{max} = K_n\delta_{\varphi=0}^n = K_n(\delta_r - \frac{1}{2}P_d)^n \tag{3.36}$$

Therefore,

$$F_r = NK_n\left(\delta_r - \frac{1}{2}P_d\right)^n J_r(\varepsilon) \tag{3.37}$$

To calculate the load distribution integral, $J_r(\varepsilon)$, for a bearing under pure radial load, the number of rolling elements and the diameter of the inner raceway has to be known. A radial deflection, δ_r, is presumed and used to solve Equation (3.27) and find the first estimated value of ε. The calculated value of ε is then utilized to solve Equation (3.37) and in the case that the result fails to balance, the method is repeated through an iterative method until the result of Equation (3.37) is balanced. As such, the initial estimate of the radial deflection is unimportant, as the iterative method will find a solution from an initial estimate. An example of the load distribution integral, $J_r(\varepsilon)$, is demonstrated in Figure 3-11 as calculated for a cylindrical roller bearing.

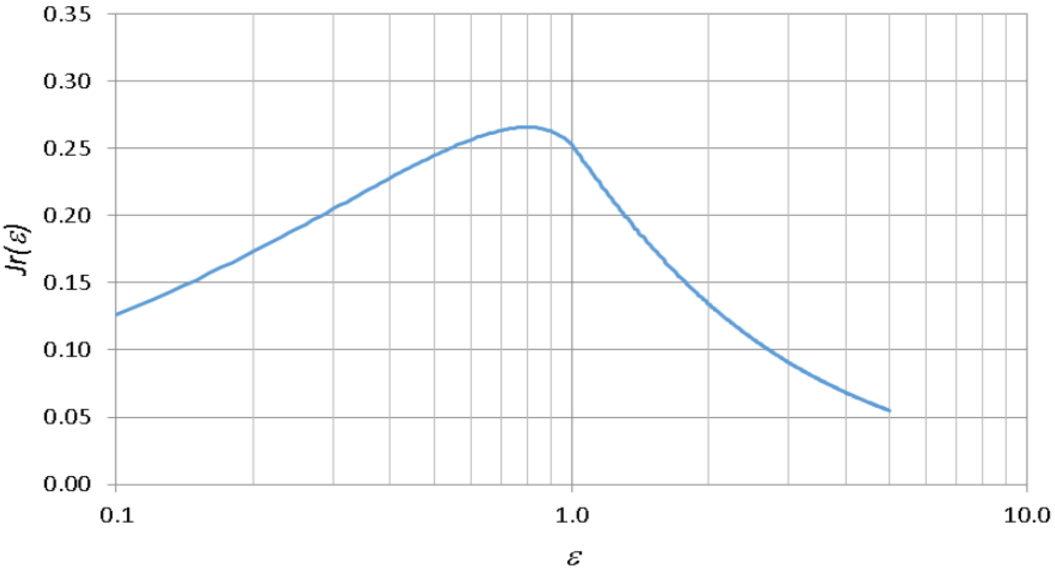

Figure 3-11: Load distribution integral, Jr (ε), for a cylindrical roller bearing.

A computational code was written using Matlab to perform the calculations for the roller bearings under investigation for the research. The load distribution code outputs the maximum rolling element load as well as the number of rollers in contact and the load on each. The maximum rolling element load is then used to determine the maximum contact pressure, as described in Section 3.4.1. Additionally, determining the minimum fluid film thickness by applying the Dowson-Higginson formula, as outlined in Section 2.5.1. The fluid film thickness results are then used in conjunction with the RMS surface roughness to determine the bearing's operational lubrication regime.

4 High-Speed Rig Design & Experimental Set Up

4.1 Chapter Overview

The high-speed test rig in use for this research required some modifications and adjustments to make it suitable for the current work. This chapter will describe the original version of the high-speed test rig in section 4.2, as well as the modifications conducted by the author in section 4.3. The related data acquisition hardware applied will be described in section 4.4 and the bearing operational conditions in section 4.5. Lastly, section 4.6 describes the experimental set up and senor locations.

4.2 High-Speed Test Rig

The original design of the high-speed test rig was made so that the test bearing is situated in between the two support bearings, the actual rig is shown in Figure 4-1 and a semi-cross sectioned Solid Works cad model of the test rig in Figure 4-2. The applied radial load on to the test bearing housing was transmitted from the loading arm via a cylindrical roller.

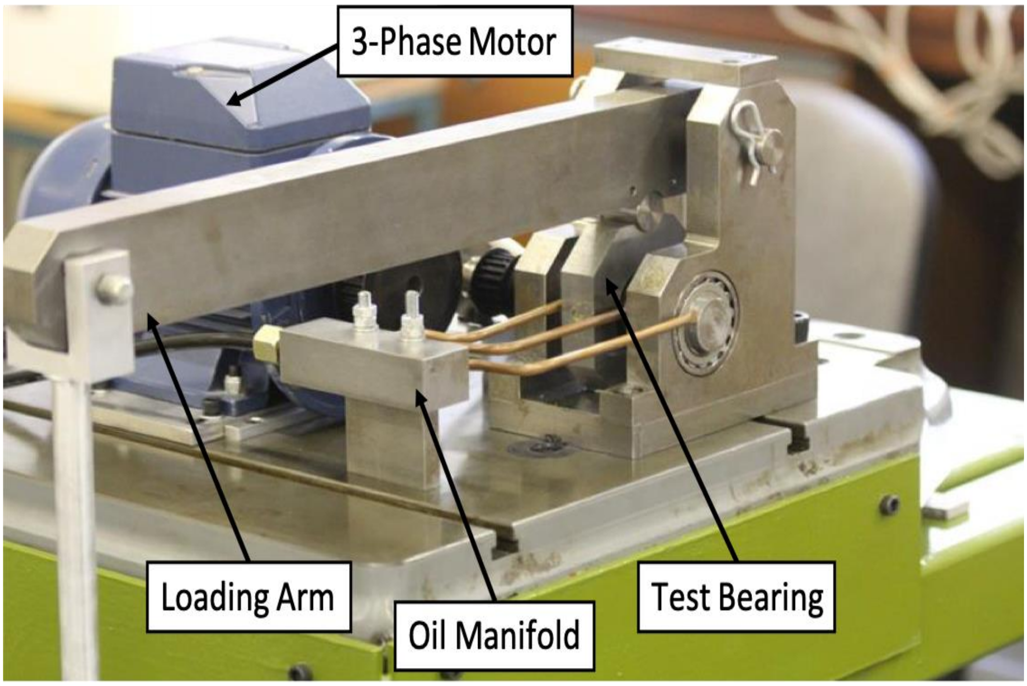

Figure 4-1: Old version of High-Speed Test Rig.

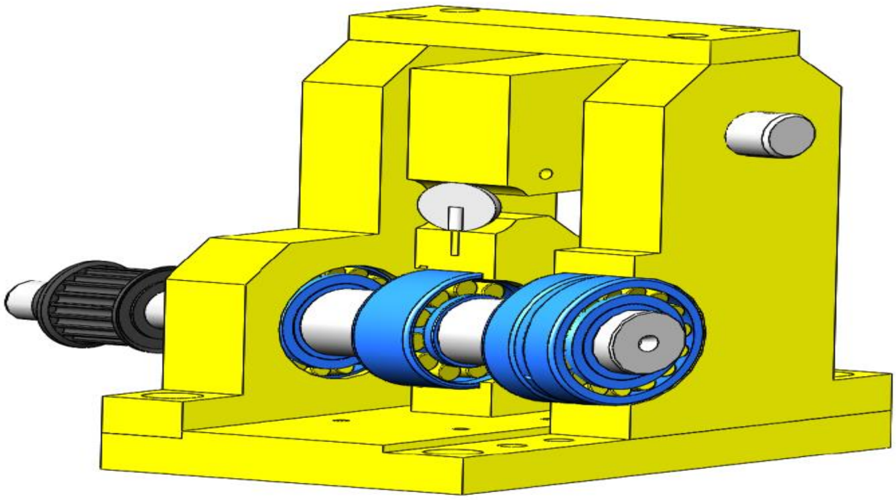

Figure 4-2: Old version of High-Speed Test Rig Solid Works Schematics.

The test bearing investigated on the high-speed rig was an SKF type N204ECP single row cylindrical roller bearing. The ‘N’ specification of the test bearing signifies caged rollers are enclosed within the inner raceway as seen in Figure 4-3. This made it easier to remove the outer raceway to be inspected in addition to facilitating the application of seeded defects onto the outer raceway.

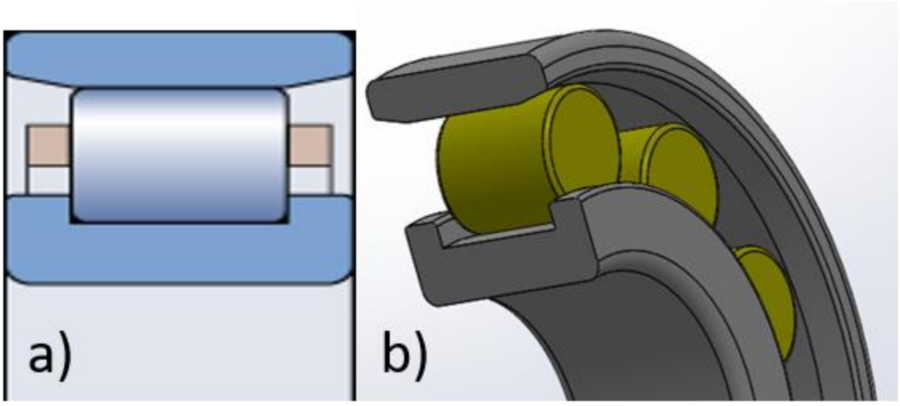

Figure 4-3: a) Cross-sectional view of a cylindrical roller bearing type ‘N’ Specification b) Similarly by Solid works.

The main advantage of this design is that the load on each of the support bearings is half of the applied load on to the test bearing, this arrangement improves the possibility in terms of any natural degradation would ensure that the test bearing fails before any of the support bearings.

The major drawback related to the original design are that, in order to replace a failed bearing or to remove it for inspection, the whole rig assembly must be taken apart. Moreover, this requires more time than the modified design described in the following section. This unfortunately could lead to undesirable decline of the sensors coupling, resulting in lower sensitivity and efficiency in repeatability of the sensors' performances. Additionally, the use of a cylindrical roller to transfer load from the loading arm to the test bearing housing via a line contact may instigate a higher risk of misalignment within the test bearing. Lastly, the copper pipes feeding the test rig were placed to the sides of the bearings to provide lubrication as seen in Figure 4-1.

4.3 Design Modification on the High-Speed Test Rig

The literature in Chapter 2, revealed that most researchers operated on a commonly designed bearing test rig, designed with an over-slung test bearing at the end of the shaft and two support bearings on one side of the test bearing. An existing test rig from previous research shown in Figure 4-1 has been modified to match this configuration for this research as shown in Figure 4-4 and Figure 4-5.

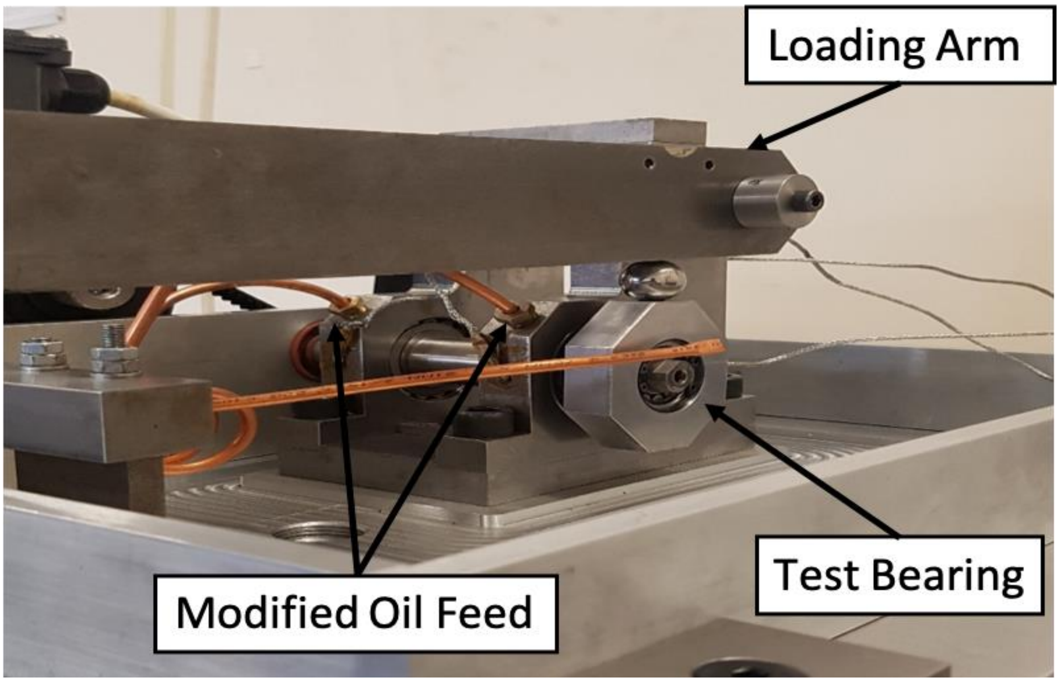

Figure 4-4: Modified High-Speed Test Rig with Test Bearing Housing on the right hand side of the rig assembly.

Figure 4-5: Two support Bearings on the left hand side of the modified High-Speed Test Rig.

This design is well regarded as it simplifies and allows the researcher to remove the test bearing from the shaft for inspection, avoiding the need to disassemble the entire test rig, which saves time in the long run for further testing. A detailed illustration of the modified test rig with new oil drainage grooves on a new base plate, drilled holes on the support bearing housing for the oil feed are shown in Figure 4-6.

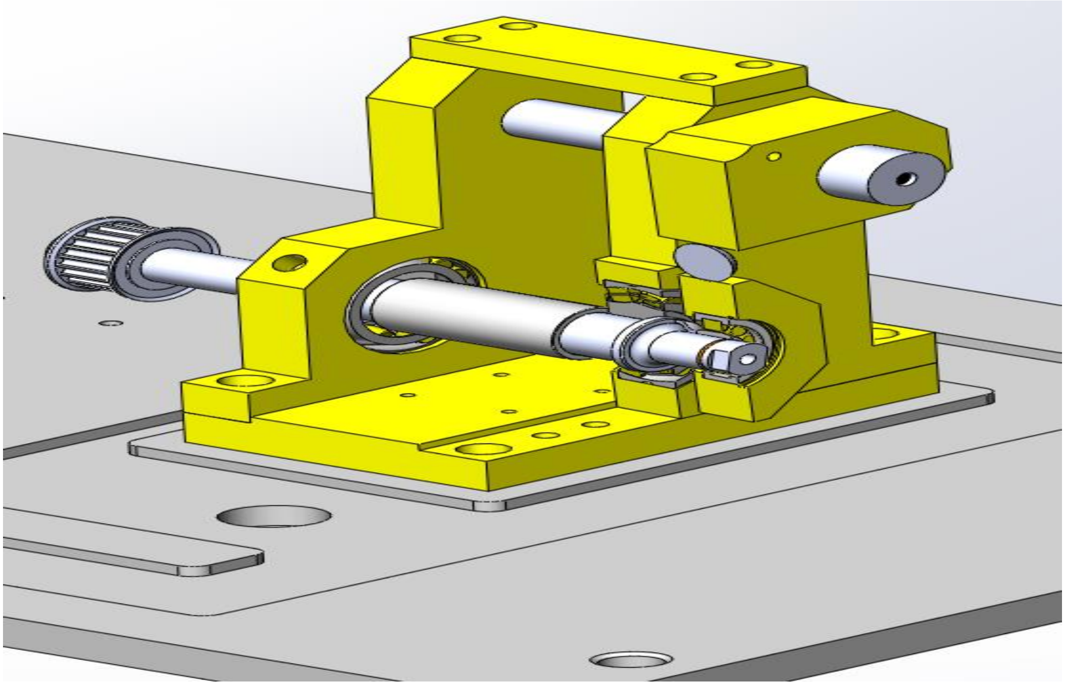

Figure 4-6: Solid Works schematics of the modified High-Speed Test Rig.

Additional advantages of this set-up is that it allows the test bearing to have a smaller bore diameter as it is on the end of the shaft and makes it likelier to fail before the support bearings, thus backing the intended investigation of roller bearing life tests. Moreover, avoiding full disassembly of the test rig diminishes the risk of having to recouple the sensors as some may become uncoupled or dismounted, which would lead to longer procedures to assemble the test rig. Since a sensor needs thorough cleaning as well as the area that the sensor needs to be mounted on, by removing all unnecessary coupling material, degreasing, drying and lastly securing the AE sensors to the test rig takes at least 24 hours to make sure that the coupling material in use has dried out and cured as shown in Figure 4-7.

Finally, the cylindrical roller that transferred the applied load from the loading arm to the test bearing housing has been replaced with a 20mm diameter ball to limit any misalignment hence the line contact becomes a point contact.

Figure 4-7: AE Sensor mounted on the test bearing housing and held with a clamp for 24 hours.

This common design, however, lays a higher percentage of the radial load on the support bearing nearest to the test bearing which may cause it to degrade sooner than the other support bearing leading to unnecessary replacement of the damaged support bearing. However, that the support bearings used in the test rig have significantly higher dynamic load capacity then the designated test bearing, hence settling the issue.

The load is applied to the test bearing by a lever arm with a 10:1 mechanical advantage. The load is then transferred from the loading arm to the test bearing housing by the 20mm ball restricting any misalignment while the load is transmitted on to the test bearing. To prevent any axial movement the test bearing housing was manufactured specifically for the roller bearing under investigation where one side of the housing has the bearing pressed against a shoulder and the other side has a circlip grove to maintain the investigated bearing in place.

The bearings under investigation are single row cylindrical roller bearings types NU202ECP, NU202ECP/C3 and NU202EM. The first two bearings are made by SKF, whilst the last bearing is a budget bearing. The 'NU' specification is designed without flanges on the inner ring and two integral flanges on the outer ring to enclose the caged rollers Figure 4-8. The bearing was selected due to its design as it enables the removal of the bearing's outer raceway and the caged rollers from the shaft by hand, by doing so the inner race way although stays on the shaft and then is removed with a three jaw bearing puller. For the bearing puller to reach behind the inner race way, a specific spacer with three inlets for the puller jaws was manufactured, which is fitted on to the shaft before pressing the inner race way as shown in Figure 4-9, as well as the 20mm ball position on top of the test bearing housing. Hence, the removal and separation of the bearing's individual components is arranged without any damage done to the bearing. This simplifies and accelerates the procedure for further testing as it is not required to disassemble the support bearings and is exceedingly advantageous when it comes to the surface inspection of especially the inner raceway of the bearing following experimentations in comparison with the N 204 ECP.

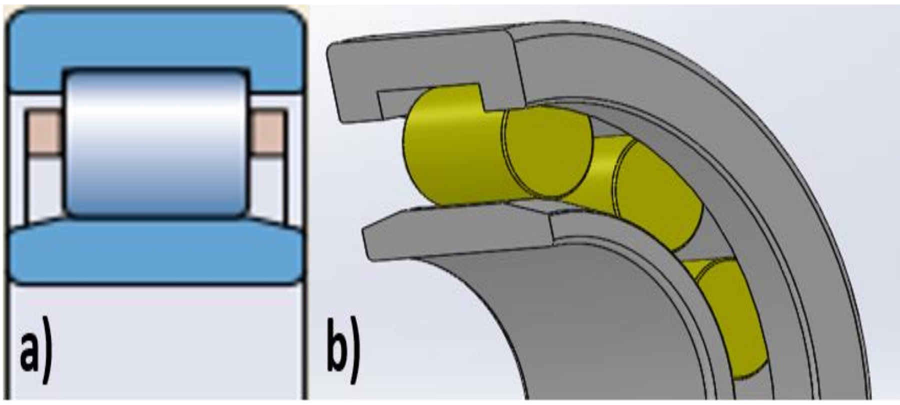

Figure 4-8: a) Cross-sectional view of a cylindrical roller bearing type 'NU' Specification b) by Solid works.

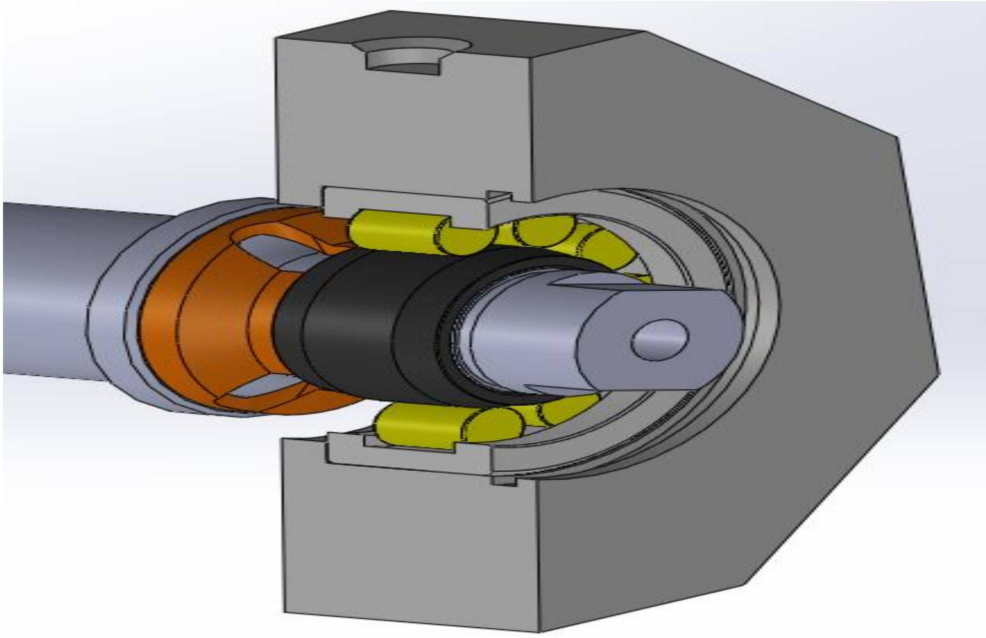

Figure 4-9: Cross section schematics of the 20mm ball position and two of the three inlets for the bearing puller.

For the support bearings a SKF type 22205/20 E double row spherical roller bearings were chosen. Differing from the test bearing, the support bearings do not require any disassembling as their key purpose is to react the applied load on the test bearing. Due to the augmented number of rollers, which reduces the likelihood of the support bearings degrading naturally before the test bearing. In addition, with an improved contact geometry, as the support bearings exhibits a greater dynamic load rating as shown in Table 4-1. What's more to the improved load capability, the support bearings design allows them to compensate for any shaft bending or slight misalignments. The selection of SKF bearings for the experimental work was due to their high quality standards bearings as SKF is recognised for manufacturing reliable bearings to the highest international quality standards.

Table 4-1: New test bearings with comparison to the old test bearing and support bearing load rating and geometry.

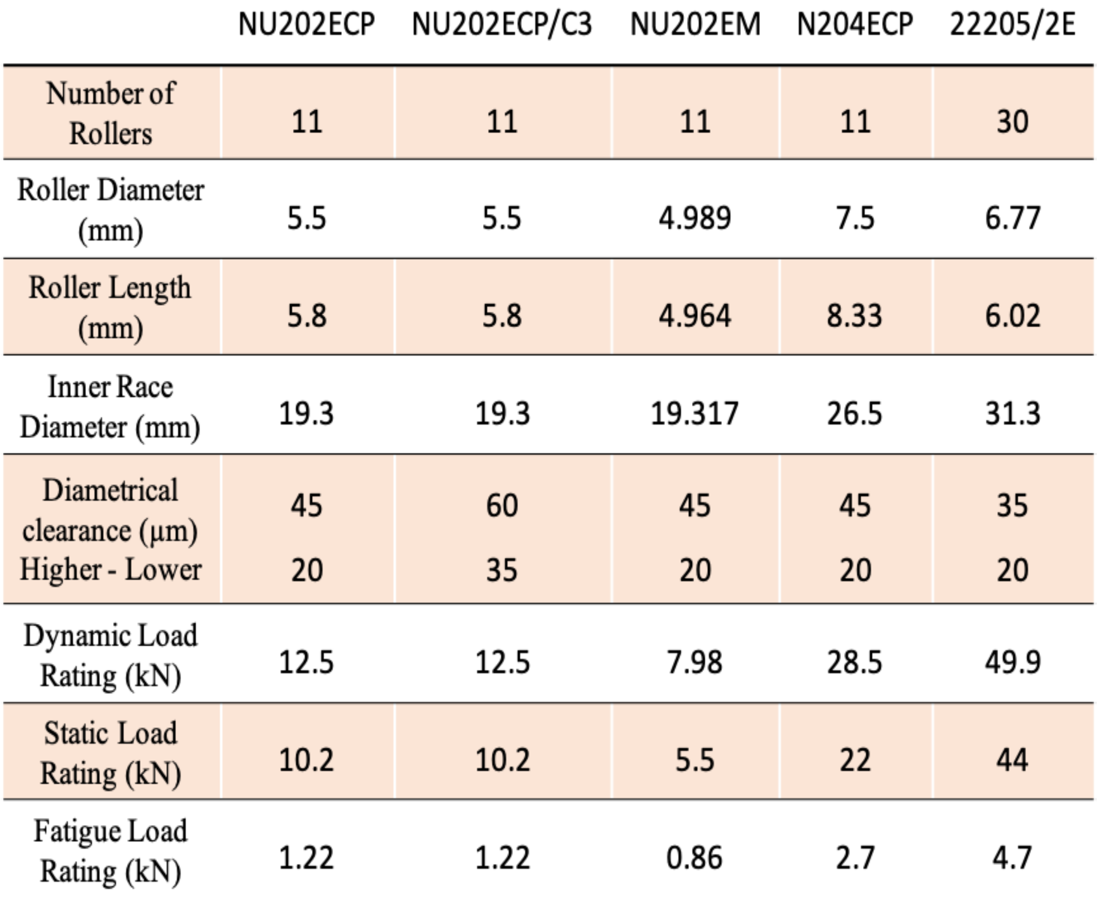

	NU202ECP	NU202ECP/C3	NU202EM	N204ECP	22205/2E
Number of Rollers	11	11	11	11	30
Roller Diameter (mm)	5.5	5.5	4.989	7.5	6.77
Roller Length (mm)	5.8	5.8	4.964	8.33	6.02
Inner Race Diameter (mm)	19.3	19.3	19.317	26.5	31.3
Diametrical clearance (µm) Higher - Lower	45 20	60 35	45 20	45 20	35 20
Dynamic Load Rating (kN)	12.5	12.5	7.98	28.5	49.9
Static Load Rating (kN)	10.2	10.2	5.5	22	44
Fatigue Load Rating (kN)	1.22	1.22	0.86	2.7	4.7

All bearings are lubricated with mineral oil with specifications corresponding to OEP-80. The oil sump has a heater to heat the oil to 50˚C, where the oil is then pumped to a central manifold and transported to the bearings by individual oil pipes. For the support bearing, as modified the oil pipes are connected directly on to the support bearing housings, where it is pumped into a grove on the outer race way of the bearing and 3 holes where the oil is then delivered to the rollers. For the test bearing the oil jet is aimed at the rollers in the region of maximum load, as the test bearing does not have a similar grove design on its outer race way.

The drained oil is then returned to an oil sump which contains a strainer, eliminating any unaccounted foreign debris from the oil prior to passing through an inline oil filter with a 140-L-101H element with an absolute micron rating of 6µm. During the bearing tests, frictional energy from the bearing running causes the temperature to rise and heat up the raceways, which results into an unwanted increase in the oil temperature. To avoid that happening, a cooled water exchanger is incorporated into the oil system to ensure the oil bath temperature remains constant at 50˚C.

The drive shaft was manufactured specifically for this investigation from EN40B steel which was nitride hardened to 750-900 Vickers (62-68 Rockwell C) to a depth of 0.25mm to support enduring the bearing life tests without any damaged occurring from fatigue. The mounting faces for the bearings were ground to tolerate a normal fit with provided tolerances based on SKF recommendations, which allows the bearings to be pressed on or removed without unsettling the radial clearance within the bearings. At the end of the shaft an SKF KM4 self-locking nut was placed to secure the shaft relative to the bearings. The drive shaft is driven by an inverter driven 0.75kW, 2-pole, and 3 phase motor with max speed output of 2985rpm. To reach the higher required bearing speeds for the investigation, the drive shaft is coupled to the motor via a couple of timing pulleys with a ratio of 1:2, boosting the max speed output to 5980rpm. The shafts speed is monitored through an optical light gate sensor assembled with a trigger disc, where the digital output is connected to a data acquisition system and digital signal analysis counts the number of pulses established over a time phase, thus enabling the shaft RPM to be calculated.

4.4 Data Acquisition

During the duration of individual tests, it is vital to maintain accurate records of the number of rotations, speed, load and temperature. To control both the number of rotations done and speed, a slotted disk is mounted at the shafts end and used simultaneously with the optical light gate sensor to generate digital pulses. A K-type thermocouple is applied on each of the bearing housings through a drilled whole reaching the outer race of the bearing to measure bearing temperatures, as shown in Figure 4-10.

Figure 4-10: Thermocouple location on the outer raceway of the test bearing housing.

The thermocouples are attached to OMEGA thermocouple amplifiers which produce a 0-10V output proportional to temperature. The produced signals are linked to a National Instruments data acquisition module, USB-6008. The USB-6008 data acquisition module is utilised to input data into a VI designed and created via National Instruments LabVIEW. The front panel of the VI demonstrated in Figure 4-11, and allows the researcher to determine the average rpm, total number of revolutions, temperatures and at which interval the data is logged. The designed VI opens and creates a text file, writes the data to the text file by accumulating to the former file then closes the text file to avoid any data loss.

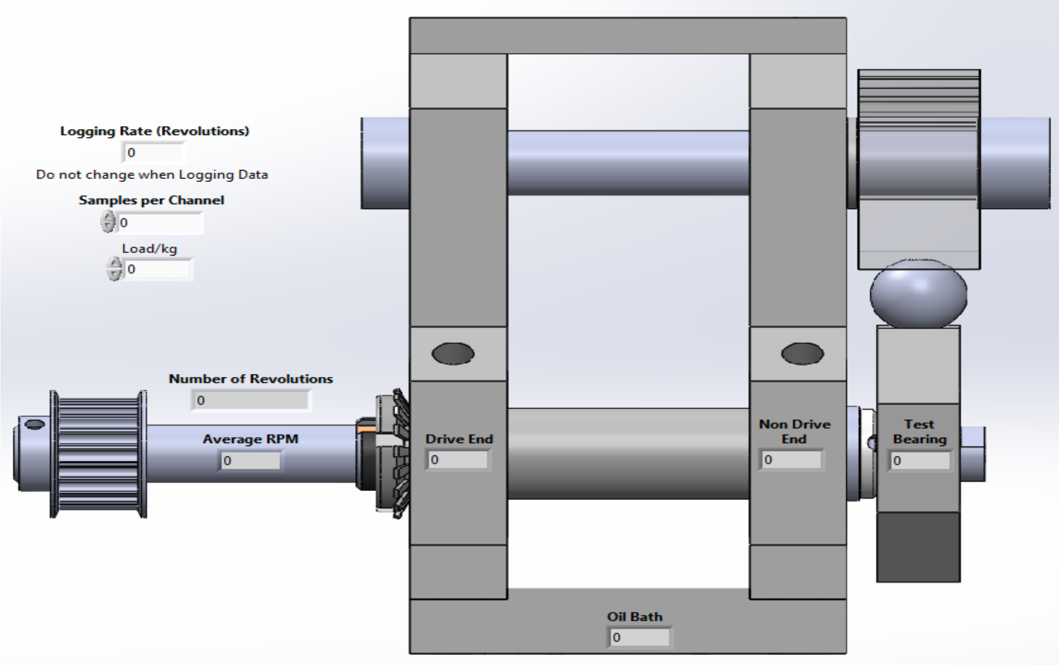

Logging Rate (Revolutions): 0
Do not change when Logging Data
Samples per Channel: 0
Load/kg: 0
Number of Revolutions: 0
Average RPM: 0
Drive End: 0
Non Drive End: 0
Test Bearing: 0
Oil Bath: 0

Figure 4-11: Designed LabView VI front panel for the high-speed test rig in use.

4.5 Bearing Operational Conditions: Load, Contact Dimension and Film Thickness

While undergoing a dynamic test there are a few variables to consider, some factors are taken into account when planning the conducted experiments. These factors are in relation with speed and load variation, test duration, increment duration, oil temperature and most importantly the bearing's condition. Primary procedures investigated the AE response on a healthy bearing, noting that it is critical that the loads applied for the investigation do not exceed the fatigue stress limit of the test bearing, determined as 1500MPa by ISO 281 (2007) Standards for rolling bearings dynamic load ratings and rating life. This was in order to reduce any prospect of damage initiation. With the use of the iterative method outlined in Chapter 3.4.2, the distributed load across each individual roller contained in the test bearings was calculated through the use of the maximum Hertzian contact pressure and maximum contact half-width respectively shown in Figure 4-12 and Figure 4-13. Due to the geometry of the test bearing, and the contact between rollers and inner raceway being less conformal, the maximum contact stress will occur at the inner race and roller contact. To ensure that the stress on the inner race is held below 1500MPa throughout the healthy characterisation experiments, the applied radial load on the test bearing was held below 1250N by applying masses up to a maximum of 8kg with respect of the higher clearances of each bearing, generating an overall radial load of 1088.5N when combining the loading arm's mass and applied mass.

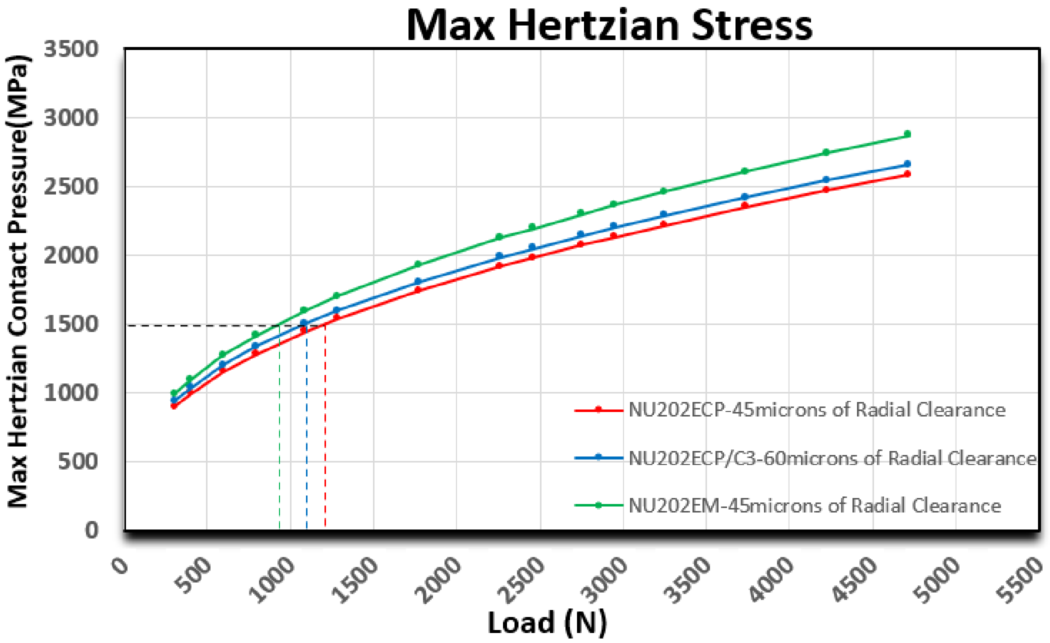

Figure 4-12: Maximum Hertzian contact stress with respect to all three test bearings.

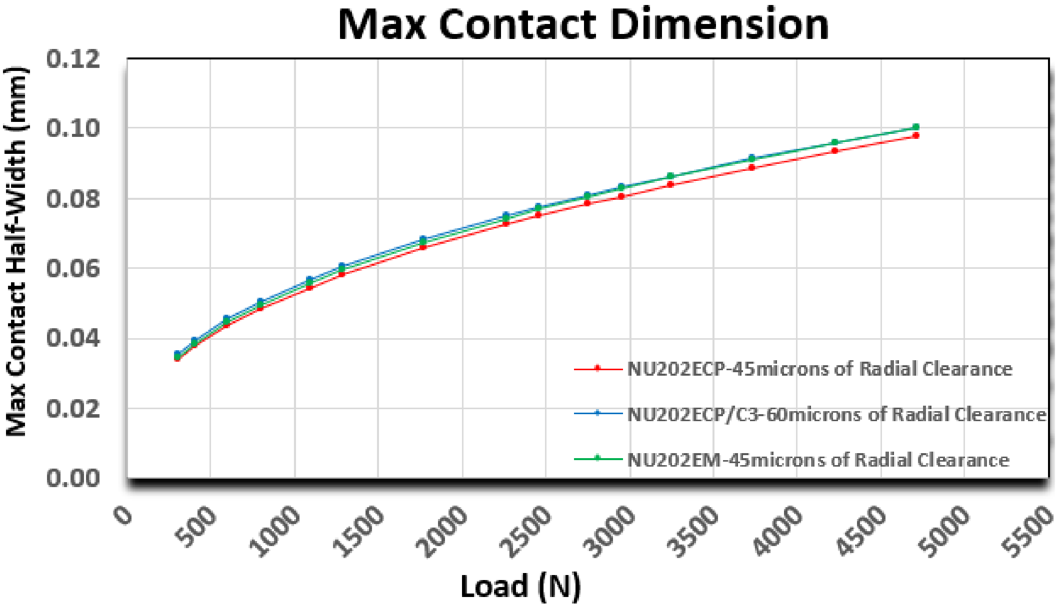

Figure 4-13: Maximum half-width contact with respect to all three test bearings.

Section 2.7 presented Equations (2.7-2.10) to calculate the bearing fundamental frequencies, and these were used to generate the characteristic frequencies for all sets of test bearings and the support bearings with respect to the drive shaft frequency, taking into consideration that the SKF test bearings have corresponding frequencies as they only vary in the radial clearances, presented in Table 4-2. Of particular note, the distinction between the frequencies will assist in localising and distinguishing during the frequency analysis.

Table 4-2: Characteristic defect frequencies of the test and support bearings with respect to shaft frequency.

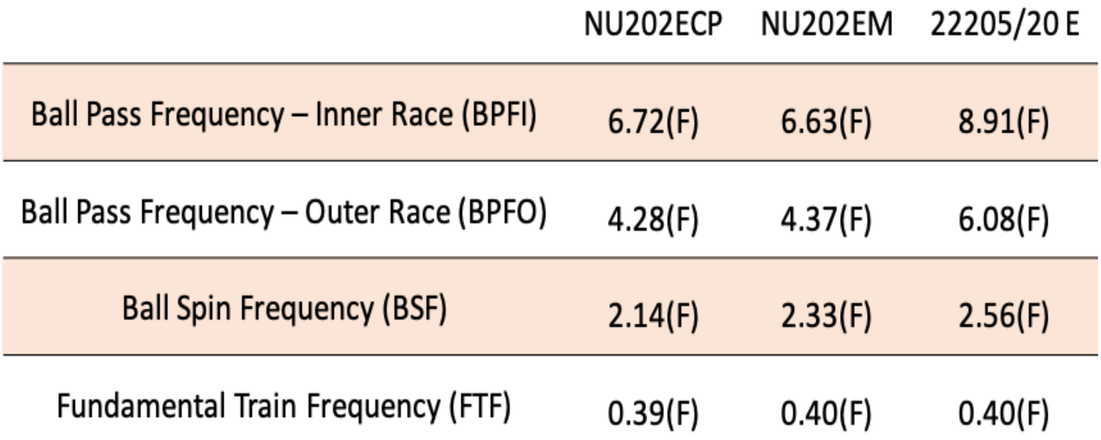

	NU202ECP	NU202EM	22205/20 E
Ball Pass Frequency – Inner Race (BPFI)	6.72(F)	6.63(F)	8.91(F)
Ball Pass Frequency – Outer Race (BPFO)	4.28(F)	4.37(F)	6.08(F)
Ball Spin Frequency (BSF)	2.14(F)	2.33(F)	2.56(F)
Fundamental Train Frequency (FTF)	0.39(F)	0.40(F)	0.40(F)

A proper approach to determine the minimum lubricant film thickness is with the use of the Dowson-Higginson formula, Equation (2.1) outlined in section 2.5.1, where the pressure/viscosity coefficient, α, and the oil viscosity at atmospheric pressure, η, must be determined from the oil properties while the mean speed at the contact, $\bar{u}$, is calculated from the speed of the roller and inner raceway respectively as the outer raceway is stationary.

Nevertheless, for the intended application, as pure rolling is presumed, the roller and the inner raceway rotate at a similar speed. Obtained from presented data by Weeks (2015), Figure 4-14 demonstrates the values of α and η for OEP-80 oil. With regards to the experimental procedure carried out for this research, the use of the outer raceway temperature of the bearings would be utilized to infer the temperature of the oil at contact area. Due to the oil film thickness present being in the order of 10 microns it is considered that there will be sufficient heat transfer from the bearing raceway to the oil, elevating the oil temperature away from that of the oil supply. Additional energy will also be added up to the oil as it gets compressed within the loaded area along with the occurrence of shearing of the oil film.

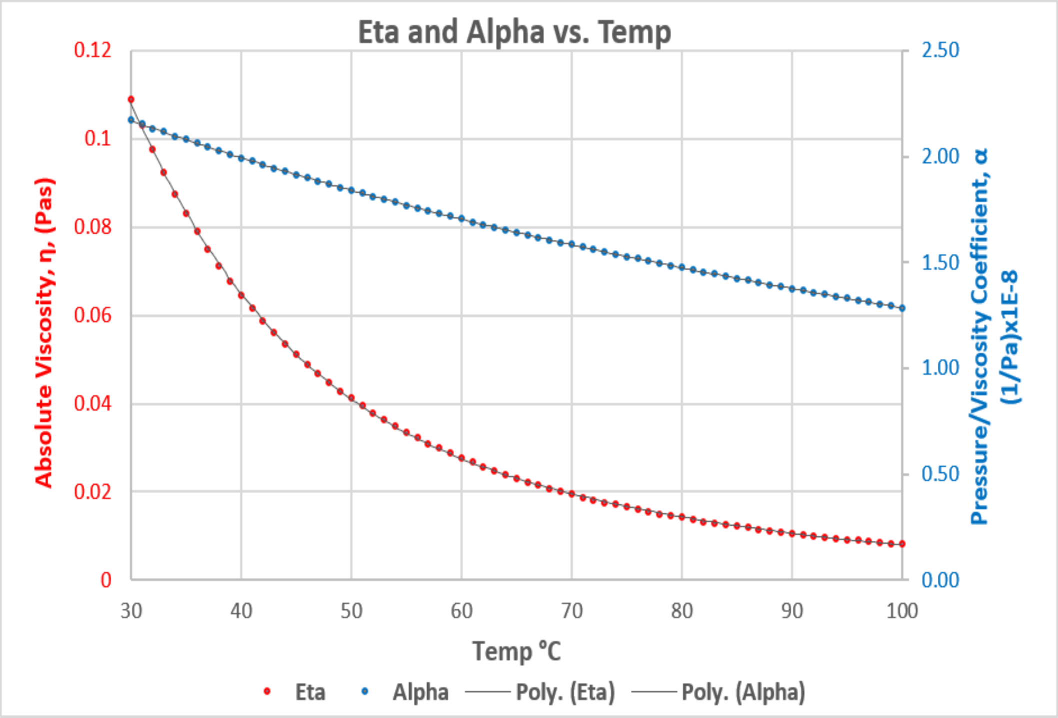

Figure 4-14: Values of Pressure/Viscosity coefficient, α, and absolute viscosity, η, of OEP 80 oil with respect to temperature Adapted from Weeks (2015).

4.6 Experimental Procedure

4.6.1 Overview of Characterisation Experiment

As load and speed have been shown to have significant influence on the generation of AE signals within a healthy running bearing it is essential to carry out characterisation experiments to understand and characterise the outcomes from a healthy bearing. Lubricated roller bearings initially rotate with a relatively high frictional moment. If they are rotating at fast speeds without a running-in stage, a considerable increase in temperature is inevitable. The high frictional moment is due to the churning of remaining lubricant, which needs time to work its way out of the contact area. Hence, the main issue before conducting any experiment is to ensure that the investigated bearings are raised up to the test temperature and speed in a controlled technique, to prevent any initiation of undesirable damage or a hasty increase in temperature. For that reason, the “running-in” of any healthy bearing during this research was done under the running in guidelines determined by SKF (2018), which recommend using speed increments to run in new bearings. The bearings outer ring absolute temperature should not exceed 70°C as the recommended absolute temperature is between 60°C-65°C. If the temperature exceeds the threshold then the test is to be stopped until the temperature is reduced. Only when the temperature has stabilised or is reducing in magnitude is the next speed to be implemented as shown in Figure 4-15.

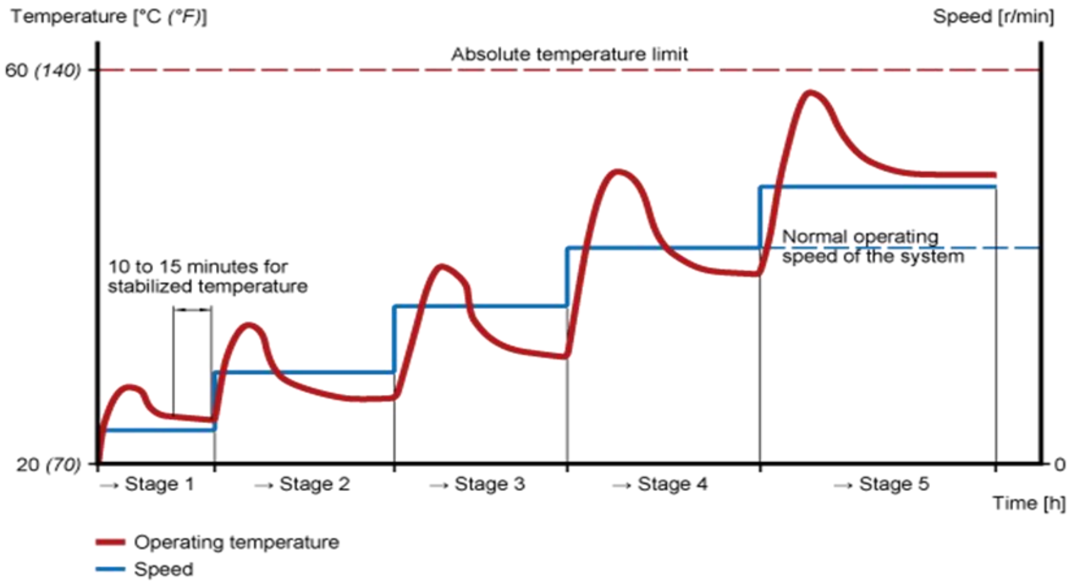

Figure 4-15: Run in test guidelines extracted from SKF (2018).

A series of standard experimental procedures were developed to first run in each bearing, and then to evaluate the AE generated by it under various load or speed combinations. Each experiment carried out initiates with 10 minutes running in the same conditions where the inner race of the bearing rotates at the lowest speed of 590rpm whilst under no applied radial load, except 304N due to the loading arms mass at the test bearing. All the experimental procedures conducted are under 20dB amplification, the acquired wavestreams are set at a sampling frequency of 2MHz and the indicated applied load is at the test bearing, rather than at the end of the loading arm.

4.6.2 Experiment Type 1: Bearing run in test

Hence, following the SKF (2018) guidelines for a run in test, experiment type: 1 is as illustrated in Figure 4-16. The rotational speed will initially start at 590rpm and will increase up to 5980rpm in increments of 590, 1190, 1790, 2380, 2980, 3580, 4180, 4790, 5380 and stop at 5980rpm. The radial load at the test bearing is to be held constant at 402N. Each speed increment will be held for 30 minutes with an AE wavestream of 0.5 seconds recorded every two minutes. The time chosen is to ensure that even at the lowest rotational speed, at least 4 rotations are recorded.

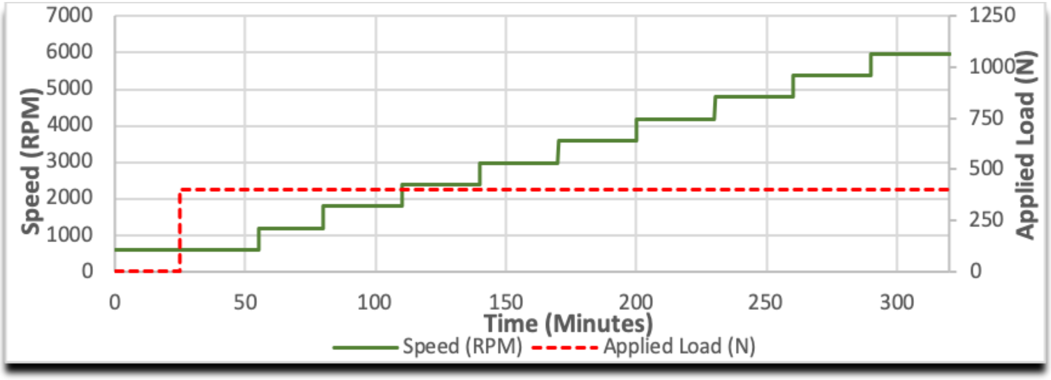

Figure 4-16: Experiment Type 1: Run in test.

4.6.3 Experiment Type 2: Speed Increments under one load

For this experiment shown in Figure 4-17, the rotational speed will initiate at 590rpm and increases up to 5980rpm, and then decrease back to starting speed at 590rpm, in increments of 590, 1190, 2380, 3580, 4790 and 5980rpm. The radial load is to be held constant at 402N. Each speed increment will be held for 10 minutes with an AE wavestream of 0.5 seconds recorded two minutes. The time chosen is to ensure that even at the lowest rotational speed, at least 4 rotations are recorded.

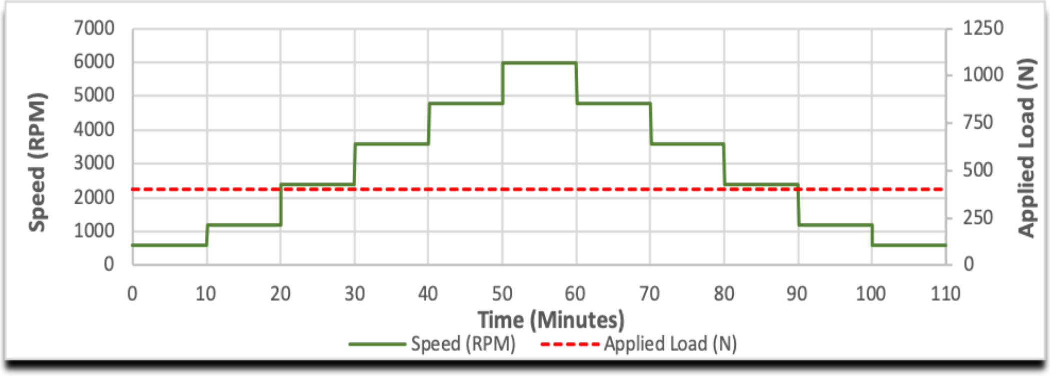

Figure 4-17: Experiment Type 2: Speed Increments under one load.

4.6.4 Experiment Type 3: Load Increments under one speed

Experiment type 3 mirrors the previous experiment as the rotational speed is held constant at 2980rpm. The radial load at the test bearing initiates at 402N and increases up to 1088N, then decreases back to 402N in increments of 402, 598, 794 and 1088N (Figure 4-18). Each load will be held respectively for 10 minutes with an AE wavestream of 0.1 seconds recorded two minutes. The time chosen is to ensure that at least 4 rotations are recorded.

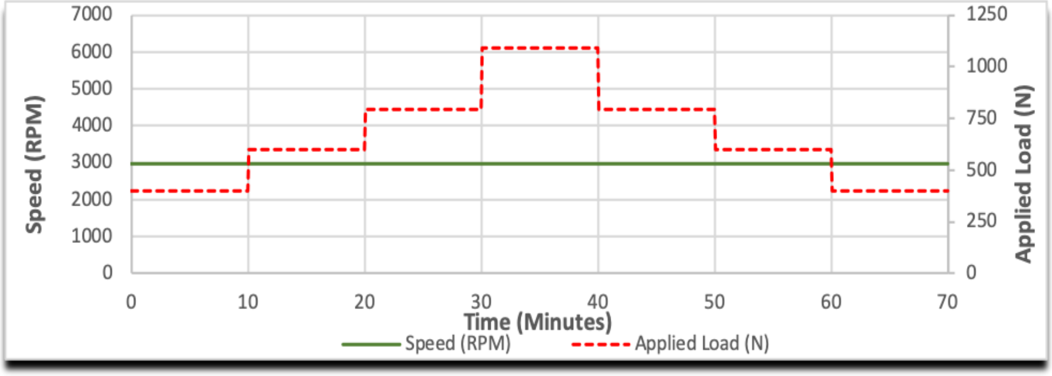

Figure 4-18: Experiment Type 3: Load Increments under one speed.

4.6.5 Experiment Type 4: Speed Increments, Load Held

The rotational speed commences at 590rpm and is raised up to 5980rpm and then dropped down to 590rpm, in increments of 590, 1190, 2380, 3580, 4790 and 5980rpm under 402N applied radial load at the test bearing. Each speed increment will be held for 10 minutes with an AE wavestream of 0.5 seconds recorded every minute. Once the preliminary speed increment set is completed under the first held load of 402N, a repeated speed increment set is conducted with the following loads 598, 794 and 1088N (Figure 4-19).

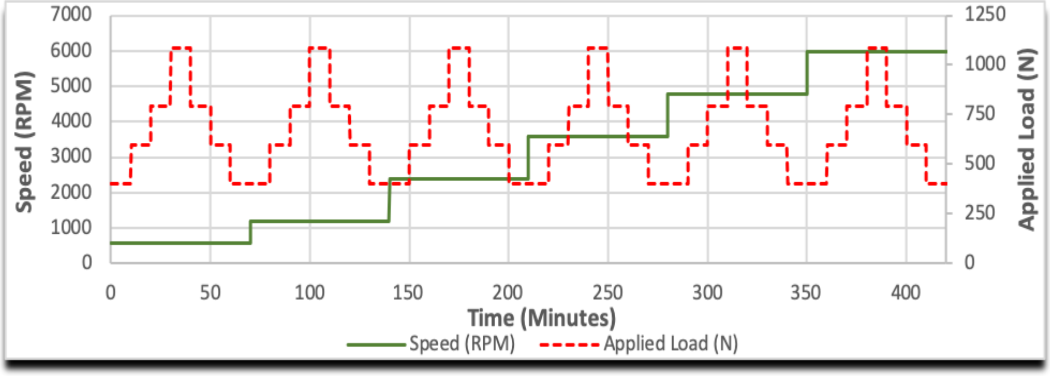

Figure 4-19: Experiment Type 4: Speed Increments while load is held.

4.6.6 Experiment Type 5: Load Increments, Speed Held

Vice versa to experiment type 4, the load in this experiment is ramped up from 402N to 1088N and descends back to 402N in increments of 402, 598, 794 and 1088N under an initial rotational speed of 590rpm. Each load increment will be held for 10 minutes with an AE wavestream of 0.5 seconds recorded every minute. The time chosen is to ensure that even at the lowest rotational speed, at least 4 rotations are recorded. Once the load ramp increment set of ups and downs is completed for the first speed at 590rpm, the rotational speed is then increased with a repetitive load ramp sequence at rotational speeds of 1190, 2380, 3580, 4790 and 5980rpm (Figure 4-20).

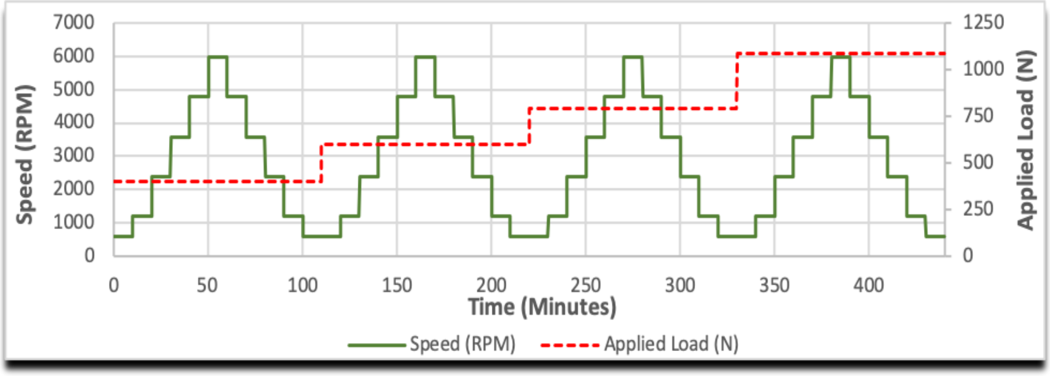

Figure 4-20: Experiment Type 5: Load increments while speed is held.

4.6.7 Locations of the Nano 30 AE Sensors

The locations of the three AE sensors of type Nano 30 are shown in Figure 4-21 as red circles, each sensor is mounted and coupled on top of the support bearing housings closest to the highest loaded zone of the bearings, as per the described techniques in Section 3.2.2 and by the use of established standard techniques such as pencil lead breaks as close as possible to the sensors to check the coupled Nano 30 bond quality before and after each test for all sensors, generally referred to as the Hsu-Nielson source (Hsu and Breckenridge 1981; ASTM 2015). For the test bearing housing the sensor is mounted as close as possible to the loaded zone where the steel ball, transmits the load from the loading arm, and is located on top of the test bearing housing. This was practically as close as the sensor could be coupled to the test bearing housing without extensive modification to the test rig. However, in reality on a gearbox there is not much choice to where the sensors could be coupled due to their original complex configuration.

The AEWin system is set to acquire data at 2MSPS per channel, as well as being set to automatically trigger and collect data as set by the researcher depending on the experiment carried out. Each sensor is then connected to a PAC 2/4/6 amplifier, with a bandpass filter of 20-1200 kHz set at 20dB gain. The positioning of the mounted Nano 30 sensors is chosen to deliver undisturbed waveforms that are relatively clean generated by each bearing.

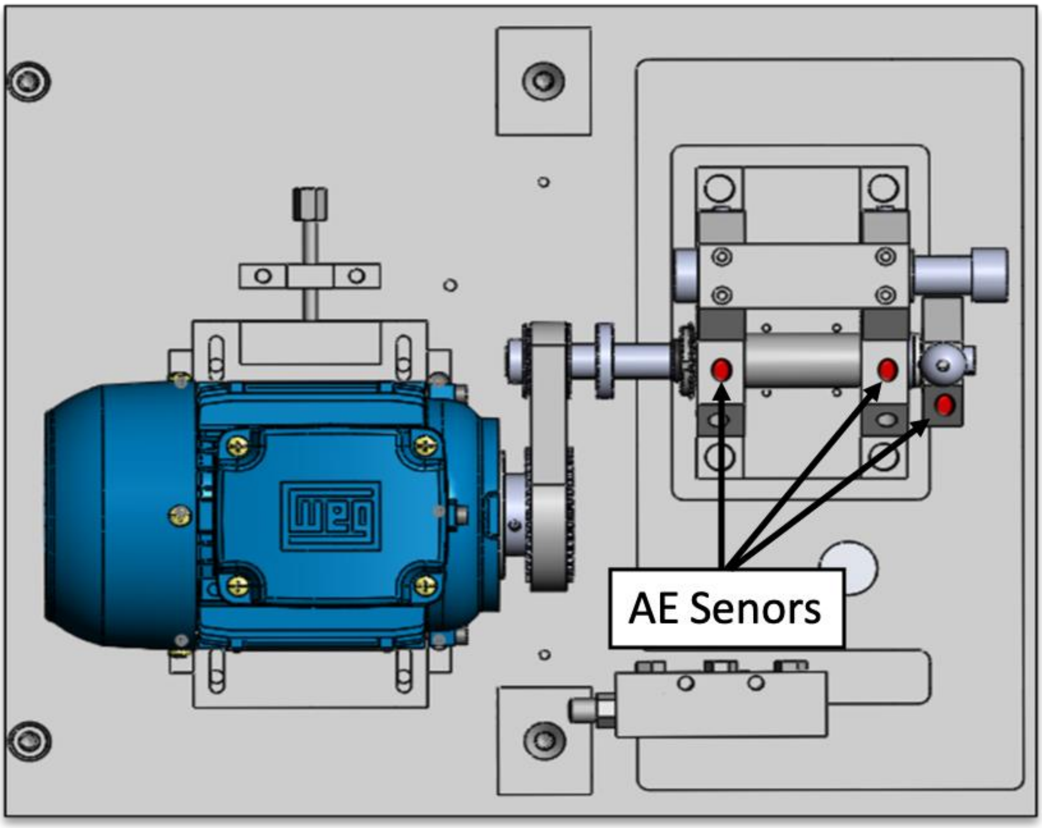

Figure 4-21: Nano 30 AE Sensor locations.

5 Healthy Bearing Characterisation Tests

5.1 Chapter Overview

Due to the overall extent of acquired data for three types of bearings for the healthy bearing characterisation tests, it would be repetitive and extensive if all of the data were analysed within this chapter. To facilitate the analysis process, the following sections reflect on the data acquired during the run-in test and largely on the speed increment load held, unless stated otherwise. As seen in previous investigations, speed has a superior primary effect far more influential than load on AE levels. The previous literature clarified that as the speed is increased so do the AE levels, as the speed essentially puts more energy into the system (Al-Ghamd and Mba 2006; Couturier and Mba 2008; Naumann 2016; Cockerill 2017; Baysec, S., Togun, N and Alsadoon 2019). Several analysis techniques are presented, including Raw Signals, RMS, Acoustic Emission Sensitivity and frequency analysis. As described in Chapter 4, the differences between the three bearing types in use for this research, are SKF Types NU202ECP with normal clearance, NU202ECP/C3 with higher radial clearance and NU202EM a budget bearing with similar radial clearance as the NU202ECP.

5.2 Raw Signal Analysis

Figures 5-1 to 5-3 are acquired signals at 5980rpm and 1088N for each bearing type NU202ECP, NU202ECP/C3 and NU202EM respectively from Experiment Type: 4 Speed Increments and Load Held as described in Chapter 4.6.5. With regards to the speed there will be approximately 50 rotations of the shaft during each raw wavestream.

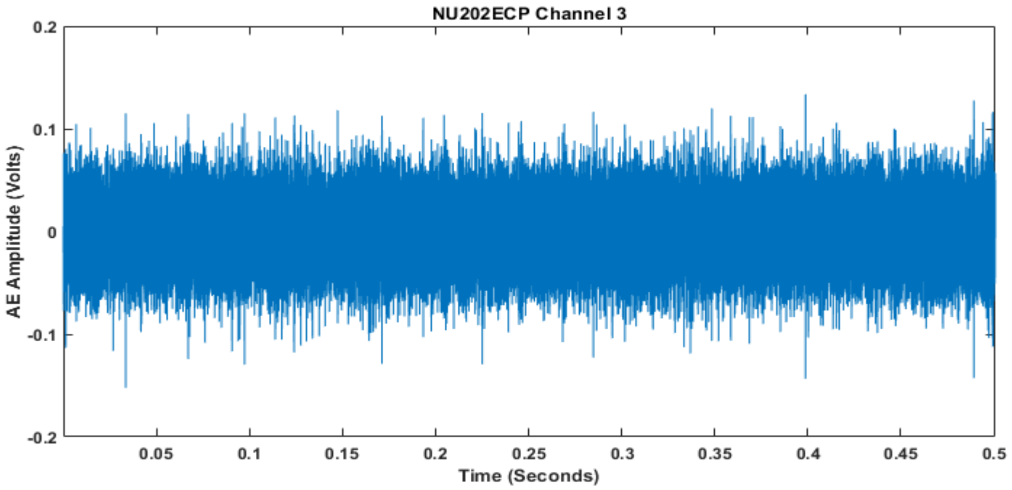

Figure 5-1: Raw signal acquired from AE Win System for NU202ECP at 5980rpm and 1088N.

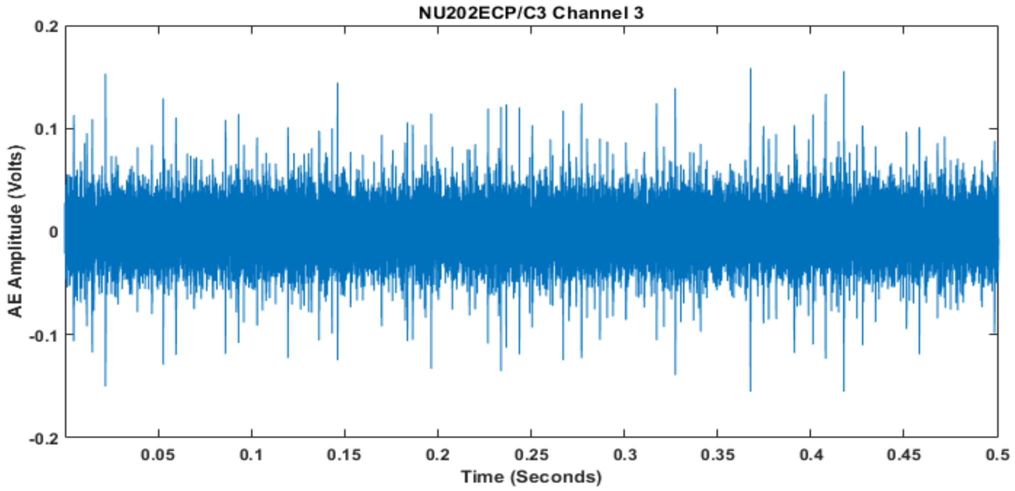

Figure 5-2: Raw signal acquired from AE Win System for NU202ECP/C3 at 5980rpm and 1088N.

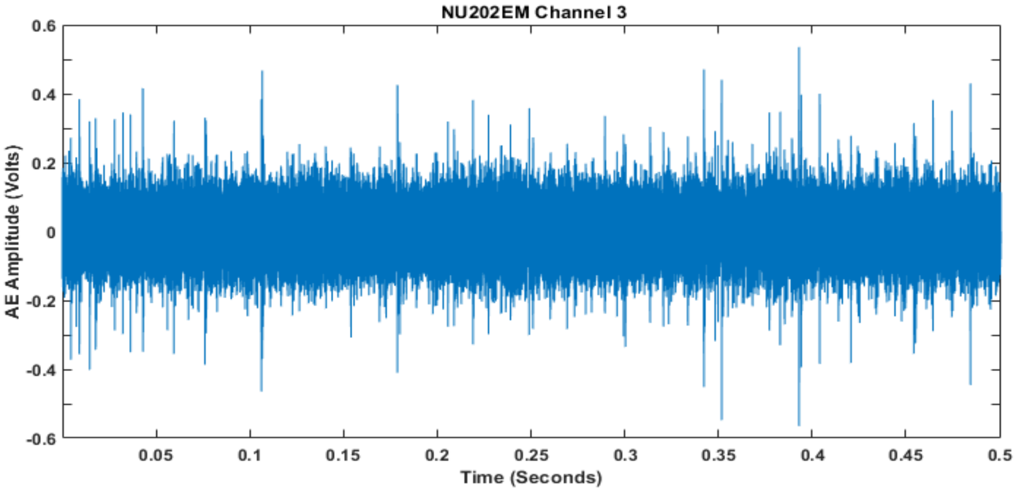

Figure 5-3: Raw signal acquired from AE Win System for NU202EM at 5980rpm and 1088N.

The energy excited from all three bearings at the same operational conditions do differ, as seen for NU202ECP the maximum amplitude of the raw AE signal is well below 0.12V, while the higher clearance bearing NU202ECP/C3 outputs signals surpassing 0.15V. Even so, this is not as significant when compared with the budget bearing NU202EM where the amplitude signal reaches above 0.5V indicating significantly higher levels of AE activity under identical operating conditions. Although there is not much change in the signal to distinguish from, and as some authors may well describe the data within the continuous waveforms demonstrated as noise, the authors would usually refer to the system as having a low SNR. These waveforms presented nonetheless are the real signals and with the purpose of filtering out data effectively, the content within the signal needs to be fully understood as what may possibly be categorized as noise may perhaps in fact assist with the analysis. The peaks illustrated in Figures 5-1 to 5-3 are thought to be caused by a mixture of reasons, as parts of the wavestream signal look relatively evenly spaced thus could be due to the rollers passing the sensor, frictional sources, or due to the fact that the rollers coming into the loaded zone could experience some sliding because when the rollers are in an unloaded zone in the bearing they may not be necessarily rolling properly and they suddenly need to get up to the raceway speed as they are loaded again. A closer view of the same raw signals is presented in Figures 5-4 to 5-6, however for a shorter time to represent one full rotation of the bearing. Similar results as noise is overwhelming within the continuous waveforms.

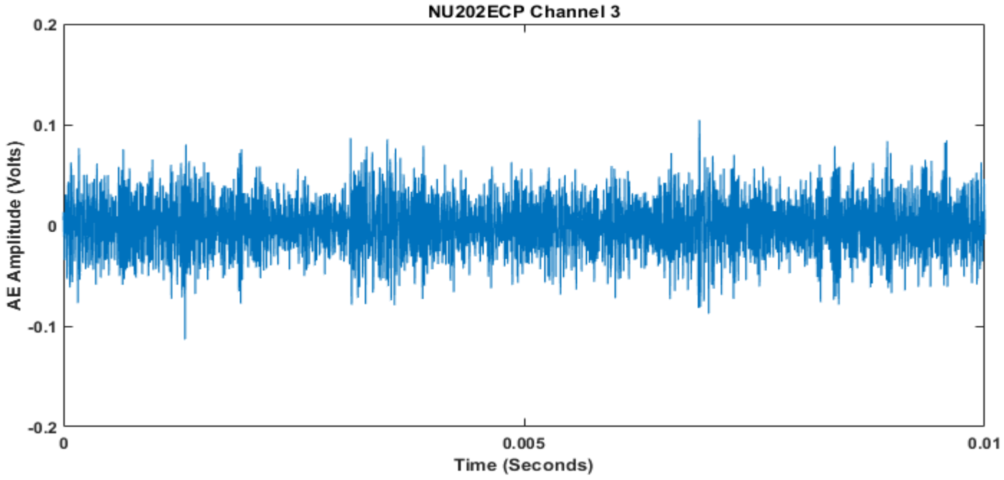

Figure 5-4: Raw signal acquired from AE Win System for NU202ECP at 5980rpm and 1088N.

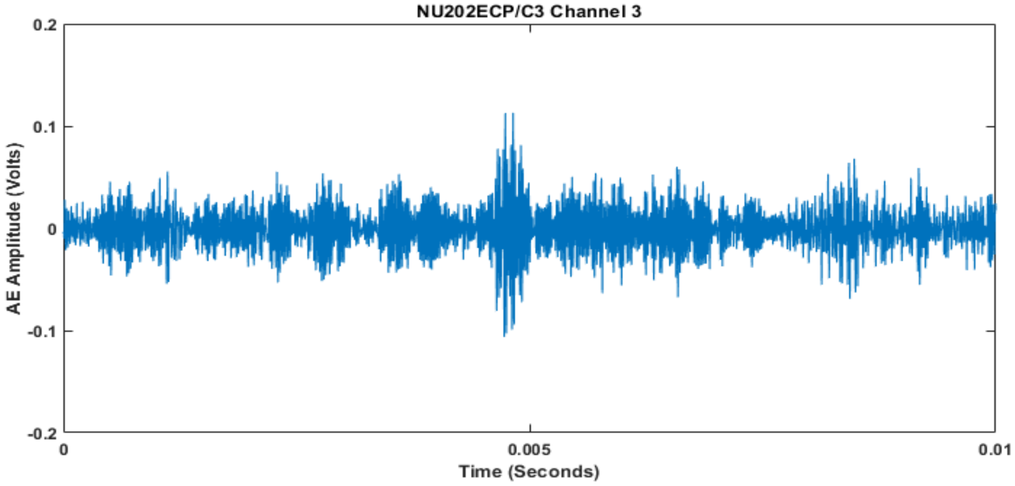

Figure 5-5: Raw signal acquired from AE Win System for NU202ECP/C3 at 5980rpm and 1088N.

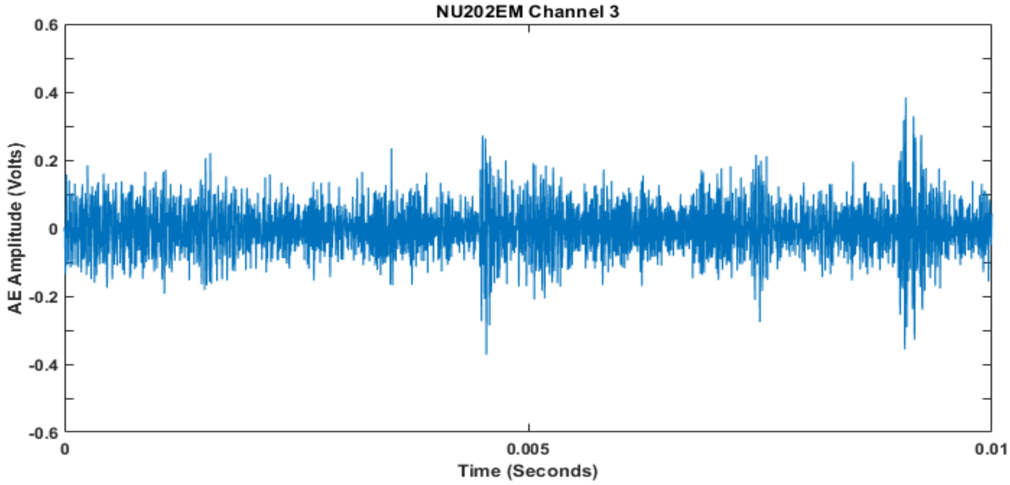

Figure 5-6: Raw signal acquired from AE Win System for NU202EM at 5980rpm and 1088N.

5.3 Acoustic Emission Statistical Parametrises

While RMS is considered as an extremely simple method to analyse data, RMS has proven to be effective by many authors, including Boness et al. (1990), Miettinen and Andersson (1998) Choudhury and Tandon (2000), Serrato et al. (2007), Elforjani and Mba (2008), He et al. (2009), Raja Hamzah and Mba (2009), Nienhaus et al. (2012) and Cockerill et al. (2016) to average out the signal into a single numerical value, which then simplifies understanding how the signal changes with respect to load and speed. Figure 5-7 demonstrates the differences in RMS between all three bearings in use as the speed is increased throughout the test as described in Chapter 4.6.2, where an AE wavestream of 0.5 seconds is recorded every two minutes. The SKF normal clearance bearing generates higher signals when compared with the SKF higher clearance bearing, possibly caused by the clearance difference. However, the results of the budget bearing produce almost double the amount of RMS generated from the SKF normal clearance bearing. This could be due to the fact that the budget bearing is made of different quality material and has a higher surface roughness.

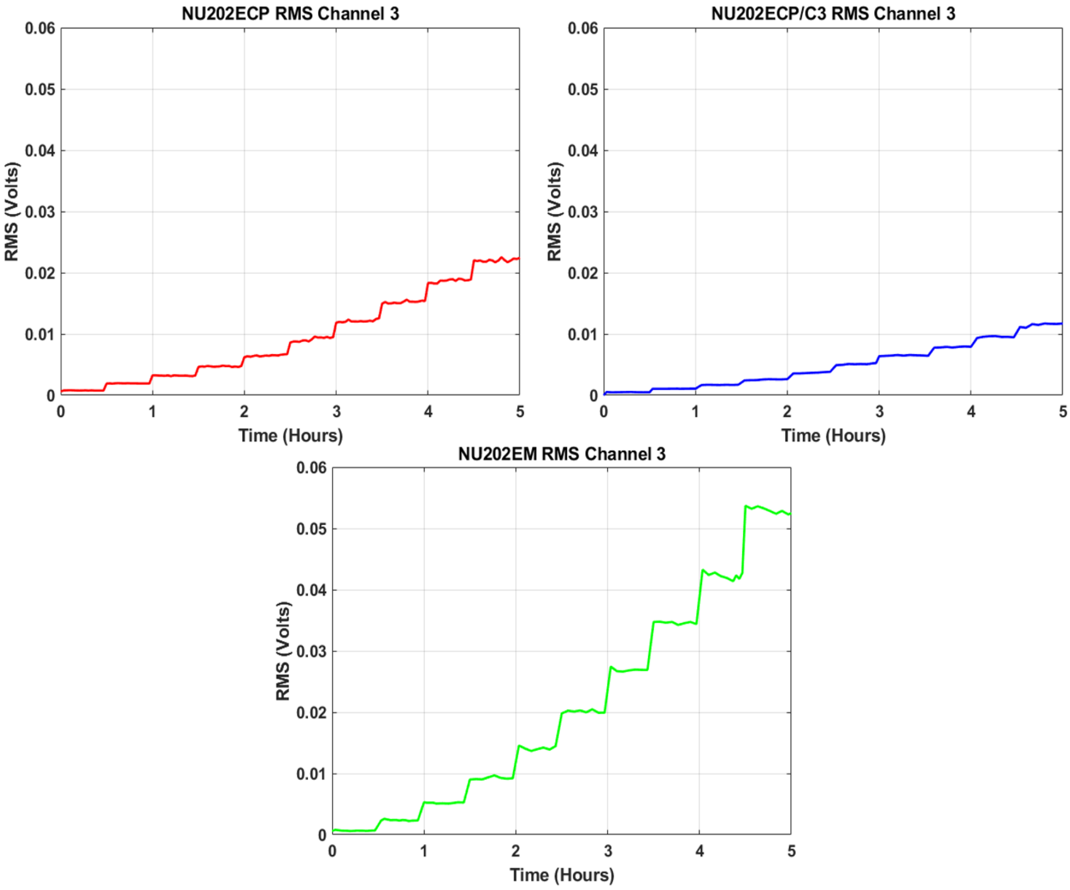

Figure 5-7: RMS amplitude for all three test bearings from Experiment Type 1: Run in test.

The RMS from all three test bearings waveforms are outlined in Figure 5-8. Considerable effect from the speed on the RMS amplitude is illustrated in the figure, creating what looks similar to a step response of each phase or increment as the speed is risen or reduced for all three bearing types and in accordance with the remarks made by Couturier and Mba (2008) and Cockerill (2017). While the load is increased in increments from 304N to 1088N, the AE generated from all three bearings rises progressively, giving indications that load has an impact on the signal with agreement to the results by (Raja Hamzah and Mba 2009; Fan et al. 2010; Sharma and Parey 2019; Patil et al. 2020), although this effect is less significant than the effect of speed. In addition, Patil et al. (2020) stated that with higher radial clearances, AE RMS excitation is far less than lower radial clearances as demonstrated in Figure 5-7 and Figure 5-8. All three bearings show parallel results from Figure 5-7 and Figure 5-8 with regards to the RMS amplitudes as the budget bearing still has the highest RMS values when compared to the normal clearance and the higher clearance SKF bearings respectively, as this may well be due to the surface roughness.

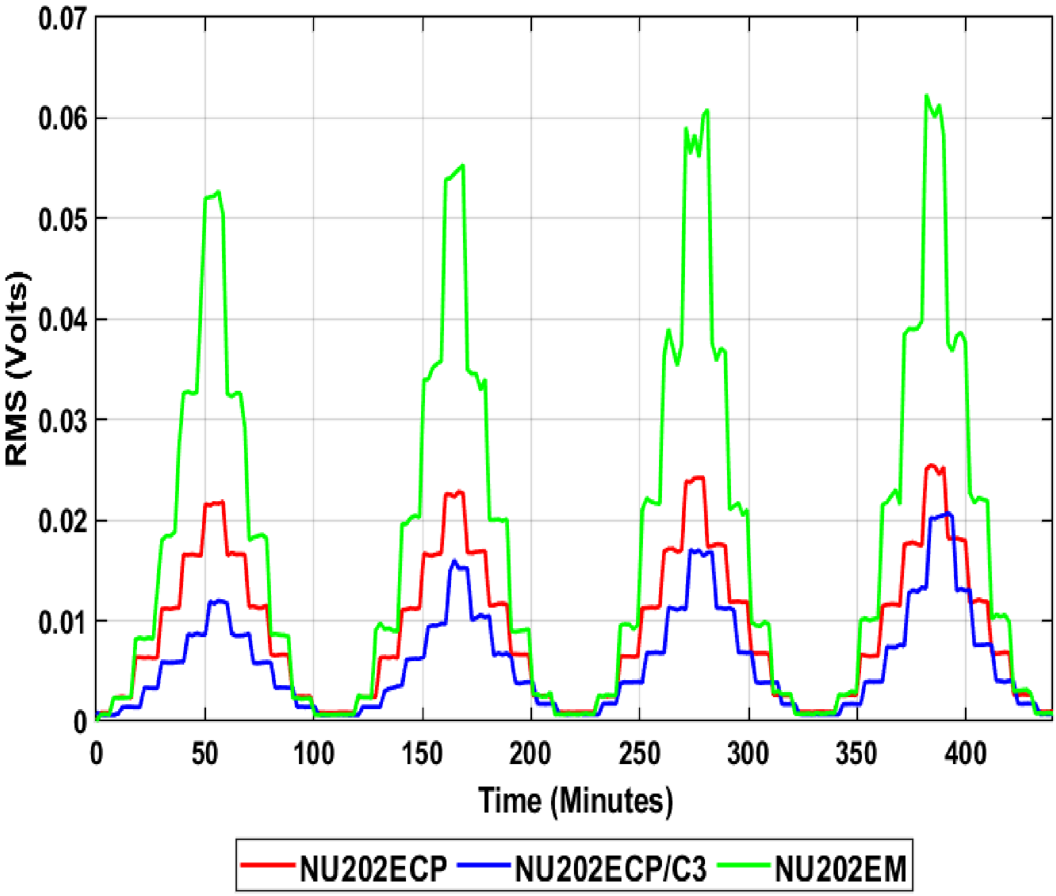

Figure 5-8: RMS amplitude of all three test bearings from Experiment Type 4: Speed Increment, Load Held.

As discussed in the raw signals section, the wavestreams are composed of a number of high frequency transients that extend beyond the base level ‘noise floor’. Increasing operational conditions such as speed shifts the amplitude of both the individual transients and the noise floor. As RMS averages a wavestream, the impact of the increasing transients is relatively minimal to the signal average. Figure 5-9 demonstrates the effect speed and load has on the averaged RMS amplitude with ±2σ for Experiment Type 4: Speed Increments, Load Held.

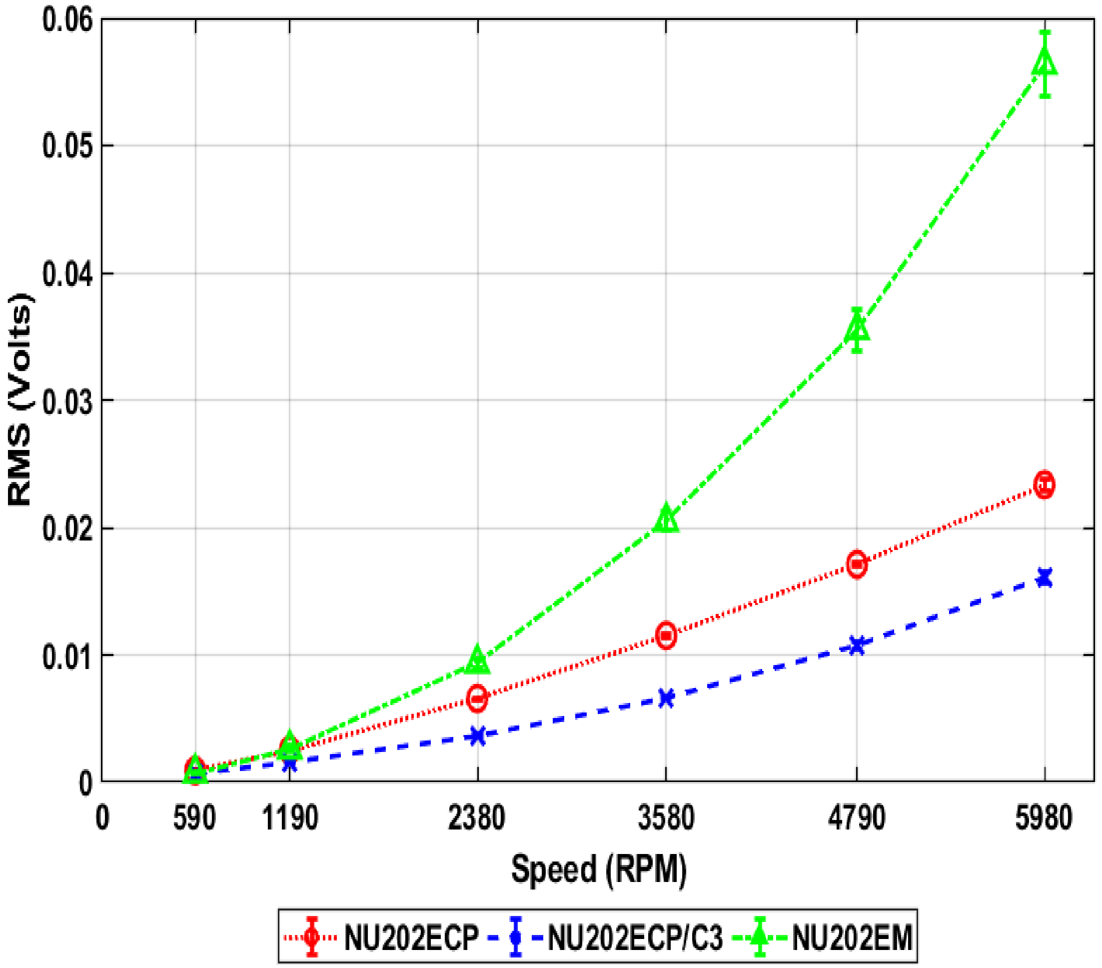

Figure 5-9: Averaged RMS amplitude with ±2σ for Experiment Type 4.

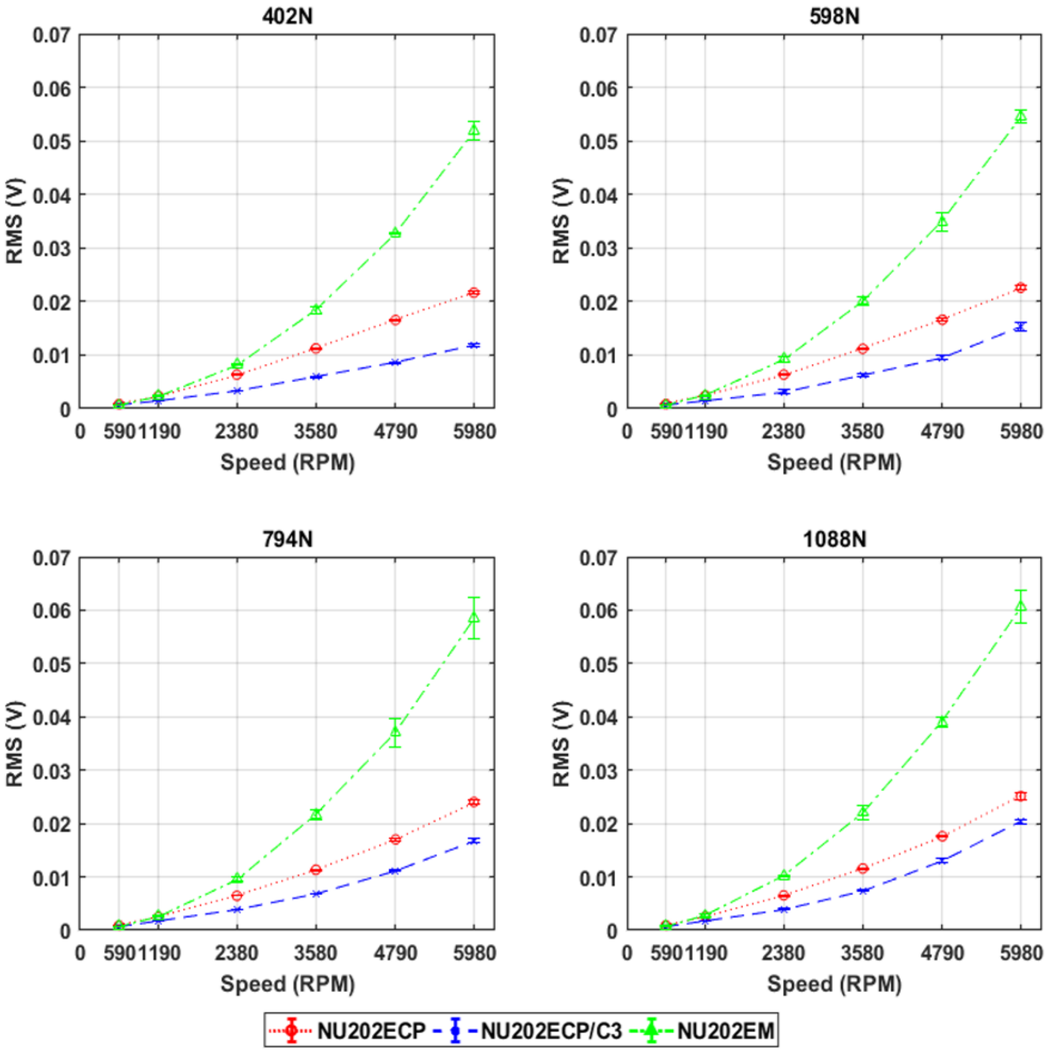

Figure 5-10: Averaged RMS amplitude with ±2σ for each Load Increment from Experiment Type 4.

The effect of speed and load on the AE RMS results from Figure 5-9 and Figure 5-10 corresponds with the results from Figure 5-8. The speed generally dictates the majority of the impact on the results as discussed in the literature in Chapter 2. Nevertheless, Figure 5-10 similarly establishes higher energy output of RMS as the load is increased from one load phase to another. The trend between speed and RMS reflects well on the surrounding results of (Al-Ghamd and Mba 2006; Naumann 2016; Baysec, S., Togun, N and Alsadoon 2019) where they have found that as the systems rotational speed increases so will the AE RMS of a healthy bearing. Due to the supplied quantity of energy to the system from load or speed, research by Couturier and Mba (2008) implied that the energy increase is because of the increased asperity contact and accordingly higher friction at the bearing surfaces.

The temperature readings from all three bearings acquired with LabView for the same experiment are demonstrated in Figure 5-11 with regards to the averaged speed from all three experiments.

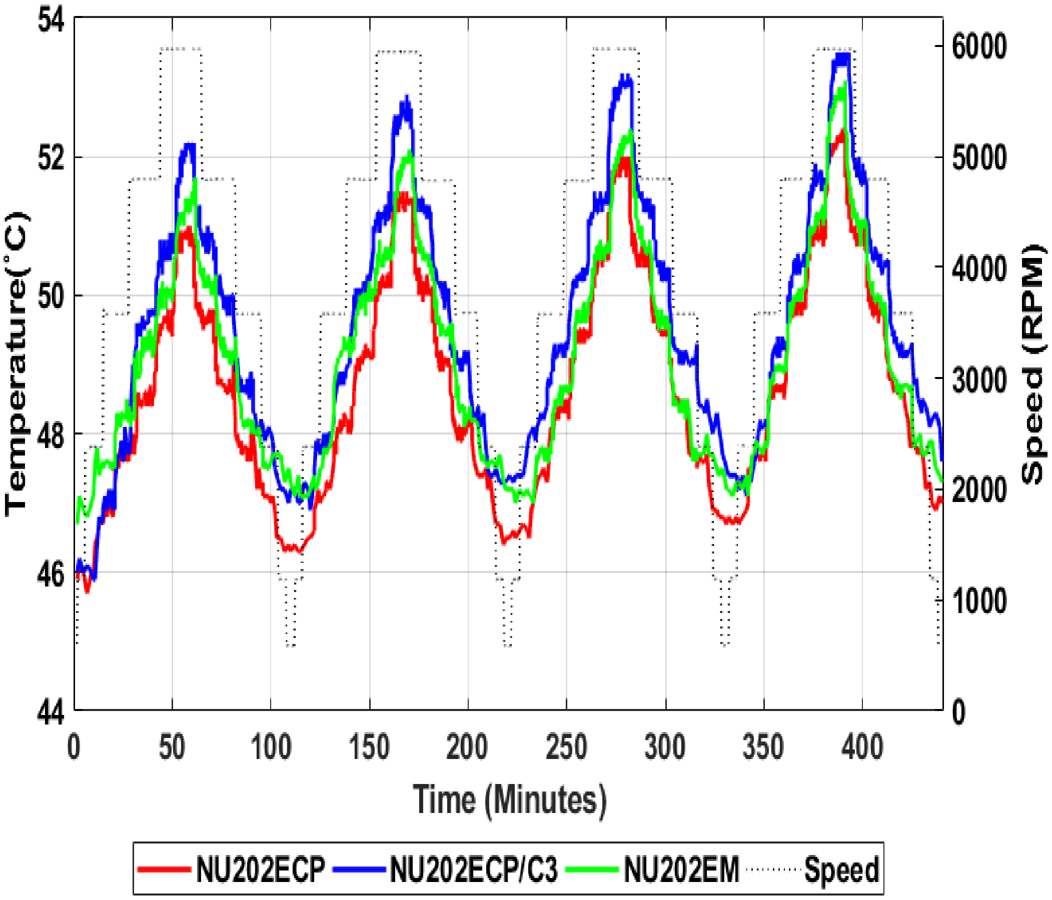

Figure 5-11: Experiment Type 4 temperature readings for all three bearings.

Merging these results with the oil specifications from Figure 4-14, and Equations (2.1-2.3) for the minimum fluid film thickness h_{min}, Barus' law for piezoviscous behaviour, along with the Tallian parameter λ, it is useful to plot the theoretical λ values versus the RMS values for the same experiment, shown in Figure 5-12. The surface roughness of the test bearings was measured using a Taylor Hobson profilometer prior to any experimentation. Given that the SKF bearings have corresponding qualities as they only differ in the radial clearances, Table 5-1 only presents one of them.

Table 5-1: RMS Surface roughness Rq, for test bearings.

Rq	NU202ECP	NU202EM
Inner Raceway	3.45E-08	2.51E-07
Outer Raceway	5.68E-08	4.61E-07
Rolling Element	4.27E-08	3.56E-07

As the outer raceway is stationary, the RMS surface roughness, Rq, for the inner raceway and rolling element were assessed. It can be seen that as the test starts at 590rpm, the bearing is not yet at a full film EHL regime, but as the speed is increased there exists a theoretical full film between the roller and the inner raceway for the SKF bearings.

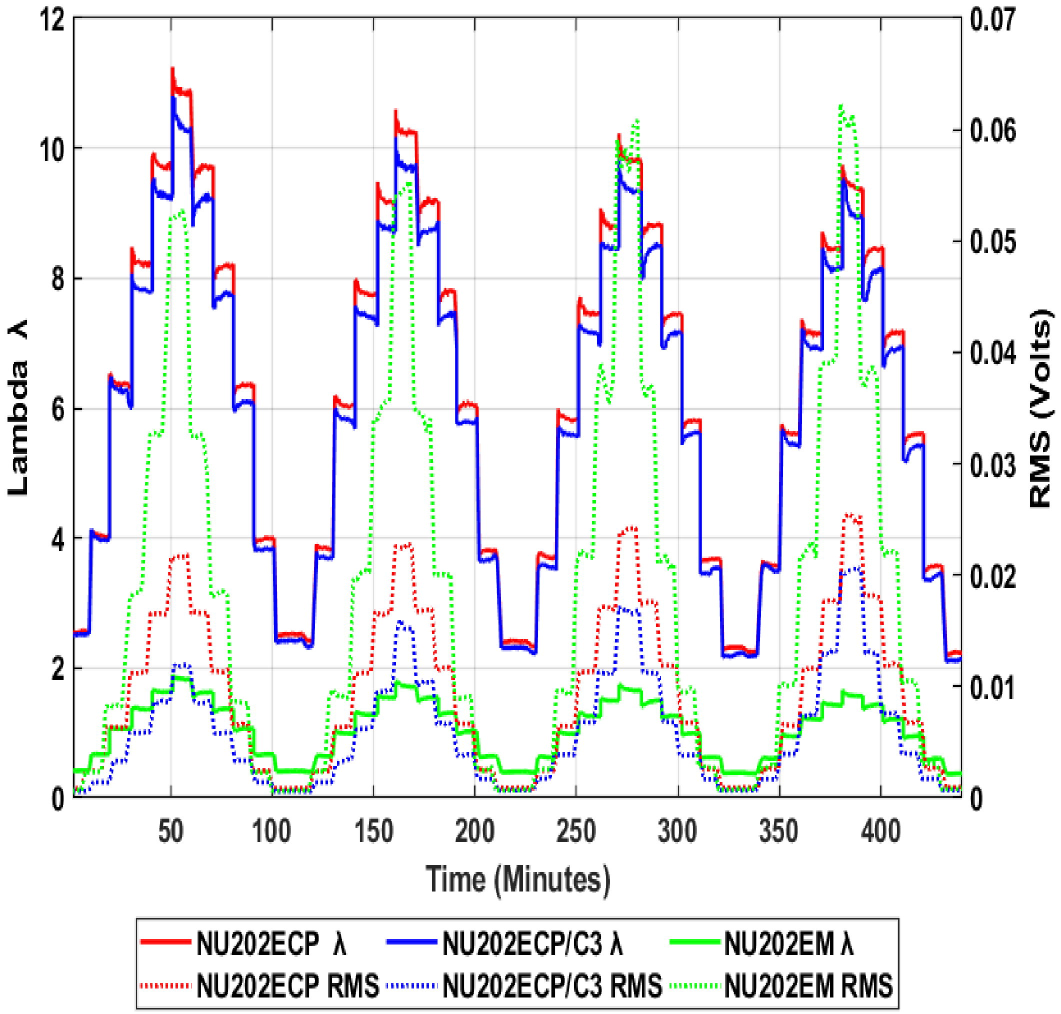

Figure 5-12: The response of λ and RMS for Experiment Type 4: Speed Increment, Load Held for all test bearings.

Observation from Figure 5-12 indicate that with the increased speed increments, the RMS and the λ values increase as well for all bearings, similar observations made previous researchers (Raja Hamzah and Mba 2009; Fan et al. 2010; Sharma and Parey 2019; Patil et al. 2020). Although, as the load is increased the λ values decrease, while the RMS showed an increase as the load was increased. Couturier and Mba (2008) stated, that RMS levels demonstrated a reverse relation with λ, a decrease in λ was noted as a result of increased load. However, for the budget bearings λ values throughout the experiment do not exceed the mixed lubrication regime of 3 λ. Which reflects immensely on the budget bearing's RMS values due to the friction produced during the experiment with regards to the SKF bearings RMS values which are much lower. Then again, the SKF bearings results are closely related and do surpass the EHL regime as soon as they reach the second speed increment of 1190rpm. However, one must note that the strong correlation between λ and the RMS values under the operational conditions of experiment type 4, develop the belief that asperity contact is not the main reason that the RMS signal average increases. As the results from the SKF bearings, signifies that even though the λ for NU202ECP is higher than the NU202ECP/C3, still the former RMS values are higher than the latter, these observations fall in line with Patil et al. (2020) conclusion, that with higher radial clearances a noticeable decrease in AE RMS signal, which was also in agreement with (Liu et al. 2017).

Such results suggest a number of issues or theories as to why the RMS values increase with speed and λ, as established by the Stribeck curve, the presence of sufficient fluid film thickness may generate friction within the contact zone caused by shearing of the oil. In addition, the rollers within the bearing start to rotate only as they enter the loaded zone of the bearing. Which results in the rollers commencing at zero velocity and sliding rather than rolling, as the resultant contact initiates at a boundary to mixed lubrication. The EHL oil film regime is established between the rolling element and the raceway once the roller starts to roll. Hence, the asperity contact may well exist even though the theoretical λ is well above 3 λ. Furthermore, as a rolling element rolls along the loaded zone a wake develops ahead of the rolling element, which will cause a separation in oil flow as each roller passes through the loaded zone and as the speed is increased, the lubricating oil jetted into the rolling elements path will be forced out quicker. As a result, if the oil jet is not able to replace the amount of oil removed by the rollers quick enough, then the leftover quantity of available oil may not be sufficient enough to form an EHL regime.

5.4 Acoustic Emission Sensitivity

The research and experimental attempts reviewed in the literature in section 2.8, focussed on the effects and results of the test bearing and unfortunately many researchers neglect to discuss the data presented from the support bearings within the same operational system or test rig, as the analysis of the signals received at the support bearing is not common, the detailed analysis of the support bearings signals in this thesis is a useful contribution to knowledge. Figures 5-13 to 5-15 represent Experiment Type 4: Speed Increments, Load Held for each test bearing separately including the support bearing results. A clear indication of the speed increments whether as it increases or decreases on the RMS values for all bearings within the system from all three experiments is demonstrated. The results also reveal that the support bearings RMS values from each individual experiment share similar responses as they are significantly higher than those of the test bearings, whilst the two support bearings do operate under the same speed conditions although are subjected to different radial loads. This may well imply that despite the fact that speed and load have significant impacts on the AE RMS response, yet factoring in the design, material and geometry of each bearing may possibly be accountable for the divergences of each bearing’s signal response. Looking at each plot independently, Figure 5-13 demonstrates that both support bearings share similar RMS amplitudes throughout the experiment and indeed as the load is increased from one phase to the next, so does the RMS amplitude from both support bearings although very steadily in the same way as the test bearing. There are two main aspects to acknowledge, firstly it demonstrates changes of the operating conditions which can help to understand the signals received and acquired, as well as to accept the fact that some of those signals may not originate from the bearing that the sensor is on. Secondly, if there is a defect as perceived in the Second SKF NU202ECP/C3 Bearing Run to Failure Test discussed further in section 6.7.1, AE signals observed from the failure of the test bearing coming through on to the support bearings sensors eventually, indicating there is change in the operational conditions within the system. As some of those signals observed at the support bearings were not due to the failure of the support bearing, those signals were from the failed test bearing. Yet there was an increase in the support bearing signals as well. Which suggests the need to understand the AE generated in healthy conditions from all bearings, before starting or trying to detect failures. Because without knowing how each bearing operates in its frequency band during the healthy characterisation tests, it will be difficult to understand any signal received in the later stages of the tests.

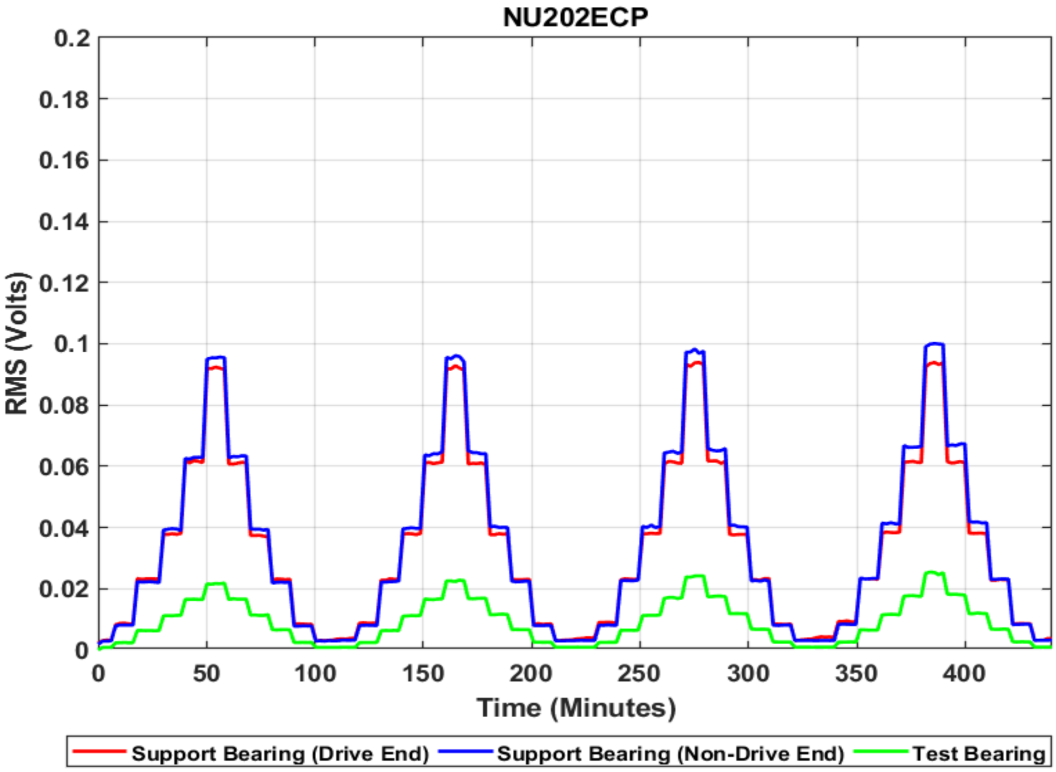

Figure 5-13: RMS amplitude of NU202ECP and 22205/20E from Experiment Type 4: Speed Increment, Load Held.

Figure 5-14 illustrates higher RMS values for the two support bearings when compared with the test bearing and are equally responsive to the added load during the experiment. The focal point of these results which represent a considerably elevated RMS value from the Non-Drive End support bearing when compared to the Drive End support bearing and the Non-Drive End support bearing from the previous experiment. One potential reason is that during the removal of the NU202ECP bearing after a run to fail test discussed later on in Chapter 6.7.1 and replacing it with the NU202ECP/C3 bearing to start with the healthy bearing characterisation experiments on it, the coupling of the AE sensor had to be recoupled as the Non-Drive End support bearing AE sensor was decoupled during the reassembly of the high speed test rig. Hence, this underlines the unfortunate event of sensitivity and repeatability for these types of experiments as it may alter or hinder the results. As Shiroishi et al. (1997) stated that AE sensors arrangement for any experiment may put the results at risk. Furthermore, Colombo et al. (2005) stressed that AE reliability depends on many factors and not restricted to its intrinsic characteristics and in order to achieve such consistency, the coupling medium quality, the sensor location and the way it is mounted as well as the individual experimental set up must be taken into account as each has its own way of effecting the signal results. These recommendations falls well with the Standard Guide for Determining the Reproducibility of AE Sensor Response (ASTM 2015). The standards also proposes examining the sensors after exposure to aggressive testing, in case of damage. In addition, the effect of removing and remounting a bearing and disassembling the rig may well have an impact on the support bearing.

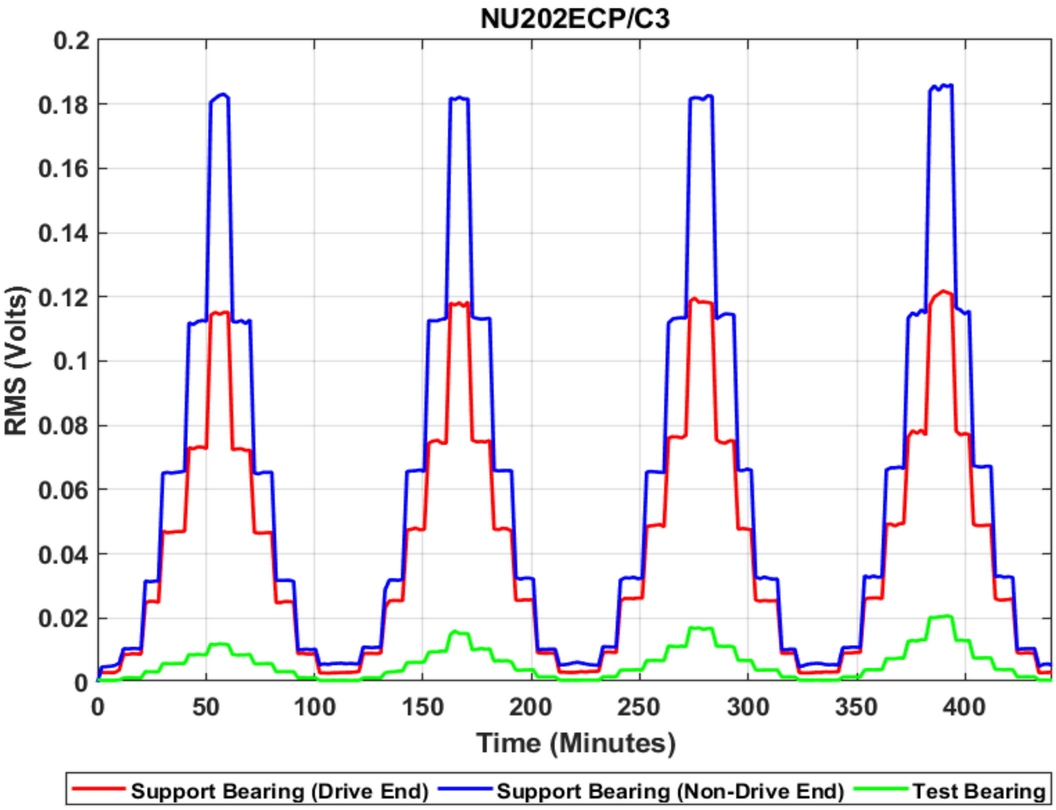

Figure 5-14: RMS amplitude of NU202ECP/C3 and 22205/20E from Experiment Type 4: Speed Increment, Load Held.

With the purpose of improving the results of the next experiment all AE sensors were removed and recoupled in the method described in Chapter 3.2.2, which may help avoid unnecessary intermixed data results, as all the sensors would have newer coupling medium during the experiment. Figure 5-15 demonstrates similar results to the previous two experiments with regards to the RMS values of the support bearings being higher than the test bearing. Although, the attempt to recouple the sensors had its benefits as the two support bearings do share similar RMS values and corresponds well with the first experiment on the NU202ECP bearing, the Drive End support bearing has the highest RMS values which has not been apparent in the previous two experiments. This denotes that the even with the pencil lead break technique to check the quality of the sensor bonding, the fewer times an AE sensor is removed or recoupled the better the consistency of the results will be.

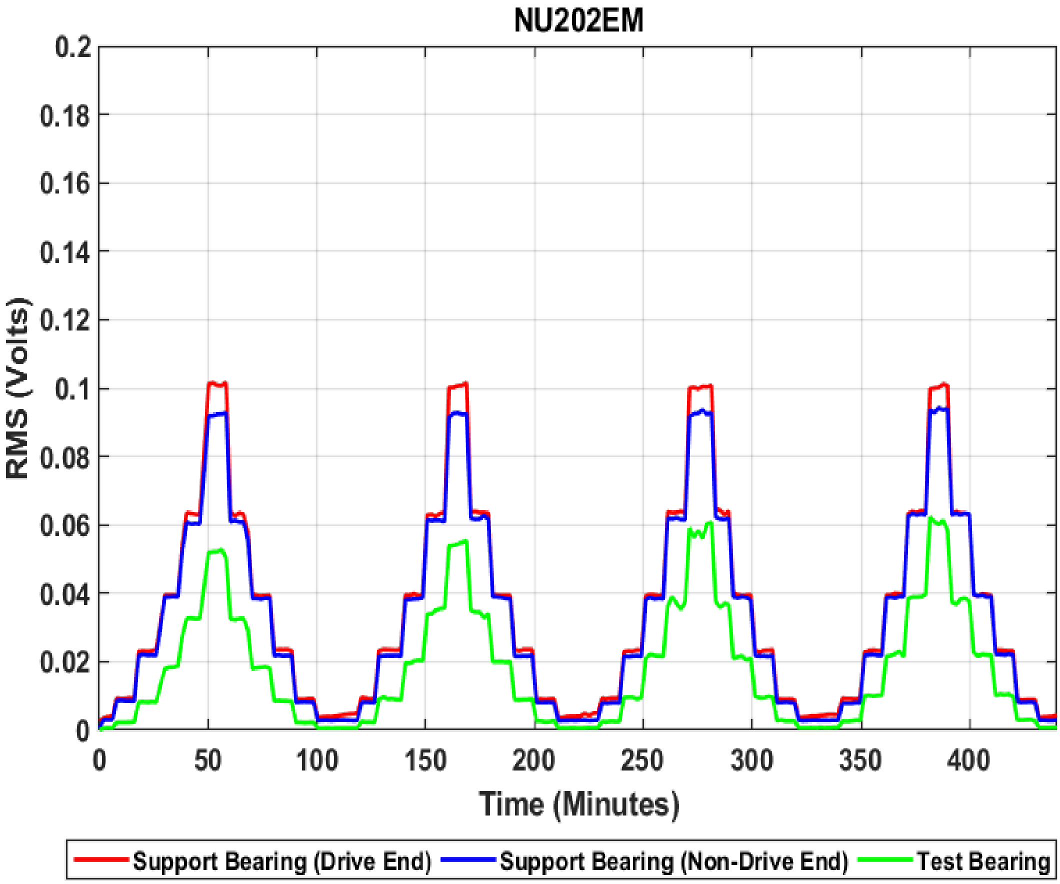

Figure 5-15: RMS amplitude of NU202EM and 22205/20E from Experiment Type 4: Speed Increment, Load Held.

5.5 Frequency Analysis

Trends from the frequency spectrum are to be examined for the AE signals to distinguish the diverse influences speed and load have on the signal results. For the trends to be defined, Fast Fourier Transforms (FFTs) were computed for all the acquired wavestreams. The sampling rate for the acquired AE data was set at 2MSPS and therefore, due to Nyquist's theorem, the FFT data is only analysed up to 1000kHz. To ameliorate the data resolution for visual analysis, the FFT frequency axis is reduced to 500kHz as no data is shown above it. Figures 5-16 to 5-18 plot the FFT frequency from the AE data recorded from Experiment Type: 4 for all three bearings. Comparable results are shown from the AE statistical parameters analysis from the RMS, the energy magnitude of the FFT's results are heavily influenced by speed. With regards to all three bearings, there is a well visualised energy excitation in the regions of 35kHz-65kHz for the SKF bearings and from 15kHz-68kHz for the budget bearing and then again as it reaches 100kHz mark and above for all three albeit with different intensities.

To further enhance the visual aspects of the plots, the FFT's are split into three different sections, 0-90kHz, 90-250kHz and 250-500kHz in that order to facilitate the signal interpretation of the bearing results respectively.

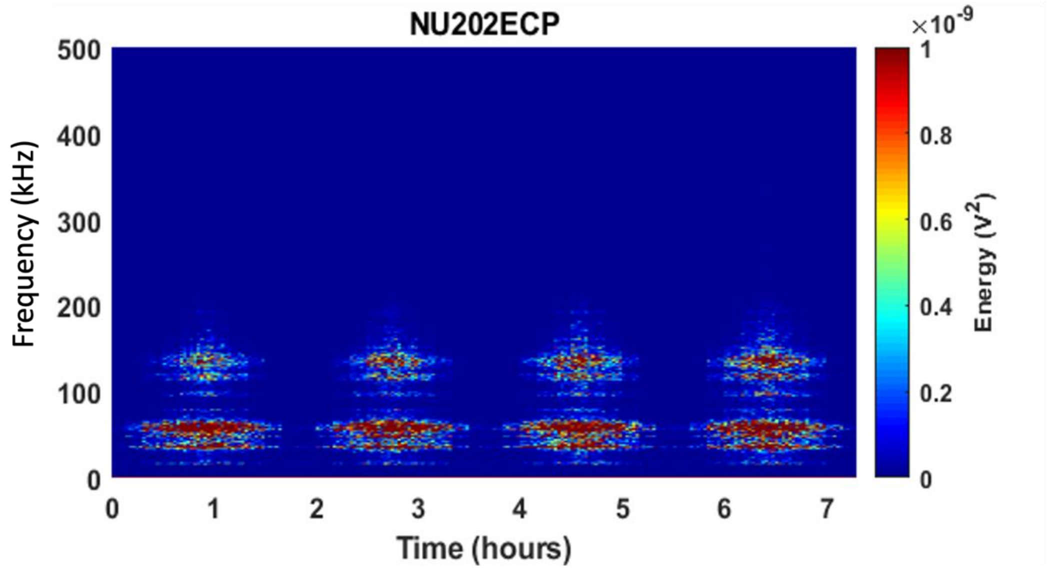

Figure 5-16: FFT of SKF Bearing NU202ECP during Experiment Type: 4.

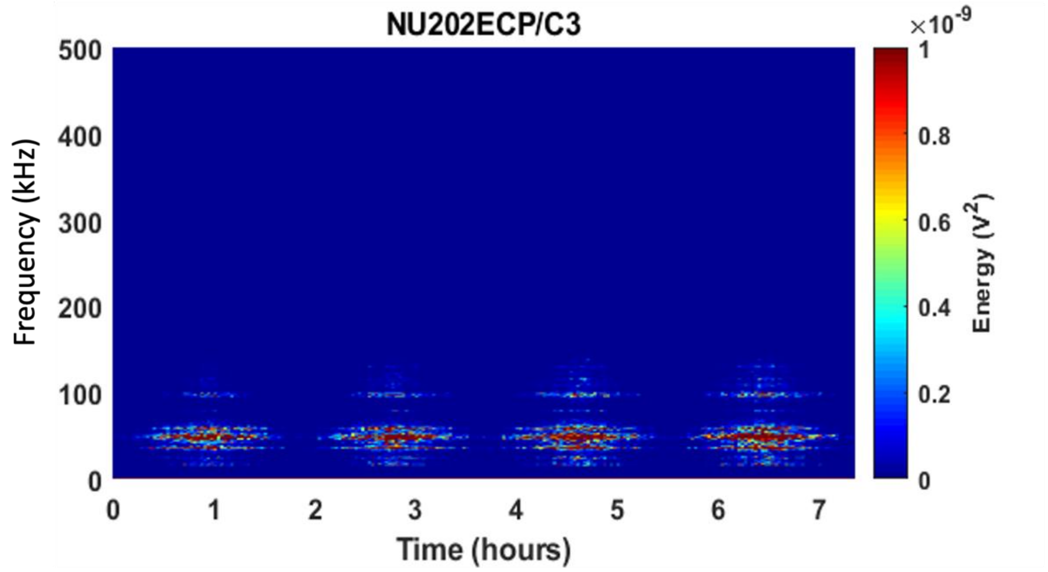

Figure 5-17: FFT of SKF Bearing NU202ECP/C3 during Experiment Type: 4.

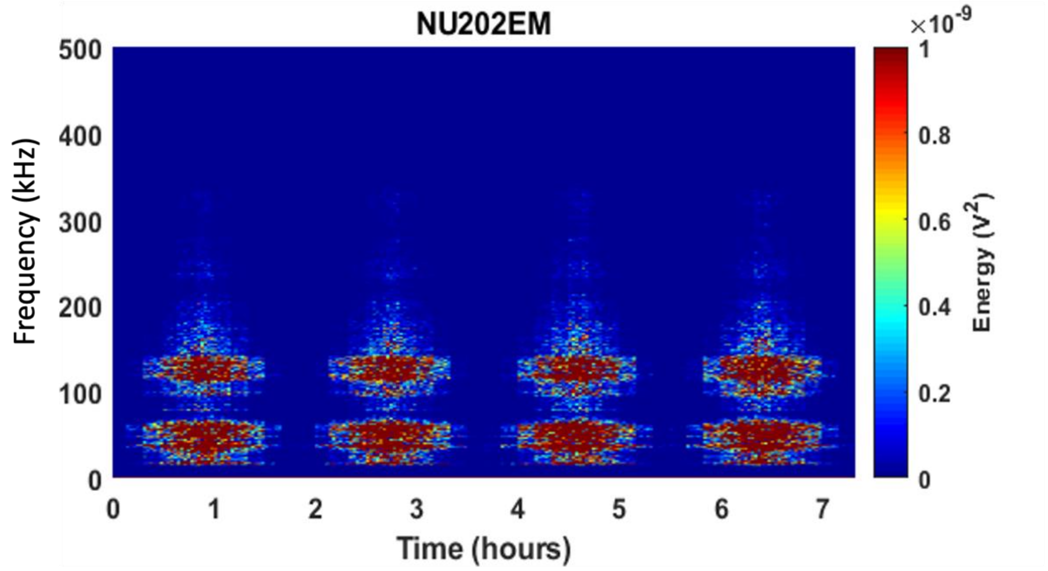

Figure 5-18: FFT of Budget Bearing NU202EM during Experiment Type: 4.

Figures 5-19 to 5-21 plot the first section of frequencies between 0-90kHz of the AE wavestreams. The frequencies excited from all three bearings are closely comparable to each other, however the energy within the frequencies differs vastly due to the way each bearing is manufactured. Figure 5-19 indicates that the NU202ECP bearing has dominant excitation at frequencies ranging from 52-65kHz as well as a less aggressive excitation at 34-42kHz. In addition, frequencies at 47-48kHz demonstrate a medium level of excitation and low energy levels are indicated at 16 and 78kHz. The NU202ECP/C3 SKF bearing establishes similar results to its counterpart NU202ECP but at a much lower scale of intensity, similar analysis were given from the RMS analysis in Figure 5-8. Figure 5-20 reveals the highest frequency levels in the ranges of 45kHz-53kHz along with medium levels of energy excitation at 35kHz-37kHz and likewise at 57kHz-60kHz, as frequency ranges of 16, 24 and 78kHz represent the lowest energy excitation. Figure 5-21 represents the budget bearing, demonstrates a significantly greater excitation than the two SKF bearings.

The plot indicates the highest frequency levels merge within the range of 28-65kHz unlike the previous two bearings, even at the lowest frequency range of 16 and 78 kHz from the SKF bearings, the budget bearing shows higher excitations within these ranges. The results do correspond again to the AE RMS results, which implies the strong correlation of the two techniques. The energy excitation at 16kHz for all three bearings suggests a strong correlation with the increase of load. Outcomes of intensified load increments conveys the incidence of an intensified amount of potential energy release as the bearing’s stiffness changes depending on the number of rollers in contact. In fact, as the speed is increased the volume of energy intensifies when matching the time of added loads to the peak speeds during each increment of the experiment.

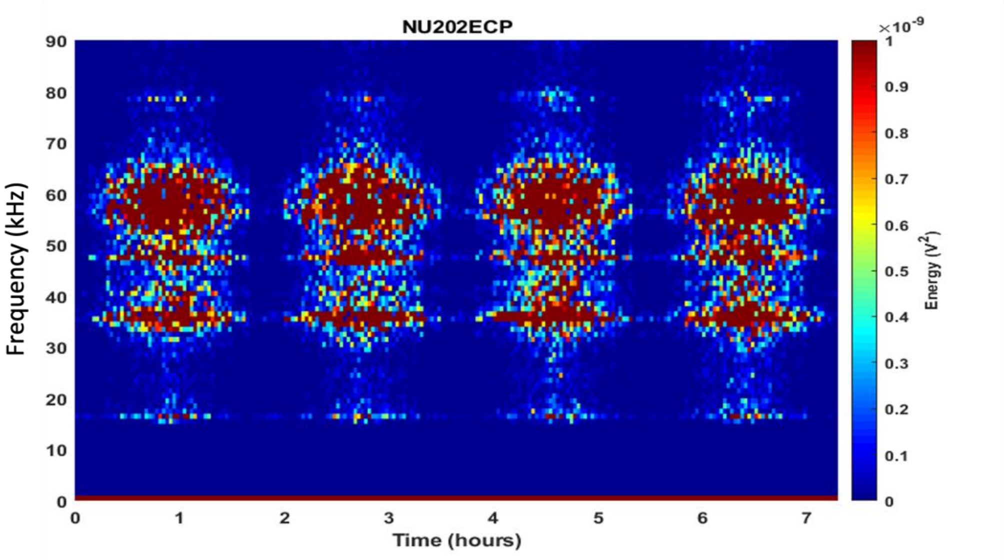

Figure 5-19: FFT ranging from 0-90kHz of SKF Bearing NU202ECP during Experiment Type 4

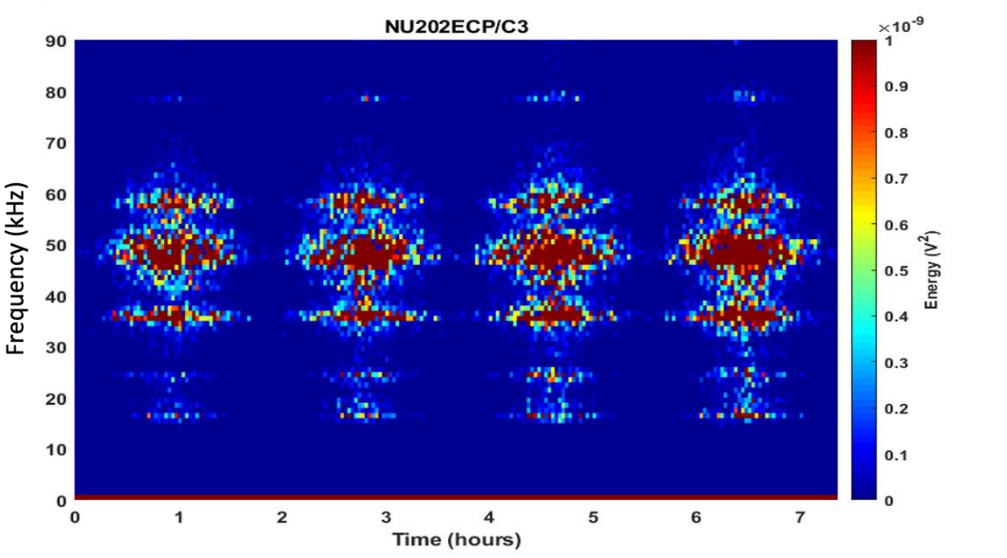

Figure 5-20: FFT ranging from 0-90kHz of SKF Bearing NU202ECP/C3 during Experiment Type 4

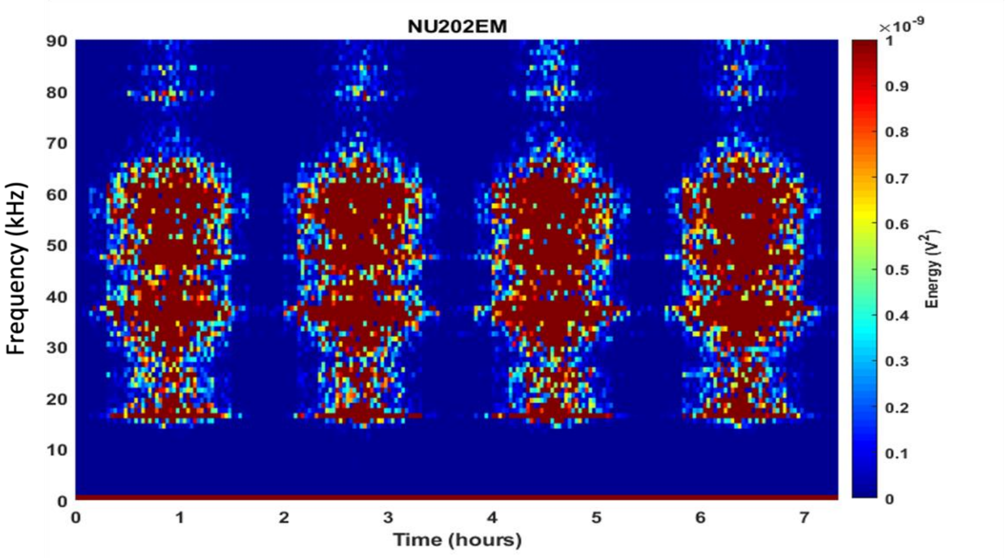

Figure 5-21: FFT ranging from 0-90kHz of Budget Bearing NU202EM during Experiment Type 4

Figures 5-22 to 5-24 plot the second frequency range from 90-250kHz for all three bearings. The NU202ECP shows a large amount of energy in two frequency ranges the first between 115-122kHz and the second between 127-145kHz, as well as medium energy levels at 100kHz and the lowest energy excitations scattered between the 160-220kHz frequency range. Whereas the NU202CEP/C3 bearing is heavily excited between 95-100kHz and the low energy excitations are scattered between 105-140kHz. The generated energy from both SKF bearings are nowhere near the amount of energy generated from the budget bearing. Although, as the NU202ECP has similar radial clearance values, the results are comparable yet at a much lower magnitude with regards to NU202EM.

Observations from the budget bearing indicate that the highest energy levels are at a much higher range of frequency between 110-142kHz, as medium levels of energy are witnessed again at the 100kHz similarly to the other two bearings in frequency range, yet not energy content. Parallel to the NU202ECP bearing the lower energy levels are dispersed between 160-225kHz. Cockerill (2017) suggested that it is reasonable to imply that the high energy levels within the second section of frequency taking place are second harmonics of those frequencies witnessed from his experiments and similarly observed in Figures 5-19 to 5-21. Whilst it is difficult to validate the statement, it is plausible to relate the peaks at 100kHz from all three bearings friction, as the load increases so does the contact pressure hence, a higher amount of energy is released at around 100 kHz. On the other hand, it could also be due to the initiation and propagation of small cracks and so the development of plastic deformation within the loaded area of the test bearing, although at these particular chosen loads are below the recommended 1500Mpa by ISO 281 (2007) standards for the SKF bearings and the highest load at 1088N represents 1596Mpa for the budget bearing it is highly doubtful that this could be the case.

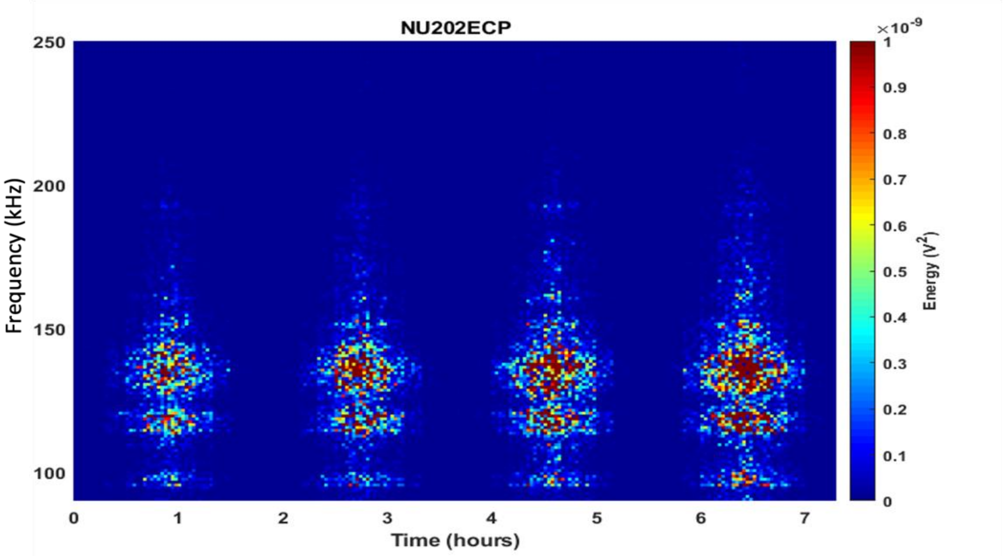

Figure 5-22: FFT ranging from 90-250kHz of SKF Bearing NU202ECP during Experiment Type: 4.

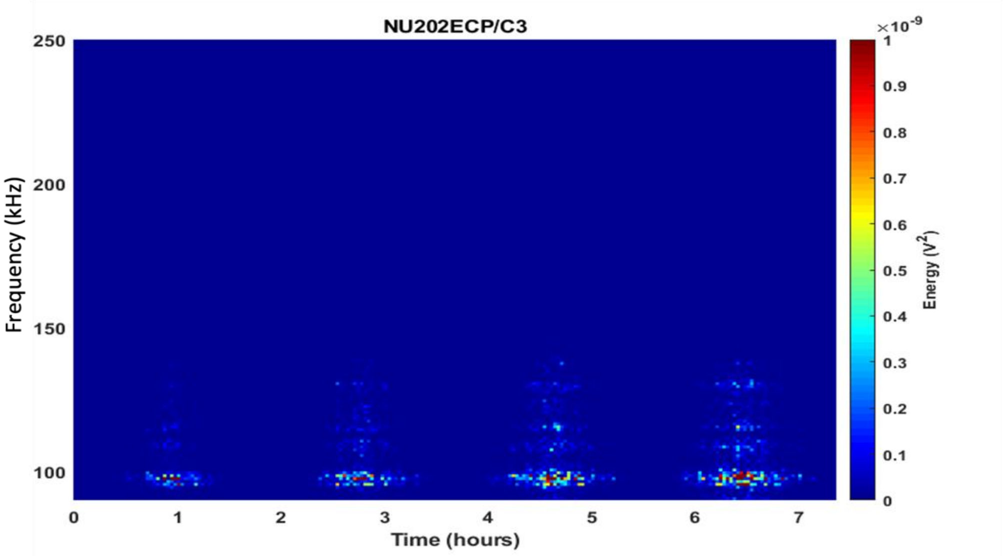

Figure 5-23: FFT ranging from 90-250kHz of SKF Bearing NU202ECP/C3 during Experiment Type: 4.

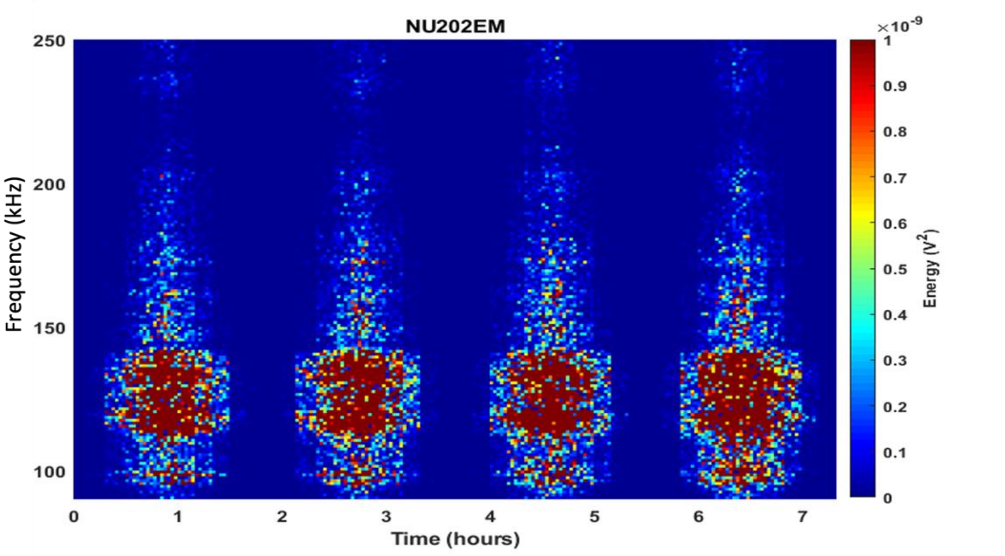

Figure 5-24: FFT ranging from 90-250kHz of Budget Bearing NU202EM during Experiment Type: 4.

Figure 5-25 plots the frequency response of the budget bearing between 250-500kHz, as it illustrates the continuance of low energy level at higher frequency ranges from 250-350kHz. Unfortunately, the SKF bearings do not show any energy excitations above the 250kHz mark as shown in Figure 5-16 and Figure 5-17.

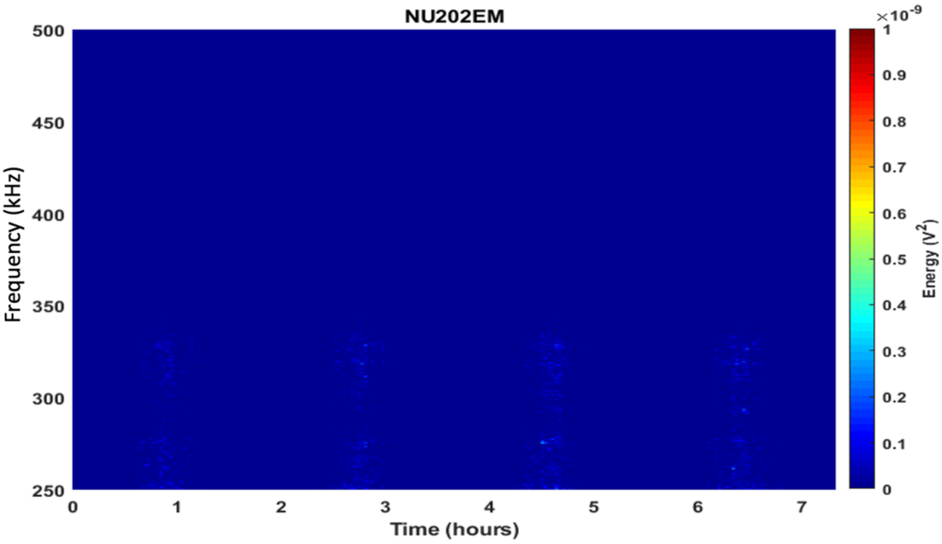

Figure 5-25: FFT ranging from 250-500kHz of Budget Bearing NU202EM during Experiment Type: 4.

5.6 Conclusion of Healthy Bearing Characterisation Tests

The healthy characterisation tests demonstrated that operational speed and load conditions influences the AE RMS and the energy content response within the frequency spectrum, with the former condition emitting superior impact on the signal as it is increased or decreased. The results also revealed that higher radial clearance bearings release lower energy excitation. In addition, the effect of AE RMS value in relation to λ was also investigated for the experiment and has revealed that the test bearings principally operated within a Hydrodynamic lubrication regime with minimal periods in mixed lubrication regime at lowest speed. Moreover, the experimental set up hand in hand with sensor mounting and coupling details heavily influence the results, as the awareness of sensor repeatability of a newly mounted sensor may not be indeed accurate.

6 Run to Failure Tests

6.1 Chapter Overview

As discussed in the literature review, the previous research and investigations were predominantly focused on artificially seeded defects on one of the bearing raceways. The approach of artificially seeded defects for the experimentations very well establishes just how AE responds to geometric alterations caused by wear or damage on either bearing raceway. However, for some experimentation where the artificial defects were enlarged as part of the same experiment, a test rig has to go through dismantling and reassembly between each test phase, consequently ensuing a significant potential for inconsistency and poor reliability of the results as discussed in section 5.4. Although with positive results, seeded defects are not truly representative of how roller bearing defects take place, propagate and naturally degrade, as the AE recorded from seeded defects cannot truly replicate the AE occurring as a defect naturally propagates. Accordingly, Run to Failure Tests on SKF bearings types NU202ECP, NU202ECP/C3 and a budget bearing NU202EM are carried out in this chapter, with the aim of establishing and clarifying the AE sensitivity and capability to detect the initiation of fault and naturally propagated damage. Section 6.2 will present the overall experimental set up of tests and the setbacks experienced to attain the ideal testing process. It also includes a summary of the tested bearings, roughness surface scans of each bearing component and 3D surface scans of the bearing's inner raceway prior to any experiment and after failure. The results are then split into sections, commencing with the full test data via AE RMS analysis, followed by raw wavestream analysis including the STFT of the same wavestreams and lastly the FFT frequency analysis.

6.2 Run to Failure Experimental Set-Up

The Run to Failure tests were typically conducted immediately following the healthy bearing characterisation tests described in the previous chapter, however the Run to Failure Tests were only started when the oil temperature was stable at around 50°C in each bearing housing of the test rig. The speed and load are then incrementally increased until maximum speed is reached of approximately 5980rpm and the selected maximum applied radial load of 4224N for the SKF bearings and 2264N for the budget bearing till failure of the bearings, presented in Figure 6-1. The budget bearing was tested under a lower load as it failed almost immediately when higher loads were applied. The bearing failure is either determined via the upsurge of signals on the AEWin system interface or due to the existence of a noticeable audible difference.

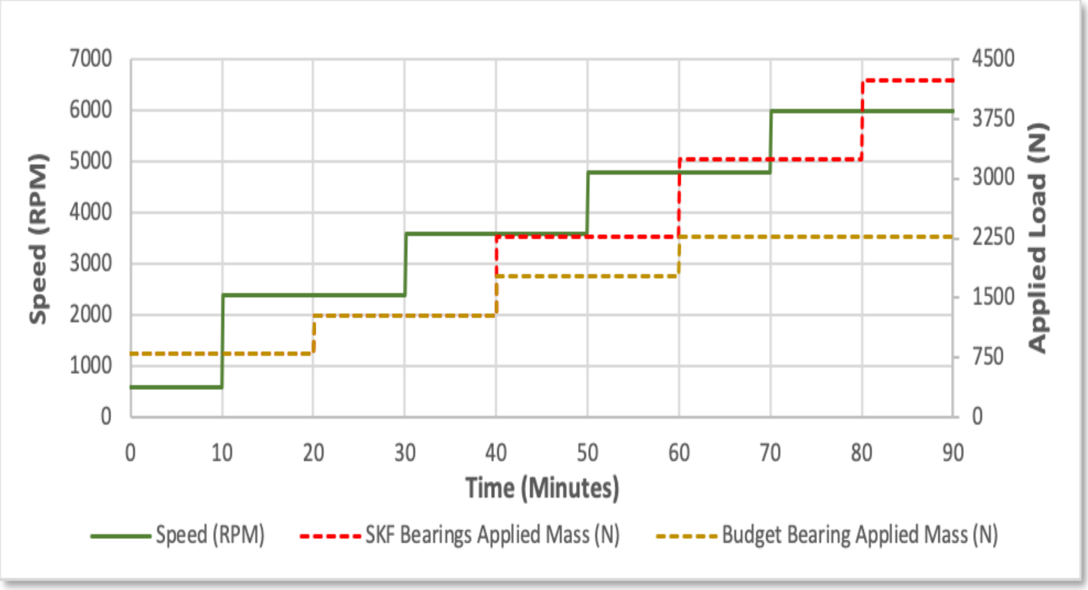

Figure 6-1: Run to Failure Test beginning procedure.

Once a Run to Failure Test is completed, the test bearing is degreased and plunged in an ultrasound bath filled with white spirit to remove any debris and persistent oil. The bearing is then 3D scanned via a Talysurf surface profilometer to characterise the defects occurring during the test and to compare with the 3D scans performed prior to any experiments for each type of test bearing. The bearing measurement setup can be seen in Figure 6-2.

Figure 6-2 Taylor Hobson Talysurf Profilometer in use to measure a roller surface roughness and an inner raceway 3D scan.

6.2.1 Endured obstacles and setbacks to preliminary attempts and recertifications

Due to unexpected delays during the first Run to Failure Test on an SKF NU202ECP bearing, a few setbacks were inevitable. The issue was that as the high-speed test rig is covered by a specifically manufactured acrylic box to avoid oil sprays (Figure 6-3), during the test and due to the immense load applied on to the loading arm, unfortunately the loading arm level slightly dropped and rested on its outlet from the acrylic box (Figure 6-4). Due to this matter in hand, the actual applied load was not fully applied on to the test bearing housing, thus delayed the projected accelerated failure of the test bearing from several days to up to 48 days. This was noticed once the lower part of the loading arm cut out from the acrylic box started to crack. Further investigation on the test rig while it was still operational revealed that the 20mm steel ball was rotating in its place, implying that the arm did not transfer sufficient load to the test bearing housing. The test was stopped, and modifications to the acrylic box were made.

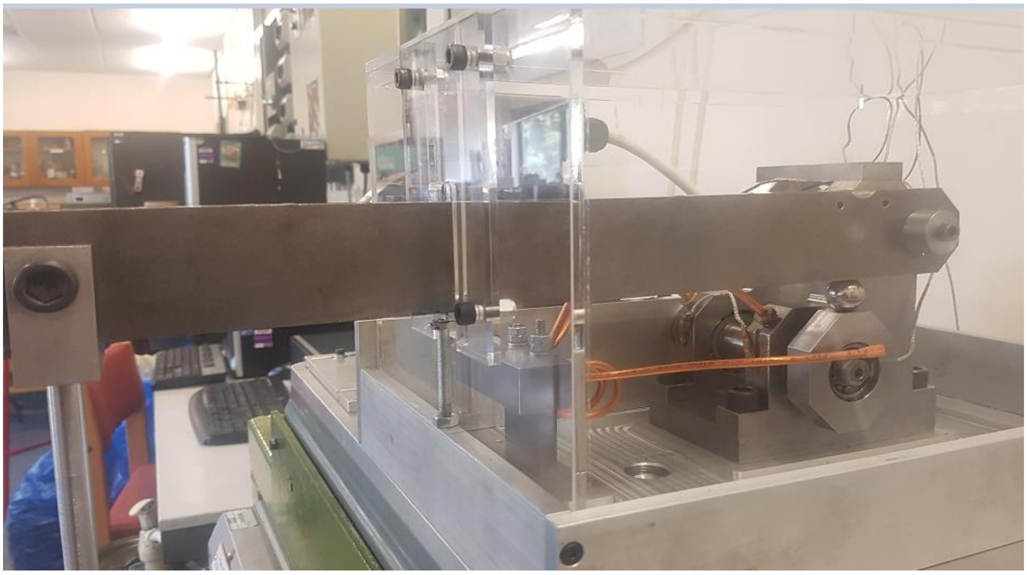

Figure 6-3: High-Speed Test Rig with acrylic box cover.

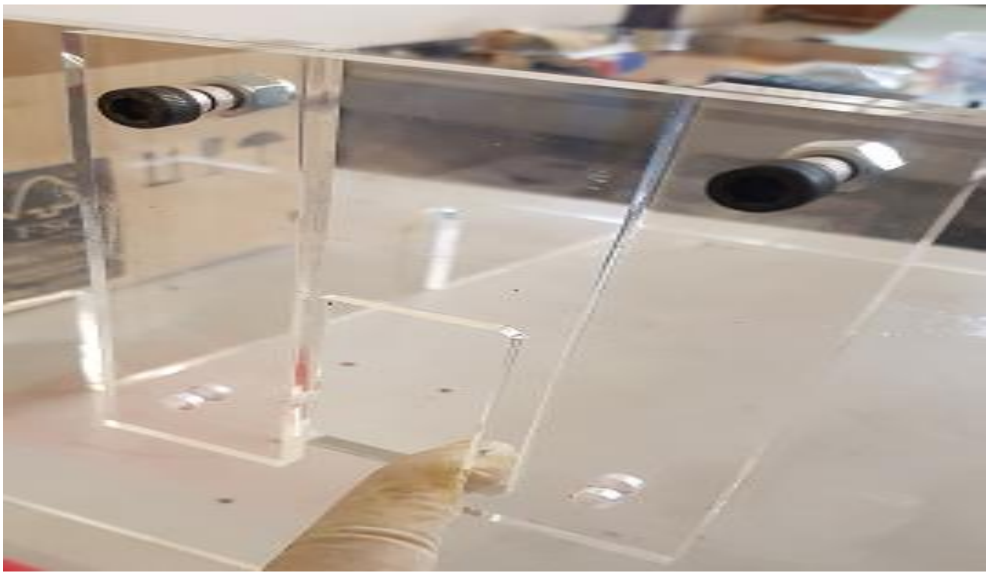

Figure 6-4: Loading arm outlet from the acrylic box cover image taken before any of the tests.

A test on a new bearing was then conducted as the previous results were not adequate to compare with forthcoming tests due to its longevity and evenly distributed data during the course of the test. On every occasion a new bearing is exchanged, a run-in test must take place. Further setbacks arose during the second attempt of the test. While attempting to reach the desired speed and load to proceed with the test as considered in section 6.2, the last increment of applied load led the steel ball to slip out of position and due to the shock and magnitude of applied load a catastrophic failure occurred of the test bearing in minutes as can be seen in Figure 6-5. The slipping of the steel ball was resolved with the use of Permabond engineering adhesives to fix it in place.

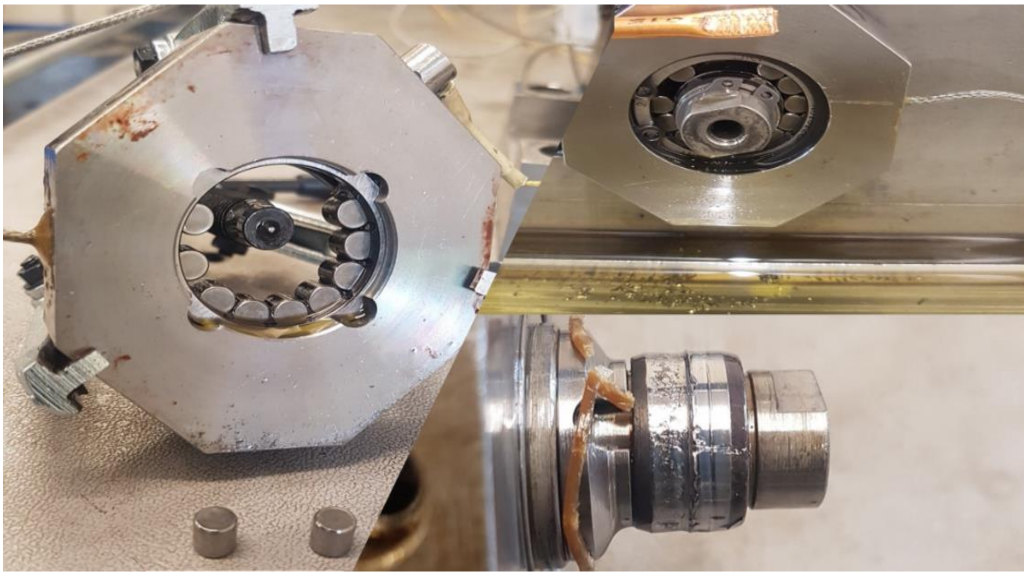

Figure 6-5: Second attempt to Run to Failure Test setback.

As soon as the Permabond adhesive cured, a third attempt was undertaken. Within the hour during the speed and load increments, the whole test bearing housing spun out of the shaft damaging the inner raceway circlips on its way out, with no indication of damage to the test bearing nor the steel ball as it is still in position on the test bearing housing (Figure 6-6).

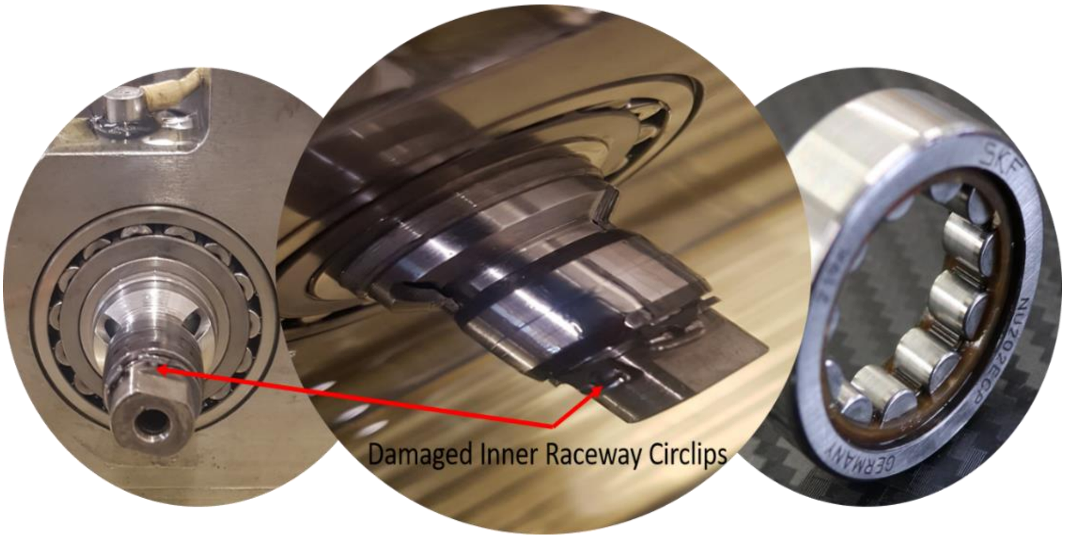

Figure 6-6: Unsuccessful third attempt at Run to Failure Test.

The issue may well have been a matter of misalignment within the high-speed test rig, even though precise measurements were undertaken through a magnetic inclinometer (spirit level) to make sure that the test rig was evenly stable on the new modified base plate and to avoid the stack up of manufacturing tolerances. Further modifications were therefore required to allow the test rig to operate in a stable fashion.

Thus, it was thought that the 20mm steel ball might have been the cause again, as it was only adhesively fixed on a grove specifically designed for it to be placed on top of the test bearing housing. This feature may well keep the steel ball in its position, but as the loads are increased a shock bounce within the adhesive material may react the load, consequently a marginal displacement might occur, thus slightly unloading the test bearing housing, permitting the test bearing housing to have axial displacement. Improvements were made to the loading arm by manufacturing parts and assembling back and side barriers for the steel ball to constrain it in position throughout a test with minimal tolerances, in an attempt to resolve the issue (Figure 6-7).

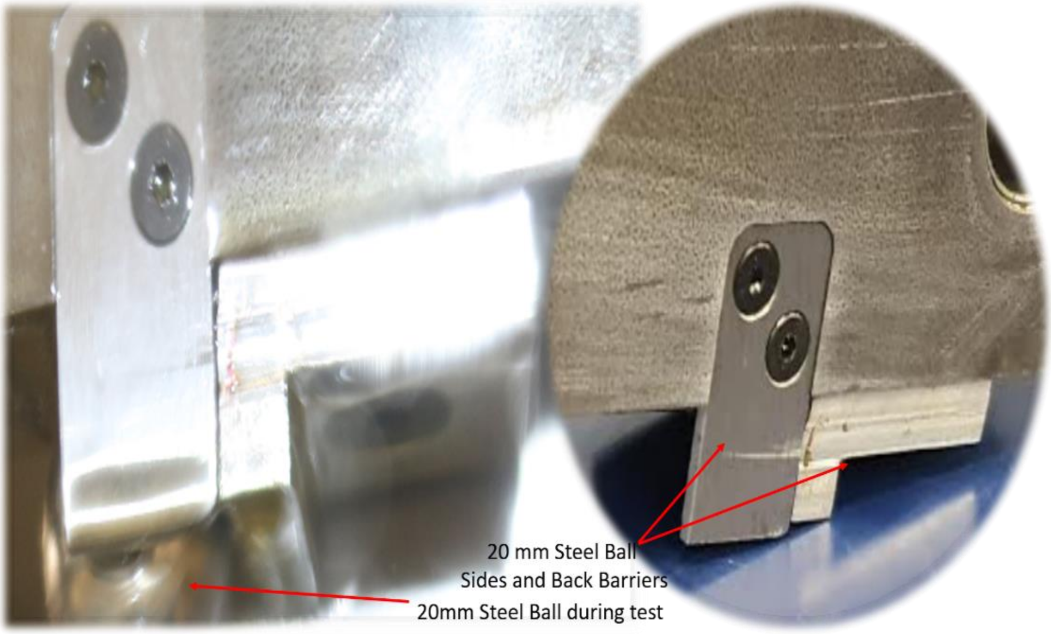

Figure 6-7: Modifications to the loading arm in order to prevent any displacement of the Steel Ball.

A fourth attempt was started, yet again with a new bearing. The experiment finally seemed to operate well over 3 hours, but then severe noise surged abruptly. Once the test rig was stopped and even though the steel ball was still in place and that the test bearing housing was still on the shaft, severe damage to the test bearing occurred as the rolling elements were forced out of the bearing and the test bearing housing was badly misaligned as may be seen in Figure 6-8.

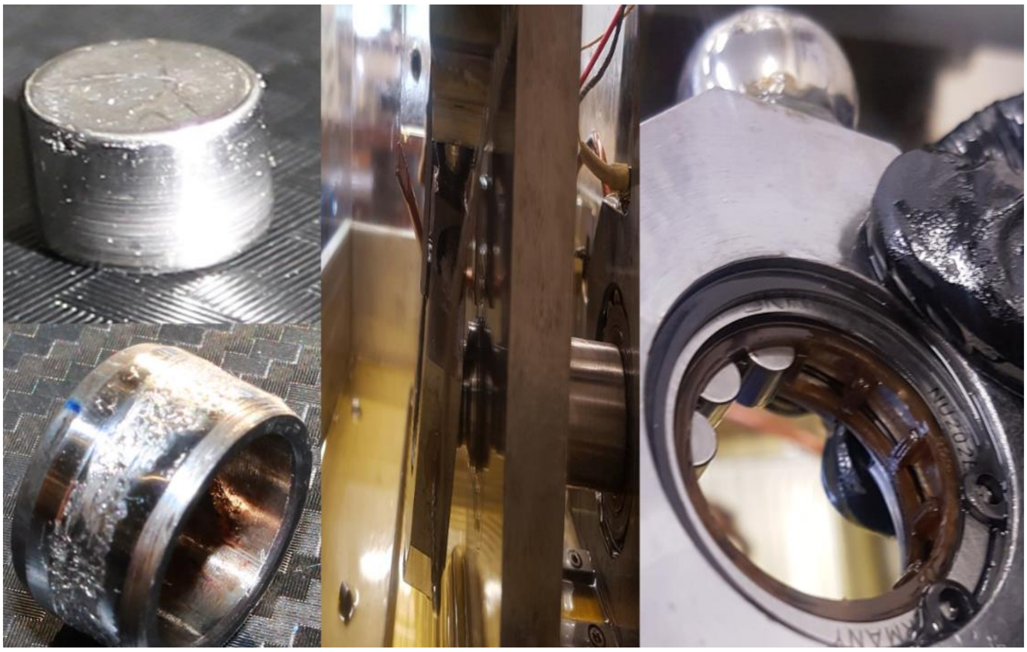

Figure 6-8: Images from the fourth attempt on SKF NIU202ECP bearing.

Modifications to hold the whole test bearing housing were necessary. Figure 6-9 shows the manufactured piece up close and during operational conditions, it is placed inline with the test bearing housing to remove and control viable axial displacement. The base plate had holes drilled so that the new part would be screwed on and fixed on to the base plate.

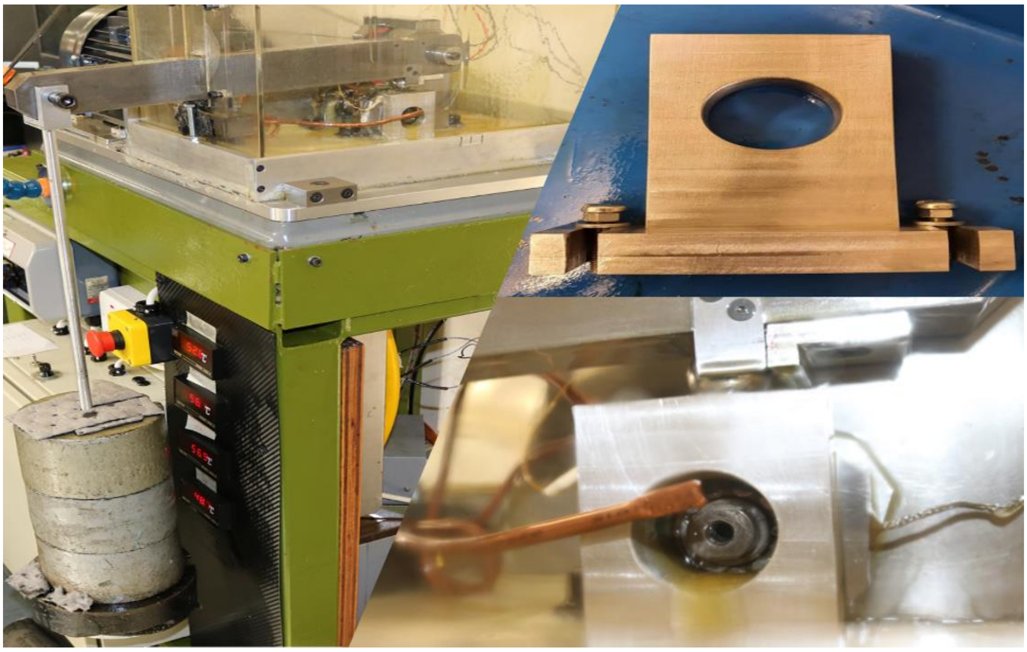

Figure 6-9: Manufactured piece to stop the test bearing housing's axial displacement.

Following this modification, two Run to Failure tests were finally achieved. The data acquired were only analysed after the second completed attempt due to the booking of the AEWin system, both attempts were done back to back. However, due to the initial settings of 40dB gain for the PAC amplifier, the signal processing analysis revealed difficulties as the results were overwhelmed caused by clipping of the signal at high amplifications, detailed examples from both attempts are presented respectively in Figures 6-10 to 6-13 and Figures 6-14 to 6-17.

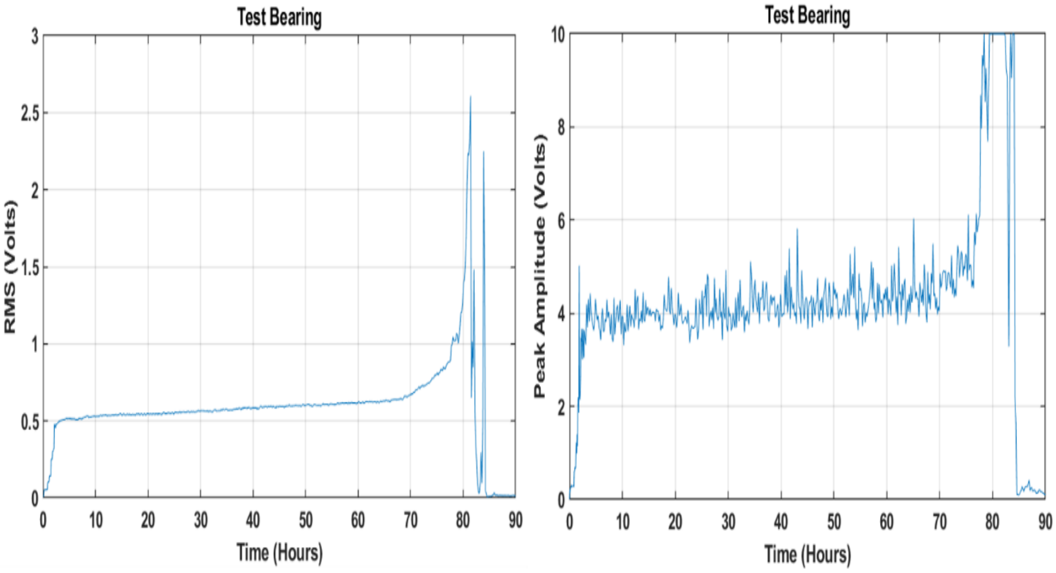

Figure 6-10: Represents the full duration of attempt 5 for RMS and Peak Amplitude.

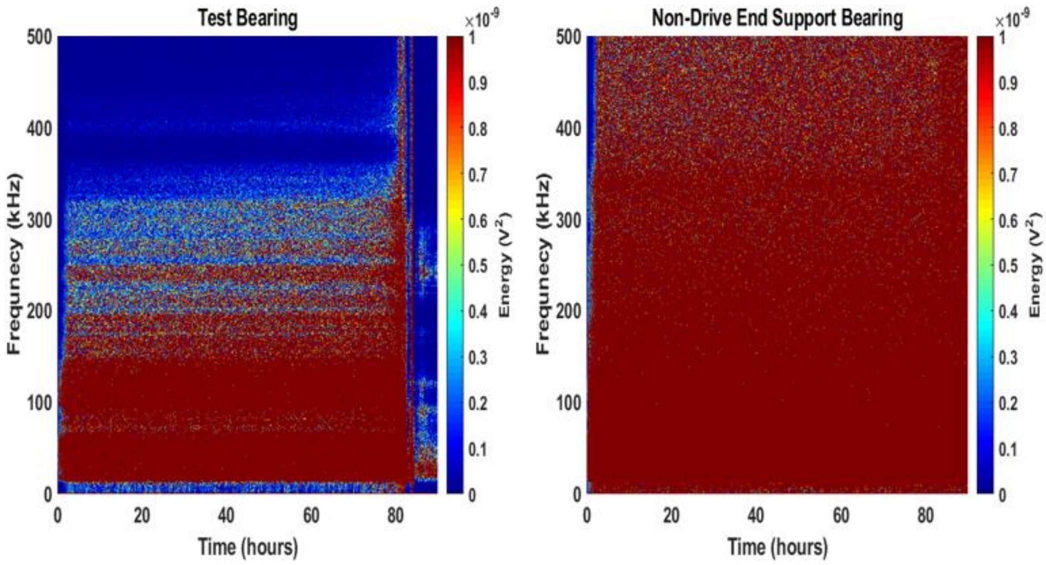

Figure 6-11: FFT representation for the full duration of attempt 5.

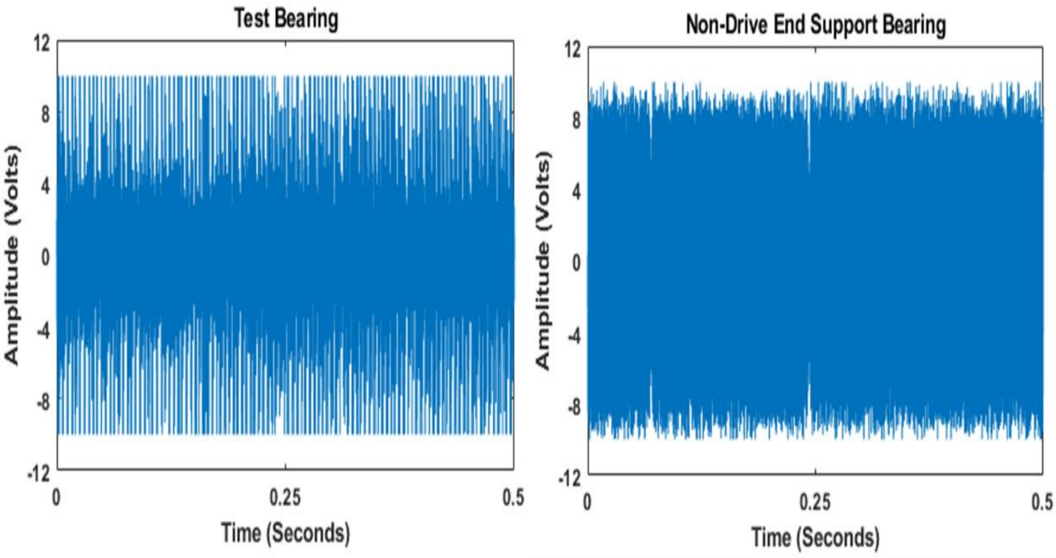

Figure 6-12: Raw signal of a wavestream recorded at 80 hours into attempt 5.

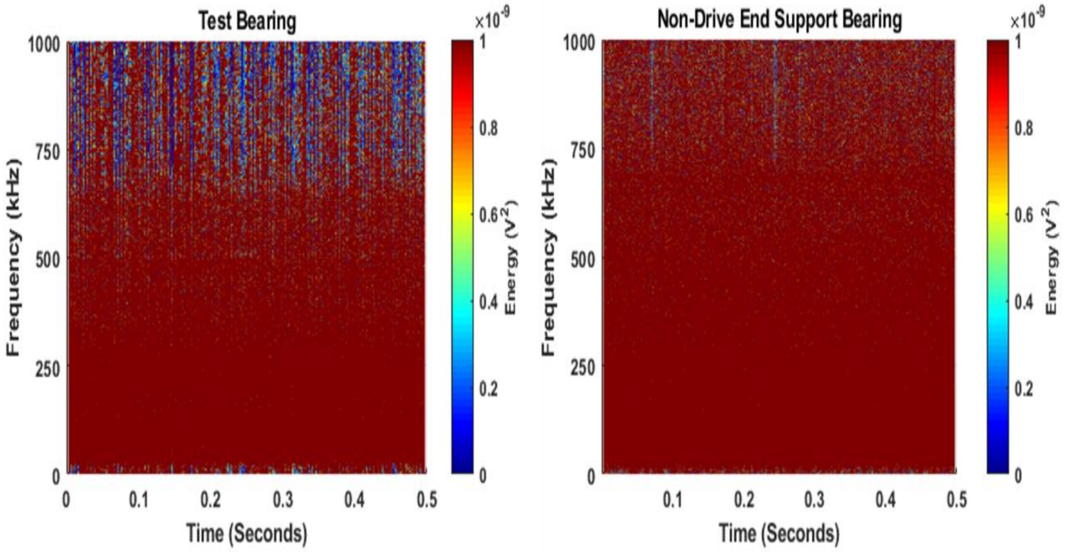

Figure 6-13: STFT of the same wavestream recorded at 80 hours into attempt 5.

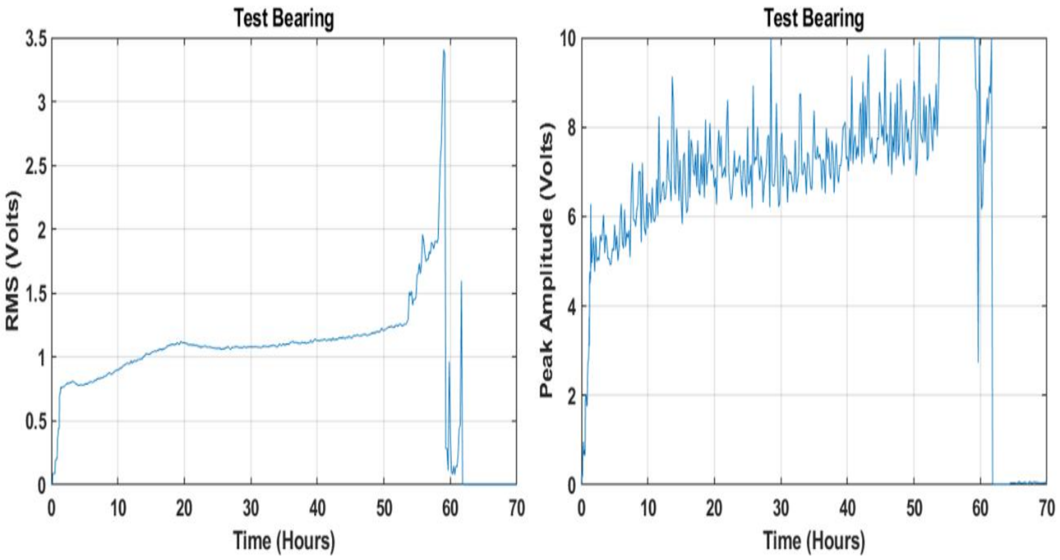

Figure 6-14: Represents the full duration of attempt 6 for RMS and Peak Amplitude.

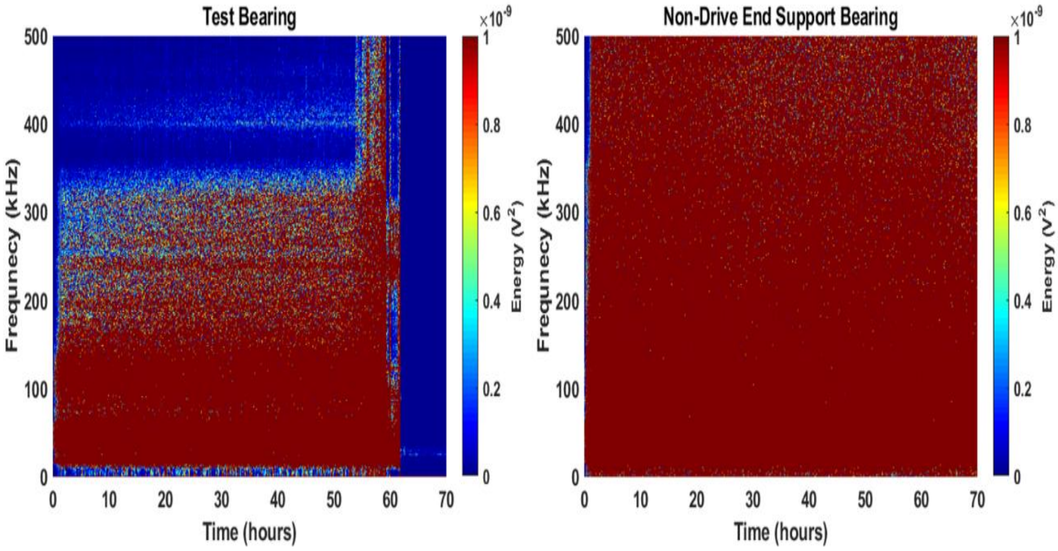

Figure 6-15: FFT representation for the full duration of attempt 6.

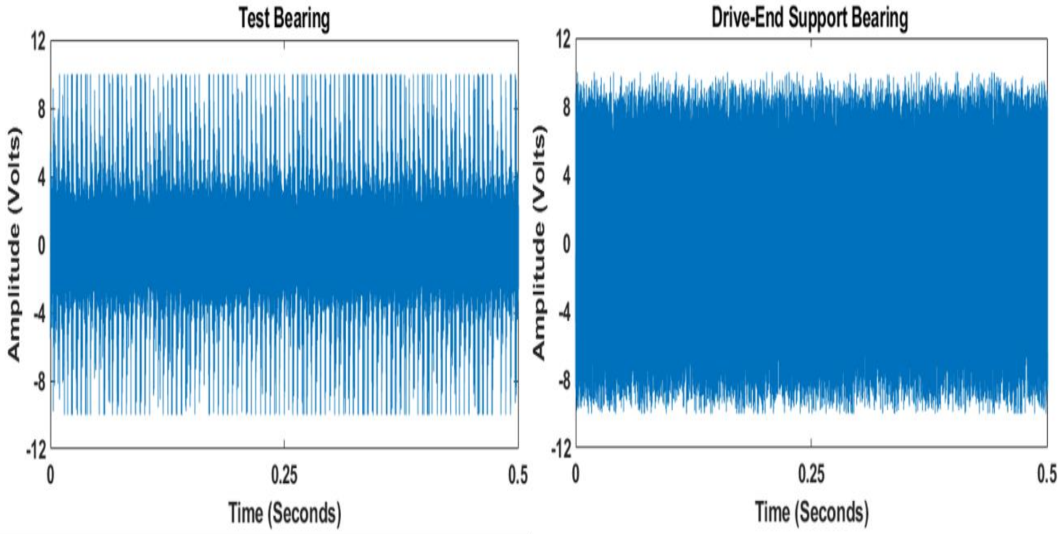

Figure 6-16: Raw signal of a wavestream recorded at 53 hours into attempt 6.

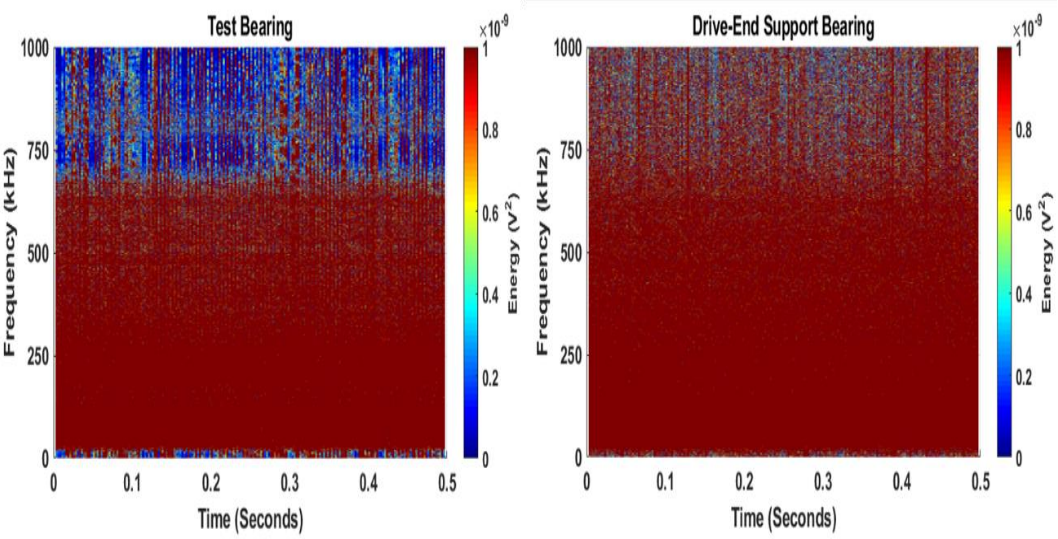

Figure 6-17: STFT of the same wavestream recorded at 53 hours into attempt 6.

The reason behind the results clipping was due to the limitation of the analogue to digital converter within the AEWin system, which could only manage voltages between ±10V after amplification to signal as seen in Figure 6-12 and Figure 6-16. Therefore, it was essential to rectify the issue and repeat the healthy bearing characterisation tests with a lower 20dB gain to avoid this problem. It is important to note that the results of the healthy characterisation tests in Chapter 5 are those from the 20dB gain settings. As the data recorded from the previous experiments set at 40dB gain were discarded, further illustrations of the clipping from different experiments are shown in Figures 6-18 to 6-20.

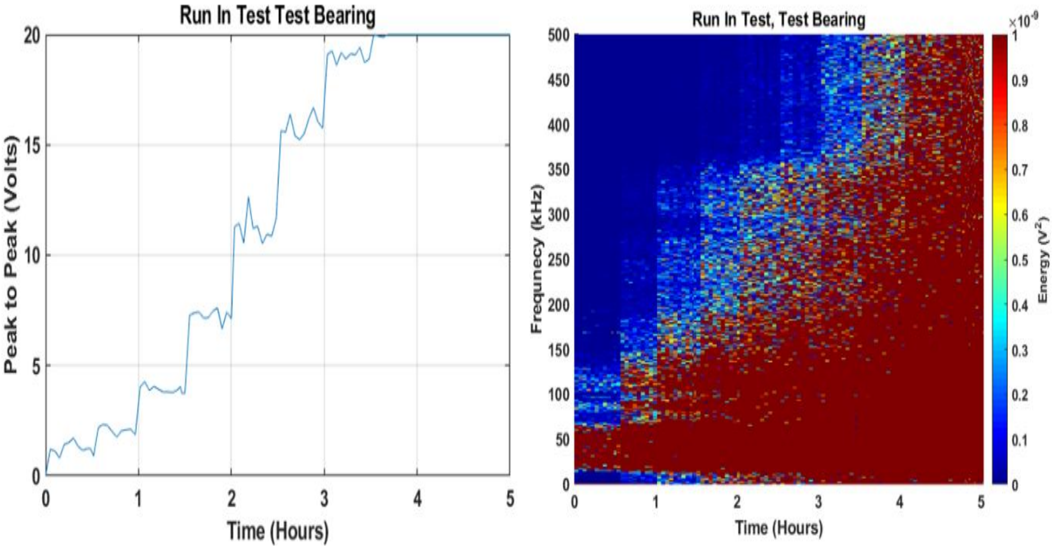

Figure 6-18: Other forms of clipping from one of the recorded data at 40dB gain for a Run in Test

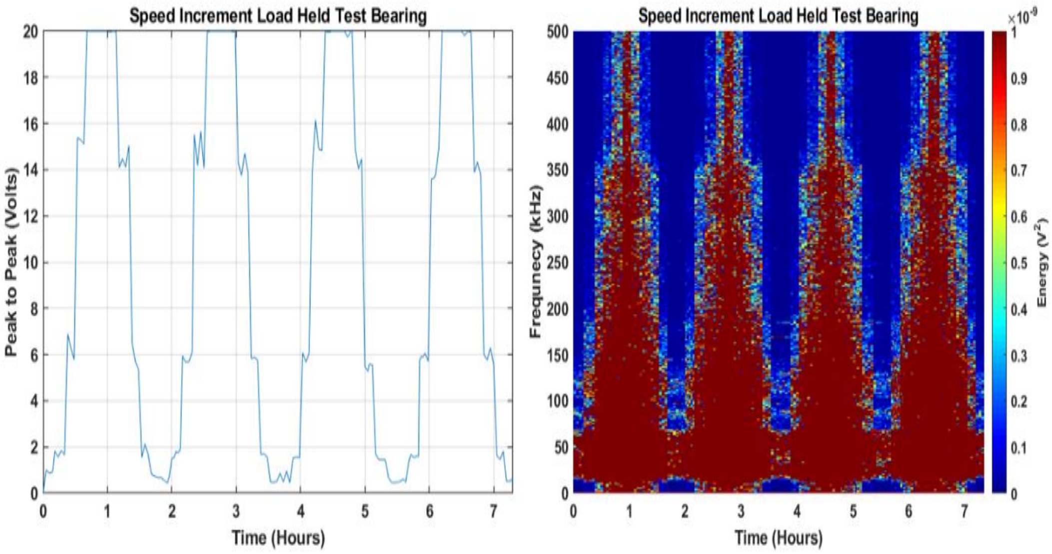

Figure 6-19: Other forms of clipping from one of the recorded data at 40dB gain for a Speed Increment Load Held Test.

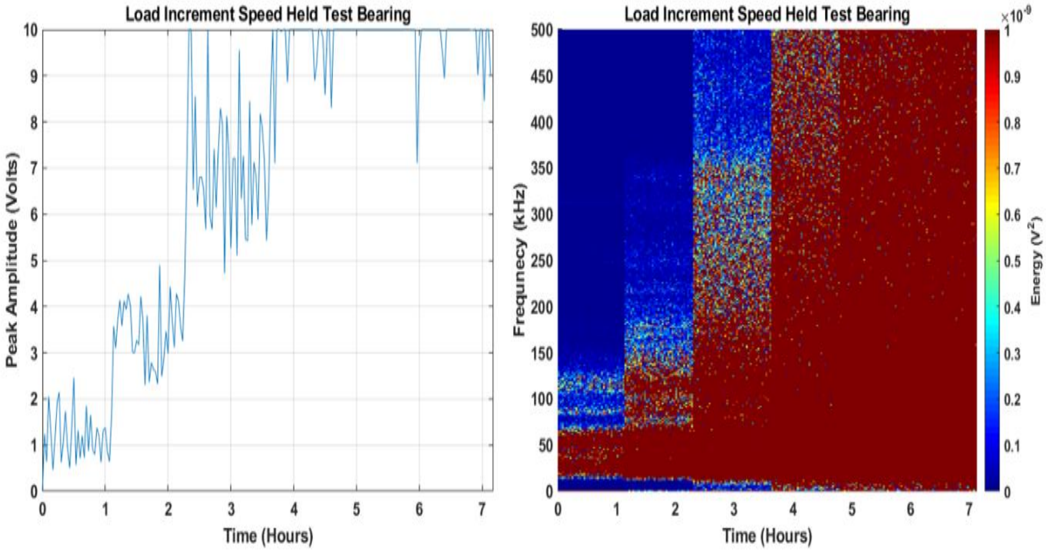

Figure 6-20: Other forms of clipping from one of the recorded data at 40dB gain for a Load Increment Speed Held Test.

The test repetitions are to ensure that the healthy characterisation tests results are within the same settings as the impending Run to Failure Tests. The initial research was to perform four Run to Failure tests on each bearing, but unfortunately the time consumed during these attempts limited the research to two tests per bearing.

6.3 Test Bearings Synopsis

Prior to any of the tests a Talysurf scan was carried out for one of the SKF bearings as they have similar manufacturing characteristics except the radial clearance and one NU202EM bearing, which included the inner raceway, outer raceway and the rolling element surface roughnesses and followed by a 3D scan of the inner raceway. The surface roughness of each component was scanned several times in different positions on the component, then the roughnesses were separately averaged for each component as shown in Table 5-1. Leading to the synopsis of each bearing failure this part of the section illustrates the generic start point for the bearings in a healthy state. Figures 6-21 to 6-24 demonstrates the scanned surface features of the SKF bearing and Figures 6-25 to 6-28 demonstrates the scanned surface features of the budget bearing, these measurements had a Gaussian filter with a cut off wavelength of 0.8mm applied.

The inner raceway of the SKF bearings demonstrates that the surface topography has a smoother and evener form than the budget bearing, as the peaks and valleys do not exceed $\pm 1\mu m$ for the full assessment length while as shown in Figure 6-21, while for the budget bearing inner raceway they surpass the $\pm 1\mu m$ with a rough and wavy form as shown in Figure 6-25. The SKF bearings outer raceway surface roughness demonstrated in Figure 6-22, reveals finer peaks and valleys and at a much lower scale when compared to the budget bearings surface as shown in Figure 6-26, as the peaks and valleys not only surpass $\pm 1\mu m$ boundaries, yet the distance between the waviness is wider. With regards to the rolling element, the SKF rollers have a distinctive finish as the surface roughness are within the $\pm 0.2\mu m$ limits as shown in Figure 6-23, unlike the budget bearing rollers where for the majority of the assessment length the surface quality is within the $\pm 1\mu m$ boundaries as shown in Figure 6-27.

Observations from the 3D surface scans exposes the roughness within the inner raceway of the budget bearing, as there are distinct visible thin lines all over the surface nothing like the SKF inner raceway which demonstrates a significantly smoother surface finish.

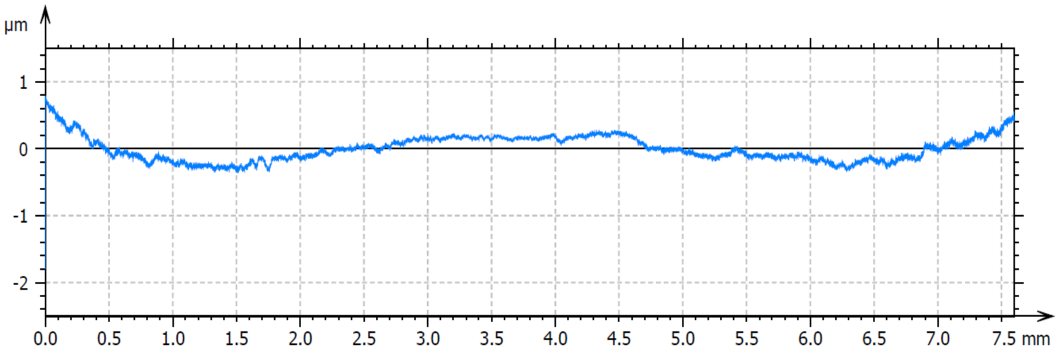

Figure 6-21: SKF Bearing, inner raceway surface roughness scan.

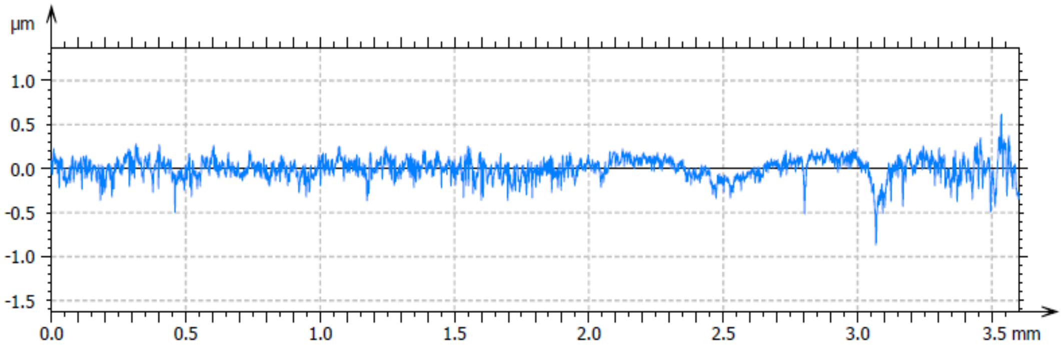

Figure 6-22: SKF Bearing, outer raceway surface roughness scan.

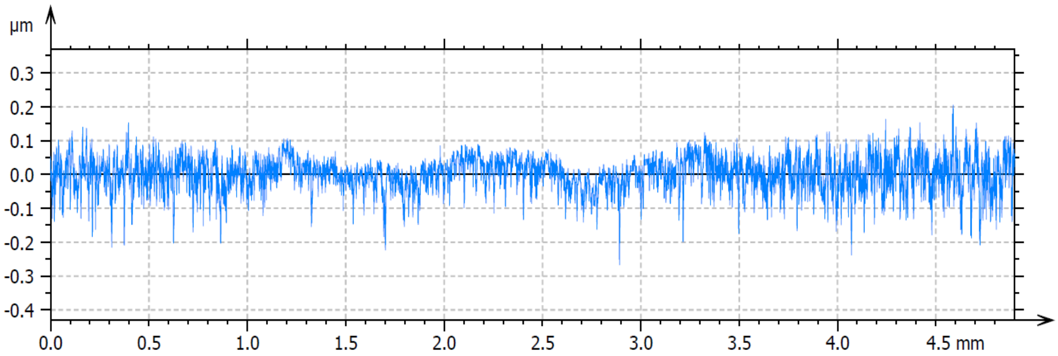

Figure 6-23: SKF Bearing, roller surface roughness scan.

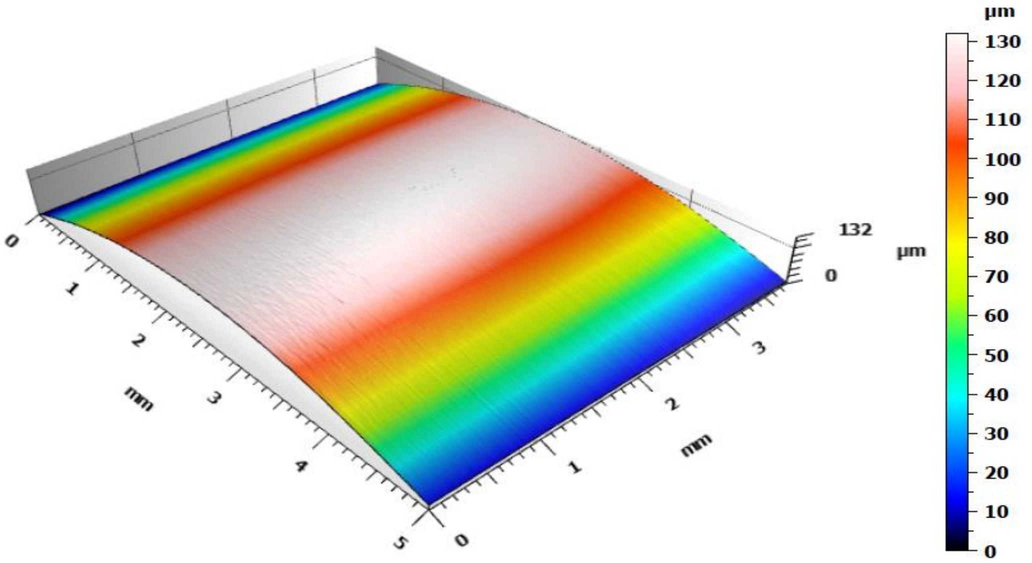

Figure 6-24: SKF Bearing, inner raceway 3D surface scan.

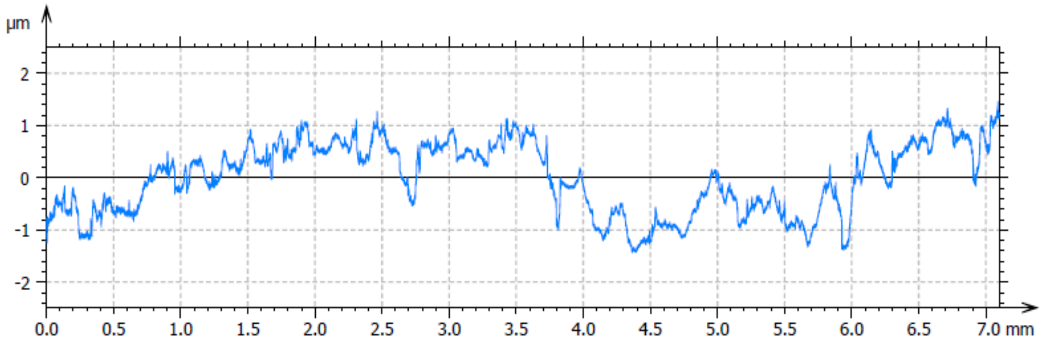

Figure 6-25:Budget Bearing, inner raceway surface roughness scan.

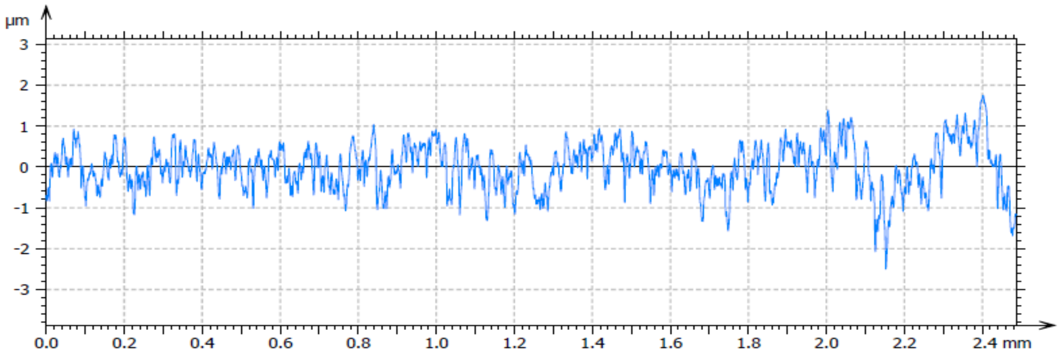

Figure 6-26:Budget Bearing, outer raceway surface roughness scan.

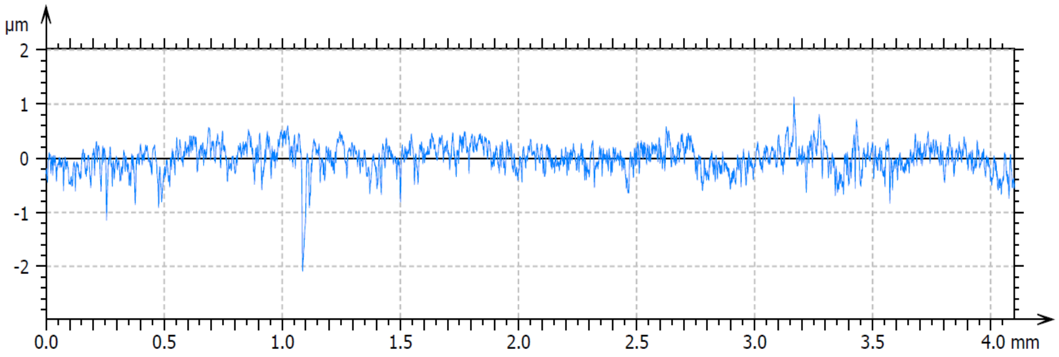

Figure 6-27: Budget Bearing, roller surface roughness scan.

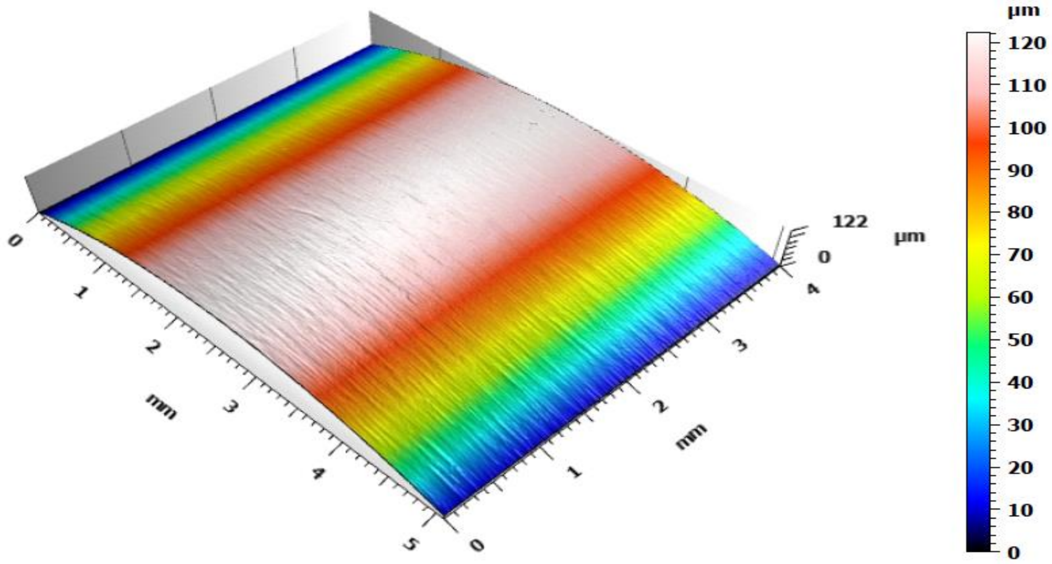

Figure 6-28: Budget Bearing, inner raceway 3D surface scan.

6.3.1 First SKF NU202ECP Bearing

Figure 6-29 and Figure 6-30 demonstrates the extent of the damages witnessed on the inner raceway at two different positions, despite the damages on the inner raceway there were no visible damage on the outer raceway nor the rollers at the end of the experiment which ran for a period of 66 hours. The damage on the inner raceway differs from one location to the other as it rotates with the shaft through the point of maximum load. As Figure 6-29 demonstrates an advanced stage of damage with more extensive wear and Figure 6-30 a later stage damage and not yet at a similar damage phase as the former. It is believed that if the test continued further, than the damage would have covered the inner raceway uniformly all across the inner raceway. The 3D scans also demonstrate the depth and severity of the damages sustained on the inner raceway.

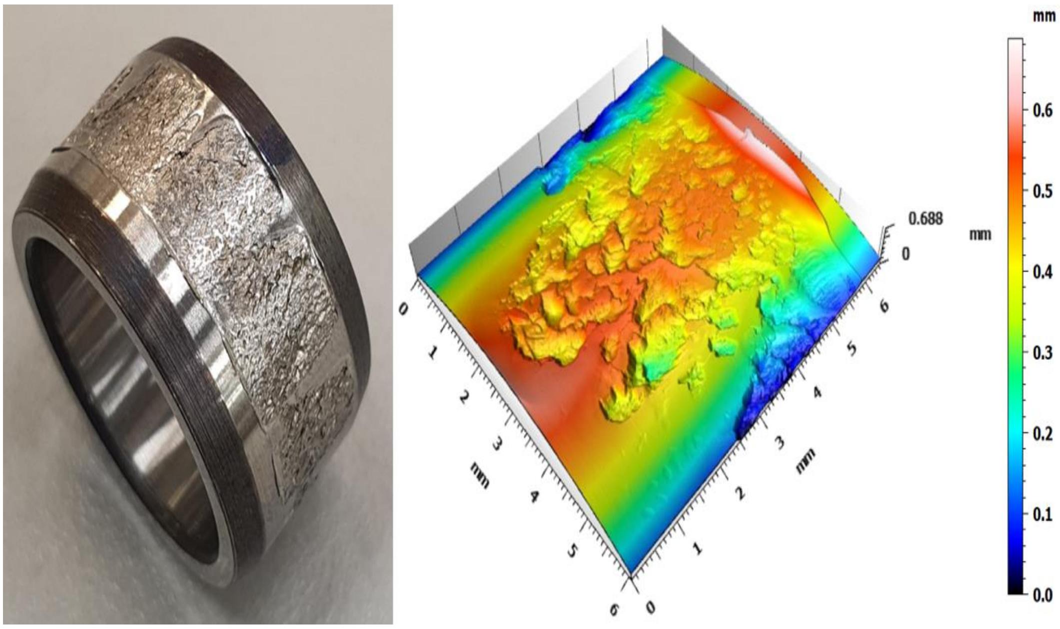

Figure 6-29: First SKF NU202ECP, one side of the inner raceway damage.

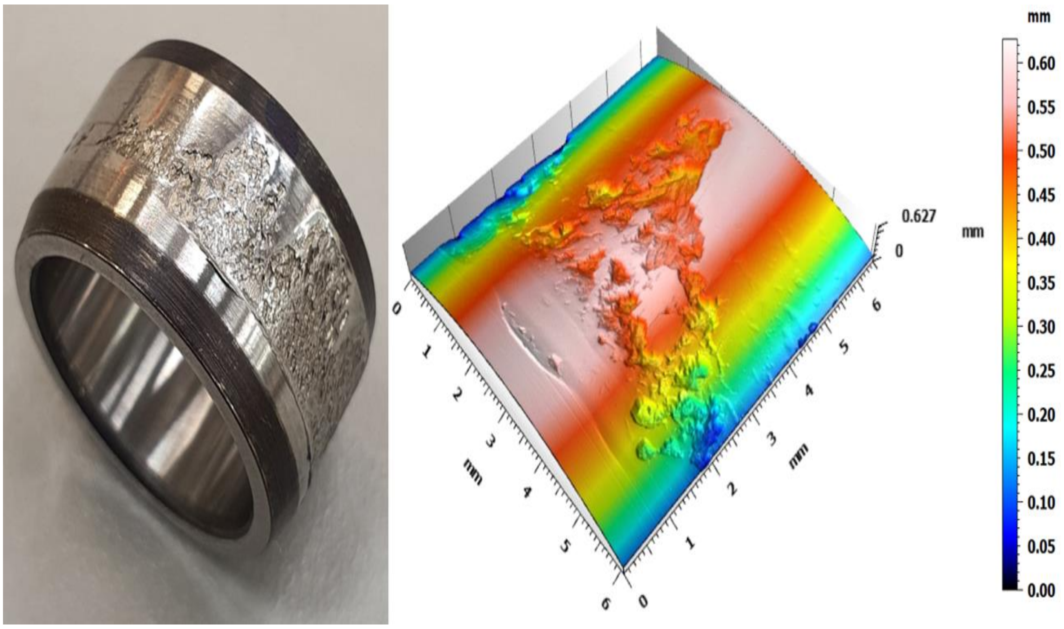

Figure 6-30: First SKF NU202ECP, another side of the inner raceway damage.

6.3.2 Second SKF NU202ECP Bearing

Figure 6-32 and Figure 6-33 provides detailed visualisation of the test bearing's components. Although, the failure experienced was at a much shorter testing period of approximately 28 hours, still the outcome was a significant level of deterioration. The inner raceway damage circles 360° around the component's area, although the damage appears not concentrated in the centre of the inner raceway, it is still within the maximum axial tolerance 'S' of 1mm set by (SKF 2019) as shown in Figure 6-31. The rollers all suffered damage on both edges, which undoubtedly negates the issue of misalignment. The centre of the outer raceway presents well-defined marks of surface fatigue confined at the maximum loaded zone.

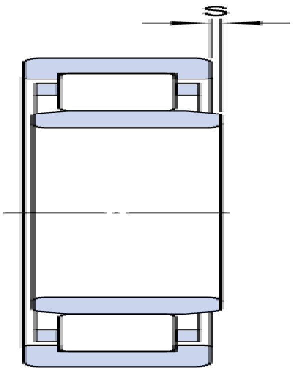

Figure 6-31: SKF axial tolerance 'S' – extracted from (SKF 2019).

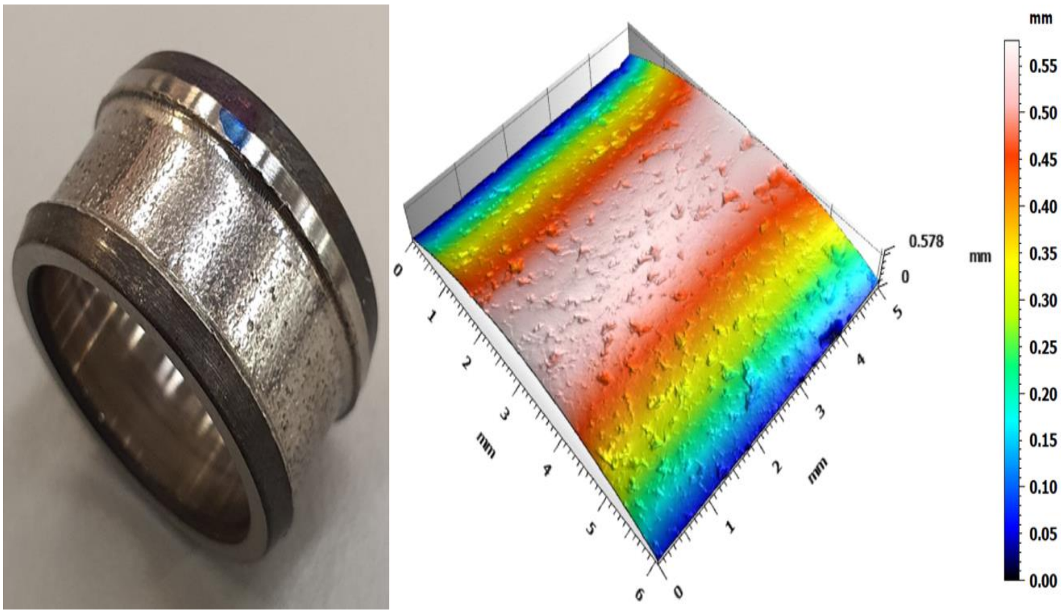

Figure 6-32: Second SKF NU202ECP, inner raceway damage.

Figure 6-33: Second SKF NU202ECP, damage sustained on rollers and outer raceway.

6.3.3 First SKF NU202ECP/C3 Bearing

After a period of approximately 88 hours of testing, Figure 6-34 and Figure 6-35 reveal the effects on the components. The inner raceway seems to have sustained comparable damage traits to the previous bearing in 6.3.2, although due to a lengthier duration of the test, the damage is overwhelming as the 3D surface profile shows the severity of the damage with respect to the previous test. The outer raceway experienced slight pitting, but no major signs of surface fatigue or deterioration. The existent damage on the rollers is again on both edges of the roller, although the main body of the roller seems smoother than the previous test and it may well be due to the fact that there was not considerable friction between the rollers and the outer raceway as previously seen.

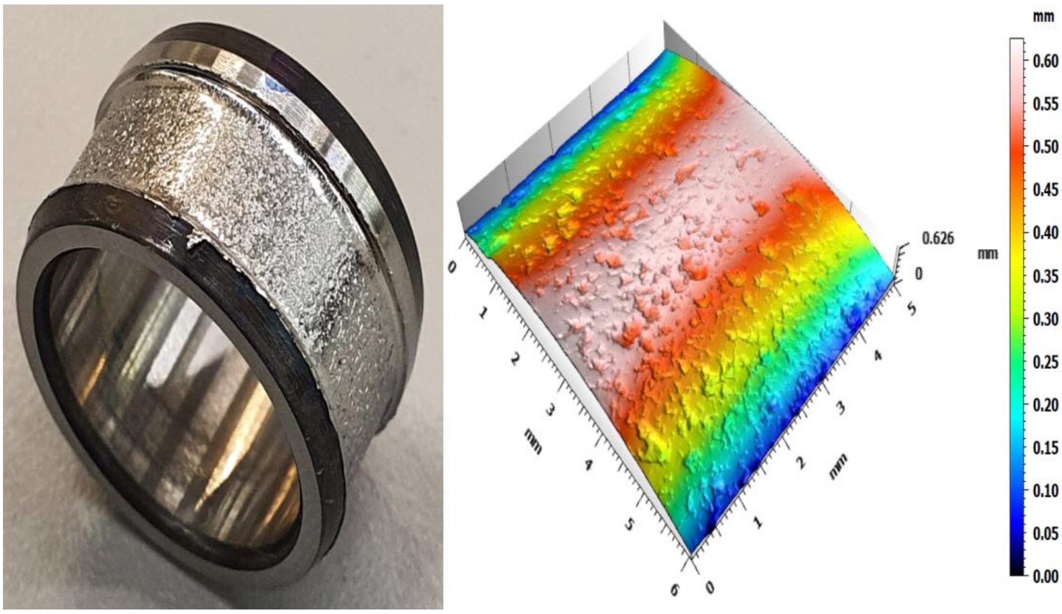

Figure 6-34: First SKF NU202ECP/C3, inner raceway damage.

Figure 6-35: First SKF NU202ECP/C3, damage sustained on rollers and outer raceway.

6.3.4 Second SKF NU202ECP/C3 Bearing

The test had to be stopped due to intense sharp audible noise at around 25 hours. Unlike the previous tests, where an intensification of the AE RMS signal indicated via the AEWin systems interface suggests an imminent failure. Once the bearing was dismantled, the damage was not as severe as any of the other tests nonetheless produced other features of wear Figure 6-36 and Figure 6-37. The inner raceway uniquely from all previous tests has sustained a series of fine lines or scores all across the surface, that are also paralleled on the rollers and evidently scuffed over on to the outer raceway. The inner raceway also showed signs of pitting as presented in the 3D surface profile image as well as the wear sustained is not as deep as the previous bearings.

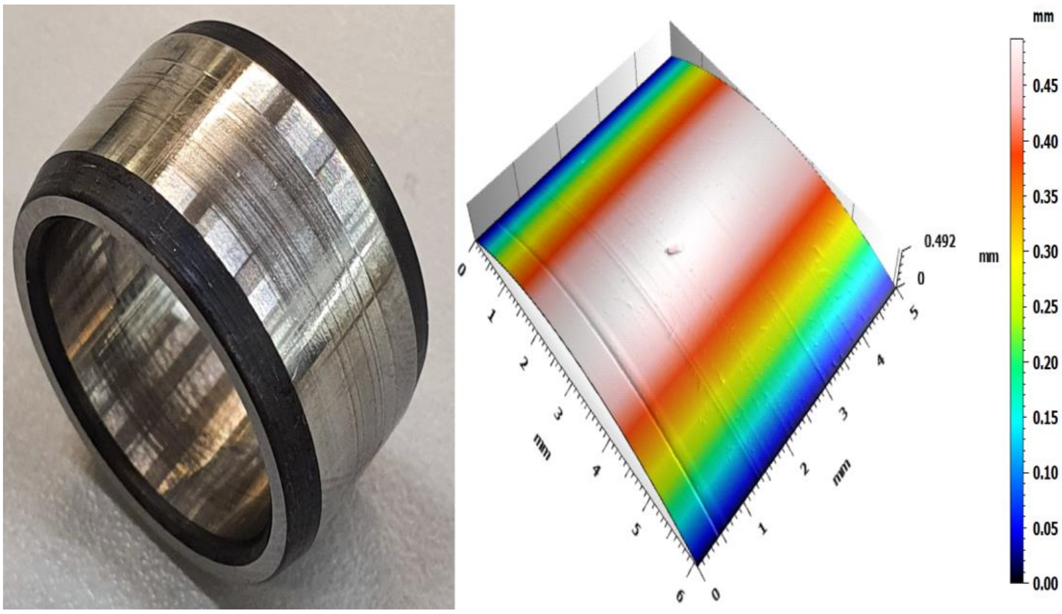

Figure 6-36: Second SKF NU202ECP/C3, inner raceway damage.

Figure 6-37: Second SKF NU202ECP/C3, damage sustained on rollers and outer raceway.

6.3.5 First Budget Bearing NU202EM

Figure 6-38 and Figure 6-39 demonstrates the damages endured during the first budget bearing Run to Failure test after 22 hours. Unlike the SKF bearings, where they come from a very renowned manufacturer which offers its clients full details of their products and capabilities, the budget bearing did not come with detailed specifications. Therefore, full reliance was placed on the AEWin system to capture and express occurring damage or by audible noise. The inner raceway revealed signs of wear and damage all across the surface, while the outer raceway did experience pitting again on the maximum loaded zone and as for the rollers thin graze lines were observed.

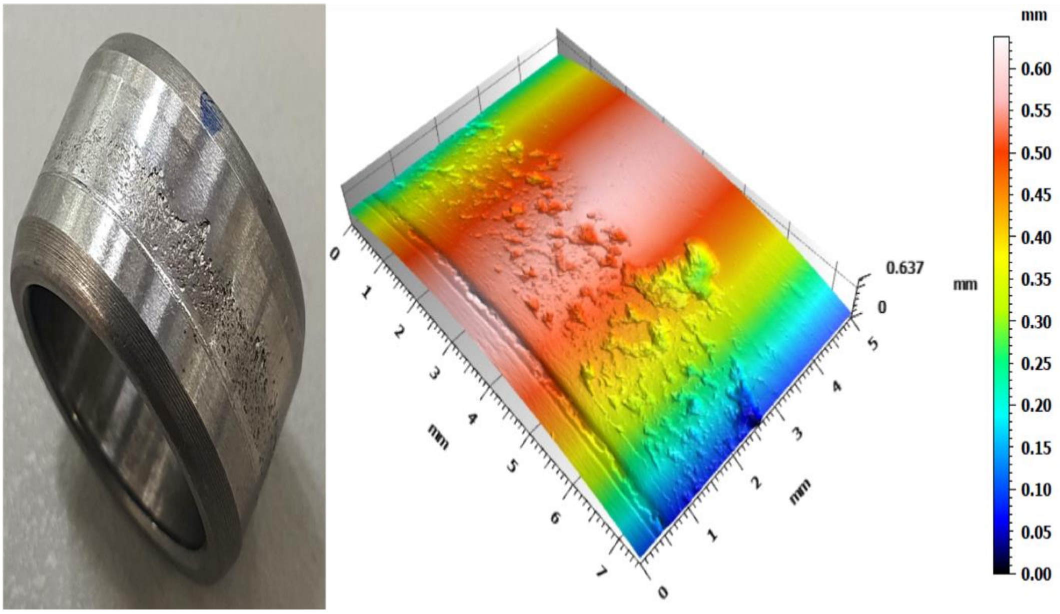

Figure 6-38: First Budget Bearing, inner raceway damage.

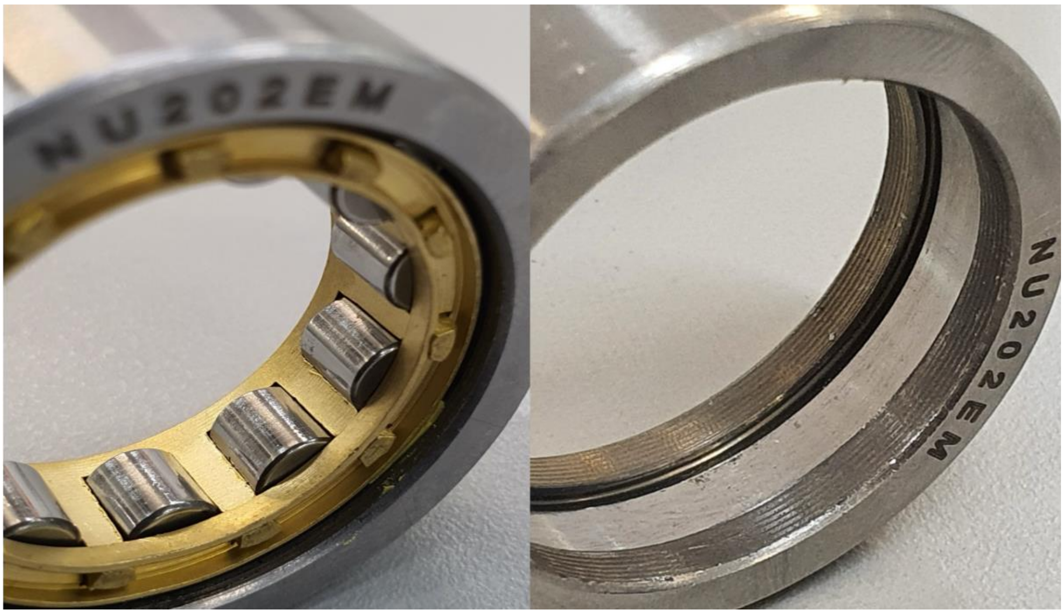

Figure 6-39: First Budget Bearing, damage sustained on rollers and outer raceway.

6.3.6 Second Budget Bearing NU202EM

After a period of 22 hours of testing, Figure 6-40 and Figure 6-41 demonstrate the damage sustained on each of the components. The inner raceway appears to have endured immense wear, relatively comparable traits to the previous damages on the inner raceway of bearings from tests in section 6.3.2 and 6.3.3. Still, observing closely to how all three inner raceways have been damaged, the budget bearing seems to have a much rounder and smoother slope at the edges of the wear, as to the other SKF inner raceways it seems more of a much sharper incline at both edges of the wear. The outer raceway exhibited significant wear and fatigue in comparison to any other outer raceway, as well as the rollers suffering considerable damage as they were loose within the damaged roller cage.

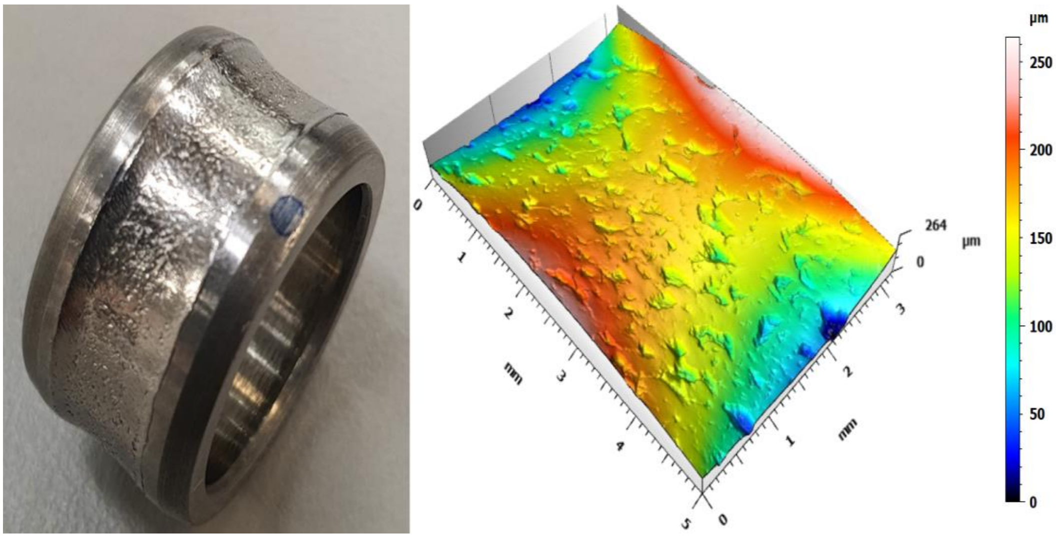

Figure 6-40: Second Budget Bearing, inner raceway damage.

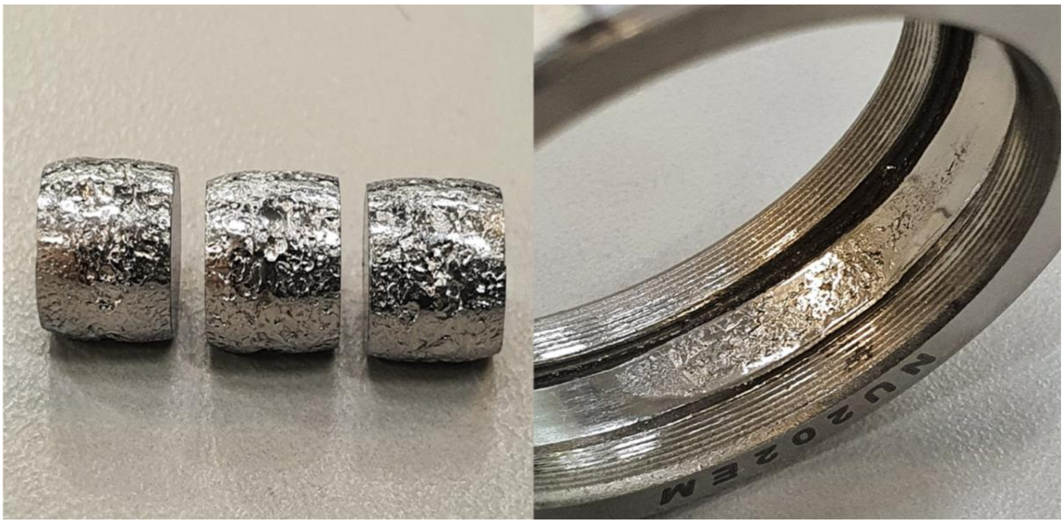

Figure 6-41:Second Budget Bearing, damage sustained on rollers and outer raceway.

6.4 First SKF NU202ECP Bearing Run to Failure Test Results

6.4.1 AE RMS Analysis

The AE RMS amplitude plot for the full duration of the test is demonstrated in Figure 6-42, Figure 6-43 represents a closer look at the results with annotations on specific wavestreams indicating key variations in the AE RMS signal that will be discussed further in the raw signal and STFT analysis sections. Of note, the drop of the RMS signal for the test bearing at the end of the test is due to the severity of the damage and the heavily vibrations, affecting the coupling medium, triggering the dislocation of the sensor from the test bearing housing. There is a clear effect of the speed and load increase on the RMS amplitude observed for all the bearings since the start of the test until the required speed and load for the test is reached, similar to the behaviour observed during the healthy characterisation experiments. A steady increase of RMS amplitude is noticed on the test bearing and the Non-Drive End support bearing, opposite to the RMS results of the Drive End support bearing as it steadily decreases during the test. The reason behind this is the distance of both support bearings from the test bearing, as the radial load applied would have a greater effect on the Non-Drive End support bearing due to its proximity to the test bearing in addition to the propagation/attenuation of the signal. Towards the end of the test, as the test bearing condition starts to change and the RMS amplitude spikes, the signals created as also detected at both support bearings. The synopsis section for this test bearing exhibited two stages of damage to the inner raceway as shown in Figure 6-29 and Figure 6-30, it is reasonable to believe that the earlier stage of the damage could be initiated at ‘b’ which represents the more heavily damaged side of the inner raceway, as the other side of the inner raceway may well be initiated at ‘c’, these remarks are concluded as there was no visual defect on the rollers nor the outer raceway. These hour marks or designated annotation during the test are chosen by running the code to find a strong variation within the signal, for data within numerous times during the test for example at 55hrs leading to 58hrs, or where observed that the AE RMS starts to increase from the plot in Figure 6-43. Yet there was no solid data before 58hrs during the run to failure tests. Hence, it is considered the starting point or initiation of damage to the bearing leading to ‘b’ in Figure 6-43 where there is a surge in the AE RMS similarly again in ‘c’. Those were chosen on the basis of running the code minutes before and after each chosen plot to see what the raw signal indicates and to further discuss the differences within the signal.

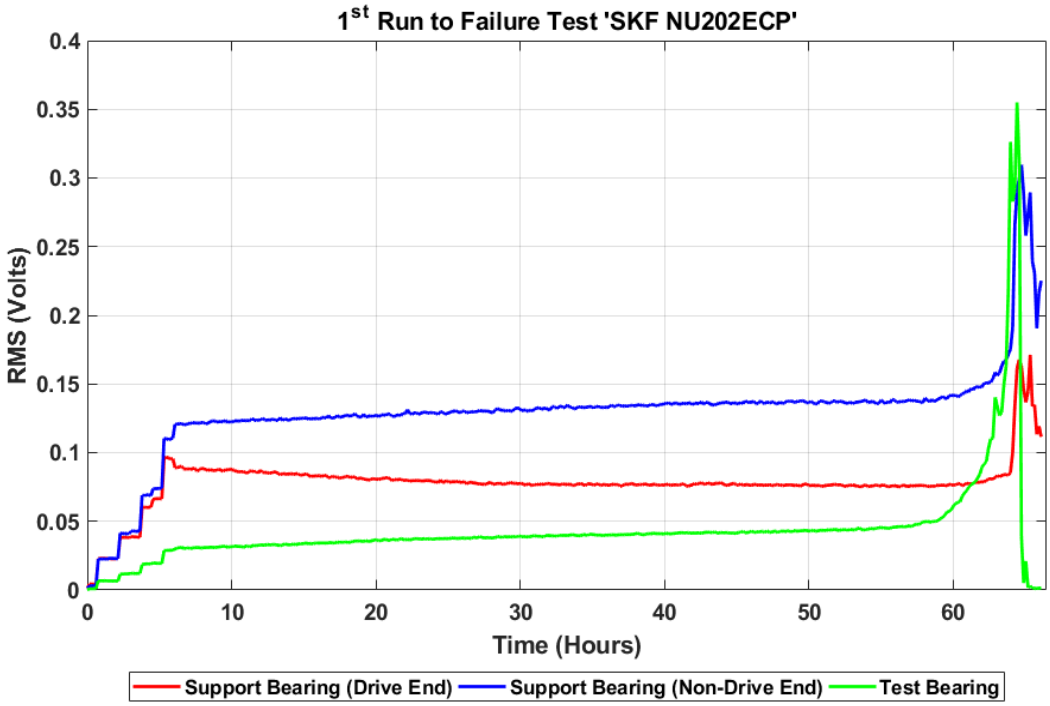

Figure 6-42: First SKF NU202ECP Bearing Run to Failure Test data of RMS amplitude.

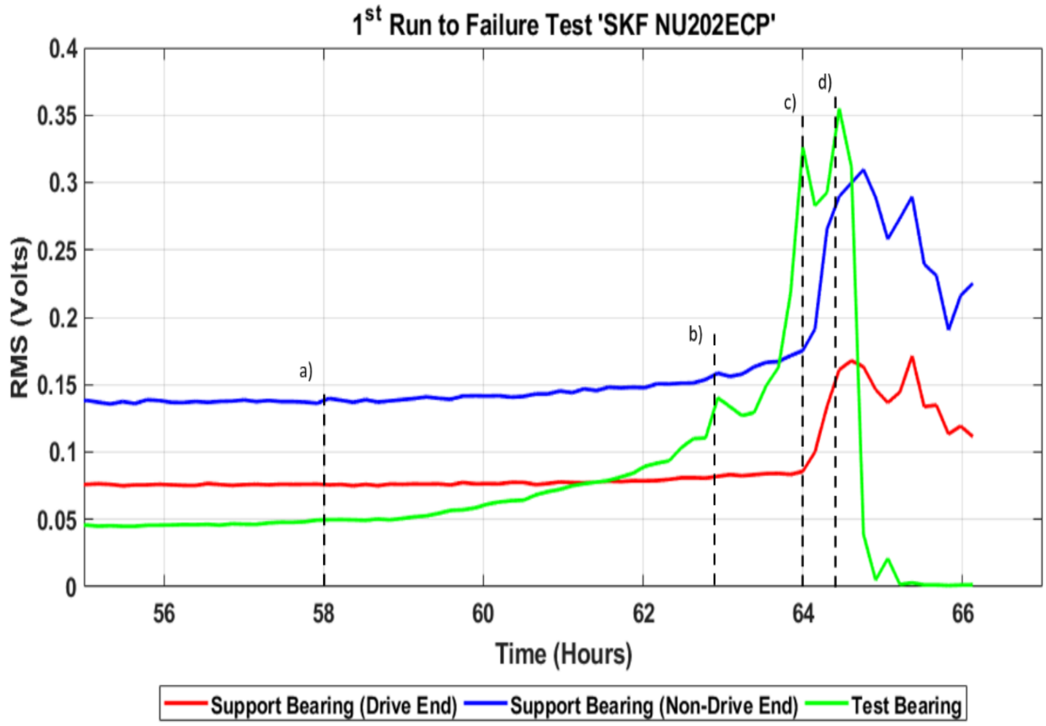

Figure 6-43: Annotations on magnified plot at a) 58 hours, b) 62 hours 50 minutes, c) 64 hours and d) 64 hours 30 minutes.

6.4.2 Raw Signal Analysis

The raw signal of the selected wavestreams from Figure 6-43 are demonstrated in Figure 6-44, although each plot has its own unique amplitude scale to aid visualisation. These wavestreams were chosen at different stages of the test to demonstrate how the bearing condition may change the raw signal results with regards to the RMS values. Raw signals were analysed at earlier stages of the test with no significant details from the signal able to be obtained as the continuous background level of noise dominates the signal, the periodic transients became clearer at the 58 hours mark of the test. All plots reveal a certain amount of continuous noise level, however as the test progresses sharper transients predominate the noise as seen in plots 'c' and 'd'. The rise in amplitude of the raw signals is positively reflected in the rise of the RMS values.

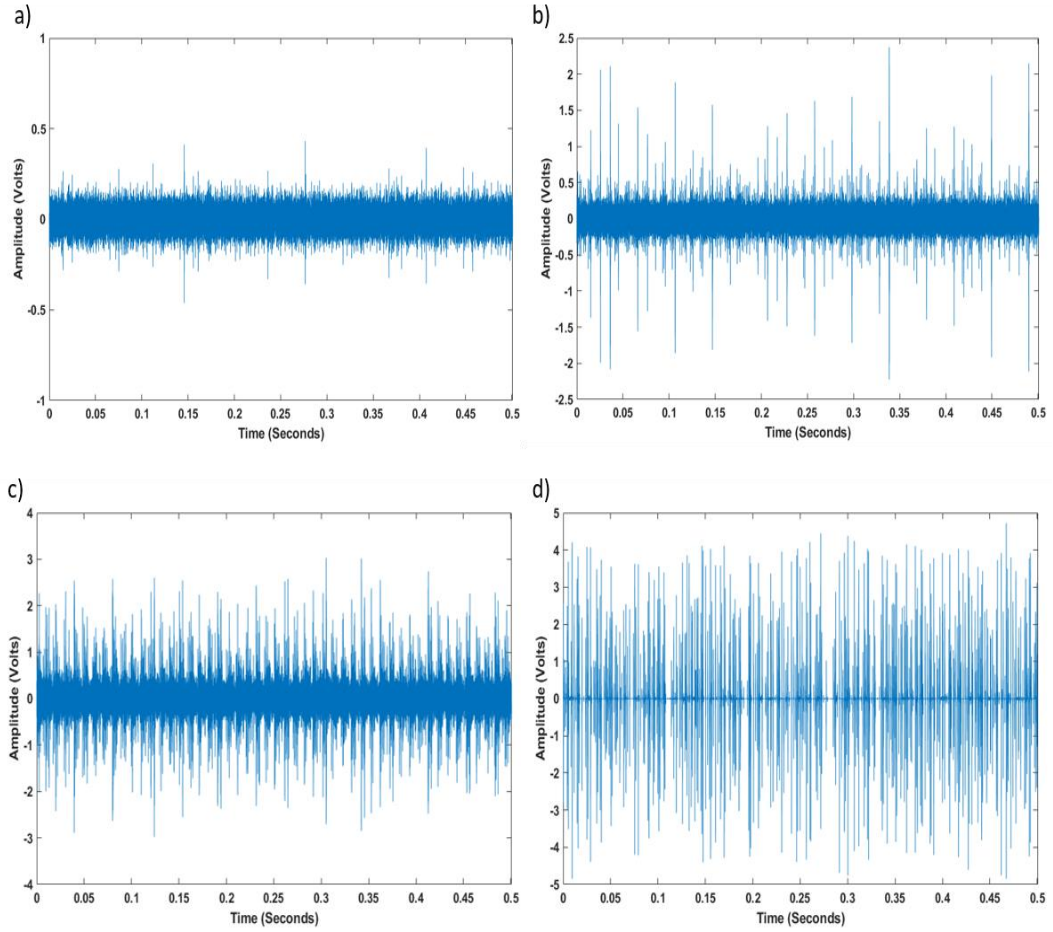

Figure 6-44: Raw signal from wavestreams at a) 58 hours, b) 62 hours 50 minutes, c) 64 hours and d) 64 hours 30 minutes.

Figure 6-45 shows shorter sections of the wavestreams from Figure 6-44 ‘c’ and ‘d’ with the data shown corresponding to one full rotation of the bearing. As the high-speed test rig theoretically runs at 5980rpm (99.66Hz), calculating it with the characteristic defect frequencies from Table 4-2, reveals with clarity what occurs within the signal vis-à-vis the bearing components. Observations from both plot ‘c’ reveals that at a time difference of 0.0014 of a seconds there tends to be transient bursts in relation with the BPFI, yet at different scales of amplitude. As the background noise levels diminish in plot ‘d’ due the clarity and strength of the transient bursts is shown and that is due to the high level of amplitude excited reaching above 3V, when compared to plot ‘a’ the amplitude levels do not surpass 0.5V.

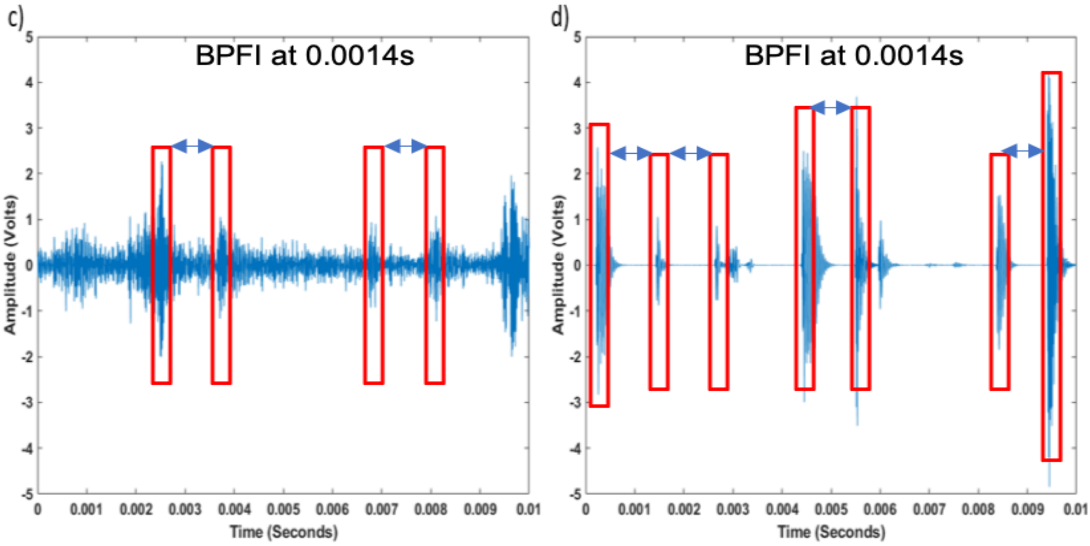

Figure 6-45: 0.01s of the wavestreams at c) 64 hours and d) 64 hours 30 minutes.

6.4.3 Short Time Fourier Transform (STFT) Analysis

The spectrogram of the same wavestreams from Figure 6-44 are presented in Figure 6-46. Observations from the plots correspond well with the positive half of the raw signal amplitude. Plot ‘a’ reveals strong energy output between 15-80kHz as well as secondary harmonics within the range of 95-160kHz, similarly to plot ‘b’ although at higher energy. Plots ‘b’, ‘c’ and ‘d’ presents clearer transient spikes similarly to its counterpart from the raw signal analysis and as the amplitude increases within the raw signal during different stages of the test, likewise the energy increases within the spectrogram for the same wavestreams. This could be caused by the amount of asperities due to the damage to the inner rolling and the time it takes for them to be pushed out of the raceway via fluid. Plot ‘d’ illustrates an immense amount of energy at higher frequency ranges due to the severity of the bearing damage at the end of the test.

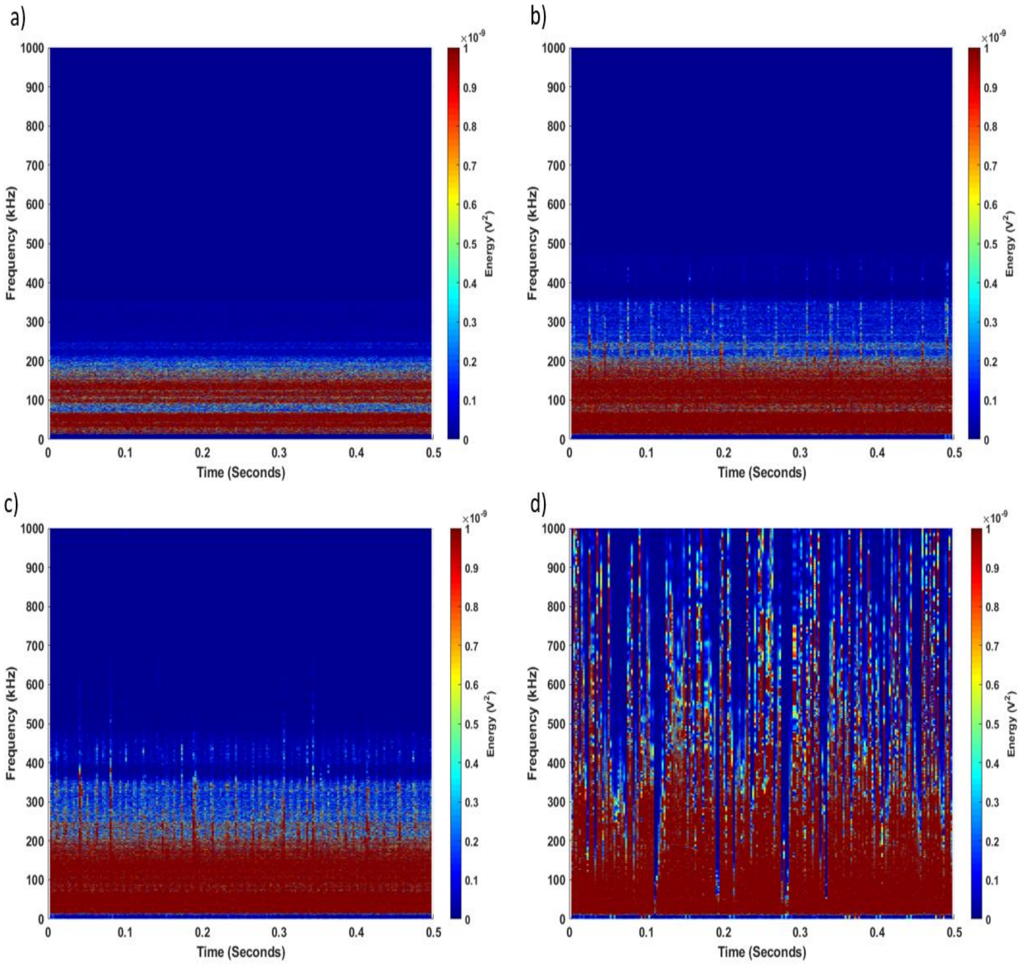

Figure 6-46: STFT Spectrogram from wavestreams at a) 58 hours, b) 62 hours 50 minutes, c) 64 hours and d) 64 hours 30 minutes.

Figure 6-47 demonstrates plots ‘c’ and ‘d’ from Figure 6-46 at shorter time to represent one full rotation of the bearing. Background noise levels dominate the signal in plot ‘c’, whether it is in the raw signal or frequency spectrum, it is clearly illustrated again, yet at 0.0024s, 0.008s and towards the end of the wavestream similarly to plot ‘c’ in Figure 6-45, the energy levels increase in frequency rising up to

500kHz. Plot ‘d’ demonstrates further details and correspondence of the transient bursts in plot ‘d’ from Figure 6-45. It even reveals the slightest bursts from the raw signal at 0.007s and 0.0075s.

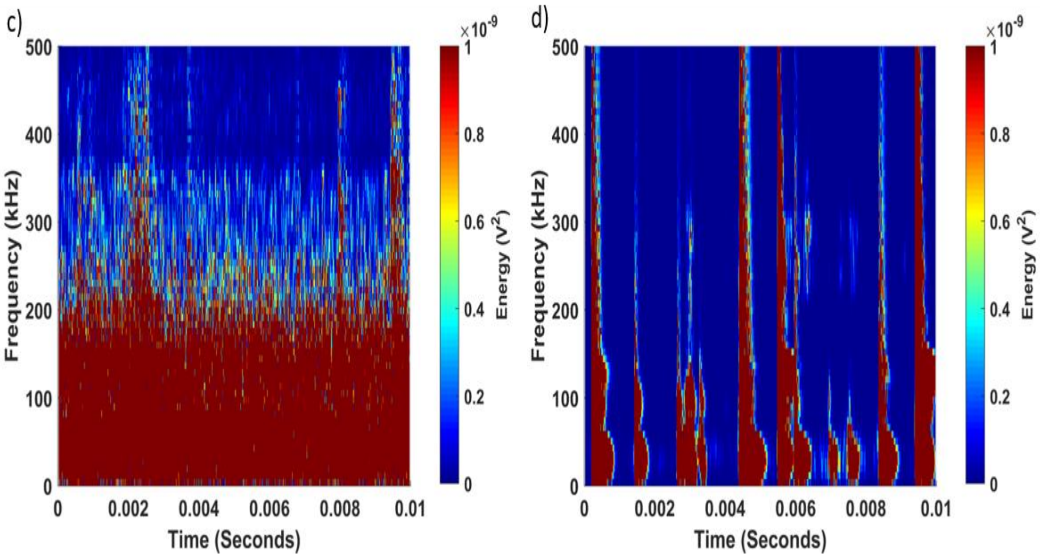

Figure 6-47: 0.01s spectrogram of the wavestreams c) 64 hours and d) 64 hours 30 minutes.

6.5 Second SKF NU202ECP Bearing Run to Failure Test Results

6.5.1 AE RMS Analysis

Figure 6-48 plots the AE RMS amplitude for the full duration of the test and Figure 6-49 represents a closer look at the results with annotations of specific wavestreams indicating significant variations in the AE RMS signal that will be discussed further in the raw signal and STFT analysis sections. A continuous, steady increase of RMS amplitude is observed on the test bearing. Towards the failure of the bearing, which is assumed at approximately 20 hours of running as designated between ‘b’ and ‘c’, the AE RMS values are close to the first SKF NU202ECP values as they range between 0.28-0.33V. There is also a clear indication from all three bearings at ‘c’ as to where the conditions have changed within the system, as all three signals tend to spike especially the Non-Drive End support bearing.

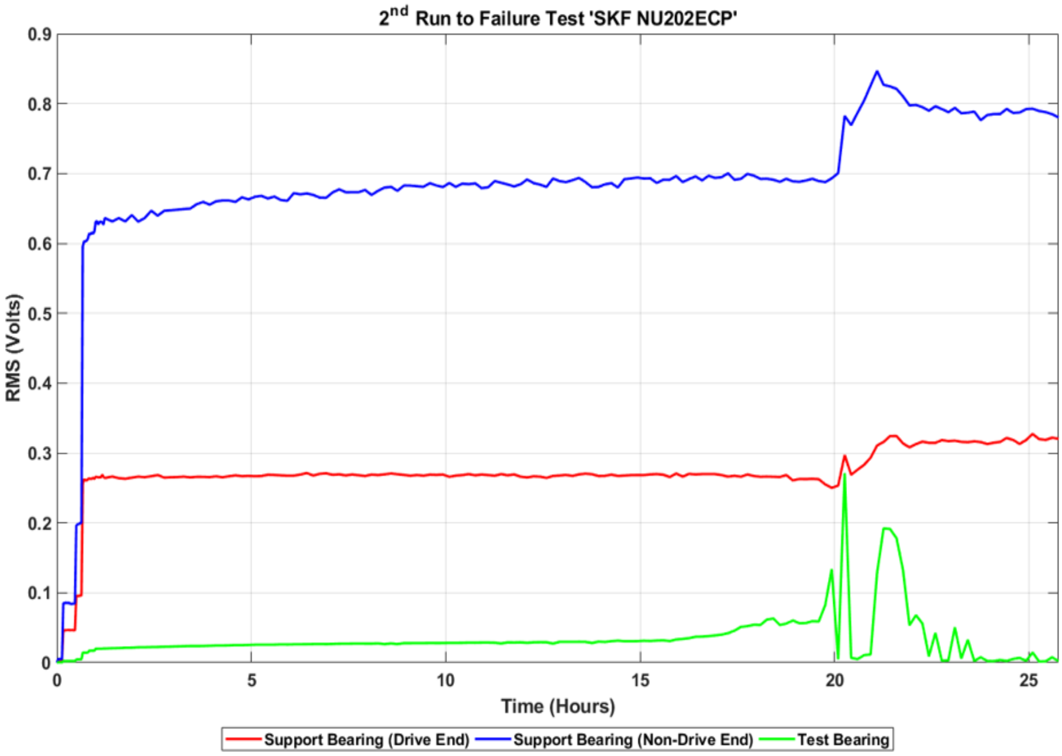

Figure 6-48: Second SKF NU202ECP Bearing Run to Failure Test data of RMS amplitude.

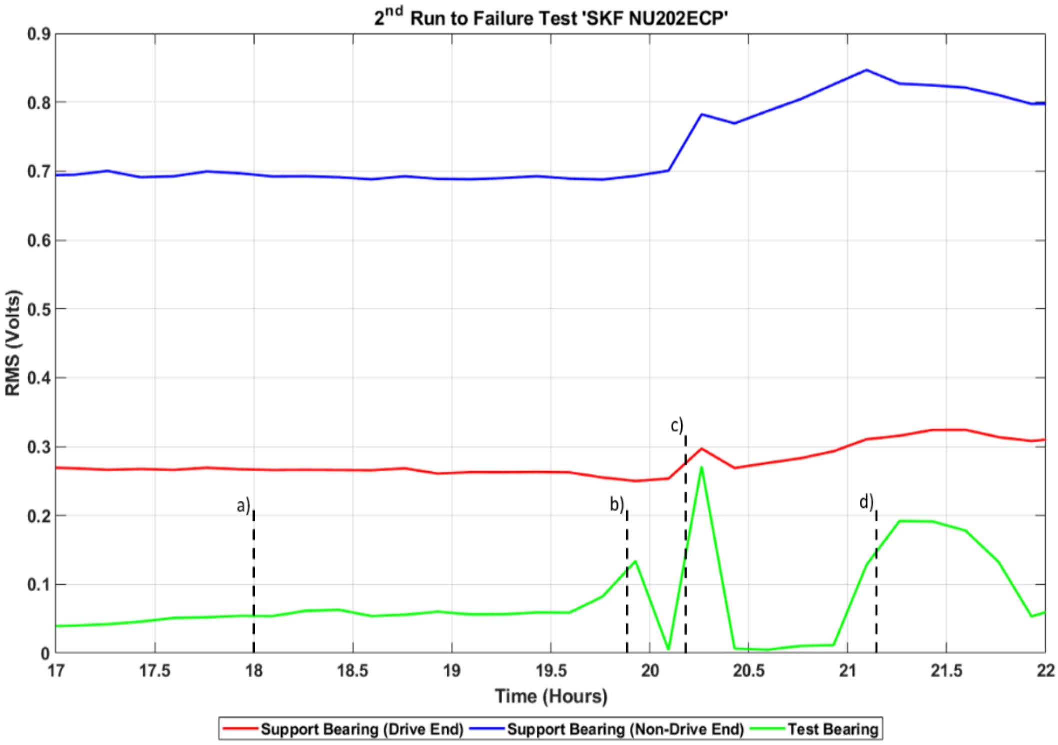

Figure 6-49: Annotations on magnified plot at 18 hours, b) 19 hours 50 minutes, c) 20 hours 10 minutes and d) 21 hours 10 minutes.

6.5.2 Raw Signal Analysis

The raw signal of the four chosen wavestreams indicated in Figure 6-49 are presented in Figure 6-50, once again each plot has its own unique amplitude scale to aid clarity. These wavestreams were selected at several stages of the test to compare the bearing condition results through raw signal analysis. Raw signals were analysed at prior stages of the test with some features in the signal yet no events exceeding the background noise, hence the first investigated wavestream is at 18 hours designation ‘a’. All plots reveal a sharp number of transient bursts, plot ‘a’ has a maximum amplitude of less than 1V, but as the AE RMS undergoes its first intense spike at position ‘b’ the amplitude output level triples its value. As for plots ‘c’ and ‘d’, where ‘c’ as discussed appears to be when the test bearing properly failed, evident periodicity of transient bursts can be clearly seen at highest levels of amplitude amongst all four plots. This may well be when the rolling elements passes through the recently damaged zone on a raceway. As the test continues to run further, the damage becomes smoother and an amount of debris may possibly be disposed or ejected from the area, providing plausible explanation for the reduction in amplitude in plot ‘d’ when compared to plot ‘c’.

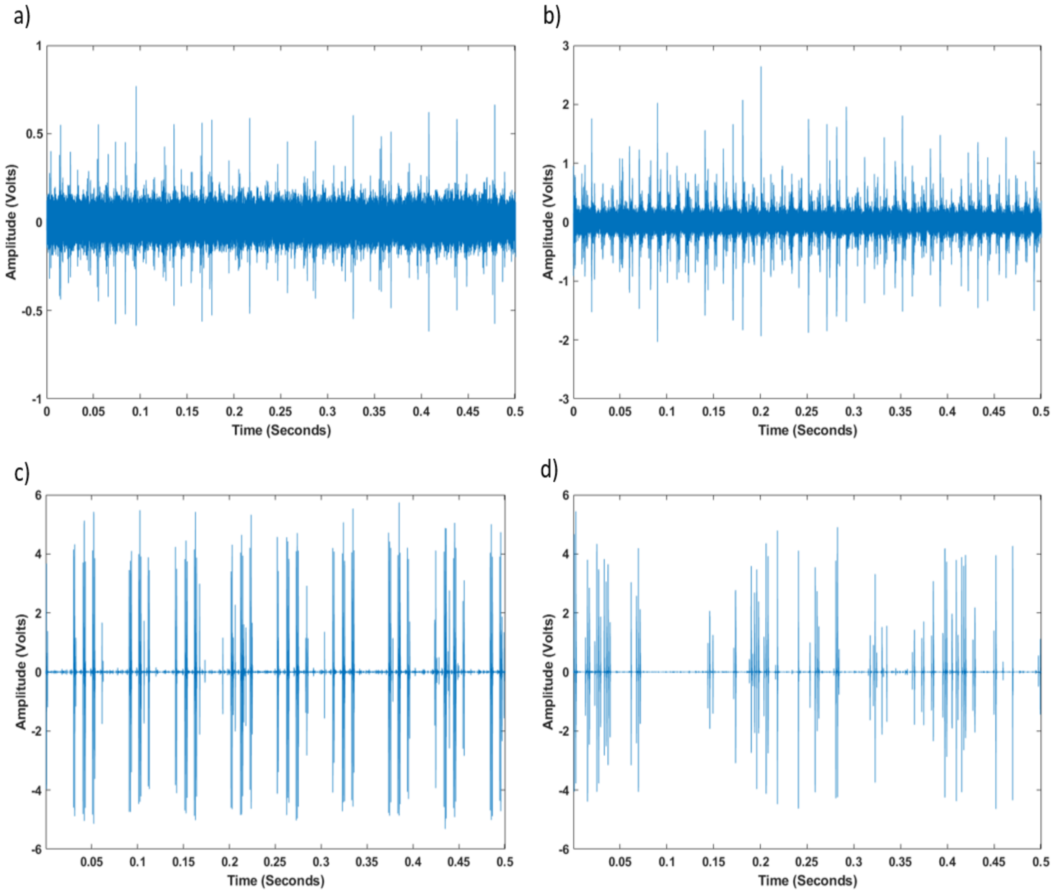

Figure 6-50: Raw signal from wavestreams at a) 18 hours, b) 19 hours 50 minutes, c) 20 hours 10 minutes and d) 21 hours 10 minutes.

Figure 6-51 demonstrates plots ‘b’ and ‘c’ from Figure 6-50. Plots ‘b’ and ‘c’ reveal a small portion of the original wavestream of 0.05s which represents 50 rotations of the bearing. Observations from both ‘b’ plots demonstrate the difference within the signals at two main stages of the tests as presumed initiation of the bearing failure. It can be seen in plot ‘d’ that higher transient bursts occur and there is a high SNR.

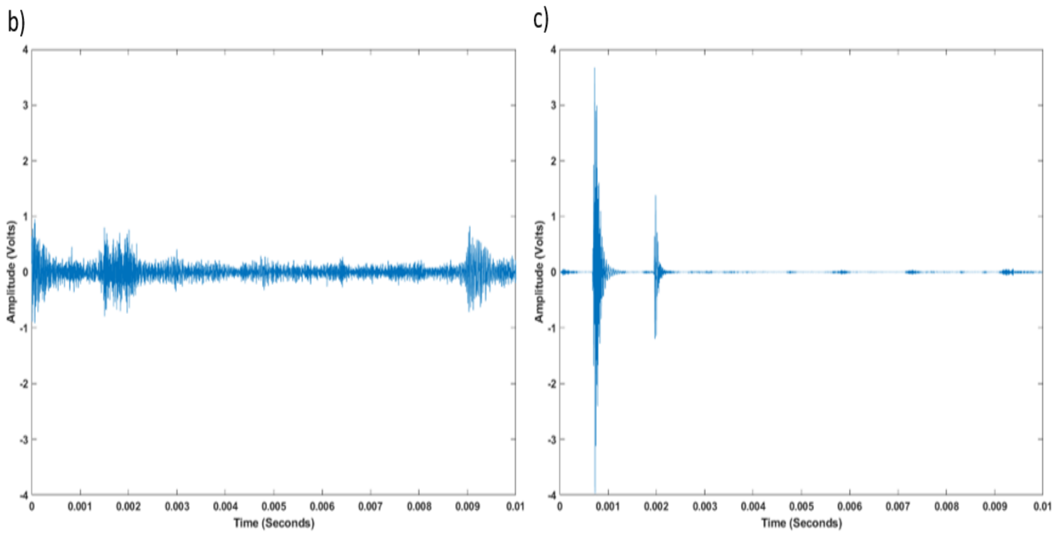

Figure 6-51: 0.01s of a wavestream at b) 19 hours 50 minutes and c) 20 hours 10 minutes.

6.5.3 Short Time Fourier Transform (STFT)

Spectrogram of the wavestreams from Figure 6-50 are shown in Figure 6-52. All plots display continuous energy within the frequency range of 260-280kHz, yet at different scales of magnitude. Plots ‘a’ and ‘b’ imply that levels of background noise still exists, as it dominates the frequency range up to 200kHz, while above that range the dictated periodic transients are clearer at higher ranges of frequencies reaching above 400kHz for the former and above 600kHz for the latter. Observations from plots ‘c’ and ‘d’ demonstrate superior frequency ranges reaching 1000kHz and due to the accumulated energy within the signal, the background noise is negligible. There is a strong correlation between the periodic transient bursts in plot ‘c’ from the raw signal analysis and plot ‘c’ of its spectrogram. Moreover, plot ‘c’ reveals high energy at frequencies between 260-290kHz across the whole wavestream similarly observed in plot ‘d’ at a lower scale of energy, which is very close to the resonant frequency of the AE sensor in use.

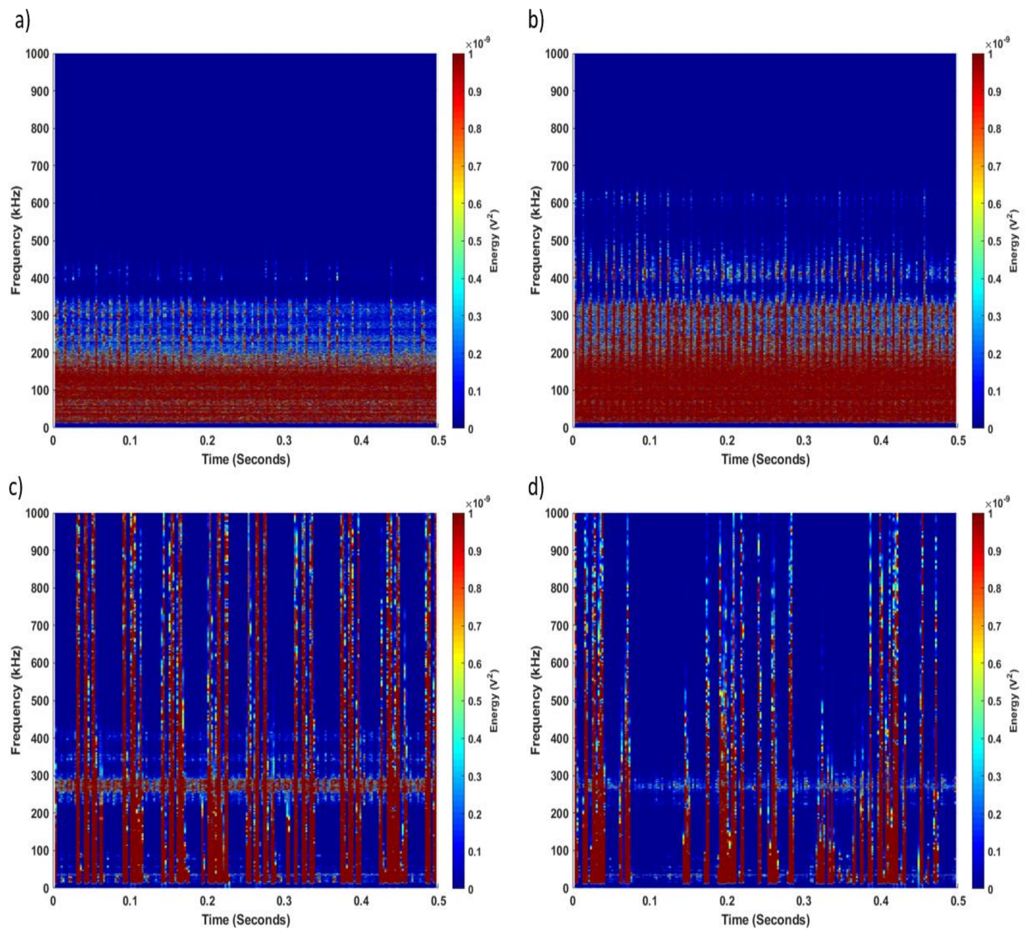

Figure 6-52: STFT Spectrogram from wavestreams at a) 18 hours, b) 19 hours 50 minutes, c) 20 hours 10 minutes and d) 21 hours 10 minutes.

Figure 6-53 shows plots ‘b’ and ‘c’ from Figure 6-52 at a shorter duration of 0.01s. Plot ‘b’ demonstrates similar high energy from background noise levels covering the frequency bands up to 220kHz, also high magnitudes of energy encompassing the frequency band at 0.002s parallel to its raw signal analysis. Plot ‘c’ reveals the two main transient bursts illustrated in plot ‘c’ from Figure 6-51, in addition to that, it clearly signifies the smaller bursts of transients across the wavestream in more detail at frequencies of 260-300kHz similarly observed in plot ‘c’ in Figure 6-52, the observed frequencies fall within the sensor’s resonant frequency spectral range of 200-350kHz. These bursts of energy are in sorts evenly spaced with correspondence to the BPFI at 0.0014s, which proves that spectrogram is an enhanced method of analysis with regards to basic raw signal analysis.

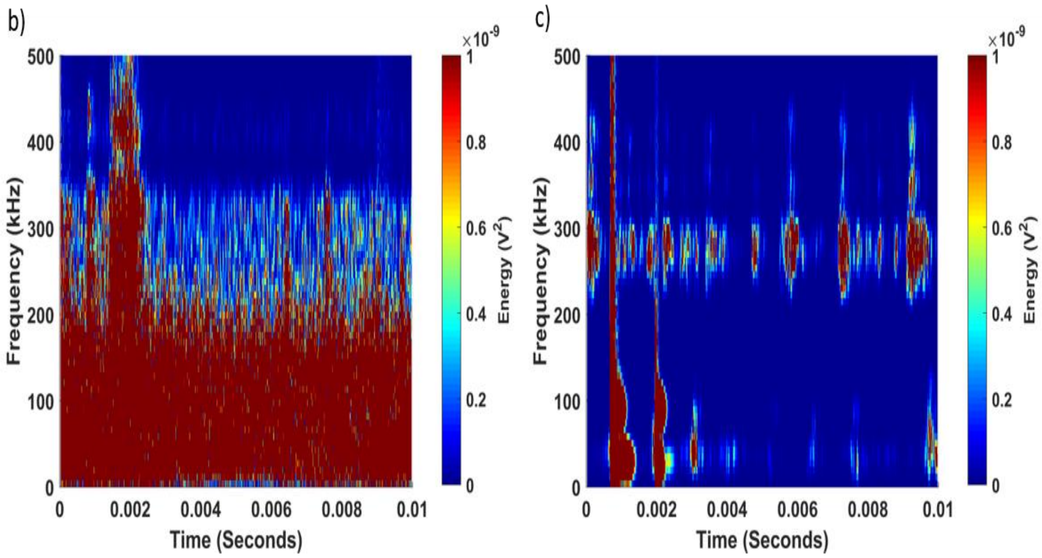

Figure 6-53: 0.01s spectrogram of the wavestreams at b) 19 hours 50 minutes and c) 20 hours 10 minutes.

6.6 First SKF NU202ECP/C3 Bearing Run to Failure Test Results

6.6.1 AE RMS Analysis

The full duration of the test is plotted in Figure 6-54 for the AE RMS results, while Figure 6-55 shows the RMS signal over the final 5.5 hours of the test, with the locations of several wavestreams identified which indicate significant variations within the AE RMS signal. The obvious influence by increasing speed and load on the RMS signal is observed for all the bearings, once again similarly to the two previous test results. As it can be seen towards the end of the test at position ‘a’ the RMS value is within similar level of the previous two tests of 0.3V, after that as the test bearing condition begins to change and the RMS amplitude continues to spike at higher levels at position ‘c’, it is correspondingly resonated through both support bearings, with a clear higher amplitude for the Non-Drive End support bearing, as has been observed in the previous tests. It has become evident from the results across all three tests, that even if there was an issue or flaw with the test bearings’ sensor readings via the AEWin systems interface, the other two sensors from the support bearings housings could definitely indicate any change to the test bearing’s conditions. Whilst this may lead to slight delays in identifying bearing damage, this result is nevertheless very beneficial.

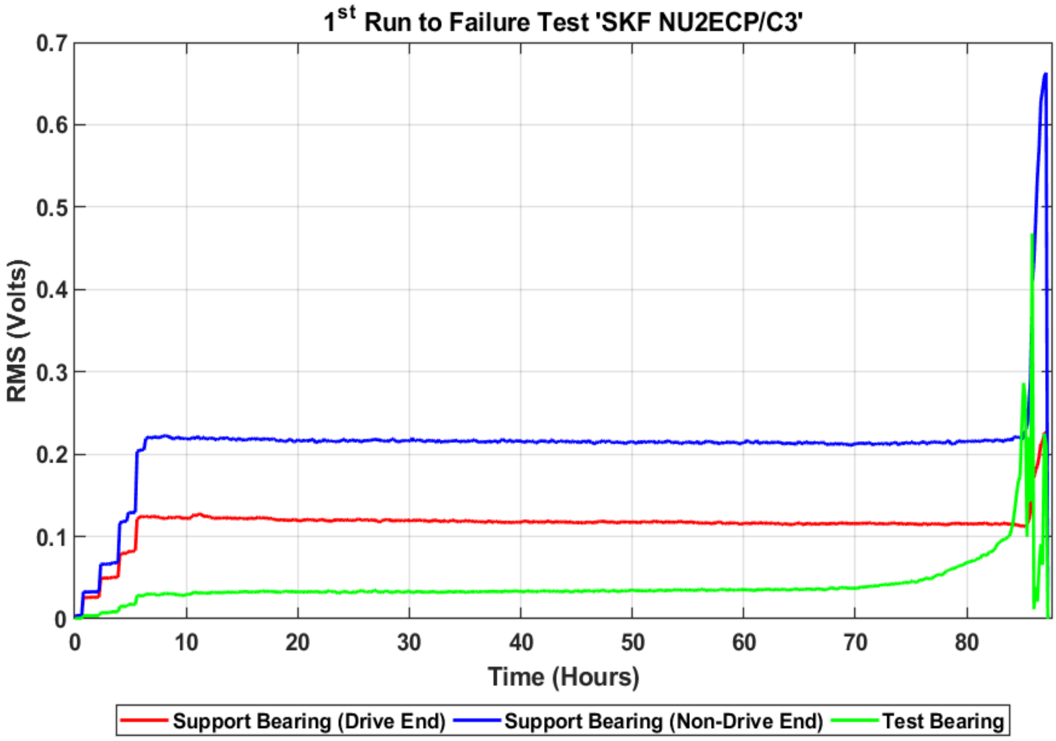

Figure 6-54: First SKF NU202ECP/C3 Bearing Run to Failure Test data of RMS amplitude.

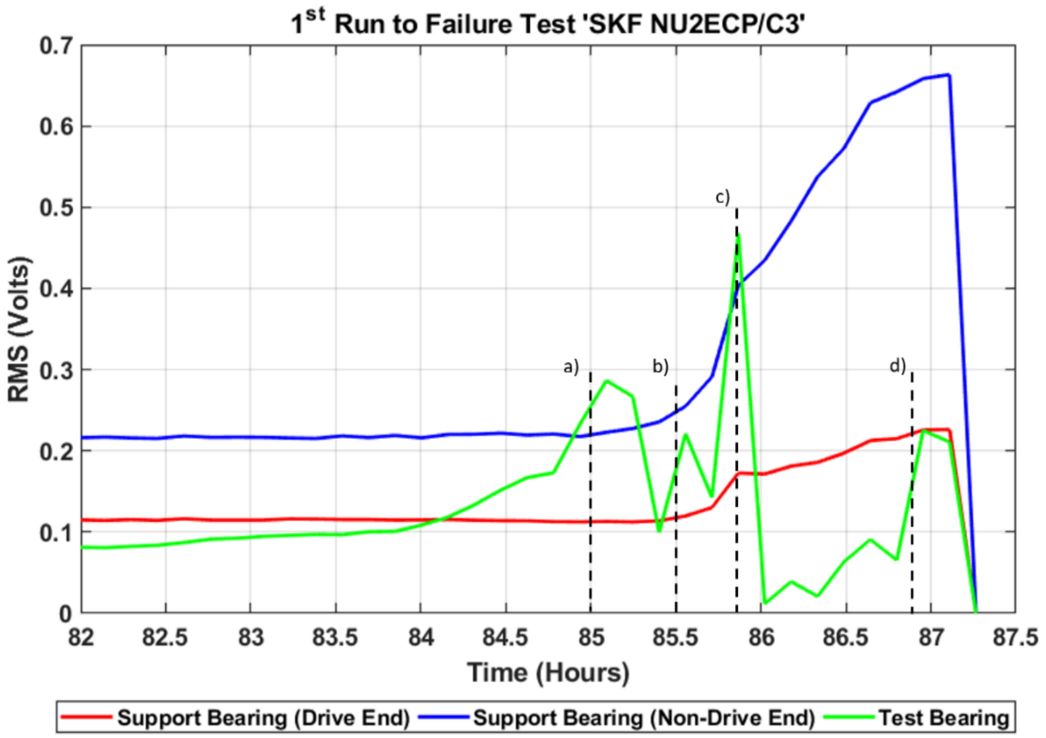

Figure 6-55: Annotations on magnified plot at a) 85 hours, b) 85 hours 30 minutes, c) 85 hours 50 minutes and d) 86 hours 50 minutes.

6.6.2 Raw Signal Analysis

The raw signal of the four wavestreams considered from Figure 6-55 are shown in Figure 6-56, for each plot a distinctive amplitude scale has been selected to improve their illustration. As there were no significant events beyond the background noise levels till 82 hours of the test, the preferred wavestreams were past that duration to assess better data, hence the first considered wavestream is at 85 hours designation ‘a’ in Figure 6-55. All plots reveal numerous transient bursts, even though the transients in plot ‘a’ are clearly pronounced yet the background noise still heavily dictates the amplitude signal range ±1V. As the test continues further and the deterioration of the test bearing worsens, the emergence of high amplitude levels is clearer as well as the periodicity of the transient especially in plot ‘c’ becomes well-defined. Similarly to the second NU202ECP test, as both test bearings endured parallel damage to the inner raceways, plots ‘c’ from the raw signal analysis from both tests reveal comparable results as to the amplitude levels along with them being higher than plots ‘d’ from the same tests.

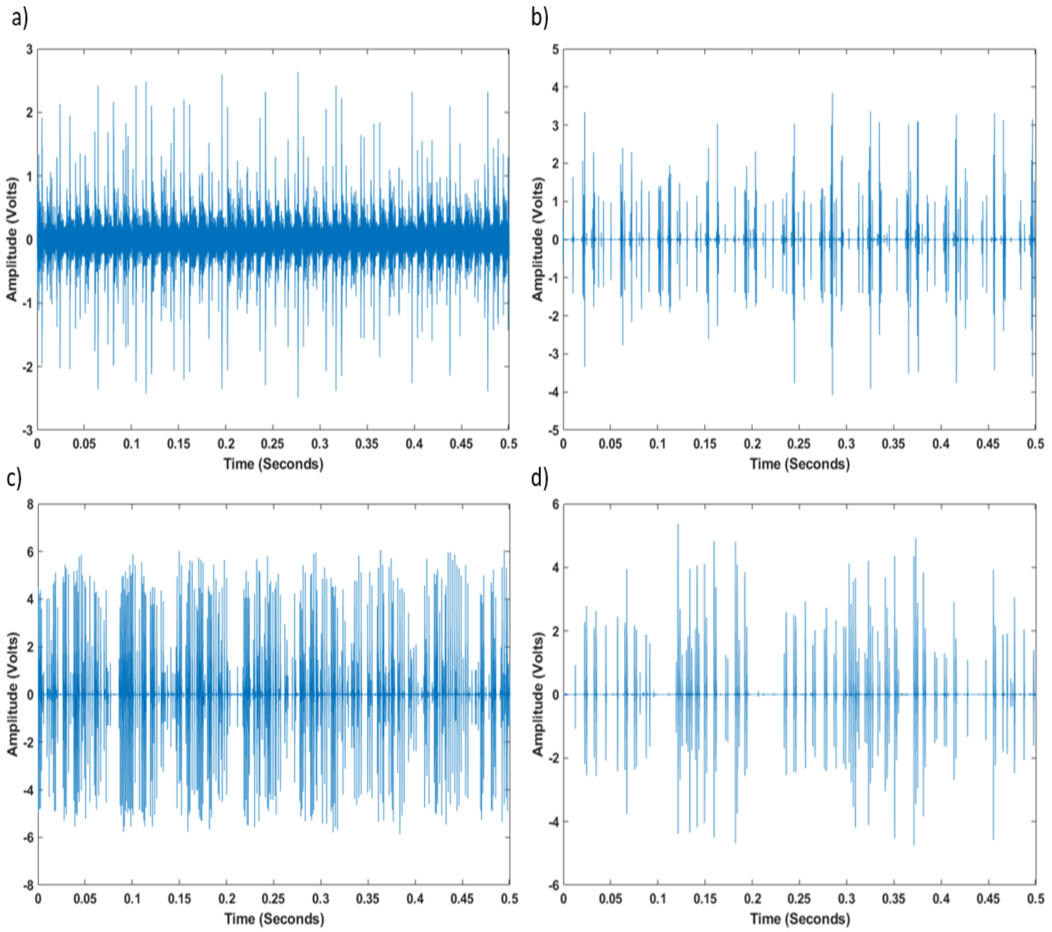

Figure 6-56: Raw signal from wavestreams at a) 85 hours, b) 85 hours 30 minutes, c) 85 hours 50 minutes and d) 86 hours 50 minutes.

Figure 6-57 shows portions of the data from plots ‘a’ and ‘c’ from Figure 6-56 at a shorter time duration. Plot ‘a’ shows just how the signal transforms within less than an hour when compared to plot ‘c’. Plot ‘c’ reveals 6 clear periodic transient bursts at BPFI of 0.0014s spaced between them and how the amplitude decreases as the signal attenuates from approximately 4.5V down to 1V, this is due to a defect within the inner raceway. The absence of the BPFO could be due to the fact that the main damage occurred on the inner race, so the amplitude is high when the damaged section of inner race goes through the loaded zone, and low when the undamaged section is in the loaded zone, thus higher clear visualisation of the BPFI is only detected.

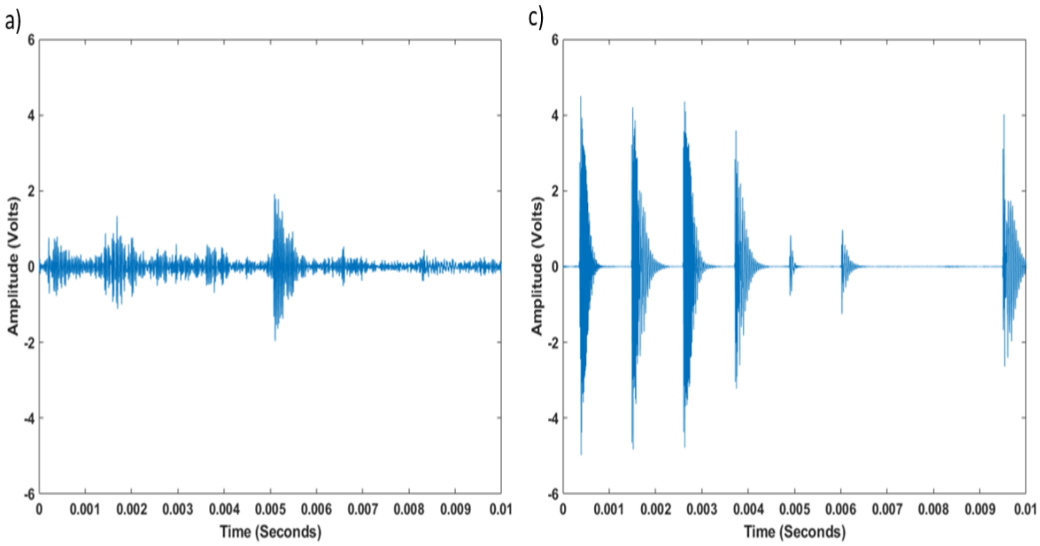

Figure 6-57: 0.01s of a wavestream at a) 85 hours and c) 85 hours 50 minutes.

6.6.3 Short Time Fourier Transform (STFT)

The spectrograms of the same wavestreams from Figure 6-56 are presented in Figure 6-58. Observations from the plots correspond well with the positive half of the raw signal amplitude. Plot ‘a’ reveals strong energy output between 15-70kHz as well as what could well be a secondary harmonic within the range of 80-130kHz. Plots ‘b’ and ‘d’ presents clearer and finer transient spikes similarly to its counterpart from the raw signal analysis and as the amplitude increases within the raw signal during different stages of the test, likewise the energy increases within the spectrogram for the same wavestreams. Plot ‘c’ demonstrates an immense amount of energy at higher frequency ranges due to the damage severity.

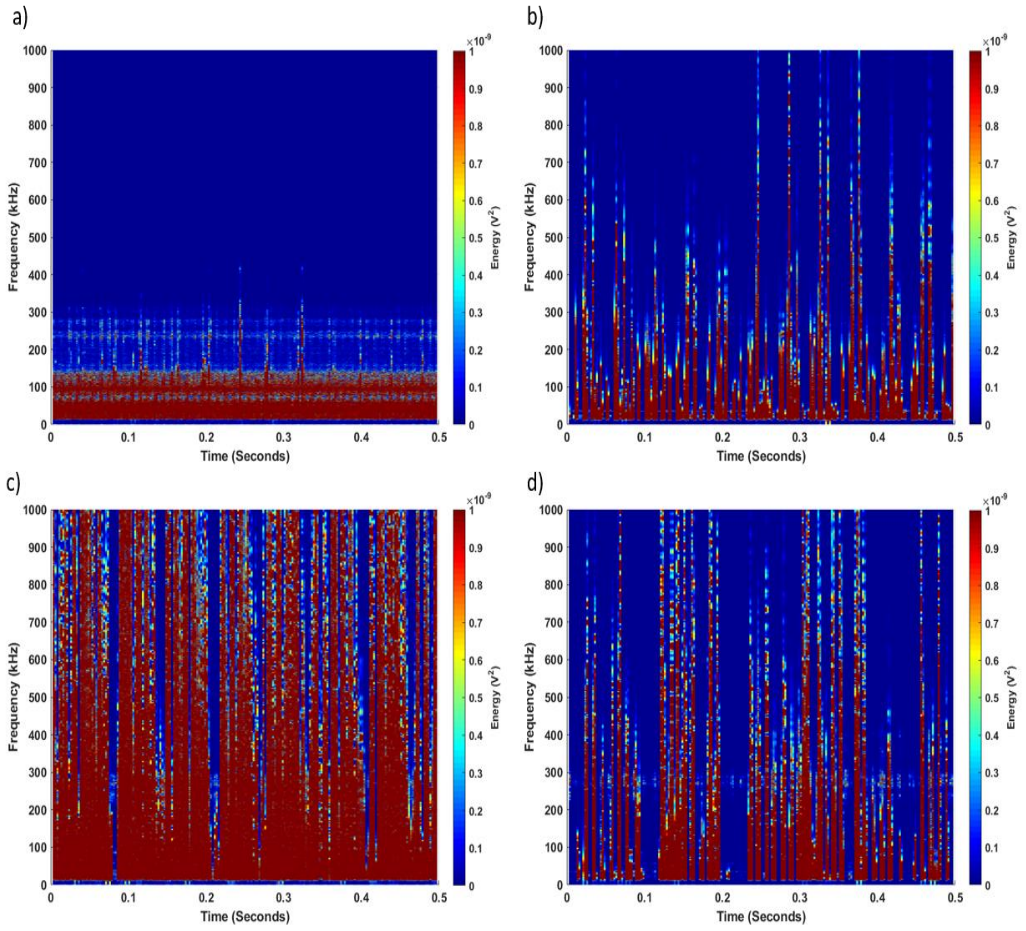

Figure 6-58: : STFT Spectrogram from wavestreams at a) 85 hours, b) 85 hours 30 minutes, c) 85 hours 50 minutes and d) 86 hours 50 minutes.

Figure 6-59 demonstrates plots ‘a’ and ‘c’ from Figure 6-58 at 0.01s duration. Plot ‘a’ demonstrates similar high energy from background noise levels covering the frequency bands up to 160kHz, also high magnitudes of energy covering the whole frequency band at 0.052s parallel to its raw signal analysis as well as two medium level spikes of energy just before 0.002s rising up to 300kHz. Plot ‘c’ illustrates the 6 periodic transient bursts from plot ‘c’ from Figure 6-57 and equally shows how the energy decreases as well as the frequency bands from the first four transient bursts to the last two.

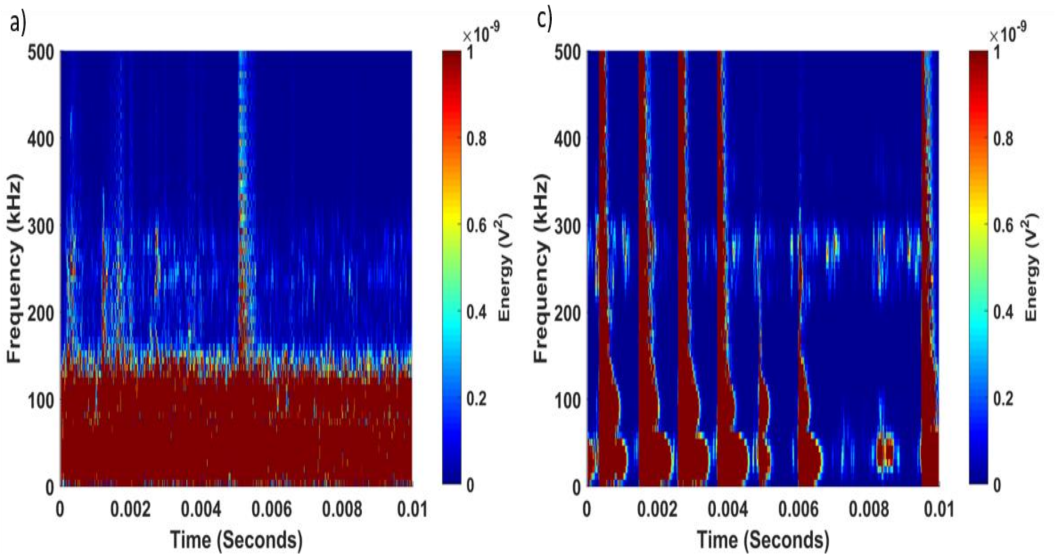

Figure 6-59: 0.01s spectrogram of the wavestreams at a) 85 hours and c) 85 hours 50 minutes.

6.7 Second SKF NU202ECP/C3 Bearing Run to Failure Test Results

6.7.1 AE RMS Analysis

Figure 6-60 plots the AE RMS amplitude for the full duration of the test and as the plot does not reveal similar AE RMS fluctuation towards the end of the test, it is unnecessary to plot it again in a closer point of view as seen in the previous test AE RMS analysis. The test was stopped due to extreme sharp noise close to the 25 hours mark. Unlike the abovementioned tests, usually an intensification of the AE RMS signal revealed via the AEWin systems interface implies an imminent failure, this was not the case for this test. Once the bearing was dismantled and inspected, marks of inner raceway deterioration were observed as shown in Figure 6-36 and Figure 6-37. A continuous, steady rise of AE RMS amplitude is observed on the Non-Drive End support bearing, as the AE RMS signal values for both support bearings are within the same levels of the second NU202ECP Run to Failure values of approximately 0.9V for the Non-Drive End support bearing and 0.3V for the Drive End support bearing. This clearly validates what has been mentioned in section 5.4, that the support bearings sensor could verify change within the system, even if the test bearing sensor may have not been reading and acquiring data accurately as it seems in Figure 6-60.

Similar results were concluded by Cockerill (2017), as the shaft deflection increased with load during the experiment, the amount of energy transmitted from the support bearings via the shaft to the test bearing increased dramatically. Then it was demonstrated that although the data is collected from sensors connected to the test bearing, the signals produced by a single bearing are also influenced by nearby bearings which may prove problematic when trying to diagnose failure location in the field. Hence, it is possible not only validate the readings from the test bearing sensor but also be a backup sensor if not adding a second sensor to the test bearing, to compare the results or in case one fails during the test, or if possible as a measure of redundancy. Annotations ‘a’, ‘b’ and ‘c’ are chosen at 5, 15 and 24 hours 40 minutes respectively for further processing. Annotation ‘a’ was chosen by running the code After each RMS plot, to find a differentiation within the signal, for data within the numerous times during the test for example at 3 hours and 4 hours and so on, or where observed from the plot. Yet there was no solid data before 5 hours during the run to failure tests, as well as after. Yet the differentiation demonstrated at both support bearings before the 5 hours mark was due to the speed increment increase.

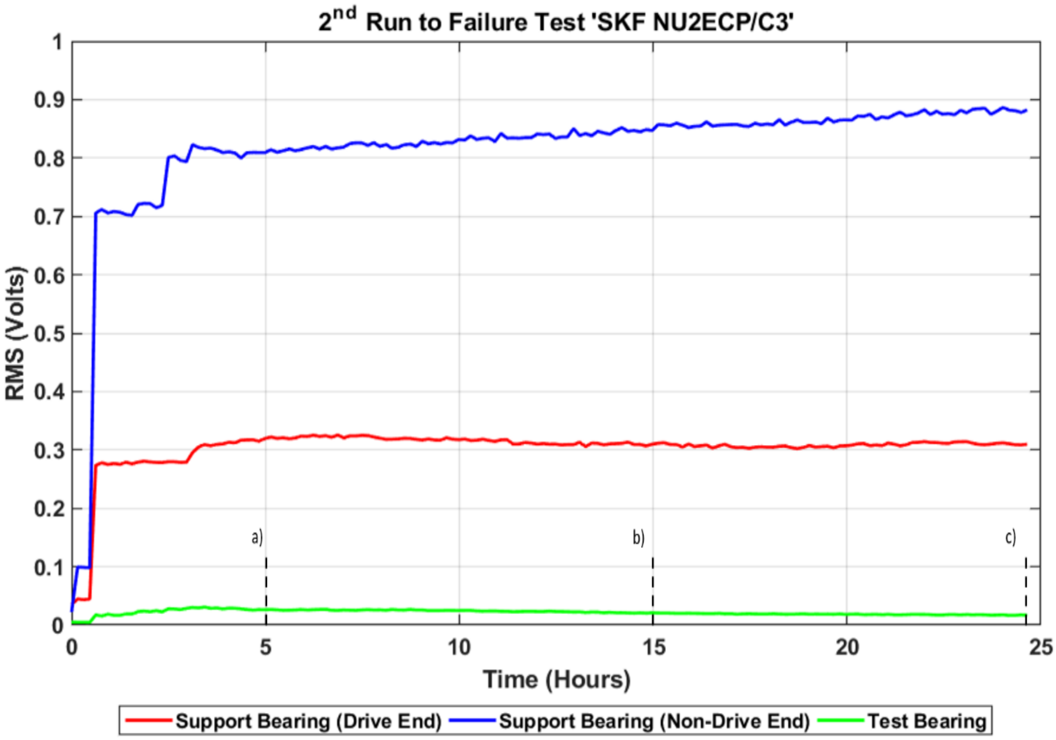

Figure 6-60: Second SKF NU202ECP/C3 Bearing Run to Failure Test data of RMS amplitude.

6.7.2 Raw Signal Analysis

The raw signal of the selected wavestreams from Figure 6-60 are demonstrated in Figure 6-61, all plots share the same amplitude scale of 0.2V. These wavestreams were chosen at different stages of the test to show if there is any change in the test bearing condition. The raw signals from all three plots reveal levels of background noise, although plot ‘a’ at the highest levels of amplitude. No significant details from the signal could be obtained as the continuous background level of noise dominates the signal, the transient bursts are only clear due to amplitude scale used for these plots. Hence no further analysis will be carried out for the same wavestreams at shorter period similar to the previous tests.

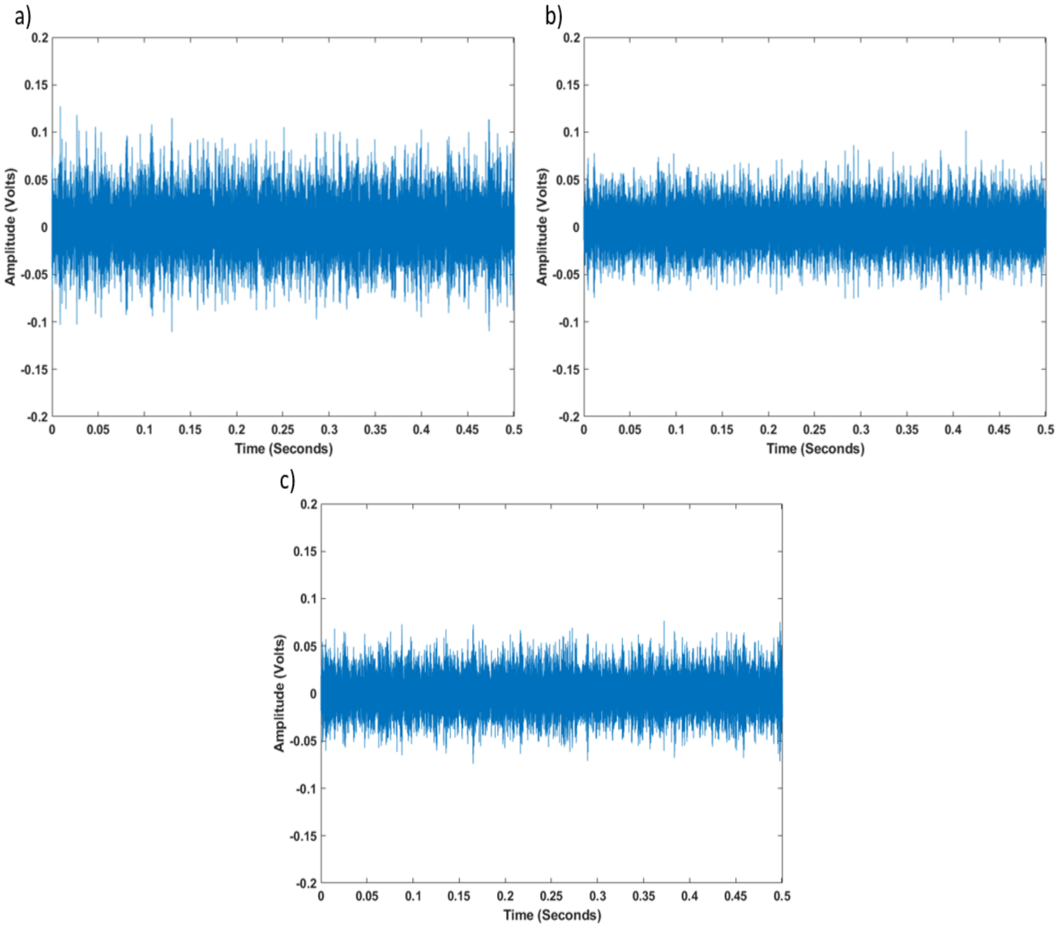

Figure 6-61: Raw signal from wavestreams at a) 5 hours, b) 15 hours and c) 24 hours 40minutes.

Figure 6-62 shows short sections of the data from plots ‘a’, ’b’ and ‘c’ of Figure 6-61. All plots are within 0.25V of amplitude scale which is very small when compared with the previous 0.01s raw signal analysis. The bursts within all three plots are still distinct even at extremely low levels of amplitude, yet not as well separated from one another to clearly define what they represent.

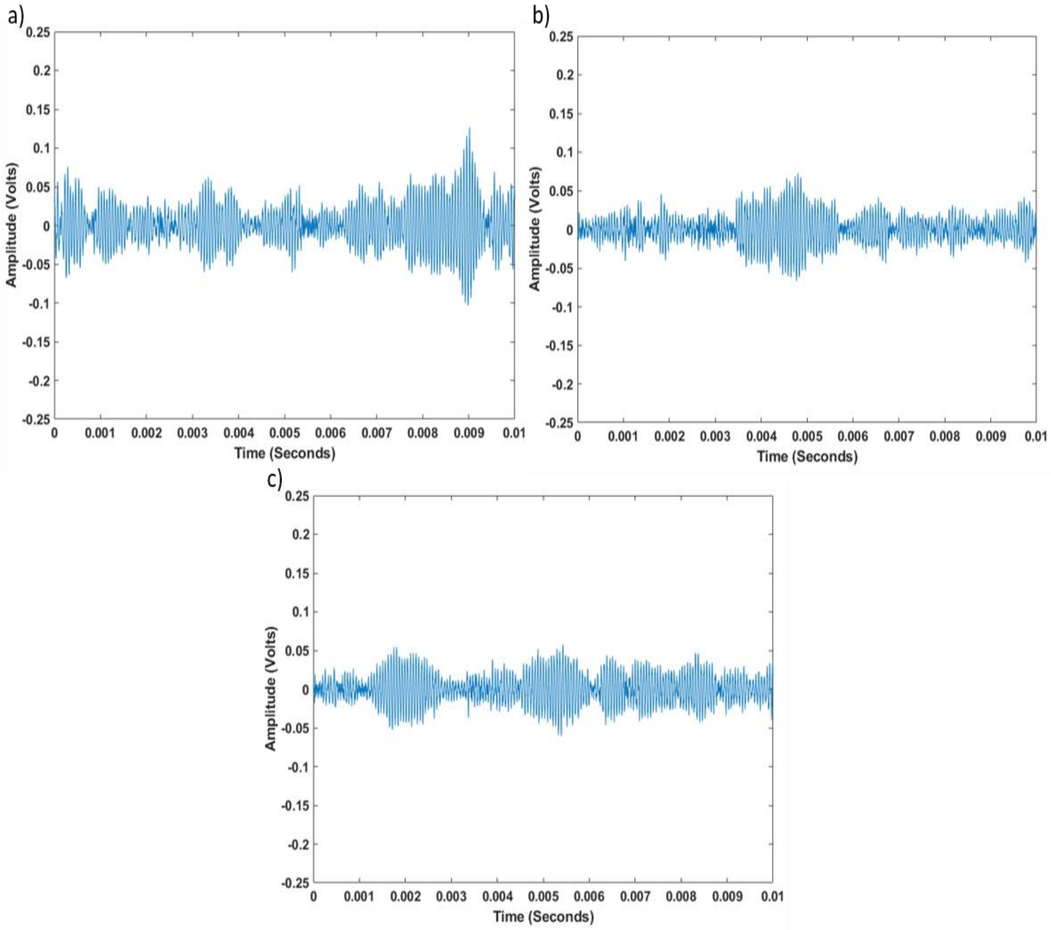

Figure 6-62: 0.01s of a wavestream at a) 5 hours, b) 15 hours and c) 24 hours 40 minutes.

6.7.3 Short Time Fourier Transform (STFT)

Spectrogram of the wavestreams from Figure 6-61 are shown in Figure 6-63. All plots exhibit low continuous energy in two frequency ranges, stronger at 100kHz yet at lower levels of energy at 200kHz, at different ranges of energy. The shorter window of the spectrogram did not reveal anything significant to plot nor mention, other than the high levels of background noise.

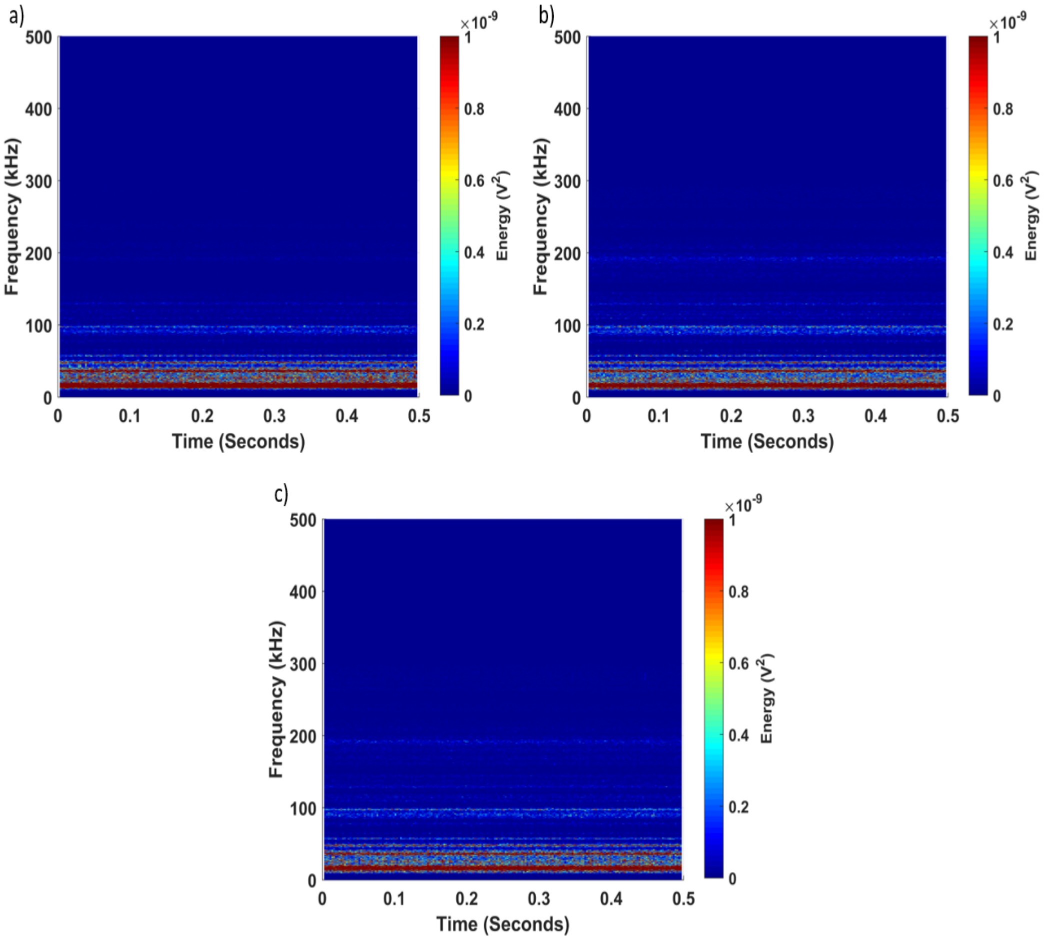

Figure 6-63: STFT Spectrogram from wavestreams at a) 5 hours, b) 15 hours and c) 24 hours 40 minutes.

Figure 6-64 demonstrates plots ‘a’, ’b’ and ‘c’ from Figure 6-63. All plots display high energy levels at low frequency bandwidth between 15-60kHz and low levels of energy at 100kHz. While, plots ‘b’ and ‘c’ continue to display lower levels of energy at 200kHz. This could perhaps be caused by coupling failure of the AE sensor mounted on the test bearing housing.

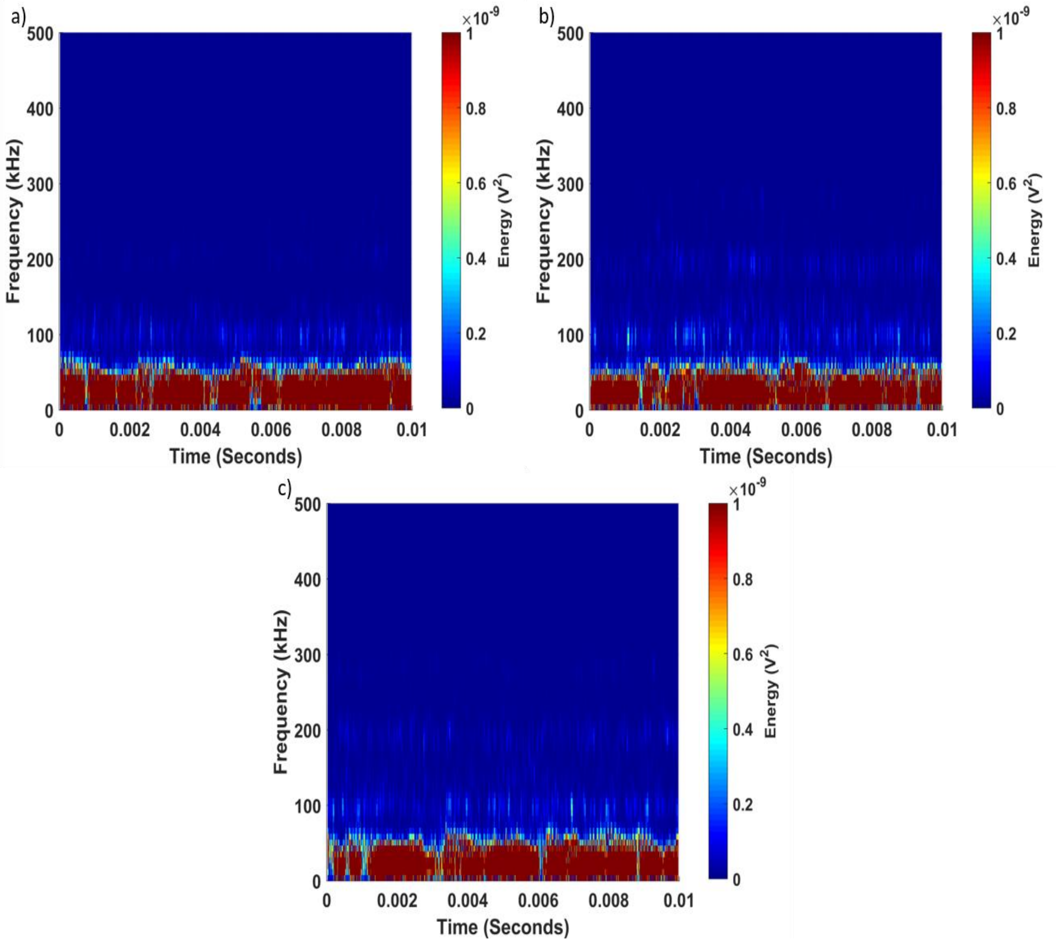

Figure 6-64: 0.01s spectrogram of the wavestreams at a) 5 hours, b) 15 hours and c) 24 hours 40 minutes.

6.8 First Budget Bearing Run to Failure Test Results

6.8.1 AE RMS Analysis

Figure 6-65 plots the AE RMS amplitude for the full duration of the test and as the designated wavestreams are spread across the whole test due to its results, four annotations are represented within it for the selected wavestreams at ‘a’, ‘b’, ‘c’ and ‘d’ for 6, 10, 20 and 22 hours throughout the test, representative of significant increases within the AE RMS signal that will be discussed further in the raw signal and STFT analysis sections. As soon as the required speed and loads are achieved, a continuous intense increase of RMS amplitude is observed for the test bearing till the end of the test. While both support bearings area steady throughout the test, there is a clear difference as the Non-Drive End support bearing AE RMS starts to rise steadily contrary to the Drive-End support bearing, similarly observed for all previous tests. As this was the first attempt for a budget bearing the test was stopped due to the ongoing surge of AE RMS levels on the test bearing observed via the AEWin system interface, as there were no similar symptoms to the previous tests where the AE RMS signal spikes significantly (excluding the second NU202ECP/C3 due to the sensors' misbehaviour). These designated marks during the test were chosen after each RMS plot, observation of where there is a major change within the RMS signal and then run the code for raw signal to identify those changes. As for Fig 6-65 there were no major effect to the raw signal at "a" as well as "b".

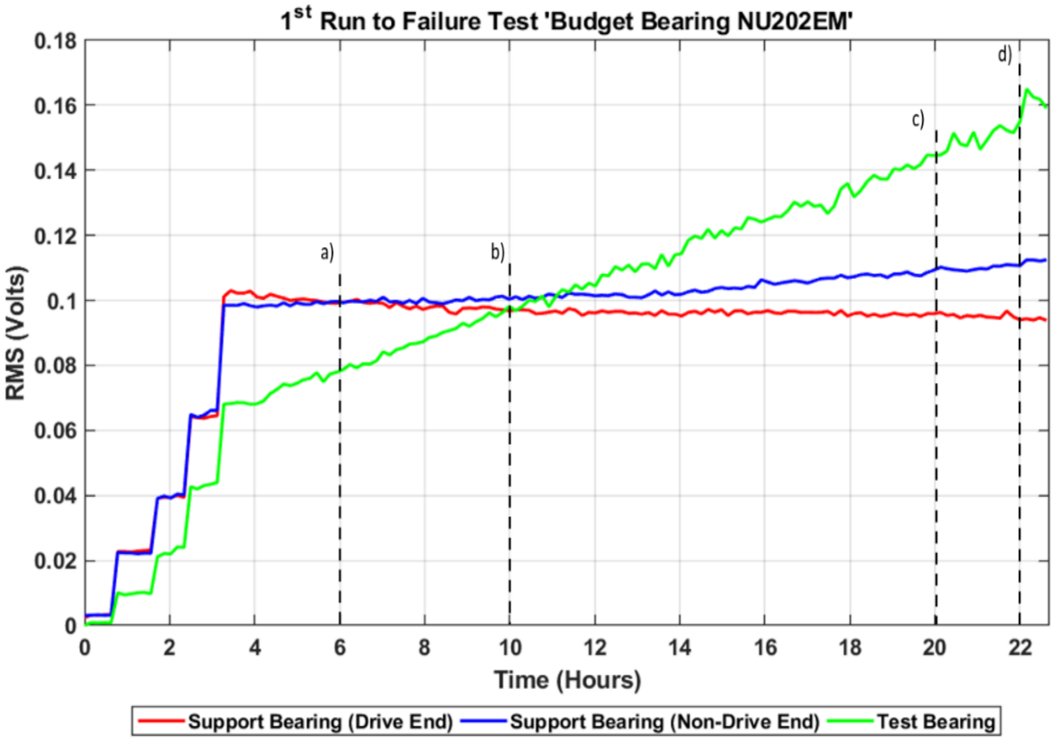

Figure 6-65: First Budget Bearing Run to Failure Test data of RMS amplitude.

6.8.2 Raw Signal Analysis

The raw signal of the four wavestreams considered from Figure 6-65 are shown in Figure 6-66, for each plot a distinctive amplitude scale has been selected to improve their visualisation. All four plots are dictated by the background noise levels at ±0.5V and the purpose of having a lengthy time span between designation 'b' and 'c' at 10 hours and 20 hours respectively is shown in the plots as nothing meaningful changes. Although the appearance of transient bursts occurs on all plots at a low level of amplitude, it is found reasonable as the AE RMS levels never surpassed the 0.18V mark, unlike all the previous tests excluding the second NU202ECP/C3, the AE RMS levels of the test bearings were between the ranges of 2.8-0.48V hence their raw signal transients were at higher levels of amplitude. Plots ‘c’ and ‘d’ represent two hours apart at the latest stage of the test, still the background noise masks the same levels of amplitude yet at designation ‘d’ the transient bursts are slightly stronger.

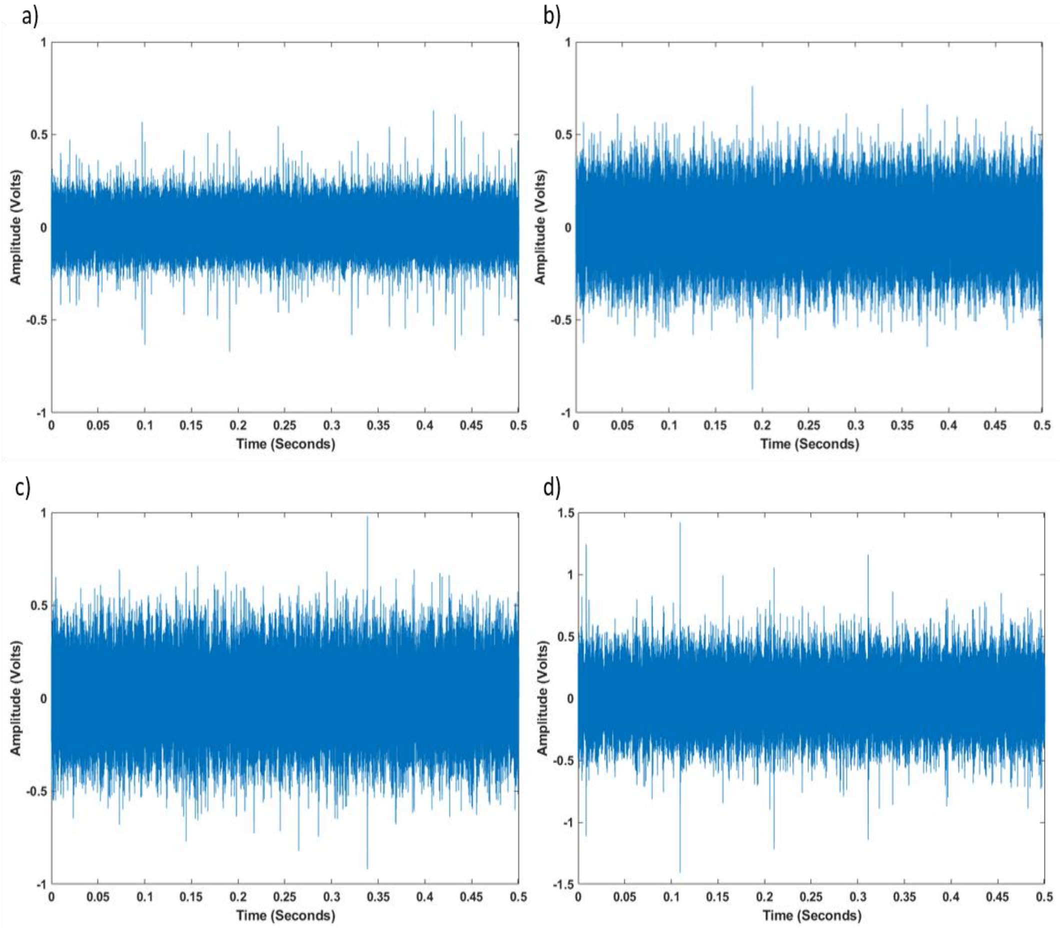

Figure 6-66: Raw signal from wavestreams at a) 6 hours, b) 10 hours, c) 20 hours and d) 22 hours.

Figure 6-67 demonstrates plots ‘c’ and ‘d’ from Figure 6-66 at a shorter time duration. Of note, the characteristic defect frequencies are slightly different for the budget bearing due to its geometry as shown in Table 4-2. Although the signals are masked by the background noise levels, plot ‘c’ reveals periodic transient bursts at very low amplitudes at the BPFO of 0.0022s intervals, sandwiched between them although still low, yet higher amplitude levels at the BPFI of 0.0015s. Plot ‘d’ represents higher levels of transient bursts at time intervals of 0.0015s with correspondence to the BPFI.

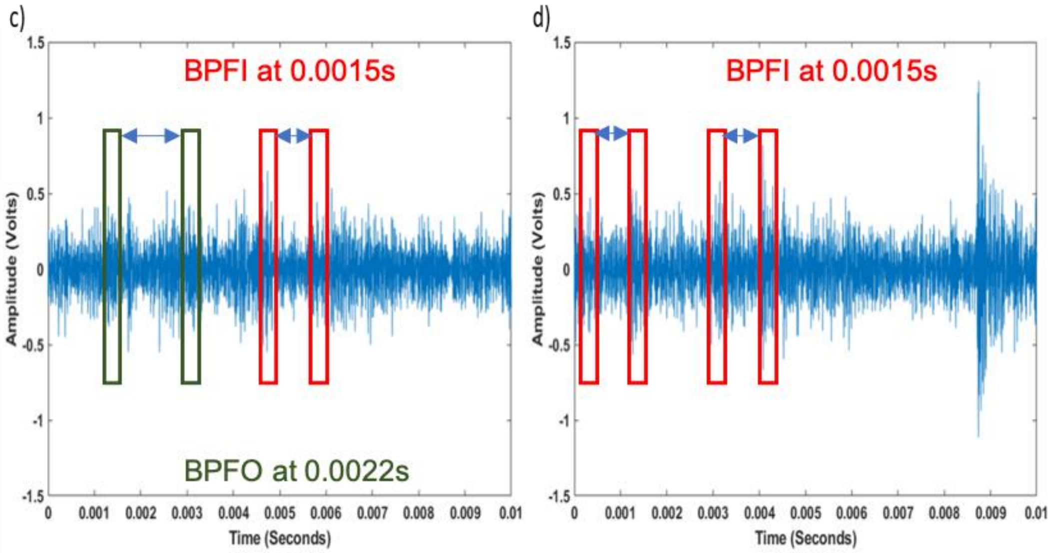

Figure 6-67: 0.01s of a wavestream at c) 20 hours and d) 22 hours.

6.8.3 Short Time Fourier Transform (STFT)

Spectrogram of the wavestreams from Figure 6-66 are shown in Figure 6-68. As mentioned in the previous section of raw signal analysis for the same wavestreams, the amplitude scale was reduced to enhance the visualisation of the plots, likewise for these plots as they are displayed with maximum frequency range of 500kHz as nothing occurs beyond that. All plots display high levels of continuous energy within the frequency range of 15-70kHz and 90-145kHz. Again, all plots show medium levels of energy at frequency ranges between 155-205kHz. Once again, signals are present, yet at a lower magnitude of energy at frequency ranges between 230kHz-270kHz and 310kHz-340kHz. There are no apparent transient bursts within the spectrogram.

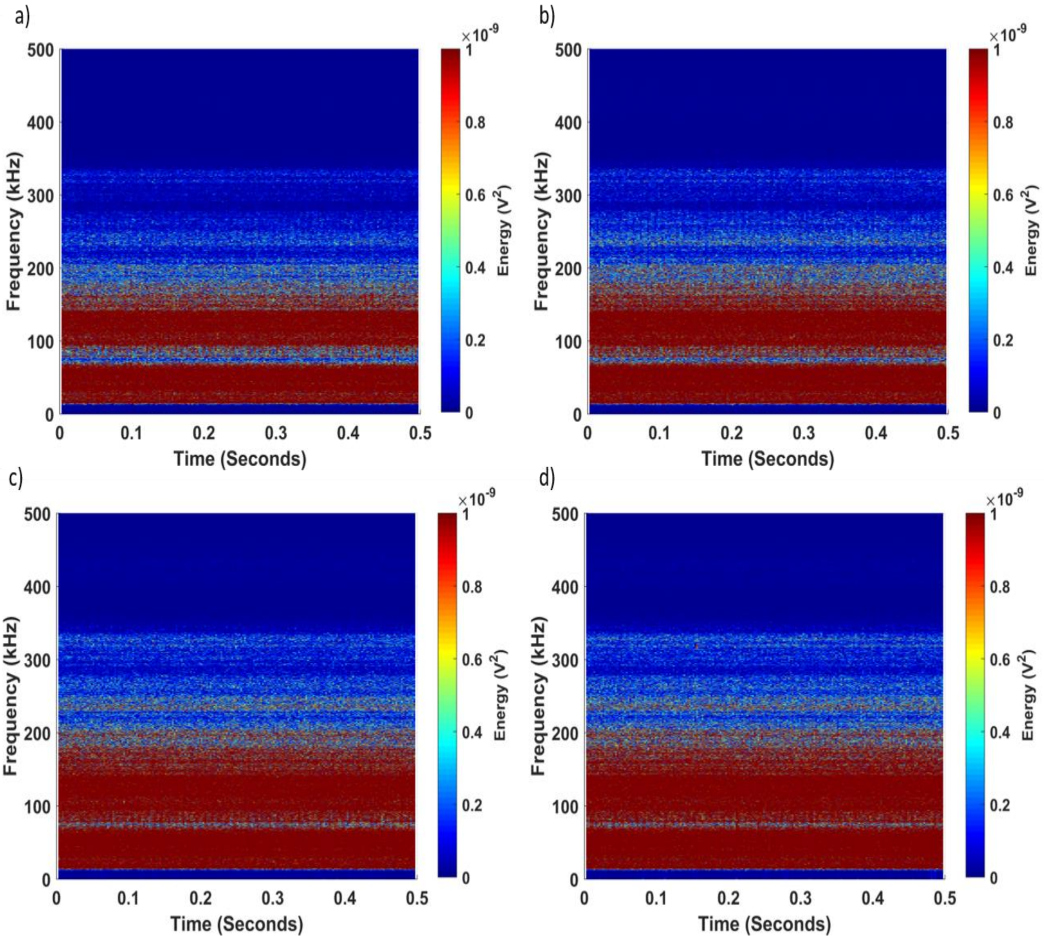

Figure 6-68: STFT Spectrogram from wavestreams at a) 6 hours, b) 10 hours, c) 20 hours and d) 22 hours.

Figure 6-69 demonstrates plots ’c’ and ‘d’ from Figure 6-68. All plots display high energy levels at frequencies up to 200kHz, as they continue up to 340kHz at lower levels of energy.

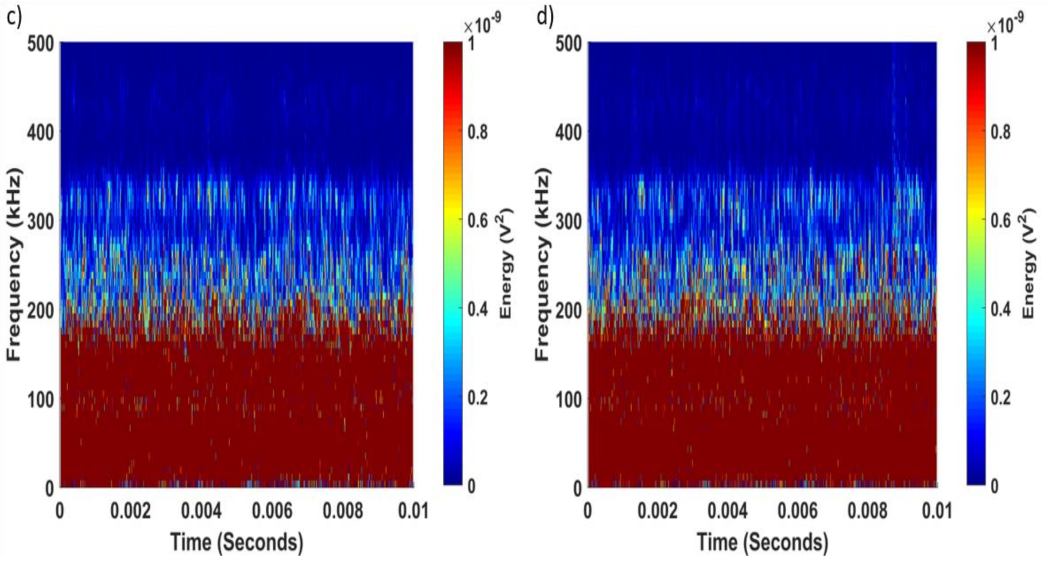

Figure 6-69: 0.01s spectrogram of the wavestreams at c) 20 hours and d) 22 hours.

6.9 Second Budget Bearing Run to Failure Test Results

6.9.1 AE RMS Analysis

The full duration of the test is demonstrated in Figure 6-70 for the AE RMS results, while Figure 6-71 indicates the positions of several wavestreams corresponding to significant variations within the AE RMS signal. The evident influence of increasing speed and load on the RMS signal is observed for all the bearings at the start of the test. It can be seen towards 9 hours of the test in designation 'a', where the test bearing AE RMS has been increasing similarly to the first budget bearing, bearing in mind the RMS scale is different, yet both signals of the test bearings start to intensify at 1.5V. There is an apparent blip in the signal which may represent a change in the bearing's condition just after designation 'a'. As the test continues further, designation 'b' represents a major surge in the signal at similar AE RMS levels witnessed from the first three tests at approximately 0.3V. Designation 'b' also shows changes in the Non-Drive End support bearing signal and as discussed previously that the support bearing signals could inform the researcher of any change within the system. As some of these tests run over night and as so fail at night or dawn, they are not stopped until next morning, which may jeopardise the test bearings physical aspects as they have run further during damaged conditions. Designations 'c' and 'd' represent more signal spikes towards the end of the test, where ‘d’ is also reflected on both support bearings signals as seen in Figure 6-71.

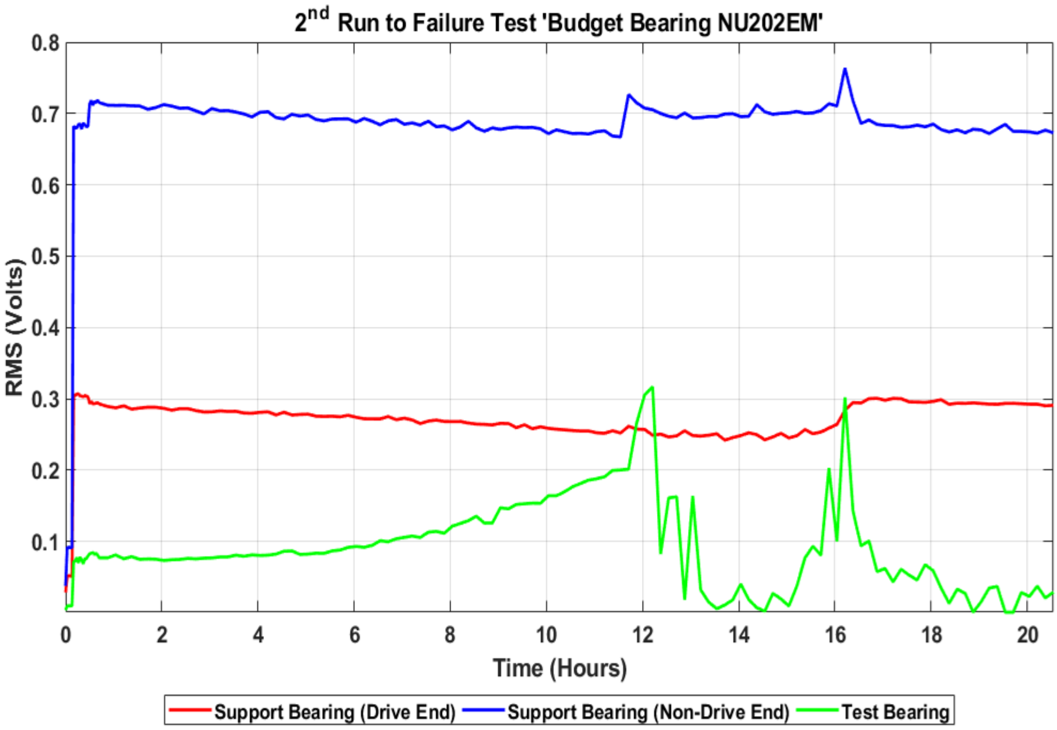

Figure 6-70: Second Budget Bearing Run to Failure Test data of RMS amplitude.

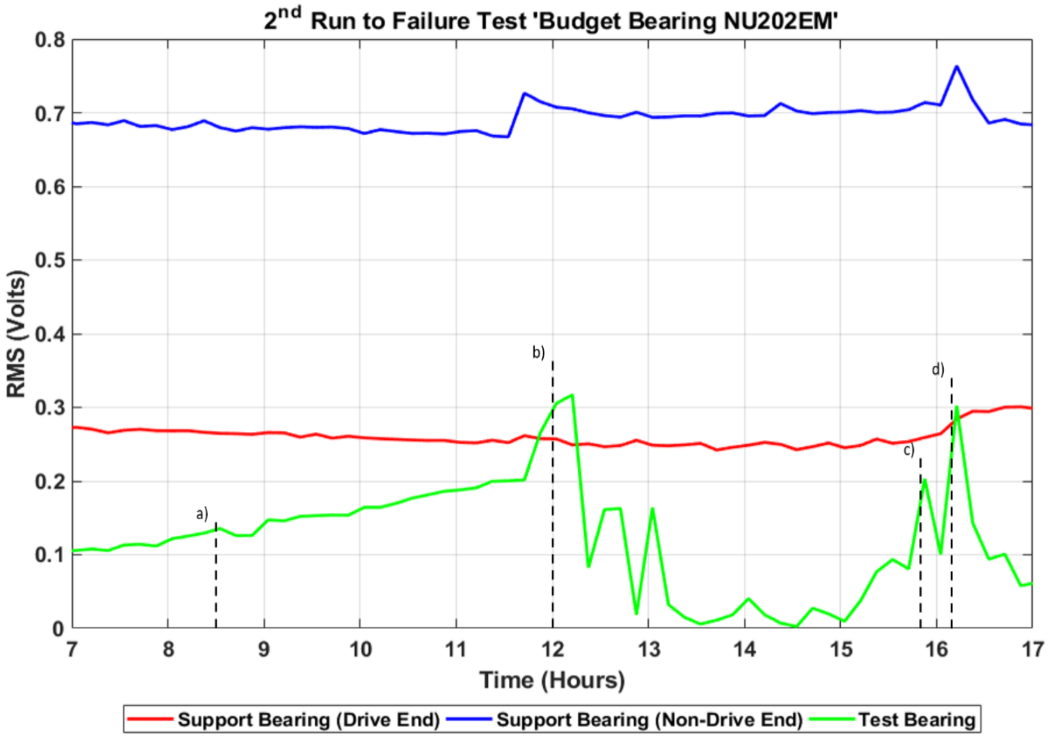

Figure 6-71: Annotations on magnified plot at a) 8 hours 30 minutes, b) 12 hours, c) 15 hours 50 minutes and d) 16 hours 10 minutes.

6.9.2 Raw Signal Analysis

The raw signal of the four wavestreams considered from Figure 6-71 are shown in Figure 6-72, for each plot a distinctive amplitude scale has been selected to improve their illustration. As there were no significant events beyond the background noise levels till approaching 10 hours of the test and so the first considered wavestream is at 8 hours and 30 minutes at designation ‘a’ in Figure 6-71. All plots reveal numerous transient bursts, even though the transients in plot ‘a’ are clearly pronounced but due to the ±1V of amplitude scale, yet the background noise still dominates the amplitude signal range ±0.5V. While plot ’b’ shows higher amplitude levels, the dominance of the background noise is still there. Plot ‘c’ characterizes similarities to some of the previous test plots, where the signal fluctuates relentlessly towards the end of the tests, the transient bursts become very clear yet below the amplitude levels of the nearby designated wavestream and in this case plot ‘d’, where in the second NU202ECP and first NU202ECP/C3, plots ‘c’ from both tests demonstrated higher amplitude levels than plot ‘d’. For those two tests, the reason is obvious the last designation ‘d’ on the AE RMS plot have lower RMS values when compared to designation ‘c’, as for this test scenario designation ‘d’ had higher RMS values than designation ‘c’. This reveals that there is a strong correlation between the raw signal and the AE RMS results.

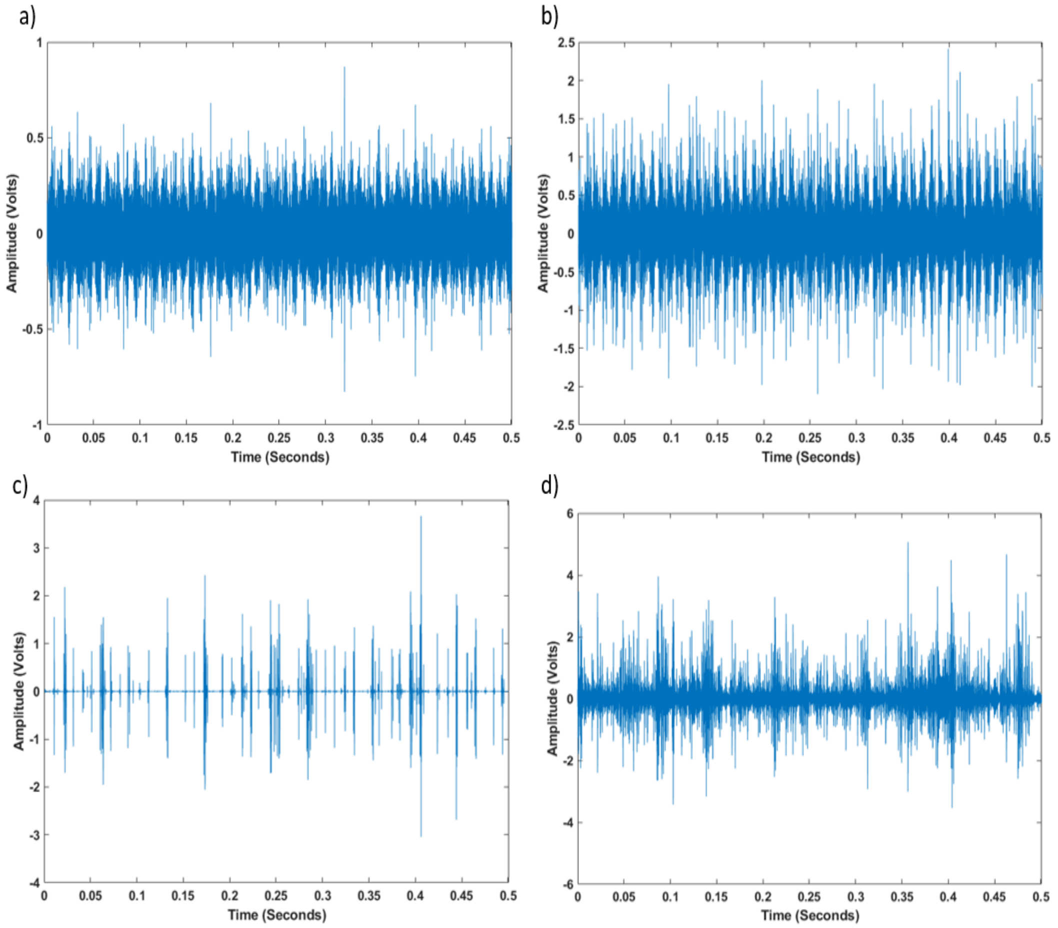

Figure 6-72: Raw signal from wavestreams at a) 8 hours 30 minutes, b) 12 hours, c) 15 hours 50 minutes and d) 16 hours 10 minutes.

Figure 6-73 shows plots ‘b’ and ‘d’ from Figure 6-72 at a shorter time duration. As the second budget bearing failed in a more intense manner than the first one, the signals are more representative of the characteristic defect frequencies at higher amplitude levels. Plot ‘b’ exposes periodic transient bursts at intervals of the BPFI of 0.0015s, as well as lower amplitude levels for the BPFO at 0.0022s within the signal. As the bearing condition worsens, the impact is revealed in plot ‘d’, as the BPFO is clearer at 0.0022s intervals and the periodic transient bursts are observed at 0.001s and 0.0032s within the signal, again at 0.0054s at lower amplitudes and again 0.0076s. The effect is more obvious within this test results as the outer raceway endures heavier damage in comparison to any of the other tests as illustrated in Figure 6-41.

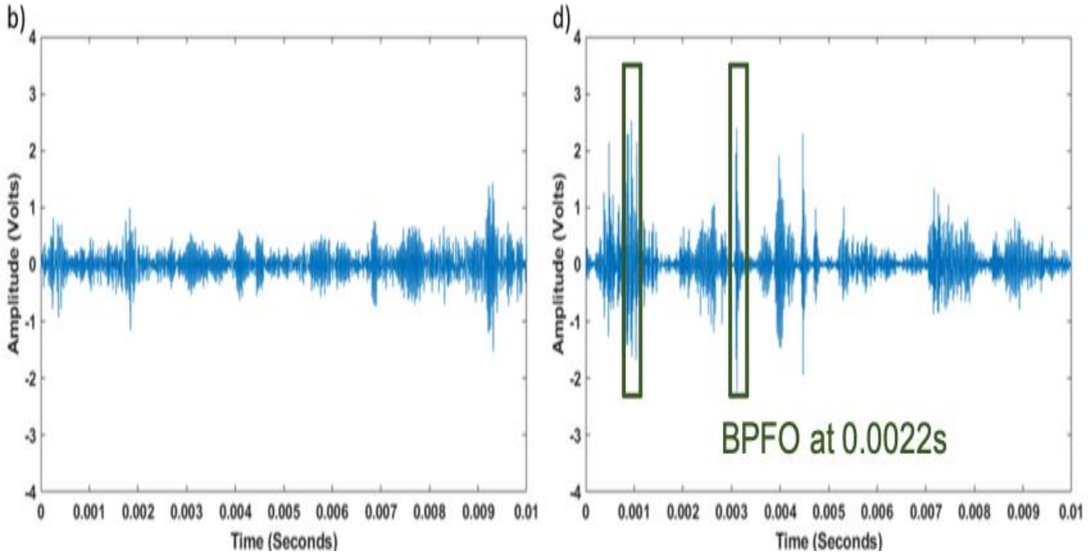

Figure 6-73: 0.01s of a wavestream at b) 12 hours and d) 16 hours 10 minutes.

6.9.3 Short Time Fourier Transform (STFT)

Spectrograms of the wavestreams from Figure 6-72 are shown in Figure 6-74. Plots ‘a’, ‘b’ and ‘c’ display continuous energy within the frequency range of 15-65kHz and again 80-135kHz, albeit at different levels of magnitude. Plots ‘a’ and ‘b’ imply that levels of background noise still exists, as it dominates the frequency range up to 135kHz, with a low level of energy at 240kHz. While this frequency range and beyond reveal clear periodic transient forms of broad-band energy reaching a 1000kHz in plot ‘d’. Plot ‘c’ exhibits similar aspects of its raw signal counterpart as there are clear periodic energy spikes throughout the spectrogram, yet at lower magnitudes than plot ‘d’ as also been noticed in the raw signal analysis.

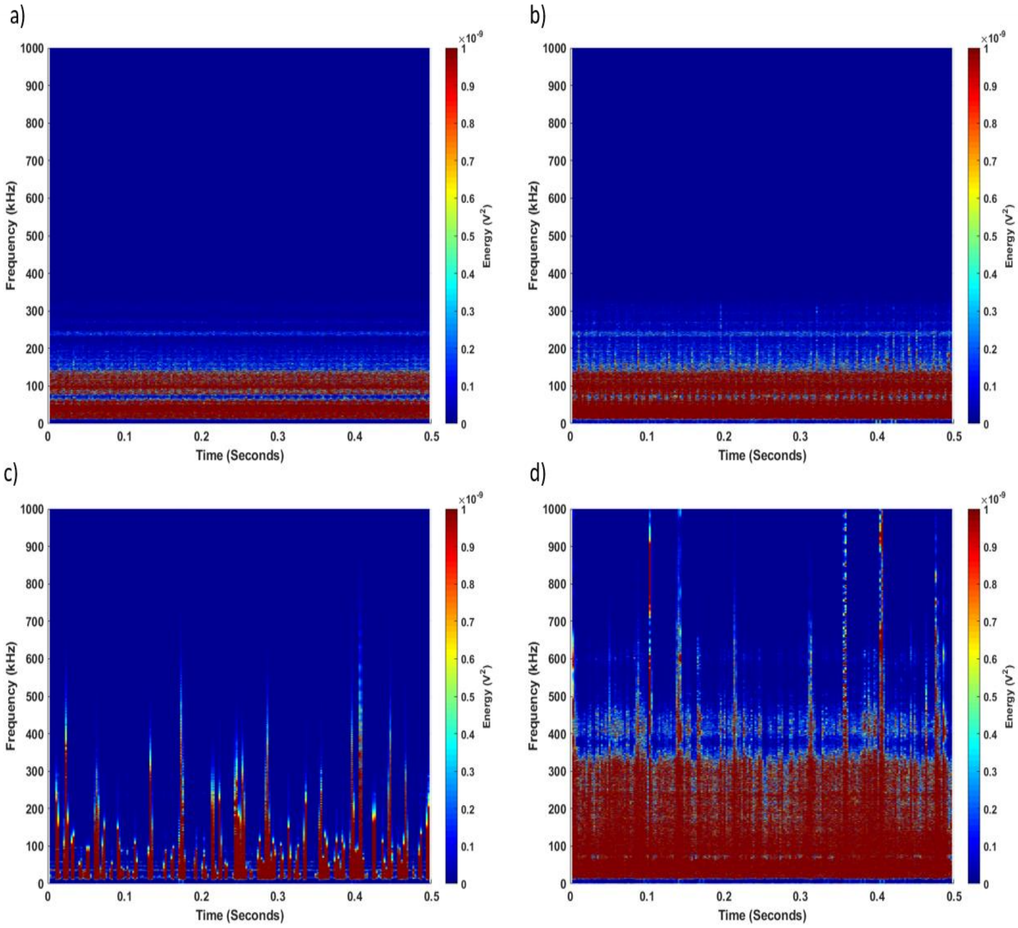

Figure 6-74: STFT Spectrogram from at a) 8 hours 30 minutes, b) 12 hours, c) 15 hours 50 minutes and d) 16 hours 10 minutes.

Figure 6-75 demonstrates plots ‘b’ and ‘d’ from Figure 6-74 at a shorter time duration. As the second budget bearing failed in a more intense manner than the first one, the signals are more representative of the characteristic defect frequencies at higher amplitude levels. Plot ‘b’ exposes periodic transient bursts at intervals of the BPFI of 0.0015s, as well as lower amplitude levels for the BPFO at 0.0022s within the signal. As the bearing condition worsens, the impact is revealed in plot ‘d’, as the BPFO is clearer at 0.0022s intervals and the periodic transient bursts are marked and observed at 0.001s and 0.0032s within the signal, again at 0.0054s at lower amplitudes and again 0.0076s. The effect is more obvious within this test results as the outer raceway endures heavier damage in comparison to any of the other tests as illustrated in Figure 6-41.

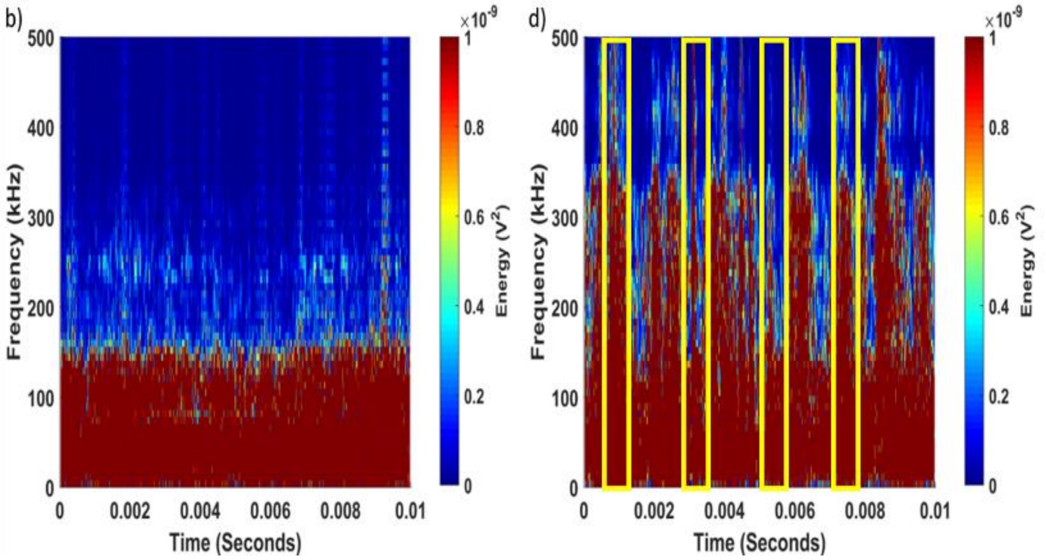

Figure 6-75: 0.01s spectrogram of the wavestreams at b) 12 hours and d) 16 hours 10 minutes.

6.10 Frequency Analysis of all tests

The frequency analysis will be divided into two components for each test. The first will consist of the full FFT's from the Run to Failure Test's full duration at half of the 2MHz sampling rate, due to Nyquist's theorem, hence the FFT data is only analysed up to 1000kHz, for all the bearings within the test rig. The second will split the FFT's frequency range of the test bearing into several sections in such order 0-90kHz, 90-250kHz and 250-500kHz to expand the visual resolution for clearer interpretation of the test results. The 250-500kHz frequency range will be presented when critical, as not all the failure tests show significant signal energy at this range or above.

6.10.1 First SKF NU202ECP Bearing

Figure 6-76 plots the FFT's for the full duration of the test across all three bearings within the system as titled. As witnessed during the analysis of healthy bearings characterisation in Section 5.5, when operational conditions are at lower loads energy content is significantly lower than at maximum desired load, this can be observed from the test bearing plot that low energy initiates at approximately 30 minutes of the test and continue to rise significantly until the desired load is reached, then the energy levels continues to increase steadily throughout the test till it reaches 60 hours towards the end of the test, where the frequencies clearly commences to merge into one another between 15kHz-160kHz with a clear upsurge at the final stage of the test. At the latest stage of the test just before the 65 hours mark, the Non-Drive End support bearing displays similar effects to the test bearing as the frequency range starts to increase, similar analogy was revealed from the AE RMS analysis in Figure 6-42, and as it is closer to the test bearing than the Drive-End support bearing, it indicates low levels of energy from 200-350kHz similarly to the other Drive-End support bearing yet higher in energy degree.

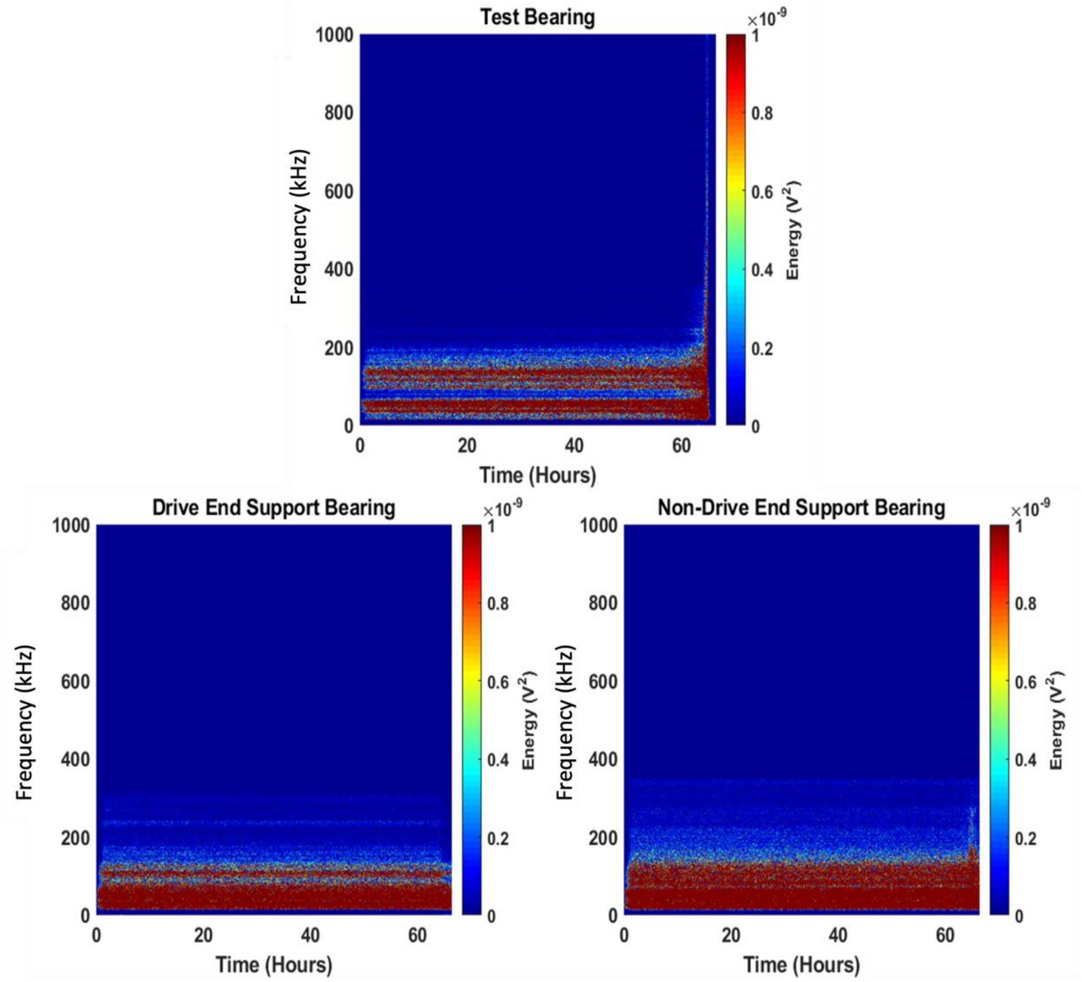

Figure 6-76: First SKF NU202ECP Bearing FFT's from Run to Failure Test data.

Figure 6-77 illustrates three sectioned plots of the FFT at 0-90kHz, 90-250kHz and 250-500kHz for the test bearing. The first section of the FFT at 0-90kHz, clearly shows strong energy content at frequencies between 15-19kHz, 33-43kHz and 45-65kHz throughout the test as they merge into one at the end of test due to the condition of the bearing and damage propagation. The three dominant frequency ranges are similarly observed in the second section of the FFT ranging from 90-250kHz, still strong energy content yet a lower level of magnitude at frequencies between 95-105kHz, 110-121kHz and 128-145kHz, these frequencies may be due to second harmonics of the frequencies observed in the first sectioned FFT, in addition to lower levels of energy at higher frequency ranges at 160kHz dropping down in energy levels as they reach 220kHz. All the mentioned frequencies tend to merge towards the end of the test, similar observations were discussed by Cockerill (2017). The last sectioned FFT range from 250-500kHz only illustrates the final energy surge at the end of the test that dominates the whole frequency band as seen in Figure 6-76.

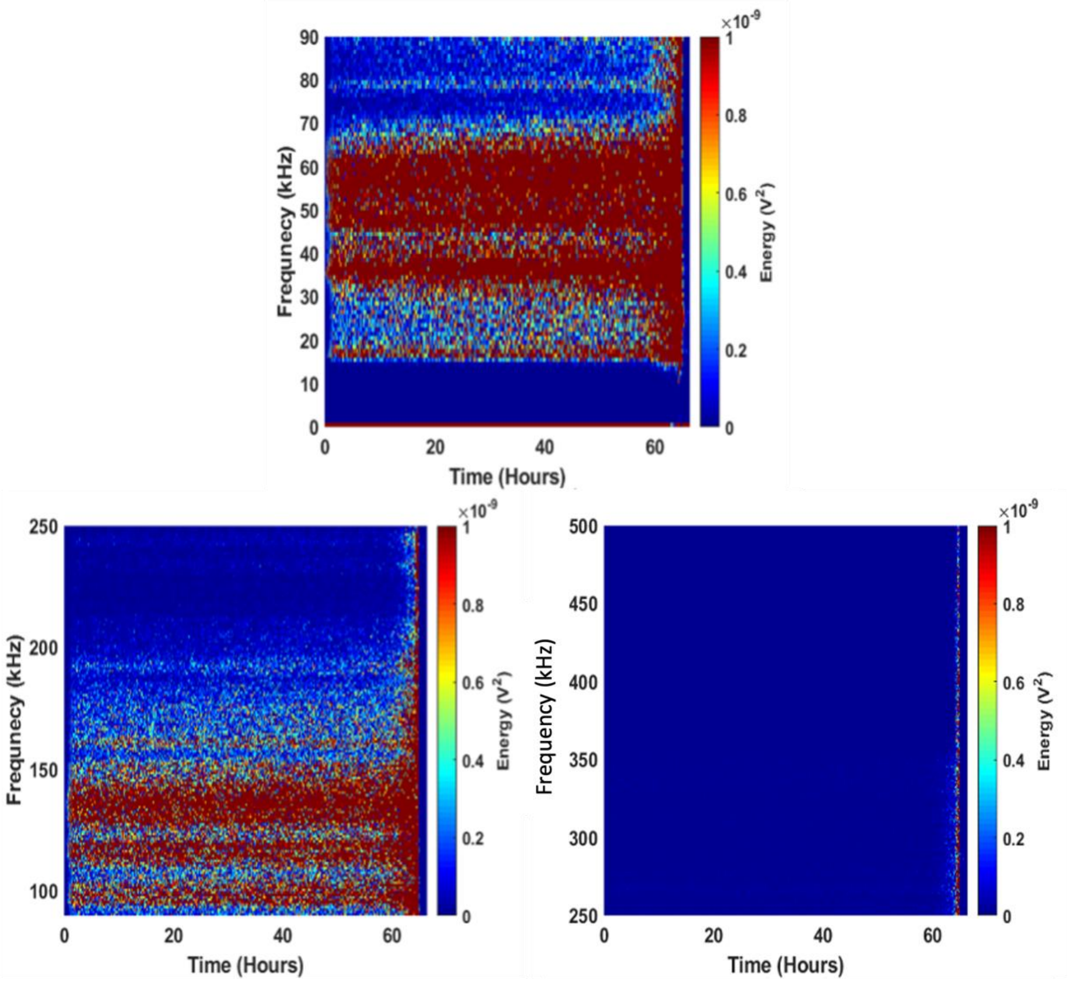

Figure 6-77: First SKF NU202ECP Bearing Sectioned FFT's at 0-90kHz, 90-250kHz and 250-500kHz.

6.10.2 Second SKF NU202ECP Bearing

Figure 6-78 plots the FFT's for the full duration of the test across all three bearings within the test rig as labelled. The energy content at the start of the test relates to the previous test analysis, with regards to its energy levels rising following the load increase, as perceived within all three bearings within the system. The Non-Drive End support bearing plot conveys parallel frequency results to the Drive-End support bearing plot, yet at higher energy concentrations. However, no association between the energy content of the Non-Drive End support bearing to the test bearing as noticed in the previous test, where an energy surge from the test bearing would be seen in the Non-Drive End support bearing.

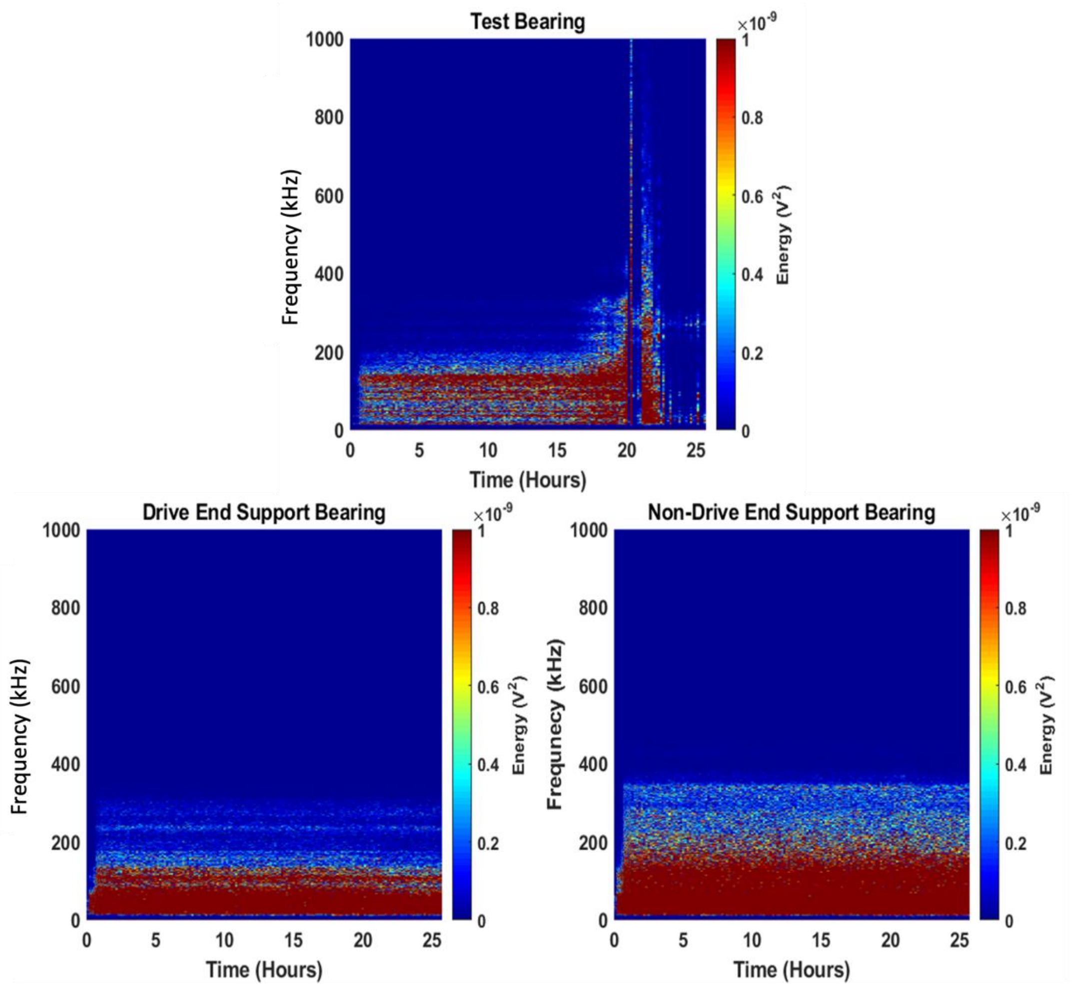

Figure 6-78: Second SKF NU202ECP Bearing FFT's from Run to Failure Test data.

Figure 6-79 demonstrates the three sectioned plots of the FFT at 0-90kHz, 90-250kHz and 250-500kHz for the test bearing. The first section of the FFT at 0-90kHz, demonstrates strong energy content at frequencies between 15-20kHz, 34-40kHz, 47-51kHz, 56-59kHz and 77-82kHz during the test, as well as expanding ±2kHz from those frequencies as the test runs further. All of the five frequency ranges start to merge towards the end of the test as well as being one strong expanding continues frequency as seen in the second section of the FFT ranging from 90-250kHz. Frequencies ranging from 95-145kHz represent growth in amplitude till the end of the test, as they are considered second harmonics from the previous data in the FFT region of 0-90kHz. The last sectioned FFT range from 250-500kHz illustrates the last stage of the test with an intense energy surge that dominates the whole frequency band as seen in Figure 6-78.

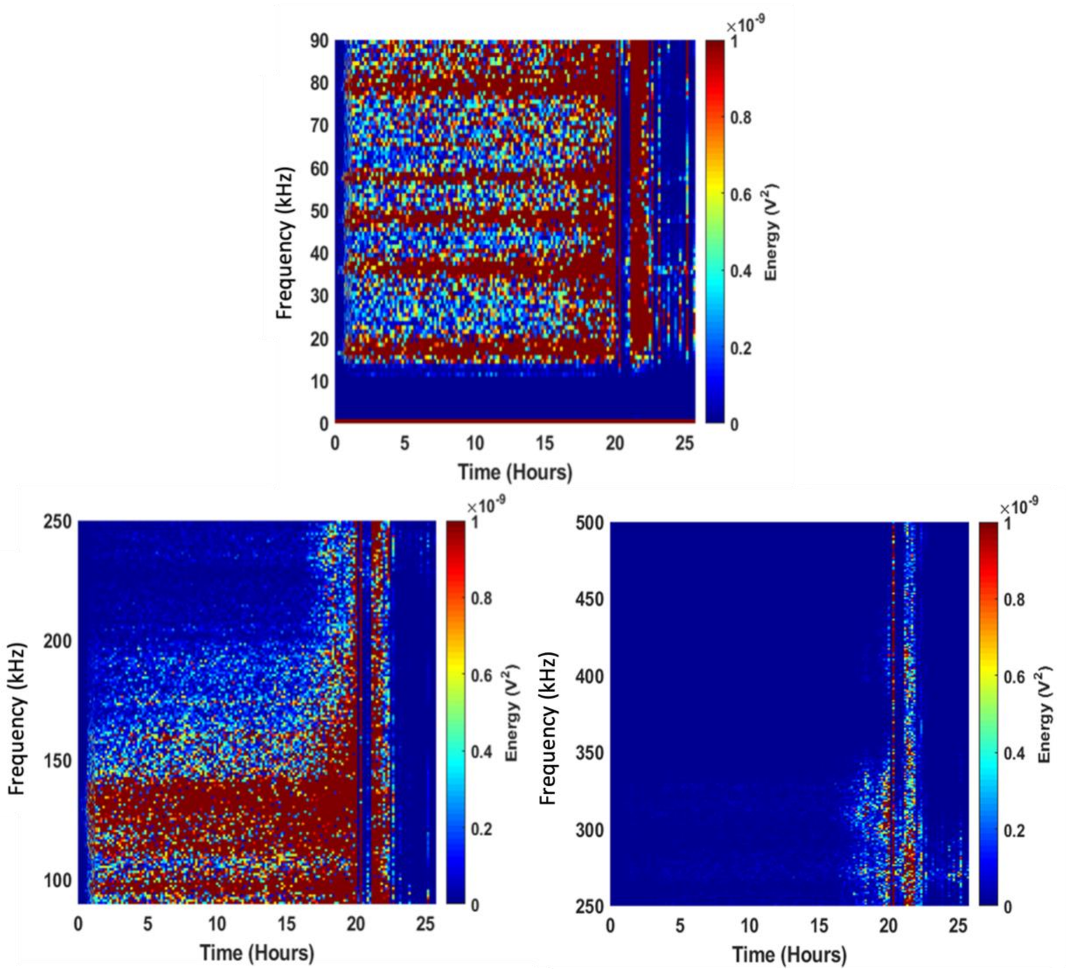

Figure 6-79: Second SKF NU202ECP Bearing Sectioned FFT’s at 0-90kHz, 90-250kHz and 250-500kHz.

6.10.3 First SKF NU202ECP/C3 Bearing

Figure 6-80 plots the FFT’s for the full duration of the test across all three bearings within the system as titled. Once again, the Non-Drive End support bearing shows more dominant energy than the Drive-End support bearing during the test, masking the thin thread of low energy excitation at the Drive-End support bearing at frequencies between 85-95kHz. The Non-Drive End support bearing mirrors the test bearings high levels of energy towards the end of the test, in relation with the AE RMS results as shown in Figure 6-54 as well as the resemblance to the first NU202ECP FFT results.

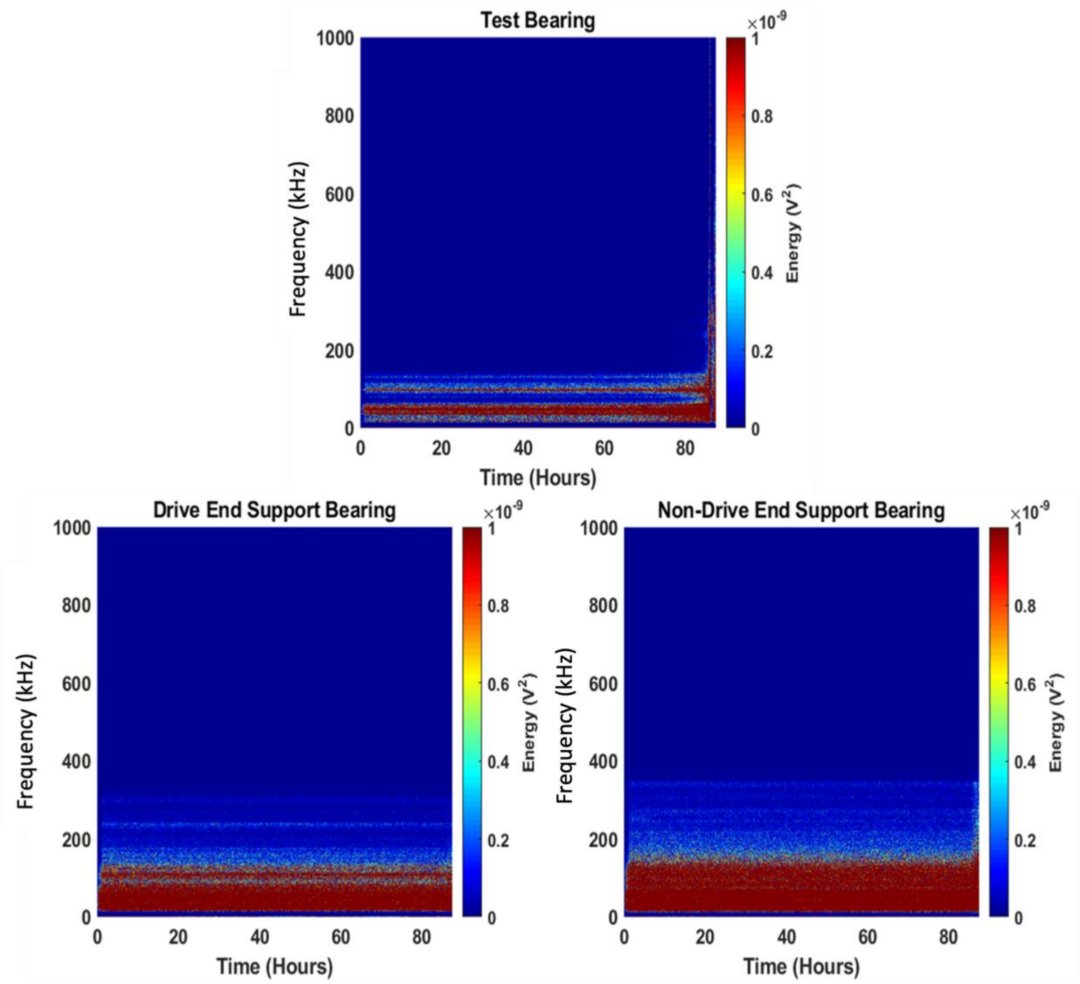

Figure 6-80: First SKF NU202ECP/C3 Bearing FFT's from Run to Failure Test data.

Figure 6-81 illustrates three sectioned plots of the FFT at 0-90kHz, 90-250kHz and 250-500kHz for the test bearing. The first section of the FFT at 0-90kHz, presents high levels of energy in different frequency ranges between 16-20kHz, 35-53kHz and 57-61kHz throughout the test as they merge into one another towards the end of test due to the bearing condition and damage propagation. Low level of energy content is also revealed at frequencies between 78-80kHz. The 90-250kHz plot indicates high energy content at 94-102kHz throughout the test as it intensifies towards the end of the test and merges with the medium levels of energy excitation at frequencies between 103-120kHz and 128-135kHz. The merged frequencies at the end of the test continue to rise in energy and frequency range as observed in the last sectioned FFT range from 250-500kHz.

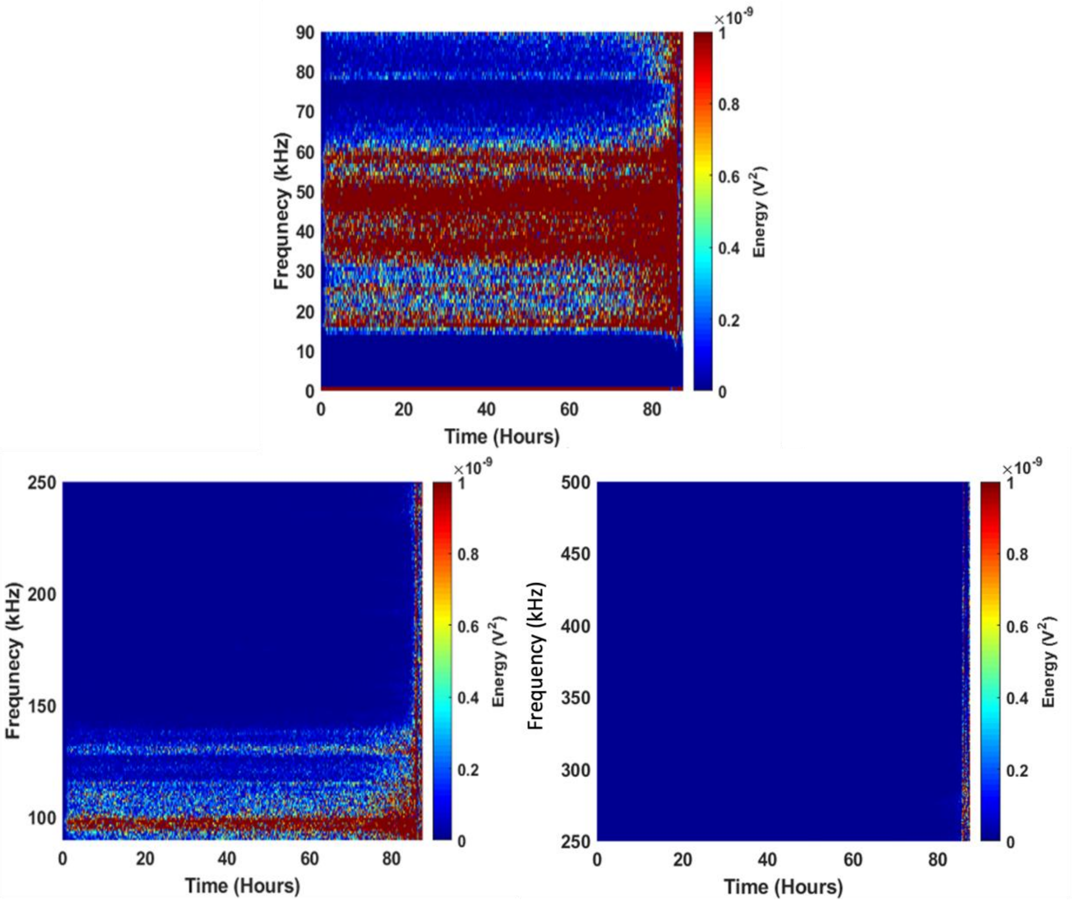

Figure 6-81: First SKF NU202ECP/C3 Bearing Sectioned FFT's at 0-90kHz, 90-250kHz and 250-500kHz.

6.10.4 Second SKF NU202ECP/C3 Bearing

Figure 6-82 plots for the full duration of the test across all three bearings within the test rig as titled. As this test was stopped due to intense noise from the test rig and that the test bearing sensor may have been deficient as discussed in section 6.7.1, the outcome results are not as vague as thought. The energy content at the start of the test relates to the previous tests analyses, with regards to its energy levels rising following the load increase during the first half an hour of the test improved demonstration in Figure 6-83. The Non-Drive End support bearing plot shows approximately double the amount of energy excited by the Drive-End support bearing at related frequencies.

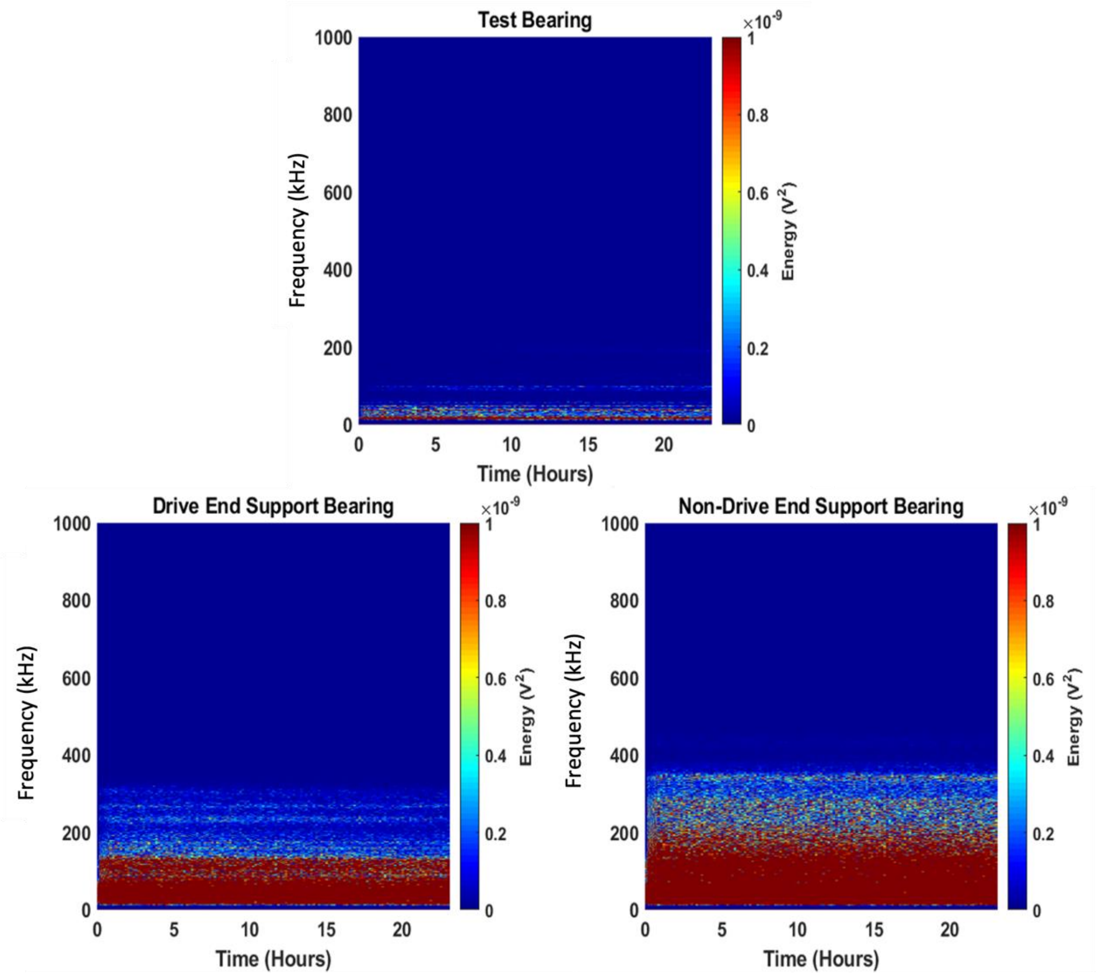

Figure 6-82: Second SKF NU202ECP/C3 Bearing FFT's from Run to Failure Test data.

Figure 6-83 illustrates two sectioned plots of the FFT at 0-90kHz and 90-250kHz for the test bearing, as there is no energy excitation above the 250kHz frequency range, the 250-500kHz plot is not illustrated. The first section of the FFT at 0-90kHz, illustrates dominant energy content at frequencies between 15-21Hz. Comparable energy level excitations yet not as strong throughout the test are seen at 35-38kHz and 47-49kHz, unlike all the previous tests where similar energy content would merge towards the end of the test, these haven't. Nevertheless, the frequencies in between the beforementioned frequencies show lower energy contents during the course of the test, which may have well merged and developed higher levels of energy if the test continued to run further. The second plot of the FFT at 90-250kHz represent a medium level of energy at the 98-99kHz and the levels of energy tend to reduce over higher bands of frequencies.

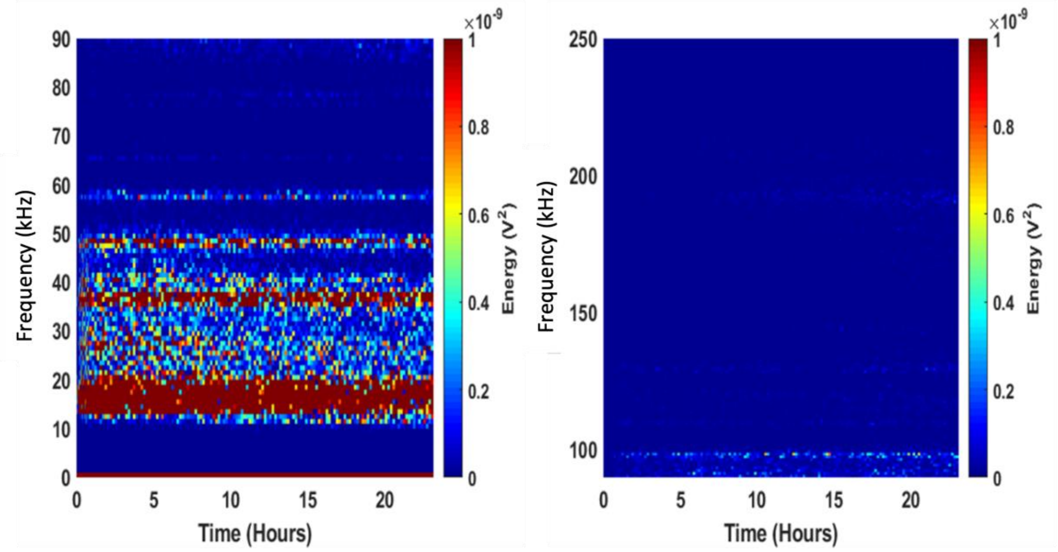

Figure 6-83: Second SKF NU202ECP/C3 Bearing Sectioned FFT's at 0-90kHz and 90-250kHz.

6.10.5 First Budget Bearing NU202EM

Figure 6-84 plots the FFT's for the full duration of the test across all three bearings within the system as titled. As witnessed previously during the healthy bearings characterisation analysis and the SKF bearings test results, while operational conditions are under an increase of load and speed at the early stage of the test, the energy content for the budget bearing similarly starts at low levels and begins to intensify as both parameters are increased. This can be observed from all bearing plots in Figure 6-84, after the 30 minutes from the start of the test. The energy levels are yet again higher in magnitude for the Non-Drive End support bearing at frequencies between 15kHz-140kHz and with lower excitations of energy from 160-380kHz, when compared to the Drive End support bearing.

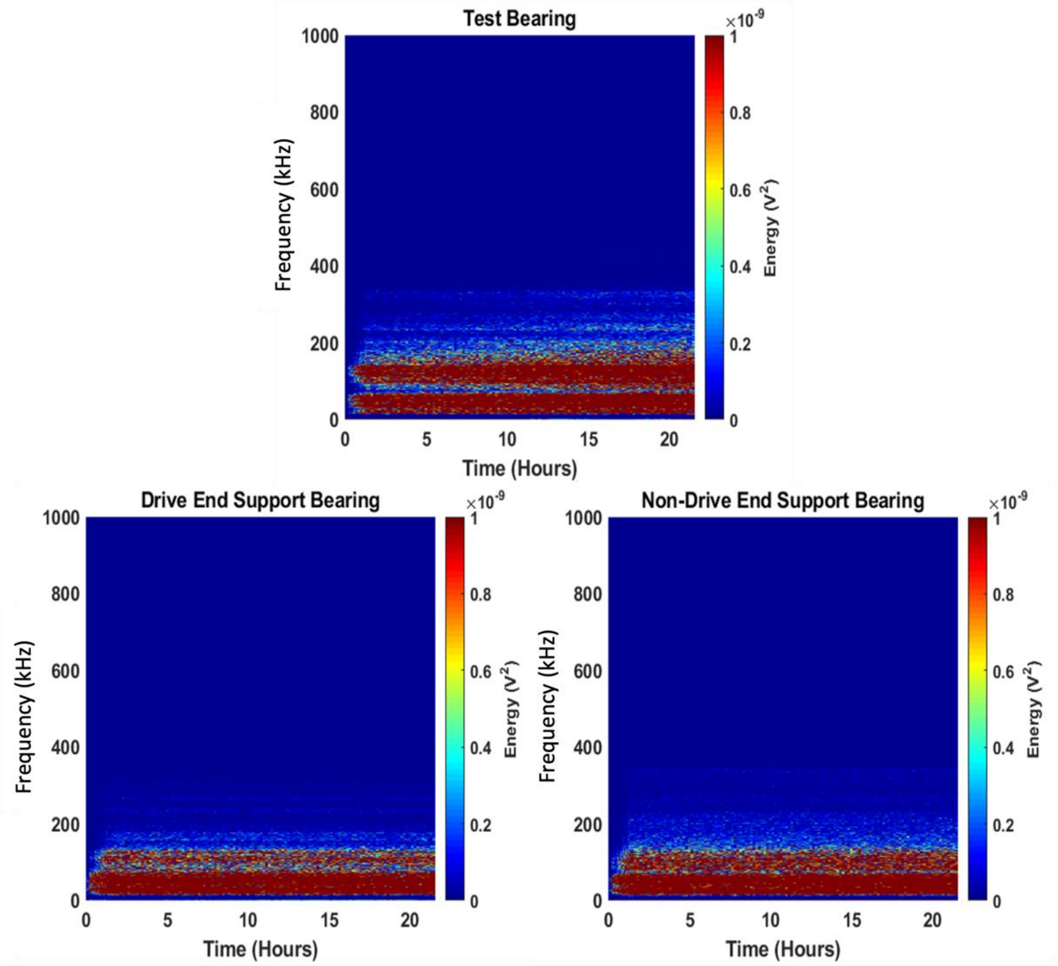

Figure 6-84: First Budget Bearing FFT's from Run to Failure Test data.

Figure 6-85 demonstrates the first two sectioned plots of the FFT at 0-90kHz and 90-250kHz for the test bearing, as there is no significant emergence of energy excitation above the 250kHz frequency range, the 250-500kHz plot is not shown. The first section of the FFT at 0-90kHz, demonstrates dominant energy content at frequencies between 15-68kHz and another strong energy sequence of frequencies between 80-90kHz, yet at a later stage of the test at approximately 12 hours. The second plot of the FFT at 90-250kHz embodies a constant frequency excitation from the start of the test that is stretched from 94-145kHz and similarly after 12 hours the intensity of the energy grows within the same frequencies till the end of the test. Medium level energy excitation continues to be present at higher frequencies.

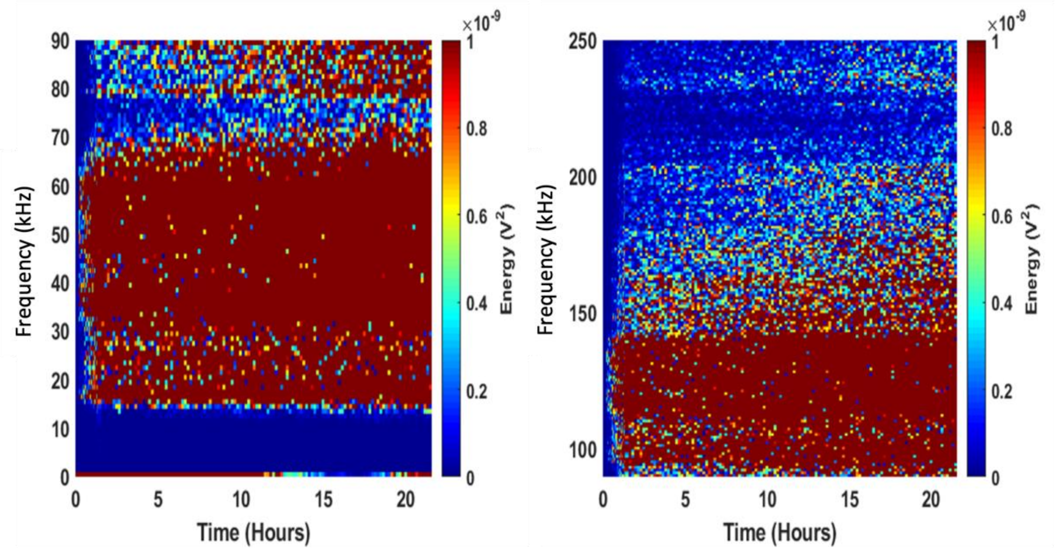

Figure 6-85: First Budget Bearing Sectioned FFT's at 0-90kHz and 90-250kHz.

6.10.6Second Budget Bearing NU202EM

Figure 6-86 plots the FFT's for the full duration of the test across all three bearings within the test rig as titled. After reaching the speed and load required for the test, the energy levels observed appear similar throughout the test for both support bearings. However, two noticeable characteristics from the Non-Drive End support bearings signal are considered absent, the first is to how the energy excitation drops sharply after 16 hours at frequencies between 200-350kHz as well as no apparent association with any of the high energy levels witnessed from the test bearing at two significant durations of the test at 12 and 16 hours of the test.

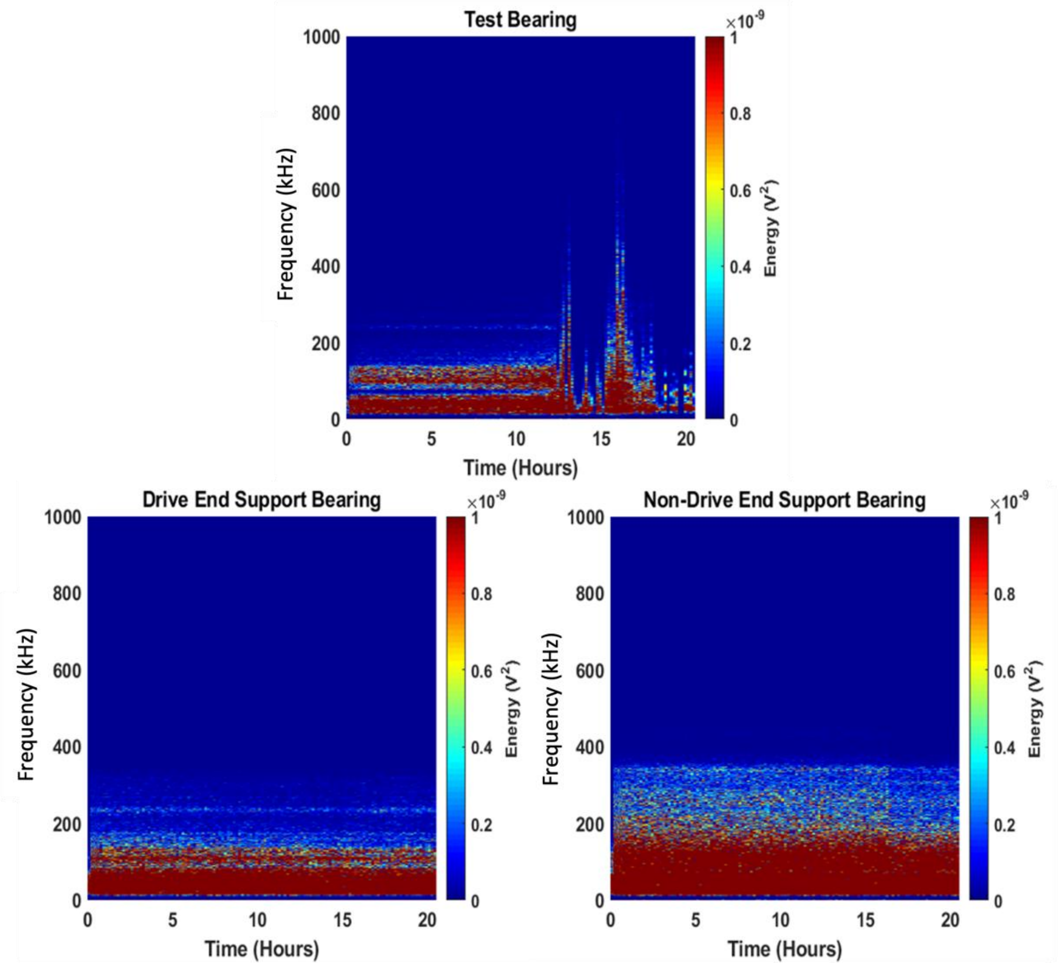

Figure 6-86: Second Budget Bearing FFT's from Run to Failure Test data.

Figure 6-87 demonstrates the three sectioned plots of the FFT at 0-90kHz, 90-250kHz and 250-500kHz for the test bearing. The first section of the FFT at 0-90kHz, demonstrates strong energy content at frequencies between 15-50kHz and 57-61kHz as these two frequency bands tend to merge after 10 hours of the test, as well as at frequencies above 80kHz but at a later stage of the test. As all the beforementioned frequencies emerge together as one strong energy excitation at 12 hours into the test, as their frequency band grows to be from 15-480kHz as seen in the 90-250kHz and 250-500kHz plots. In fact, those frequencies drop massively as it does in the AE RMS signal analysis and then intensify again just before 16 hours of the test, with another energy surge crossing all frequencies up to 500kHz. Similarly, to the previous budget bearing FFT results, the second section of FFT 90-250kHz demonstrates high energy levels at frequencies ranges of 95-140kHz and keeps intensifying for the first 12 hours of the test. Low levels of energy excitation continue to appear at higher frequencies, although most are clearly observed after 5 hours into the test. The last sectioned FFT range from 250-500kHz demonstrates the last stage of the test with two energy surges that dominates the frequency band at 12 and 16 hours of the test.

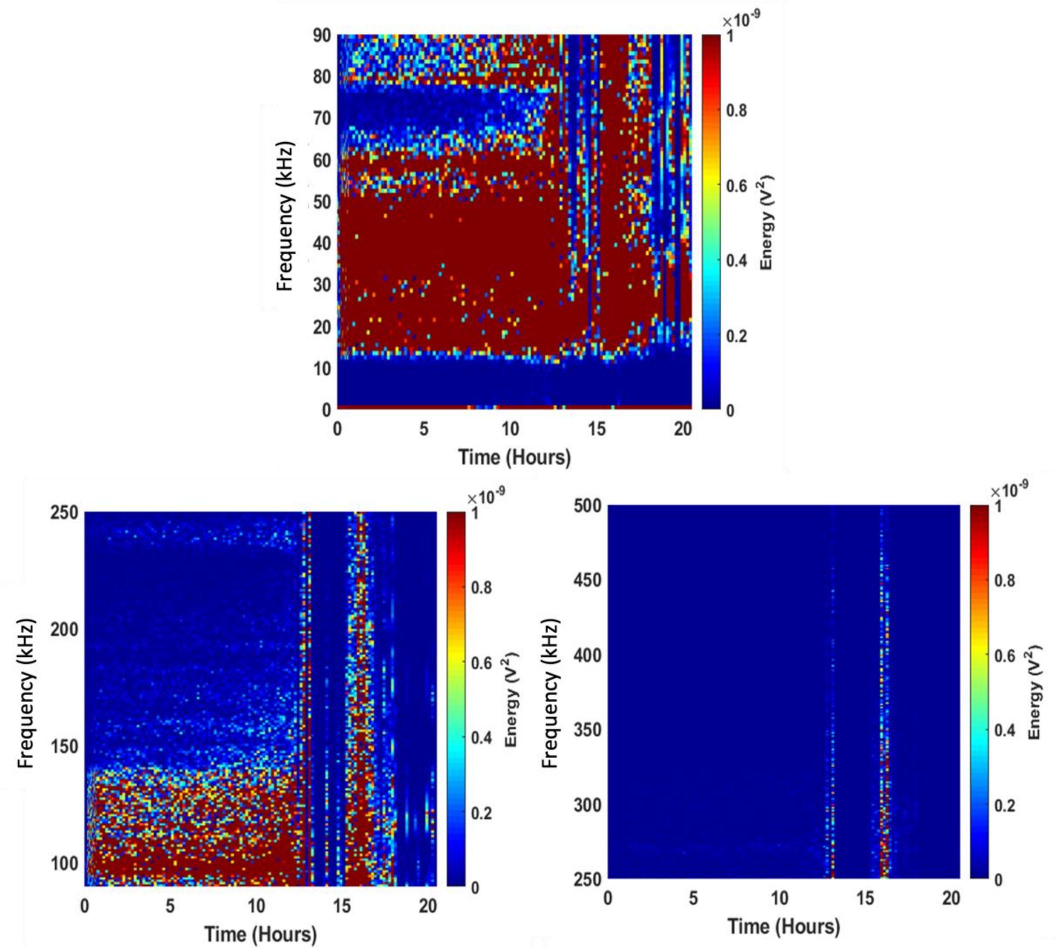

Figure 6-87: Second Budget Bearing Sectioned FFT’s at 0-90kHz, 90-250kHz and 25-500kHz.

6.10.7Summary of FFT results

All tests revealed common threads in three aspects, the first is that high energy excitation within the system starts to increase once the maximum speed and maximum load is reached and keeps increasing in intensity during the test until failure. The second noticeable fact is that the energy excitation as well as the frequency bands from the Non-Drive End support bearings are at higher levels when compared to the Drive End support bearings. Lastly, for all test bearing regardless the quality or the clearance, the frequency bands of 250-500kHz are not revealing any form of energy excitation till the end of the run to failure test, where in most results a spike of energy is excited due to the amount of damage within the test bearing. Table 2-1 demonstrates the energy excited at the highest and lowest frequency bands for all tests for the sectioned frequencies mentioned. It can be seen that the frequency bands are highest for the budget bearing at from 0-90kHz as the energy is excited from 15kHz, this may well be due to the surface roughness quality of the budget bearing. Never the less, for the test bearings the energy excited at the highest frequency band seems to operate in the same range except for the higher clearance test bearing NU202ECP/C3 which may well be due to the stress relief of higher clearances as perceived also in the RMS analysis, revealing lower levels of AE RMS excitation when compared to the other two types of test bearings. These results can also be correlated with those for the lowest frequency band excitation for the higher clearance, as they are excited between 125-135kHz in comparison to the other two test bearings operating at higher frequencies reaching 200kHz.

Table 2-1 Highest and lowest frequency bands during the run to failure tests.

Test Bearing	Highest Frequency		Lowest Frequency	
	0-90kHz	90-250kHz	0-90kHz	90-250kHz
1st NU202ECP	30-68kHz	110-145kHz	72-80kHz	190-220kHz
2nd NU202ECP	35-60Khz	95-145kHz	65-78kHz	170-210kHz
1st NU202ECP/C3	30-65kHz	95-105kHz	70-90kHz	125-130kHz
2nd NU202ECP/C3	15-22kHz	96-99kHz	58-60kHz	130-135kHz
1st Budget	15-70kHz	95-145kHz	70-80kHz	200-230kHz
2nd Budget	15-60kHz	95-140Hz	65-78kHz	145-200kHz

6.11 Chapter summary

The work presented was performed on a high-speed test rig designed to replicate natural failures on rolling element bearings in an accelerated controlled manner, by exceeding specified operational conditions to reduce the life expectancy of the test bearing as much as possible. The load was applied radially over a non-conformal line contact within the bearing and the outer raceway was stationary. Generally, the Run to Failure Tests were constructive, yet exceptionally aggressive and as the acquired data was recorded at 10 minutes intervals, it is challenging to confidently define the timing or status of damage initiation within the recorded wavestreams. However, by use of straightforward data analysis techniques, the results were able to demonstrate changes in the signals values, as the bearing conditions start to change due to expected damage propagation. The limitation and difficulty of these techniques lies in diagnosing and pinpointing the damage initiation within the bearing.

In the early stages of the Run to Failure tests, analysis of the recorded wavestreams formed evident weak periodic transient bursts within the signal prior to any considerable increase in the AE RMS values. The reason behind this trend may possibly be due to early pitting within the bearing components as the damage initiates, inherent debris generation that is rested or rolled onto either surface of the raceways. This is believed to be the main reason of low level transients observed at the early stages of the tests dominated by the background noise levels. However, as the damage propagates further across the damaged surface, the imminent increase of AE RMS signal is clear along with the transient bursts within the raw signal.

The results from the data analysis process demonstrate that the AE RMS signal is a robust technique and capable of perceiving present damage within the rolling element bearing. In addition, the AE RMS results from most carried out tests were proportional to the frequency spectrum analysis results of the energy levels presented within the domain. Along with RMS being an incorporated statistical parameter within most condition monitoring systems, there is no reasonable advantage of further analysing the data in the frequency spectrum for damage detection, as it can be observed live via the AEWin system in this case.

7 Conclusion

7.1 Critical Findings

As the investigation comes to an end, these are the main topics surrounding the aims and objectives proposed during this research. The research has led to realise new data sets for three types of bearings with different characteristics yet with similar size. These data sets include the healthy bearing characterisation tests as well as naturally failed roller bearing. These investigation have also established the usefulness and validity of the support bearing results in correspondence to the test bearing.

- **Healthy Bearing Characterisation Tests**

Healthy bearing characterisation tests were valuable in determining a benchmark to compare the results. It has shown that both speed and load influenced the AE signals and frequency spectrum, however the greater influence came from the increase and decrease of the speed. In addition, the higher radial clearance bearings had lowest energy excitation. Furthermore, the budget bearing produced the highest AE RMS values of all three bearings, due to its operating within the mixed lubrication regime and also potentially having poorer quality-control in manufacture. The AE RMS levels of the budget bearing are approximately three times higher than the SKF bearings at 0.063V and 0.025 for the higher clearance and 0.021V for the normal clearance SKF.

- **Lubrication regime**

An investigation into the mechanics of AE generation and the effect of the lubrication regime was established. The effect of AE RMS value in relation to λ ratio revealed that the SKF test bearings at higher speeds principally operated within the hydrodynamic lubrication regime, where the budget bearing operated predominantly within the mixed lubrication regime and at lower speeds was operational under the boundary lubrication regime. However, the one common observation between all three types of bearings was that as the load increased the λ values decreased, with a corresponding increase in AE signals, although this correlation was by no means as strong as that between AE and rotational speed.

- **Run to Failure Bearing Tests**

Throughout the run to failure bearing tests a number of similarities are drawn, principally that the AE RMS data is able to detect present damage within the roller bearing. The Non-Drive End Support Bearing also showed clear signs of change to the AE RMS signals, at parallel timings of the test bearings AE RMS signal variations towards the end of each test. Other particular similarities was found between the excitation bands within the frequency analysis. In addition, it was observed that the AE RMS signals were proportional to the frequency energy levels, showing no clear advantage of further analysing the frequency of the signals, with the techniques used within this research. Lastly, the higher clearance SKF bearings had a higher durability rate as it reached 80 hours till failure when compared to the normal clearance which ran for 60 hours till failure, where the budget bearing ran for approximately 20 hours till failure.

- **Limitations and Encountered setbacks**

Unique planning and tailored setups are made to minimise obstacles and setbacks, yet unfortunately they are inevitable. Whether it is from misalignments, the disassembly and reassembly of the test rig between different sets of tests and on different test bearings, emphasis on the AE sensitivity and repeatability must be taken into consideration especially when there is a need to recouple or mount an AE sensor and its proper location on the test rig. As all of the aforementioned details may heavily influence results of the AE signals.

7.2 Novelty

The section presents the novelty within this research. Fundamentally it is centred around three types of bearings, which were investigated and compared in characterisation of a healthy bearing through extensive testing to contribute to the discussions surrounding the effect of operational conditions and how they influence the AE signals generated, as well as expanding the literature and knowledge on the effect of λ on the AE signal. Establishing the benefits of analysing the support bearing data and not to overlook them in the future as the data demonstrated to be useful in detecting abnormality within the system. Changes caused by natural and progressive damage to the roller bearing were investigated through Run to Failure Tests, whereas the majority of the previous investigations were conducted on rolling element bearings with artificially seeded defects. In addition, supporting damage growth detection within the bearings was realised through the AE wavestreams analysis. This demonstrated that complex test rigs introduce certain limitations and obstacles which may affect the implementation of AE as a condition monitoring tool in the industries, as the AE sensitivity, reliability and repeatability may be obscured.

7.3 Further Work

Recommendations for further work are given in this section. Firstly, as an extensive amount of wavestreams data was obtained, it can be further analysed with different and more sophisticated techniques to broaden the knowledge and understandings of the signals information, as the obtained data within this thesis has not been fully exhausted.

Secondly, healthy bearings characterisation tests could be reinvestigated yet with the oil temperature at the test bearing set at a lower temperature or higher to be able to manipulate the oil viscosity in order to establish a different λ and be able to compare the operational lubrication regimes and their effects on the AE signals.

Thirdly, the data acquired from both support bearings should not be neglected as it has shown significant results and may well be further investigated with further techniques. Bearing in mind that access to the test bearing may not always be easy, it would be beneficial to use the data to corelate the findings from all bearings within the test rig.

Lastly, perhaps an unusual form of testing, yet hopefully yields great results in the repeatability and sensitivity of the AE sensors. This could be in the form of repeating a set of tests on the same bearing several times yet by removing and remounting the

AE sensor to see if the results are repeated. Another example could be the usage of different AE sensors, yet from the same manufacturer just to see if the end results are repeatable. Such results would establish a unique and reliant data.

References

Aggelis, D.G. et al. 2011. Acoustic emission for fatigue damage characterization in metal plates. In: *Mechanics Research Communications*. doi: 10.1016/j.mechrescom.2011.01.011.

Al-Balushi, K.R. et al. 2010. Energy index technique for detection of acoustic emissions associated with incipient bearing failures. *Applied Acoustics* 71(9), pp. 812–821. doi: 10.1016/j.apacoust.2010.04.006.

Al-Dossary, S. et al. 2009. Observations of changes in acoustic emission waveform for varying seeded defect sizes in a rolling element bearing. *Applied Acoustics* 70(1), pp. 58–81. doi: 10.1016/j.apacoust.2008.01.005.

Al-Ghamd, A.M. and Mba, D. 2006. A comparative experimental study on the use of acoustic emission and vibration analysis for bearing defect identification and estimation of defect size. *Mechanical Systems and Signal Processing* 20(7), pp. 1537–1571. doi: 10.1016/j.ymssp.2004.10.013.

Amontons, G. 1699. De la resistance causee dans les machines. *Memoires de l'Academie Royale des Sciences* , pp. 257–282.

ASTM 2015. Standard Guide for Determining the Reproducibility of Acoustic Emission Sensor ResponSe. *ASTM Standard* . doi: 10.1520/E0976-15.2.

ASTM E1316-13a 2004. Nondestructive Examinations 1. *Policy* , pp. 1–40. doi: 10.1520/E1316-13A.Copyright.

Badgujar, M. and Patil, A. 2014. Fault Diagnosis of Roller Bearing Using Acoustic Emission Technique and Fuzzy Logic. *Ijltet.Org* 3(4), pp. 170–175.

Balan, M.R. et al. 2016. A case study on relation between roughness, lubrication and fatigue life of rolling bearings. In: *IOP Conference Series: Materials Science and Engineering*. doi: 10.1088/1757-899X/147/1/012013.

Balderston, H.L. 1969. The detection of incipient failure in bearings. *Materials Evaluation,* 27(6), pp. 121–128.

Bansal, V. et al. 1990. Quality inspection of rolling element bearing using acoustic emission technique. *Journal of Acoustic Emission*

Bashir, I. et al. 1999. Release of acoustic energy during the fatiguing of a rolling-element bearing. *Applied Energy* . doi: 10.1016/S0306-2619(99)00002-1.

Baysec, S., Togun, N and Alsadoon, H. 2019. Experimental study based on acousitc emission and vibration signals to detect the presence of defects in rolling element. *International Journal of Scientific Research* 8(9), pp. 28–34.

Bhushan, B. 2013. *Introduction to Tribology, Second Edition*. New York: Hohn Wiley & Sons, Ltd. doi: 10.1002/9781118403259.

Boness, R.J. et al. 1990. Wear studies using acoustic emission techniques. *Tribology International* . doi: 10.1016/0301-679X(90)90001-6.

Boness, R.J. and McBride, S.L. 1991. Adhesive and abrasive wear studies using acoustic emission techniques. *Wear* . doi: 10.1016/0043-1648(91)90363-Y.

Bowden, F. P. and Tabor, D. 1950. *The Friction and Lubrication of Solids. Part I*. New York: Oxford University Press Inc.

Brahimi, M. and Leouatni, M. 2016. Development of A Prognostics and Health Management System for the Railway Infrastructure – Review and Methodology. *Prognostics and System Health Management Conference (PHM-Chengdu)* , pp. 1–8. doi: 10.1109/PHM.2016.7819783.

Bruce, T. et al. 2015. Characterisation of white etching crack damage in wind turbine gearbox bearings. *Wear* 338–339, pp. 164–177. doi: 10.1016/J.WEAR.2015.06.008.

Cahill, B. 2018. *Use of rate of change of torque to detect damage in gear systems.* PhD Thesis, Cardiff University.

Campbell, C. 1989. Surface Acoustic Wave Devices and their Signal Processing Applications. Copyright © 1989 Elsevier Inc. All rights reserved. doi: https://doi.org/10.1016/B978-0-12-157345-4.X5001-2.

Chang, H. et al. 2009. Acoustic emission study of fatigue crack closure of physical short and long cracks for aluminum alloy LY12CZ. *International Journal of Fatigue* 31(3), pp. 403–407. doi: 10.1016/j.ijfatigue.2008.08.008.

Choudhury, A. and Tandon, N. 2000. Application of acoustic emission technique for the detection of defects in rolling element bearings. *Tribology International,* 33(1), pp. 39–45. doi: 10.1016/S0301-679X(00)00012-8.

Cockerill, A. et al. 2015. Use of high frequency analysis of acoustic emission signals to determine rolling element bearing condition. *Journal of Physics: Conference Series*

628(1). doi: 10.1088/1742-6596/628/1/012074.

Cockerill, A. et al. 2016. Determination of rolling element bearing condition via acoustic emission. *Proceedings of the Institution of Mechanical Engineers, Part J: Journal of Engineering Tribology* 230(11), pp. 1377–1388. doi: 10.1177/1350650116638612.

Cockerill, A. 2017. *Damage Detection of Rotating Machinery*. Cardiff University.

Colombo, S. et al. 2005. Frequency response of different couplant materials for mounting transducers. In: *NDT and E International*. doi: 10.1016/j.ndteint.2004.03.008.

Corso, C. 2018.*Theoretical and experimental development of a ZnO-based laterally excited thickness shear mode acoustic wave immunosensor for cancer biomarker detection.* Georgia Institute of Technology.

Coulomb, C.A. 1785. Theorie des machines simples. *Memoire de Mathematique et de Physique de l’Academie Royale* , pp. 145–173.

Couturier, J. and Mba, D. 2008. Operational Bearing Parameters and Acoustic Emission Generation. *Journal of Vibration and Acoustics* 130(April 2008), p. 024502. doi: 10.1115/1.2776339.

Crivelli, D. and Bland, S. 2016. Structural health monitoring via acoustic emission. *Reinforced Plastics* 60(6), pp. 390–392. doi: 10.1016/j.repl.2015.05.004.

Davidson, C. 1957. Bearings since the stone age. *Engineering* 183, p. 2.

Ding, Y. and Kuhnell B.T. 1997. The Physical Cause of Spalling in Gears. *Machine Condition Monitoring, The Research Bulletin of the Centre for Machine Condition Monitoring, Vol. 9. Monash University*.

Dornfeld, D. 1992. Application of acoustic emission techniques in manufacturing. *NDT and E International* . doi: 10.1016/0963-8695(92)90636-U.

Dowson, D. and Higginson, G.R. 1959. A numerical solution to the elasto-hydrodynamic problem. *Journal of mechanical engineering science* 1(1), pp. 6–15. doi: 10.1243/JMES_JOUR_1959_001_004_02.

Duncan Dowson 1998. *History of Tribology, 2nd Edition*. Wiley-Blackwell; 2nd edition.

Ehrich, F.E. 1992. *Handbook of rotordynamics*. McGraw-Hill, New York, USA.

Elforjani, M. and Mba, D. 2008. Observations and location of acoustic emissions for a naturally degrading rolling element thrust bearing. *Journal of Failure Analysis and Prevention* 8(4), pp. 370–385. doi: 10.1007/s11668-008-9141-x.

Elforjani, M. and Mba, D. 2009a. Detecting natural crack initiation and growth in slow speed shafts with the Acoustic Emission technology. *Engineering Failure Analysis* 16(7), pp. 2121–2129. doi: 10.1016/j.engfailanal.2009.02.005.

Elforjani, M. and Mba, D. 2009b. Natural mechanical degradation measurements in slow speed bearings. *Engineering Failure Analysis* 16(1), pp. 521–532. doi: 10.1016/j.engfailanal.2008.06.005.

Elforjani, M. and Mba, D. 2010. Accelerated natural fault diagnosis in slow speed bearings with Acoustic Emission. *Engineering Fracture Mechanics* . doi:

10.1016/j.engfracmech.2009.09.016.

Evans, M.-H. 2012. White structure flaking (WSF) in wind turbine gearbox bearings: effects of ‘butterflies’ and white etching cracks (WECs). *Materials Science and Technology* 28(1), pp. 3–22. doi: 10.1179/026708311X13135950699254.

Evans, M.-H. et al 2013. Serial sectioning investigation of butterfly and white etching crack (WEC) formation in wind turbine gearbox bearings. *Wear.* 302(1):1573–1582. doi: 10.1016/j.wear.2012.12.031.

Fan, Y. et al. 2010. Modelling acoustic emissions generated by sliding friction. *Wear* . doi: 10.1016/j.wear.2009.12.010.

Ferrer, C. et al. 2010. Discrete acoustic emission waves during stick-slip friction between steel samples. *Tribology International* 43(1–2), pp. 1–6. doi: 10.1016/j.triboint.2009.02.009.

Fitch, J. 2003. Silent Assumptions of Bearing Reliability.

Freeth, T. et al. 2006. Decoding the Antikythera Mechanism : Investigation of an Ancient Astronomical Calculator. *Notes* 444(7119), pp. 587–591.

García Márquez, F.P. et al. 2012. Condition monitoring of wind turbines: Techniques and methods. *Renewable Energy* 46, pp. 169–178. doi: 10.1016/j.renene.2012.03.003.

Gegner, J. 2011. Tribological aspects of rolling bearing failures. *INTECH Open Access Publisher.*

Graney, B.P. and Starry, K. 2011. Rolling element bearing analysis crosses threshold. *Materials Evaluation* 70(1), pp. 78–85. doi: 10.1016/0308-9126(80)90087-5.

Gould, B. and Greco, A. 2016. Investigating the process of white etching crack initiation in bearing steel. *Tribol. Lett.* 62(2):1–14. doi: 10.1007/s11249-016-0673-z.

Gould, B. et al 2019. The influence of steelmicrostructure and inclusion characteristics on the formation ofpremature bearing failures with microstructural alterations. Mat.Sci. Eng. doi: https://www.sciencedirect.com/science/article/pii/S0921509319302576?via%3Dihub.

GWEC 2023 Global Wind Energy Council. doi: https://gwec.net/wp-content/uploads/2023/04/GWEC-2023_interactive.pdf.

Halme, J. and Andersson, P. 2010. Rolling contact fatigue and wear fundamentals for rolling bearing diagnostics - State of the art. *Proceedings of the Institution of Mechanical Engineers, Part J: Journal of Engineering Tribology* 224(4), pp. 377–393. doi: 10.1243/13506501JET656.

Hamrock, B., Schmid, S., Jacobson, B., Faulkner, L. 2004. *Fundamentals of Fluid Film Lubrication*. Boca Raton: CRC Press.

Hao, R. et al. 2009. Defects diagnosis of bearing by means of acoustic emission and continuous wavelet transform. *Key Engineering Materials* 414, pp. 651–657. doi: 10.4028/www.scientific.net/KEM.413-414.651.

Harris, T.A. and Kotzalas, M.N. 2006. *Essential Concepts of bearing technology*. doi:

10.1201/b15723-9.

Hase, A. et al. 2012. Correlation between features of acoustic emission signals and mechanical wear mechanisms. *Wear* . doi: 10.1016/j.wear.2012.05.019.

Hau, E. and von Renouard, H. 2006. Wind Turbines. 3. doi: 10.1007/3-540-29284-5.

Hawman, M.W. and Galinaitis, W.S. 1988. Acoustic emission monitoring of rolling element bearings. *IEEE 1988 Ultrasonics Symposium Proceedings* 2, pp. 885–889. doi: 10.1109/ULTSYM.1988.49503.

He, Y. et al. 2009. Defect Diagnosis for Rolling Element Bearings Using Acoustic Emission. *Journal of Vibration and Acoustics* 131(6), p. 061012. doi: 10.1115/1.4000480.

Heiple, C. R and Carpenter, S. 1987. Acoustic emission produced by deformation of metals and alloys- a review. *J. Acoustic Emission* 6(4), pp. 215–237.

Hertz, H. 1882. “Uber die Beruhrung Fester Elastischer Korper (On the Contact of Elastic Solids)”. *J Reine und Angewandte Mathematik* 92, pp. 156–171.

Hellier, C.J. 2020. The Signal-Shaping Chain. *Handbook of Nondestructive Evaluation, 3rd ed. McGraw-Hill Education; New York, NY, USA.* doi: https://www.accessengineeringlibrary.com/content/book/9781260441437/toc-chapter/chapter10/section/section23.

Holford, K. M. , Carter, D.C. 1999. Acoustic Emission Source Location. *Key Engineering Materials* 167–168, pp. 162–171. doi: https://doi.org/10.4028/www.scientific.net/KEM.167-168.162.

Holland, S.D. and Sachse, W. 2006. Automatic Determination of Acoustic Plate Source-Detector Separation from One Waveform. *IEEE Transactions on Ultrasonics, Ferroelectrics, and Frequency Control* . doi: 10.1109/TUFFC.2006.1593375.

Holroyd, T.J. and Randall, N. 1993. Use of Acoustic Emission for Machine Condition Monitoring,. *British Journal of Non-Destructive Testing* 35(2), pp. 75–78.

Howard, I. 1994. A Review of Rolling Element Bearing Vibration 'Detection, Diagnosis and Prognosis'. *DSTO Aeronautical and Maritime Research Laboratory*

Hsu, N.N. and Breckenridge, F.R. 1981. CHARACTERIZATION AND CALIBRATION OF ACOUSTIC EMISSION SENSORS. *Materials Evaluation* 39(1), pp. 60–68.

Huang, M., Jiang L., Liaw, P.K., Brooks, C. R., Seeley, R., and Klarstrom, D.L. 1998. Using Acoustic Emission in Fatigue and Fracture. *Journal of Materials* 50(11)

Hubner, H.B. et al. 2020. A comparative study of two indirect methods to monitor surface integrity of ground components, *Structural Health Monitoring-an*

International Journal, 19, pp. 1856-1870.

Hutchings, I.M. 2016. Leonardo da Vinci's studies of friction. *Wear* 360–361, pp. 51–66. doi: 10.1016/j.wear.2016.04.019.

Hutt, S. et al. 2019. The acoustic emission from asperity interactions in mixed lubrication. *Proc. R. Soc. A* **475**: 20180900. http://dx.doi.org/10.1098/rspa.2018.0900

ISO/TR 13881:2000 2000. Petroleum and natural gas industries -- Classification and conformity assessment of products, processes and services.

ISO 281 1990. Rolling bearings -- Dynamic load ratings and rating life.

ISO 281 2007. Rolling bearings -- Dynamic load ratings and rating life.

ISO 683-17 2014. Heat-treated steels, alloys steels and free-cutting steels. *Part 17: Ball and roller bearing steels*

Jamaludin, N. et al. 2001. Condition monitoring of slow-speed rolling element bearings using stress waves. *Proceedings of the Institution of Mechanical Engineers, Part E: Journal of Process Mechanical Engineering* . doi: 10.1177/095440890121500401.

Jane Wang, Q. and Chung, Y.-W. 2013. *Encyclopedia of Tribolgy*. New York: Springer-Verlag New York Inc.

Jardine, A.K.S. et al. 2006. A review on machinery diagnostics and prognostics implementing condition-based maintenance. *Mechanical Systems and Signal Processing* . doi: 10.1016/j.ymssp.2005.09.012.

Javed, K. et al. 2015. A new multivariate approach for prognostics based on extreme learning machine and fuzzy clustering. *IEEE Transactions on Cybernetics* . doi: 10.1109/TCYB.2014.2378056.

Jeevagan, N. et al. 2014. Project Stay Alert. In: *Proceedings of the 4th IEEE Global Humanitarian Technology Conference, GHTC 2014*. doi: 10.1109/GHTC.2014.6970361.

Johnson, K.L. 1985. *Contact Mechanics*. doi: 10.1115/1.3261297.

Jost, H.P. 1992. Tribology: The first 25 years and beyond - achievements, shortcomings and future tasks. *Industrial lubrication and tribology* 44, p. 22.

Kakishima, H. et al. 2000. Measurement of acoustic emission and vibration of rolling bearings with an artificial defect. *Quarterly Report of RTRI* 41(3), pp. 127–130. doi: 10.2219/rtriqr.41.127.

Kaydon Bearings. 2014. Bearing selection for low-speed applications. An SKF Group brand. doi: https://www.kaydonbearings.com/white_papers_8.htm

Keller, J. 2021. WhiteWind : White Etching Crack (WEC) Bearing Failures in Wind Turbines. *Cooperative Research and Development Final Report CRADA Number: CRD-18-00758 NREL. Golden, CO Natl Renew Energy Lab NREL/TP-5000-81232.*

Lebold, M. et al. 2002. OSA-CBM architecture development with emphasis on XML implementations. *Maintenance and Reliability Conference (MARCON)*

Li, C.J. and Li, S.Y. 1995. Acoustic emission analysis for bearing condition monitoring. *Wear* 185(1), pp. 67–74. doi: 10.1016/0043-1648(95)06591-1.

Li G.-l., et al. 2013. Acoustic emission monitoring and failure mechanism analysis of rolling contact fatigue for Fe-based alloy coating. *Tribol Int, 61, pp. 129-137.*

Lin, T.R. 1996. Hydrodynamic lubrication of journal bearings including micropolar lubricants and three-dimensional irregularities. *Wear* 192(1–2), pp. 21–28. doi: 10.1016/0043-1648(95)06740-X.

Liu, C. et al. 2017. Acoustic emission signal processing for rolling bearing running state assessment using compressive sensing. *Mechanical Systems and Signal Processing* .

doi: 10.1016/j.ymssp.2016.12.010.

Liu, J.Y. et al. 1975. Dependence of bearing fatigue life on film thickness to surface roughness ratio. *ASLE Transactions* . doi: 10.1080/05698197508982757.

Liu, X. et al. 2011. A comparison of acoustic emission and vibration on bearing fault detection. *2011 International Conference on Transportation, Mechanical, and Electrical Engineering (TMEE): 16-18 December* , pp. 922–926. doi: 10.1109/TMEE.2011.6199353.

López-Uruñuela, F. et al. 2021. Broad review of “White Etching Crack” failure in wind turbine gearbox bearings: Main factors and experimental investigations. *International Journal of Fatigue Vol 145.* doi: https://www.sciencedirect.com/science/article/pii/S014211232030623X#b0010

Lord, J. and Larsson, R. 2001. Effects of slide-roll ratio and lubricant properties on elastohydrodynamic lubrication film thickness and traction. *Proceedings of the Institution of Mechanical Engineers, Part J: Journal of Engineering Tribology* . doi: 10.1243/1350650011543556.

Lundberg, G. and Palmgren, A. 1947. Dynamic Capacity of Rolling Bearings. *Acta Polytechnica* 1(3), pp. 1–52.

Luyckx, J. 2012: White etching crack failure mode in roller bearings: from observation via analysis to understanding and an industrial solution. *In Rolling element bearings. ASTM International.*

Mathew, S. et al. 2012. Identification of failure mechanisms to enhance prognostic outcomes. *Journal of Failure Analysis and Prevention* . doi: 10.1007/s11668-011-9508-2.

Mathews, J.R. 1983. *Acoustic emission.* New York: Gordon and Breach Science Publishers Inc.

Mba, D. 2003. Acoustic emissions and monitoring bearing health. *Tribology Transactions* 46(3), pp. 447–451. doi: 10.1080/10402000308982649.

Mba, D. and Rao, R.B.K.N. 2006. Development of acoustic emission technology for condition monitoring and diagnosis of rotating machines: Bearings, pumps, gearboxes, engines, and rotating structures. *Shock and Vibration Digest* 38(2), pp. 3–16. doi: 10.1177/0583102405059054.

Mcfadden, P.D. and Smith, J.D. 1984. Acoustic Emission Transducers for the Vibration Monitoring of Bearings at Low Speeds. *Proceedings of the Institution of Mechanical Engineers, Part C: Journal of Mechanical Engineering Science* 198(2), pp. 127–130.

Miettinen, J. and Andersson, P. 1998. Methods to monitor the running situation of grease lubricated rolling bearings. *In VTT Symposium,* 180, pp. 92-101. Valtion Teknillinen Tutkimuskeskus.

Miettinen, J. and Andersson, P. 2000. Acoustic emission of rolling bearings lubricated with contaminated grease. *Tribology International* 33(11), pp. 777–787. doi: 10.1016/S0301-679X(00)00124-9.

Miller, R. K., Hill, E. v. K. and Moore, P.O. 2005. *Acoustic Emission Testing, Vol. 6*. 3rd ed. American Society for Nondestructive Testing, ASNT.

Mobil, 2020. The white etching cracking phenomenon: how to minimise it and keep your wind turbines turning.

MORALES-ESPEJEL, G.E. and GABELLI, A. 2015. THE PROGRESSION OF SURFACE ROLLING CONTACT FATIGUE DAMAGE OF ROLLING BEARINGS. *Evolution, BUSINESS AND TECHNOLOGY FROM SKF*.

Ruiz-Cárcel, C. et al. 2014. Use of Spectral Kurtosis for Improving Signal to Noise Ratio of Acoustic Emission Signal from Defective Bearings. *J Fail. Anal. and Preven.* 14, 363–371.. https://doi.org/10.1007/s11668-014-9805-7.

Rother, A. et al.2015. A brief review and a first application of time-frequency-based analysis methods for monitoring of strip rolling mills. *J Process Contr*; 35: 65–79.

Morhain, A. and Mba, D. 2003. Bearing defect diagnosis and acoustic emission. *Proceedings of the Institution of Mechanical Engineers, Part J: Journal of Engineering Tribology* 217(4), pp. 257–272. doi: 10.1243/135065003768618614.

Nair, A. and Cai, C.S. 2010. Acoustic emission monitoring of bridges: Review and case studies. *Engineering Structures* . doi: 10.1016/j.engstruct.2010.02.020.

Naumann, J.R. 2016. *Acoustic Emission Monitoring of Wind Turbine Bearings*. University of Sheffield.

NDT Resource Center 2018. AE Signal Features.

Neale, M.J. 1995. *Component Failures, Maintenance and Repair: Tribology Handbook*. Butterworth-Heinemann Ltd.

Nienhaus, K. et al. 2012. Development of Acoustic Emission (AE) based defect parameters for slow rotating roller bearings. In: *Journal of Physics: Conference Series*. doi: 10.1088/1742-6596/364/1/012034.

NSK 2009. New Bearing Doctor - Maintenance of Bearings.

Orhan, S. et al. 2006. Vibration monitoring for defect diagnosis of rolling element bearings as a predictive maintenance tool: Comprehensive case studies. *NDT and E International* . doi: 10.1016/j.ndteint.2005.08.008.

Patil, A.P. et al. 2020. Vibration based modelling of acoustic emission of rolling element bearings. *Journal of Sound and Vibration* . doi: 10.1016/j.jsv.2019.115117.

Pollock, A.A. 1989. *Acoustic Emission Inspection, Metals Handbook.* 9th ed. ASM International. 17:278-294.

Pullin, R. et al., 2012. Identification of the Onset of Cracking in Gear Teeth Using Acoustic Emission. *Journal of Physics: Conference Series*, 382(1), p.12050.

Qi, G. 2000. Wavelet-based AE characterization of composite materials. *NDT and E International* . doi: 10.1016/S0963-8695(99)00037-7.

Raharjo, P. et al. 2011. An Investigation of Acoustic Emission Responses of a Self Aligning Spherical Journal Bearing. *The Eighth International Conference on Condition Monitoring and Machinery Failure Prevention Technologies*

Raja Hamzah, R.I. and Mba, D. 2009. The influence of operating condition on acoustic emission (AE) generation during meshing of helical and spur gear. *Tribology International* 42(1), pp. 3–14. doi: 10.1016/j.triboint.2008.06.003.

Ramadan, S. et al. 2008. Detection of stress corrosion cracking of high-strength steel used in prestressed concrete structures by acoustic emission technique. *Applied Surface Science* 254(8), pp. 2255–2261. doi: 10.1016/j.apsusc.2007.09.011.

Rao, V. et al. 2013. Study of fault in outer race of Roller Bearings using Acoustic emission and Vibration analysis. *Advances In Modelling And Analysis Of Aerodynamic Systems* , pp. 62–66.

Reeves, C.J. and Menezes, P.L. 2016. Advancements in Eco-friendly Lubricants for Tribological Applications: Past, Present, and Future. In: Davim, J. P. ed. *Ecotribology: Research Developments*. Cham: Springer International Publishing, pp. 41–61. doi: 10.1007/978-3-319-24007-7_2.

Richardson A.D. et al 2018. The evolution of white etching cracks (WECs) in rolling contact fatigue-tested 100Cr6 steel. Tribol. Lett. 66:6.

Rindorf, H.J. 1981. *Acoustic Emission Source Location in Theory and in Practice*. Bruel and Kjaer Technical Review. 2: 3-44.

Rogers, L.M. 1979. The application of vibration signature analysis and acoustic emission source location to on-line condition monitoring of anti-friction bearings. *Tribology International* 12(2), pp. 51–58. doi: https://doi.org/10.1016/0301-679X(79)90001-X.

Rynearson, S.R. 2022. Understanding Bearing Life. doi: https://www.bartlettbearing.com/understanding-bearing-life/

Sandoval, H. et al. 2013. Acoustic emission-based early fault detection in tapered roller bearings. *Ingeniería E Investigación* 33(3), pp. 5–10.

Schey, J.A. 1984. Tribology in Metalworking: Friction, Lubrication, and Wear. *Journal of Applied Metalworking,* 3(2), p. 173. doi: 10.1007/BF02833697.

Schnabel, S. et al. 2017. The detection of plastic deformation in rolling element bearings by acoustic emission. *Tribology International* 110(February), pp. 209–215. Available at: http://dx.doi.org/10.1016/j.triboint.2017.02.021.

Scruby, C.B. 1987. An introduction to acoustic emission. *Journal of Physics E: Scientific Instruments* . doi: 10.1088/0022-3735/20/8/001.

Serrato, R. et al. 2007. Effect of lubricant viscosity grade on mechanical vibration of roller bearings. *Tribology International* . doi: 10.1016/j.triboint.2007.01.025.

Sharma, R.B. and Parey, A. 2019. Modelling of acoustic emission generated in rolling element bearing. *Applied Acoustics* . doi: 10.1016/j.apacoust.2017.07.015.

Shiroishi, J. et al. 1997. Bearing Condition Diagnosis via Vibration and Acoustic Emission Measurements. *Mechanical Systems and Signal Processing* 11(5), pp. 693–705.

SKF 2012. Bearing calculation.

SKF 2017. "Bearings" doi: https://www.skf.com/group/investors/bearings-market.

SKF 2018. White Etching Cracks are a Symptom of Bearing Failure.

SKF 2019. Radial bearings. Available at: https://www.skf.com/group/products/rolling-bearings/roller-bearings/cylindrical-roller-bearings/single-row-cylindrical-roller-bearings/productid-NU 202 ECP.

SKF 2022. "Annual Report 2021". doi: https://investors.skf.com/sites/default/files/pr/202203022809-1.pdf

Smith, J.D. 1982. Vibration monitoring of bearings at low speeds. *Tribology International,* 15(3), pp. 139–144. doi: 10.1016/0301-679X(82)90130-X.

Spikes, H. and Olver, A. 2003. Basics of mixed lubrication. *Lubrication Science* . doi: 10.1002/ls.3010160102.

Stachowiak, G. and Batchelor, A. 2006. *Engineering Tribology (Third Edition)*. doi: 10.1016/B978-0-08-097053-0.00001-7.

Stewart S, Ahmed R. Rolling contact fatigue of surface coatings—a review. *Wear; 253: 1132–44.*

Tahir, M.M. et al. 2017. Enhancing Fault Classification Accuracy of Ball Bearing Using Central Tendency Based Time Domain Features. *IEEE Access* . doi: 10.1109/ACCESS.2016.2608505.

Tallian, T.E. 1967. On competing failure modes in rolling contact. *ASLE Transactions* . doi: 10.1080/05698196708972201.

Tan, C. 1990. Application of acoustic emission to the detection of bearing failures. In: *International Tribology conference*. Brisbane.

Tan, C.K. and Mba, D. 2005. Limitation of acoustic emission for identifying seeded defects in gearboxes. *Journal of Nondestructive Evaluation* . doi: 10.1007/s10921-

005-6657-9.

Tandon, N. et al. 2007. A comparison of some condition monitoring techniques for the detection of defect in induction motor ball bearings. *Mechanical Systems and Signal Processing* 21(1), pp. 244–256. doi: 10.1016/j.ymssp.2005.08.005.

Tandon, N. and Choudhury, A. 1999. A review of vibration and acoustics measurement methods for the detection of defects in rolling element bearing. *Tribology International,* 32(8), pp. 469–480. doi: 10.1016/S0301-679X(99)00077-8.

Tandon, N. and Nakra, B. 1990. Defect detection in rolling element bearings by acoustic emission method. *Journal of Acoustic Emission* 9, pp. 25–28.

Technavio Research 2016. doi: https://www.businesswire.com/news/home/20161012005036/en/Top-5-Vendors-in-the-Wind-Turbine-Bearing-Market-from-2016-to-2020-Technavio

Torkamani, S. et al. 2014. A novel damage index for damage identification using guided waves with application in laminated composites. *Smart Materials and Structures* . doi: 10.1088/0964-1726/23/9/095015.

Toutountzakis, T., Tan, C.K. & Mba, D., 2005. Application of acoustic emission to seeded gear fault detection. *NDT & E International*, 38(1), pp.27–36.

Unnþórsson, R. 2013. Hit Detection and Determination in AE Bursts. *Acoustic Emission - Research and Applications* . doi: 10.5772/54754.

Vereins, V. and Gewerbejeisses, B. 1982. Tribology Group Nominated Lecture. 196

Viktorov, I.A. 1967. *Rayleigh and Lamb Waves; Physical theory and application*. New York: Plenum press.

Weeks, I. 2015. Cardiff School of Engineering An Experimental Investigation into the Mixed Lubrication of Steel Surfaces. (April)

Wiggelinkhuizen, E. et al. 2008. Assessment of Condition Monitoring Techniques for Offshore Wind Farms. *Journal of Solar Energy Engineering* . doi: 10.1115/1.2931512.

Williams, T. et al. 2001. Rolling element bearing diagnostics in run-to-failure lifetime testing. *Mechanical Systems and Signal Processing* 15(5), pp. 979–993. doi: 10.1006/mssp.2001.1418.

Wilson, B. 1998. Friction, Wear and Lubrication: A Textbook in Tribology. *Industrial Lubrication and Tribology* . doi: 10.1108/ilt.1998.01850eae.001.

Wysoclci, A. and Feest, B. 1997. Bearing failure: Causes and cures. *EC and M: Electrical Construction and Maintenance* 96(2), pp. 52-X6. doi: 10.13140/RG.2.1.4996.7525.

Yang, Z. et al. 2011. An Experimental Investigation on the Wake Characteristics of a Wind Turbine in an Atmospheric Boundary Layer Wind. *Aiaa* 3815(June), pp. 1–18. doi: 10.2514/6.2016-1732.

Yoshioka, T. 1993. Detection of rolling contact sub-surface fatigue cracks using acoustic emission technique. *Lubrication Engineering*

Yoshioka, T. and Fujiwara, T. 1982. A new acoustic emission source locating system for the study of rolling contact fatigue. *Wear* . doi: 10.1016/0043-1648(82)90314-3.

Yoshioka, T. and Fujiwara, T. 1984. Application of acoustic emission technique to detection of rolling bearing failure. *ASME Prod. Engng Div.* (14), pp. 55–76.

Yoshioka, T. and Fujiwara, T. 1987. Paper II(i) Measurement of propagation initiation and propagation time of rolling contact fatigue cracks by observation of acoustic emission and vibration. *Tribology Series* . doi: 10.1016/S0167-8922(08)71045-9.

Zaretsky, E. V et al. 1996. Comparison of life theories for rolling element bearings. *Tribology Transactions(USA)* . doi: 10.1080/10402009608983560.

Zhu, D. and Jane Wang, Q. 2011. Elastohydrodynamic Lubrication: A Gateway to Interfacial Mechanics—Review and Prospect. *Journal of Tribology* . doi: 10.1115/1.4004457.